ELECTROHYDRODYNAMIC INDUCTION AND CONDUCTION PUMPING OF DIELECTRIC LIQUID FILM: THEORETICAL AND NUMERICAL STUDIES

A Dissertation

by

SALEM A. S. AL DINI

Submitted to the Office of Graduate Studies of
Texas A&M University
in partial fulfillment of the requirements for the degree of

DOCTOR OF PHILOSOPHY

December 2005

Major Subject: Mechanical Engineering

ELECTROHYDRODYNAMIC INDUCTION AND CONDUCTION PUMPING OF DIELECTRIC LIQUID FILM: THEORETICAL AND NUMERICAL STUDIES

A Dissertation

by

SALEM A. S. AL DINI

Submitted to the Office of Graduate Studies of
Texas A&M University
in partial fulfillment of the requirements for the degree of

DOCTOR OF PHILOSOPHY

Approved by:

Chair of Committee, J. Seyed-Yagoobi
Committee Member, A. Beskok
J. C. Han
Y. A. Hassan
Head of Department, D. L. O'Neal

December 2005

Major Subject: Mechanical Engineering

ABSTRACT

Electrohydrodynamic Induction and Conduction Pumping of Dielectric Liquid Film: Theoretical and Numerical Studies. (December 2005)

Salem A. S. Al Dini, B.S.; M.S., King Fahad University of Petroleum and Minerals, Dhahran, Saudi Arabia

Chair of Advisory Committee: Dr. Jamal Seyed-Yagoobi

Electrohydrodynamic (EHD) pumping of single and two-phase media is attractive for terrestrial and outer space applications since it is non-mechanical, lightweight, and involves no moving parts. In addition to pure pumping purposes, EHD pumps are also used for the enhancement of heat transfer, as an increase in mass transport often translates to an augmentation of the heat transfer. Applications, for example, include two-phase heat exchangers, heat pipes, and capillary pumping loops.

In this research, EHD induction pumping of liquid film in annular horizontal and vertical configurations is investigated. A non-dimensional analytical model accounting for electric shear stress existing only at the liquid/vapor interface is developed for attraction and repulsion pumping modes. The effects of all involved parameters including the external load (i.e. pressure gradient) and gravitational force on the non-dimensional interfacial velocity are presented. A non-dimensional stability analysis of EHD induction pumping of liquid film in a vertical annular configuration in the presence of external load for repulsion mode is carried out. A general non-dimensional stability

criterion is presented. Stability maps are introduced allowing classification of pump operation as stable or unstable based on the input operating parameters.

An advanced numerical model accounting for the charges induced throughout the bulk of the fluid due to the temperature gradient for EHD induction pumping of liquid film in a vertical annular configuration is derived. A non-dimensional parametric study including the effects of external load is carried out for different entrance temperature profiles and in the presence of Joule heating.

Finally, a non-dimensional theoretical model is developed to investigate and to understand the EHD conduction phenomenon in electrode geometries capable of generating a net flow. It is shown that with minimal drag electrode design, the EHD conduction phenomenon is capable of providing a net flow. The theoretical model is further extended to study the effect of EHD conduction phenomenon for a two-phase flow (i.e. a stratified liquid/ vapor medium). The numerical results presented confirm the concept of liquid film net flow generation with the EHD conduction mechanism.

DEDICATION

This dissertation is dedicated to my wife, Amani Shabaan, for her continuous sacrifices, support, and encouragement not only through my doctoral program but throughout our life together.

ACKNOWLEDGMENTS

The author is deeply indebted to Professor Seyed-Yagoobi, chairman of his doctoral committee, for his guidance, encouragement, friendship, and eagerness to share his expertise in conducting this research study. The concern and support of other doctoral committee members, Professors J. C. Han, Ali Beskok, and Y. A. Hassan are also greatly appreciated.

Acknowledgement is due to King Fahad University of Petroleum and Minerals for providing scholarship to the author to complete this work.

Thanks are due to my friend Nauman Sheikh for his help and valuable suggestions regarding the finite element technique used in this research. Thanks are also extended to my friend Zahir Latheef for his time and help during this research.

The author's sincere gratitude goes to his parents, his wife, and his children for their understanding and support during the period of this study.

TABLE OF CONTENTS

CHAPTER Page

Page

LIST OF FIGURES

FIGURE Page

FIGURE Page

FIGURE Page

FIGURE Page

FIGURE Page

FIGURE Page

LIST OF TABLES

NOMENCLATURE

A = constant

a = parameter (Tables 4.5, 4.6, and 4.7)

b = parameter (Tables 4.5, 4.6, and 4.7) and mobility ($m^2 / V \cdot s$) (Ch. VI)

B = constant

c = parameter (Tables 4.5, 4.6, and 4.7) and Fourier series constant (Ch. IV)

c_p = specific heat at constant pressure (J/kg.K)

C_o = a characteristic constant ($= n_{eq} d^2 / \varepsilon V$)

d = parameter (Tables 4.6 and 4.7) and half-width of the channel (m)

d_{hg} = axial gap between the ground electrode and high voltage electrode

D = diffusion coefficient

D = displacement field ($= \varepsilon E$) (C / m^2)

e = parameter (Table 4.7) and electron charge (1.6×10^{-19} C)

E = electric field (V / m)

EC = electrode configuration

f = frequency, Hz

f_e = electric body force density (N / m^3)

F(ω) = a parameter representing field-enhanced dissociation ($= I_1(2\omega) / \omega$,

$\omega = \left[(e^3 |E|) / (4\pi\varepsilon k_B^2 T^2) \right]^{1/2}$)

g = parameter (Table 4.7) and gravitational constant (m/s^2)

G = gravitational force ($=\rho g$) ($kg/m^2.s^2$)

HV = high voltage

I = current (A)

I_0 = modified Bessel function of first kind and order zero

I_1 = modified Bessel function of first kind and order one

j = imaginary number = $\sqrt{-1}$

J = current density (A/m^2)

k = thermal conductivity (W/mK)

K = electric wave number = $2\pi/\lambda$ (1/m)

k_d = dissociation rate constant under electric field

k_{d0} = dissociation rate constant with no electric field

k_r = recombination rate constant

k_B = Boltzmann constant (1.381×10^{-23} J / K)

L = pump length (m)

m = mass flux (kg/s)

M_e^* = dimensionless number = $\rho_{b0}\varepsilon_0\hat{\varphi}^2 \big/ 2\mu_{b0}^2$

N_e^* = dimensionless number = $\mu_{b0}\varepsilon_0 \big/ \rho_{b0}\sigma_{b0}\,\delta^2$

n = negative charge density (C/m^3)

N = concentration of neutral species

p = positive charge density (C/m^3)

P = pressure (Pa)

Pr = Prandtl number = $c_p\mu/k$

q = net electric charge density (C/m^3)

q" = heat flux (W/m^2)

r = radial space coordinate

R = radius (m)

Re = real component of a complex number

S = slip coefficient $= \left[\varepsilon_0(\omega - KU)\right]/\sigma$

T = time (s)

t_T = ionic transit time ($= d/bE$) (s)

T = Temperature (K)

u = velocity in r direction (m/s) (Ch. IV and V)

u = velocity in x direction (m/s) (Ch. VI)

v = velocity in y direction (m/s)

V = voltage (V)

w = velocity in z direction (m/s)

W = interfacial velocity in z direction (m/s) (Ch. IV and V)

x = x coordinate

y = y coordinate

z = space coordinate in streamwise direction (m) (Ch. IV and V)

Greek Symbols

α = a characteristic constant ($= D / bV$)

δ = liquid film thickness (m)

ε_0 = electric permittivity of vacuum (F / m)

ε = electric permittivity (F / m)

λ = wavelength (m)

μ = dynamic viscosity ($Pa \cdot s$)

θ = circumferential angle

ϕ = electric potential (V)

Φ = viscous dissipation function (W/m^3)

Θ = electric potential time function

ρ = fluid density (kg/m^3)

σ = electric conductivity (S / m)

τ = shear stress (N/m^2)

τ = charge relaxation time ($= \varepsilon / \sigma$) (s) (only Ch. VI)

ω = electric angular wave velocity ($= 2\pi f$) (1/s)

Ψ = electric potential space function (V)

Subscripts and Superscripts

b0 = bulk value at pump entrance

c = characteristic

C = complex component of a complex number

e = electric

i = space coordinate in tensor notation

int = interface

j = space coordinate in tensor noation

l = liquid

n = Fourier series index

R = real component of a complex number

s = solid

T = total

v = vapor

r = in r direction

z = in z direction

zr = in z direction acting on a plane with normal r

^ = peak value

‘ = conjugate complex value

+ = positive ion

- = negative ion

* = non-dimensional value

eq = equilibrium state

CHAPTER I

INTRODUCTION

Background

Electrohydrodynamic (EHD) pumps have potentially significant advantages not only for pure pumping applications, but also for heat transfer augmentation. In general, EHD pumps are lightweight, non-mechanical, have simple design, produce no vibration, and require little maintenance. In addition, low power consumption and easy performance control, by varying the applied electric field, are of the significant attractive advantages of the application of EHD pump.

Enhancing the performance of the heat transfer equipments in phase-changing processes for industrial systems (i.e. HVAC&R), where heat transfer improvement is greatly desired, can be achieved by active (i.e. pumping) and/or passive (i.e. enhanced surfaces) techniques. As an example, during the evaporation process (i.e. falling film evaporators) the overall process is expected to be improved drastically by using the enhanced surface (i.e. passive technique) if the dry-out did not occur and the refrigerant liquid is getting in contact with the surface fast enough. On the other hand, during the condensation process the liquid film is required to be removed as quickly as possible from the enhanced surface in order to allow the saturated vapor to make contact with the surface in a rapid fashion. However, the increasing volume of the condensate due to the condensation heat transfer enhancement needs to be managed, hence the issue of

---

This dissertation follows the style and format of the ASME Journal of Heat Transfer.

flow management becomes more significant. EHD pumping provides a talented technology for local heat transfer enhancement in two-phase flow systems, as well as managing the fluid flow.

Two EHD mechanisms have been already explored in regards to the mass transfer and heat transfer enhancement namely: ion-drag pumping and the EHD extraction phenomena. The Ion-drag pumping produces acceptable mass transfer rates; however, it is not desirable because it can deteriorate the electrical properties of the working fluid when it operates for long time. EHD extraction has been shown to produce a considerable augmentation of two-phase heat transfer processes. When it is employed it reduces the liquid film thickness in condensers, therefore increasing the condensation heat transfer coefficient. Nevertheless, means have to be provided to transport the extracted condensate, which leads to a new set of problems, and thus has limited its potential uses.

It is here that EHD induction pumping provides a promising candidate. This mechanism (i.e. EHD induction pumping) is particularly appropriate for applications involving a liquid/vapor interfaces, since the amount of charge induced and available for pumping depends on the gradient of the electric conductivity which already exists due to the temperature gradient within the liquid film and the due to the conductivity jump across the liquid/vapor interface. The conductivity jump across the interface is generally much steeper and, consequently, much larger number of charges is induced. Therefore, for the evaporation process the EHD pumping mechanism can be utilized to wet the surface suitably, while for the condensation process, it can be implemented to pump the

condensate film layer along the condensation surface as it is formed, as well as to manage the flow as desired. Unlike the ion-drag pump, EHD induction pump can operate over long periods of time without harmfully affecting the fluid properties.

EHD induction pumping of liquids and liquid/vapor medium has been studied to some extents both with regards to pure mass transfer and heat transfer enhancement. However, EHD induction pumping of liquid film in horizontal and vertical annular configurations in presence and absence of gravity has not been studied previously.

Another attractive use for EHD pumping can be found in the outer space applications where demanding requirements for thermal control are in increase. For modern space equipments and instruments capillary devices, such as heat pipe, are usually considered as thermal control devices. However, these devices have some potential drawbacks due to the occurrence of dry-out in the evaporator during the startup and transient heat loading, as well as low heat transfer capacity considering the overall mass requirement which is a main concern in space application. It can be envisioned how an advanced thermal control device such as an EHD heat pipe can provide an exciting alternative. It provides a quick recovery from the evaporator dry-out, on top of the remarkable enhancement in heat transport capacity. In EHD heat pipe, EHD pump is installed in the liquid passage, which can be considered as isothermal section, to generate an additional pumping pressure which in turns result in an increase in the evaporation process, hence thinner liquid film in the heat pipe (i.e. enhancement in heat transfer performance). In an isothermal single phase liquid, Coulomb force which is the force acting on the free charges is the only mechanism for generating a net EHD motion.

There are three main EHD mechanisms utilizing the Coulomb force: induction pumping, conduction pumping and ion-drag pumping. As it was mentioned above, the ion-drag pumping is not appropriate for any applications since over time it results in the degradation of the working fluid electric properties. The ion-drag is also potentially hazardous to operate due to the corona discharge associated with it. The induction pumping is not suitable for pumping of an isothermal single phase liquid due to the absence of the electric conductivity gradient. Unlike the induction and the ion-drag pumping, the conduction pumping is associated with the process of dissociation of the neutral electrolytic species and recombination of the generated ions which comes from the high electric field applied. The conduction term here represents a mechanism for electric current flow in which charged carriers are produced not by injection from electrodes, but by dissociation of molecules within the fluid. This process induces layers of finite thickness in the vicinity of the electrodes where the dissociation-recombination reactions are not in equilibrium. These are known as the heterocharge layers. The heterocharges are the charges having the opposite polarity from that of the electrode they are adjacent to and the attraction between the electrodes and heterocharge layers induces the fluid motion near the electrode from the liquid side to the electrode side. The EHD conduction pumping can be applied to the isothermal working fluid and will not degrade the electric properties of the working fluid since the imposed electric field will be below the intensity level necessary for the ion-drag pumping. The EHD conduction pumps can be fabricated in large and micro scales to accommodate for various needs in the presence and absence of gravity.

However, the concept of conduction pumping mechanism has been studied only very recently. The theoretical model has not been completely established for single phase and no theoretical or experimental work has been done with regards to its application for two-phase flow in a channel. Therefore, the in details study on the theoretical model and the feasibility of conduction pumping is enthusiastically required.

Objectives

The overall objective of this research is to provide a fundamental understanding of the EHD induction and conduction pumping through theoretical and numerical investigations.

Induction Pumping

The main objective of this part of the research is to provide a fundamental understanding of EHD induction pumping of liquid film in vertical and horizontal annular configurations in the presence and absence of gravity. No work has been done before in regards to such configuration. The gained knowledge from this study provides a valuable tool which should help in designing and operating EHD induction pump. Particular objectives are to:

1) develop a non-dimensional analytical model for the fully developed induction pumping process assuming constant temperature across the liquid layer and considering only electric shear stress at the interface for a liquid film in horizontal annular configuration

2) conduct a parametric study and explain the results fundamentally
3) investigate the unstable pump performance, determine the stability criteria, and present a stability map ensuring stable pump operation (for repulsion pumping) for liquid film in vertical annular configuration
4) derive an advanced non-dimensional theoretical model for the pumping process accounting for both bulk and interfacial electric shear stresses considering three different inlet temperature profiles leading to hydrodynamically developing flow
5) conduct comparisons between both numerical and analytical models
6) obtain numerical solutions and conduct parametric study to understand the flow behavior and determining the controlling parameters

Conduction Pumping

The core objective of this part is to provide theoretical and numerical studies for EHD conduction pumping phenomena with particular focus on in-depth fundamental understanding of the pumping mechanism of a single phase dielectric liquid generated solely due to EHD conduction pumping phenomena in a channel. This study also includes a theoretical/numerical investigation of isothermal two-phase (i.e. stratified liquid/vapor medium) flow, which has not been investigated previously.

Specific objectives are as follows:

1) develop a theoretical model to predict the EHD conduction pumping performance for single phase dielectric liquid in a horizontal channel flow

2) obtain numerical solutions of the theoretical model to confirm the concept of EHD conduction pumping of a single-phase dielectric liquid in a horizontal channel configuration
3) obtain numerical solution for another pair of electrode design (i.e. electrode design with minimum-drag coefficient)
4) extend the theoretical model to a stratified liquid/vapor medium in a channel to understand EHD conduction pumping of dielectric liquid film

CHAPTER II

ELECTROHYDRODYNAMIC PUMPING

Electromagnetic fields can set up a mechanical body force in a material medium that can cause motion and deformation in the medium. Depending on the media of interest, two distinct fields of study have emerged from the models of a fluid flow under the influence of electromagnetic field; magnetohydrodynamics (MHD) and electrohydrodynamics (EHD). The MHD deals with the flow field under the influence of magnetic field with no charged particles and no influence from the electric fields. On the other hand, the EHD deals with flow field under the influence of an electric field with electrically charged particles and having insignificant magnetic effects. Generally, for dielectric liquids with very low values of electric conductivity such as refrigerants, hydrocarbons with the conductivity range from 10^{-14} to 10^{-8} S/m the effects of electric fields are more dominant, thus we are in the realm of EHD. On contrary, for highly conductive fluids such as mercury or molten metals, magnetic effects will be dominant and therefore falling in the domain of MHD [1]. In this study, the working fluid is a refrigerant, R-123, with electric conductivity of 10^{-8} S/m where the effects of the electric fields and therefore EHD are prevailing.

The EHD phenomena deal with the interaction between electric fields and flow fields in a dielectric fluid medium. This interaction between electric fields and flow fields can induce flow motion due to the electric force exerted by the electric field on the fluid. The electric body force acting on the molecules of the fluid can be expressed as [2]

$$f_e = qE - \frac{1}{2}E^2\nabla\varepsilon + \frac{1}{2}\nabla\left[E^2\left(\frac{\partial\varepsilon}{\partial\rho}\right)_T\rho\right], \tag{2.1}$$

The first term represents the Coulomb force or electrophoretic force, which is the force acting on the free charges in an electric field. The second term, is referred as the dielectrophoretic force, is related to the gradient of the electric permittivity. The third term is the gradient of the electrostriction pressure. The electrostriction term is not relevant in fluid systems where the material properties and boundary conditions are independent of normal stresses thus making it relevant only for compressible fluids. The second and third terms act on polarized charges, and both represent the polarization forces. Thus, for incompressible fluids EHD pumps require either a free space charge or a gradient in permittivity within a liquid.

Figure 2.1 represents the mechanism by which the second term of Eq. (2.1) acts. An electric permittivity gradient exists across the interface separating the two different

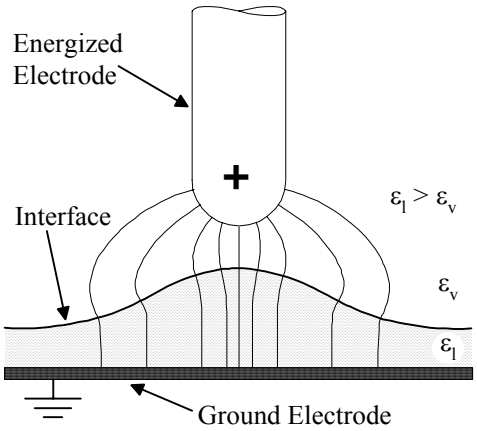

Fig. 2.1 Polarization force due to a permittivity gradient

fluids. The resulting polarization force exerted on the interface is proportional to the electric field strength and in the direction of decreasing electric permittivity. Consequently, the fluid with higher permittivity is attracted by the energized electrode, thus causing the interface to be lifted. This phenomenon is associated with the EHD extraction phenomena and can be successfully used to enhance the heat transfer rate in condensation and boiling process in which phase-change phenomenon occurs.

When the electric permittivity gradient, $\nabla\varepsilon$, vanishes, as it is the case in an isothermal single phase liquid or when its contribution is insignificant compared to the Coulomb force such as in the case for EHD pumping of insulating fluids, the latter becomes the only mechanism for generating a net EHD motion. There are three kinds of EHD pumps operating based on the Coulomb force: induction pumping [3-16], ion-drag pumping [17-25], and conduction pumping [26, 27]. For these three mechanisms the electric field accelerates charges or dipoles in a fluid. Consequently, these accelerated charges loose some of their momentum to the surrounding fluid due to viscous effects, thus inducing bulk fluid motion. The aforementioned three mechanisms are explained in more details in the following sections.

EHD Ion-drag Pumping

The ion-drag pumping is associated with the ion-injection at a metal/liquid interface and accelerated due to a DC electric field. According to the polarity of the high voltage electrode, two kinds of ion-injection modes exist; field ionization, and field emission [28].

Field ionization occurs when a positive high voltage is applied to a sharp electrode. Electrons are transferred by high electric field strength from the fluid to the positive electrode generating positive ions in the fluid as represented in (Fig. 2.2.a). Since these generated ions are of the same polarity of the energized electrode, they will be repelled from it by the Coulomb force acting along the electric field lines. These ions impart momentum to the fluid. Thus fluid motion from the high voltage electrode towards the ground electrode is induced.

Field emission occurs when a high voltage with negative polarity is applied to a sharp electrode. Electron transfer is induced by high electric field strength from the negative high voltage electrode to the fluid generating negative ions in the fluid as shown in (Fig. 2.2.b). These generated ions are pulled towards the ground electrode inducing flow from the high voltage electrode with negative polarity towards the ground electrode. Previous studies on the ion-drag pumping showed significant pressure generation and heat transfer enhancement. However, the ion-drag pumping is not desirable because it can deteriorate the electrical properties of the working fluid due to ion-injection and it can be hazardous to operate due to the corona discharge.

EHD Induction Pumping

The EHD induction pumping relies on the generation of induced charges. This charge induction occurs in the presence of an electric field when an electric conductivity gradient acting perpendicularly to the desired direction of fluid motion exists. Such a gradient could be present due to a temperature gradient within the bulk of the liquid, as

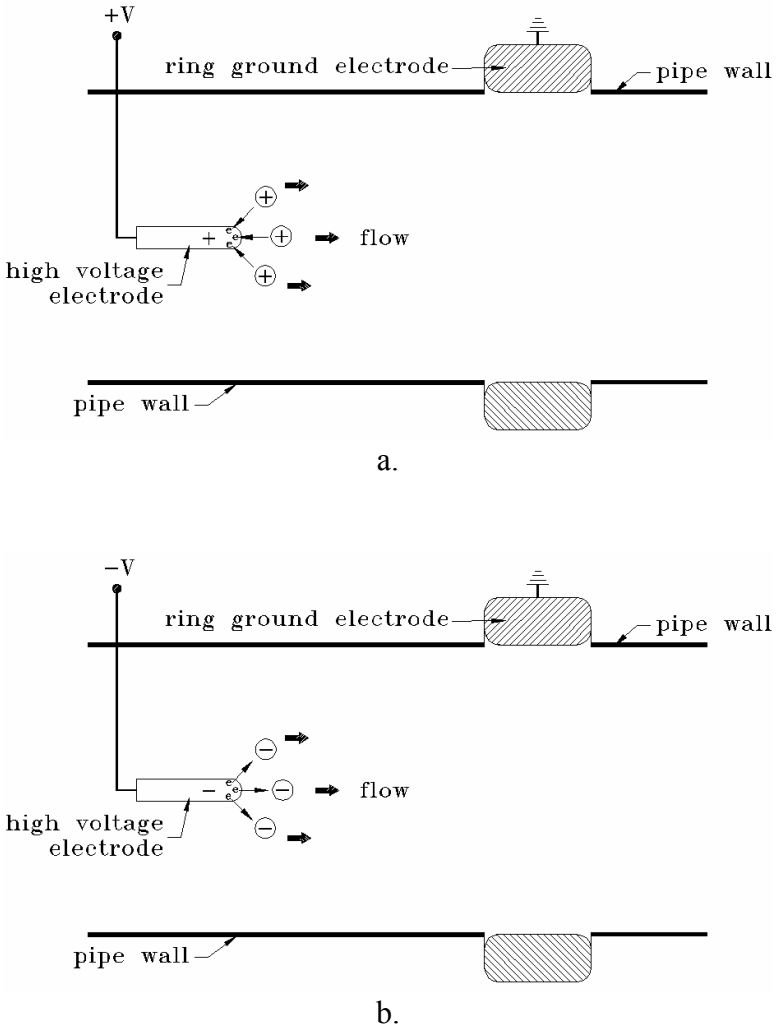

Fig. 2.2 Schematic of ion-injection: a) field ionization; b) field emission

the electric conductivity is a strong function of temperature or at the interfaces between two fluids or a liquid/vapor interface. Upon The establishment of an electric field in the form of a traveling wave (ac) through electrodes mounted along a flow passage, a net fluid motion could be produced.

Depending on the location of the fluid with higher electric conductivity with respect to the energized electrodes, the EHD induction pump will operate in two different modes: attraction and repulsion modes. Generally, in the attraction modes, the fluid with higher electric conductivity is away from the electrodes, on the other hand, when the fluid with higher electric conductivity is adjacent to the electrodes, the EHD induction pump is operating in the repulsion mode.

Figure 2.3 represents the principle for induction pumping in attraction (Fig. 2.3.a) and repulsion (Fig. 2.3.c) modes. A fluid with no net charge is composed of molecules experiencing a continuous process of electron transfer. Accordingly, the fluid consists of an approximately equal number of positive and negative charges at any given moment in time. On applying an electric field, and depending on the electrode configuration, the charges will arrange themselves so that they will be attracted to locations exhibiting opposite polarity to a voltage source (Fig. 2.3.a), or they will be repelled from locations with like polarity to a voltage source (Fig. 2.3.c), therefore, accumulating at the liquid/vapor interface. By establishing an AC electric field to the electrodes and if the voltage at each electrode vary with respect to time in, e.g., a sinusoidal wave (Fig. 2.3.b), fluid motion will result.

For example, for attraction pumping the leftmost electrode has a positive polarity while the polarity of the charge opposite to it is negative. As the time advances the electrode will pass on its positive polarity to the neighboring electrode, thus causing the negative charge to realign itself underneath the current positive electrode. A three-phase

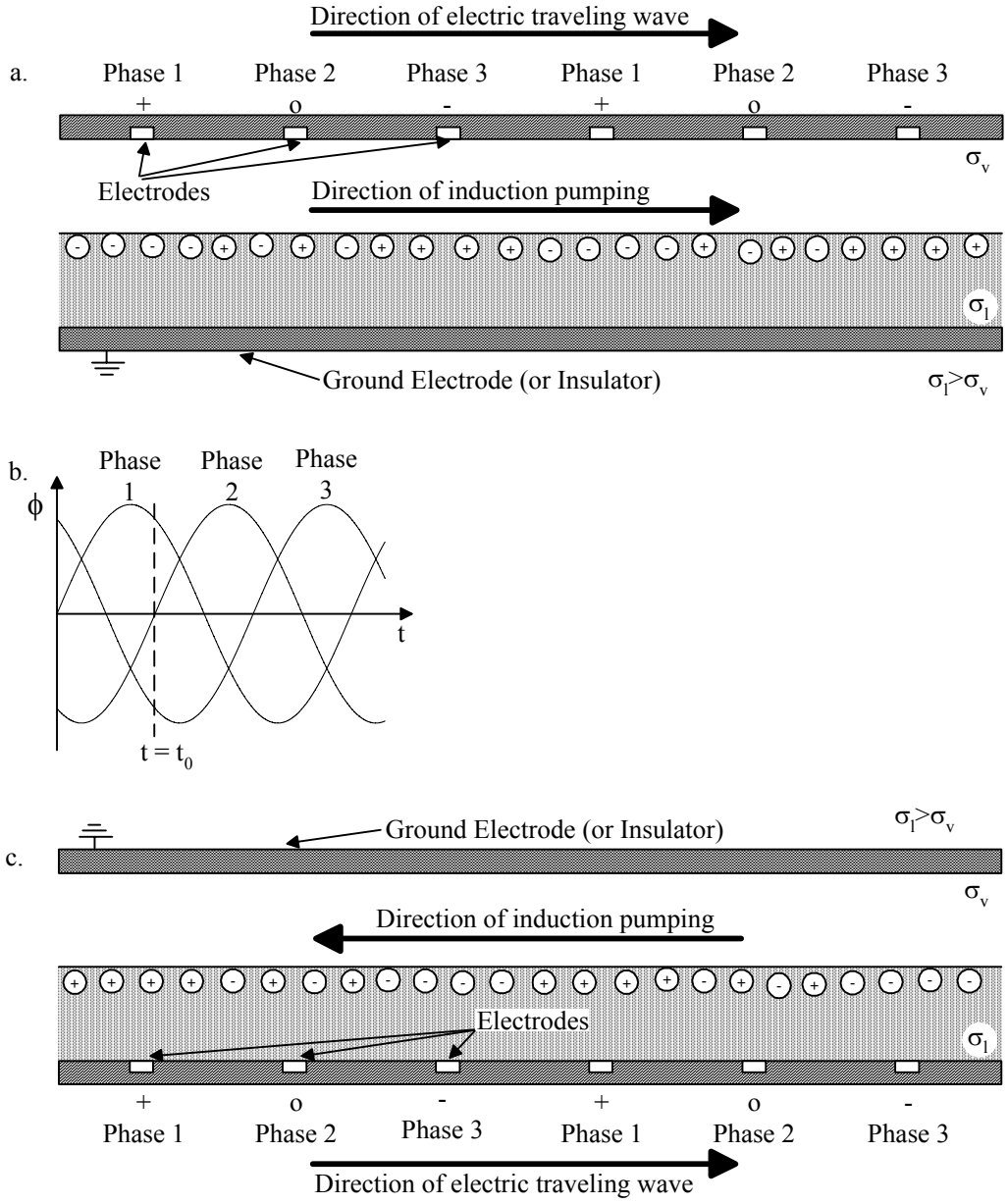

Fig. 2.3 EHD induction pumping of liquid/vapor medium: a) attraction mode; b) three-phase AC voltage signal; c) repulsion mode

electric traveling wave (Fig. 2.3.b) will continuously move to the right and the charges at the interface will follow accordingly in the same direction. Consequently, the surrounding fluid will be set in motion. The same is true for repulsion pumping (Fig. 2.3.c), with the exception being that the charges are now located across from the electrodes with the same polarity. As the electric traveling wave moves to the right, the charges at the interface will move to the opposite direction. Hence, the surrounding fluid will be set in motion in the opposite direction of the traveling wave.

EHD Conduction Pumping

The electric conduction mechanism in a pure dielectric liquid is associated with a reversible process of dissociation-recombination between a neutral electrolytic species (denoted AB) and its corresponding positive A^+ and negative B^+ ions [26]:

$$AB \leftrightarrow A^+ + B^- \tag{2.2}$$

The conduction term here represents a mechanism for the electric current flow in which charged carriers are produced not by the injection from electrodes, but by the dissociation of molecules within the fluid. When the applied electric field is low, dissociation and recombination are in dynamic equilibrium. The rate of dissociation increases as the magnitude of the applied electric field increases, on the contrary, the rate of recombination is independent of the applied electric field [29]. Therefore, when the applied electric field exceeds (approximately > 1kV/cm, depending on the liquid characteristics) the rate of dissociation exceeds that of the recombination and it

continues to increase at higher electric fields. Consequently, there is a non-equilibrium layer where the dissociation-recombination reactions are not in equilibrium [29]. The charges generated by dissociation are redistributed in the region by the applied electric field resulting in the heterocharge layers in the vicinity of the electrodes. Heterocharge means that the charge has the opposite polarity from that of the adjacent electrode. The thickness of the heterocharge layer can be up to several millimeters and is proportional to the corresponding relaxation time of the working fluid, τ, and depends on the applied electric field. The attraction between the electrode and the charges within the heterocharge layer induces a fluid motion near the electrode from the liquid side to the electrode side.

In order to explain how EHD conduction can produce a net flow, an electrode configuration as an example is shown in Fig. 2.4. Since the field is clearly grater near the

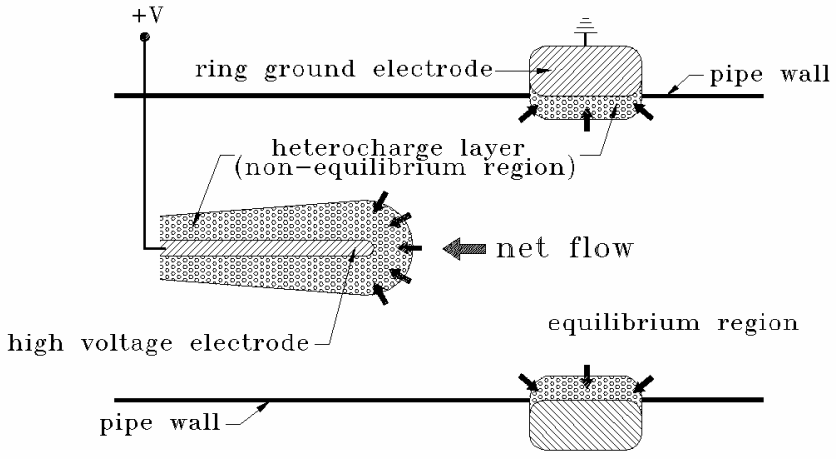

Fig. 2.4 Illustration of conduction pumping mechanism

high voltage electrode, the thickness of the corresponding heterocharge layer and the pressure difference across it will be greater. In this electrode configuration, the motion (i.e. pressure generation) around the high voltage electrode primarily contributes to the net axial flow. This is because the net axial motion around the ring ground electrode is almost canceled because of the symmetrical electrode configuration. Therefore, the flow direction (i.e. pressure generation) will be from the ground electrode towards the high voltage electrode. The current (I) versus voltage (V) behavior in this regime is sub-ohmic showing only a slightly increased current with increased voltage.

In designing an EHD conduction pump the electrodes should not contain any points or sharp edges to avoid the effect of ion injection. In addition, electrodes with relatively large radius of curvature are required to provide significant projected area in the direction perpendicular to the net flow direction. Furthermore, depending on the liquid characteristics and electrode material, ion injection at the electrode/liquid interface is considered to be negligible for electric fields less than ≈100 kV/cm. In the high electric field regime beyond this critical value, the current suddenly increases sharply with an increase in the voltage due to the injection of ions from the electrodes into the liquid. The occurrence of this phenomenon is primarily governed by the electrochemical reactions at the electrode/liquid interface and therefore depends significantly on the composition and geometry of the electrodes. Beyond this electric field level, the ion-drag pumping mechanism is expected to be dominant.

It is noteworthy to mention that the voltage and, hence the electric field strength, required for ion-drag (i.e. field ionization) in saturated hydrocarbons is usually higher

than that for ion-drag (field emission) [28]. Therefore, in order to avoid the ion-injection in the high electric field region, it is better to design a conduction pump with high voltage electrode of positive polarity.

Even though the flow direction is mainly dependent on the electrode (high voltage and ground) designs, the obvious difference between the operation of the ion-drag (field emission) pumping and conduction pumping is in the flow direction. In a typical ion-drag pump, the flow direction is from the high voltage emitter electrode to the ground collector electrode. However, for the conduction pumping with the same particular design, the flow direction is from the ground electrode towards the high voltage electrode.

CHAPTER III

LITERATURE REVIEW

Theoretical Studies of EHD Induction Pumping of Liquids

Melcher [3] was the first to introduce the basic concept of EHD induction pumping. His theoretical model represents a horizontal configuration of a two-phase flow. The domain considered is bounded from below by a conducting plate, where the liquid is resting, whereas the segmented electrode with imposed traveling wave is placed above the free interface. The model did not include the effects of a temperature gradient imposed externally or due to Joule heating. Therefore, no charges are induced in the bulk of the liquid, confiding the interaction between the electric filed and the flow field to the interface. The electric field were considered to be in the direction of the flow only, in addition, the liquid/vapor interface were assumed to be flat by neglecting the interfacial waves due to hydrodynamic stability. The flow was modeled as fully developed laminar Couette flow. He presented results for the interfacial velocity as a function of the applied voltage and frequency of the traveling wave. The theoretical curves have been scaled to one of the data points obtained experimentally to overcome the need for providing an accurate value for the electric conductivity of the working fluid in the pump at the same time allowing for a comparison to the experimental data.

Melcher [2] presented an improved version of the aforementioned theoretical model describes attraction and repulsion pumping modes, as well as pumping of liquid/liquid interfaces. He presented plots for the electric and viscous shear stresses as a function of the interfacial velocity. These diagrams serve as a simple convenient tool to

understand the characteristics of EHD induction pump operation. It also helps explaining the stable (one single operating point possible) and unstable (two or three operating points possible) pump operation, and can be utilized to determine a stable operating point for a pump experiencing unstable operation (two or three operating points possible).

Crowley [4, 5] used this improved model to represent single phase temperature induced EHD pumping. The fluid was modeled as two layers of fluid having a different constant temperature, separated by a temperature jump, i.e. an electric conductivity discontinuity. Therefore, all charges were assumed to be concentrated at this fictitious interface. In his first study [4], he investigated the effect of various pump parameters on the efficiency of EHD induction pumps operating in the attraction mode. The upper electrode, near the more conducting fluid, provides a traveling electric wave while the lower one is grounded. He concluded that high efficiency could be obtained if the thickness of the upper fluid layer is small; the applied frequency is high compared to the inverse of the charge relaxation time of both fluids, and the electric conductivity ratio between both fluids is high .

In his latter work [5], he extensively investigated for the first time the issues of stability of EHD induction pumps for both attraction and repulsion pumping modes. Although, the study assumed an overly simplified expression for the electric shear stress, it presents a valuable mean for the prediction of pumping behavior. He also provided a stability criterion for EHD induction pump operating in attraction and repulsion modes.

Melcher and Firebaugh [6] developed a theoretical model considering a thermally induced induction pumping of a single phase fluid. They assumed that an imposed external temperature gradient across the channel results in a linear conductivity profile across the liquid. The resultant electric shear stress was set equal to the viscous shear stress for a fully developed plane channel, and was solved numerically to obtain the velocity profile. The authors presented figures for the peak velocity profiles as function of applied voltage and frequency. An excellent agreement between the theoretical and experimental results was reported.

Kuo et al. [7] solved the coupled continuity, momentum, energy, and electric field equations for a single phase fluid in a horizontal pipe, using a finite element method. He presented results for the average velocity as a function wavelength, electric conductivity, and external pressure gradient.

Seyed-Yagoobi et al. [8] also solved the above set of equations for EHD induction pumping in a vertical configuration of single phase, using a finite difference method. Their model includes the effect of entrance conditions, bouncy effect, secondary flow, and Joule heating. Both forward (i.e. cooled wall) and backward (i.e. heated wall) pumping modes were investigated. They also presented results for the average pump velocity as a function of electric conductivity, wavelength, voltage, frequency, and external pressure gradient, as well as velocity profiles in the pipe. In addition, Seyed-Yagoobi et al. confirmed their numerical predictions with experimental results and obtained good agreement between the two.

Wawzyniak and Seyed-Yagoobi [9] further developed an analytical model for EHD induction pumping of a stratified liquid/vapor medium in light of the analytical model developed by Melcher [3]. They assumed charges to be present only at the liquid/vapor interface and investigated four different electrode configurations. Non-dimensional parameters accounting for the applied voltage, fluid properties, and geometry were defined and varied over a ranges, which represent those likely to be encountered in a practical EHD induction pump. In further study, Wawzyniak and Seyed-Yagoobi [10] studied the effect of an external load on the pump performance and stability. Quantitative values were given, allowing for simple characterization of stable or unstable pump behavior based on non-dimensional values of electric conductivity, dielectric constant, and non-dimensional liquid and vapor height for both attraction and repulsion pump modes.

Furthermore, they improved their first theoretical model [9] by accounting for the induced charges not only at the interface but also through the bulk of the liquid, for only one electrode configuration [11]. They presented parametric studies and showed that bulk charge induction can have a significant effect on the performance of the EHD induction pump.

Brand and Seyed-Yagoobi [12] extended the model developed by Wawzyniak and Seyed-Yagoobi [11] to investigate the effect of different electrode configurations on the pump performance. A numerical parametric study was carried out to compare all four electrode configurations with respect to five controlling parameters: vapor height, liquid height, voltage, wavelength, and frequency.

Experimental Studies of EHD Induction Pumping of Liquids

Melcher [3] presented the only experimental investigation which concern itself with EHD induction pumping solely due to the interfacial electric shear stress. The working fluid (Monsanto Aroclor 1232) was contained within a re-entrant channel having insulating walls and a conducting bottom. The electrodes were positioned at the top of the channel and separated from the interface by a layer of air. He only measured the interfacial velocity and presented results for it as a function of the applied voltage and frequency.

Melcher and Firebaugh [6] carried out an experimental investigation, with corn oil as a working fluid, using a similar apparatus as the one used in [3]. A temperature gradient was introduced in the liquid by cooling the bottom of the channel using ice water and heating the top of it by means of circulation of hot oil. Velocity measurements were conducted and results of peak velocity as a function of applied voltage and frequency were provided.

Kervin et al. [13] conducted velocity measurements of EHD induction pump, using Sun #4 transformer oil as a working fluid, under the effects of electric conductivity (altered by adding conductive liquid additives to the working fluid), wavelength, frequency, wave form (square versus sine), temperature difference, and voltage.

Seyed-Yagoobi et al. [14] carried out their experiment utilizing Sun #4 transformer oil, with three electrical conductivity level, as working fluid. The experimental apparatus was a vertical pump loop in which one of its vertical sections was equipped with electrodes. Bulk velocity measurements were conducted and plots for bulk velocity as a

function of frequency, voltage, temperature, electric conductivity, and external pressure gradient were presented.

Wawzyniak et al. [15] investigated experimentally the EHD induction pumping of a stratified liquid/vapor medium, using a horizontal pump loop including two long straight sections equipped with electrode plates located in the liquid. They presented velocity profiles inside the liquid film at different frequencies and voltages. Maximum velocity of about 10 cm/s, for a liquid height of 10 mm, was achieved, using the refrigerant R-123 as working fluid.

Brand and Seyed-Yagoobi [16] studied experimentally the EHD induction pumping of a dielectric micro liquid film in external horizontal condensation process. Both attraction and repulsion pumping modes were observed in their experiment. The effect of voltage, frequency of the electric wave, and the heat flux were investigated. Bi-directional flow and flow reversal were observed under certain operating conditions.

EHD Ion-drag Pumping

Ion-drag pumping theory was initially presented by Stuetzer [17]. He investigated the ion-drag pressure generation theoretically as well as experimentally. He presented an approximate theory applicable for unipolar ion conduction in gases and in insulating liquids. The experiment agreed with theory but it was limited to the case of static fluid. Later on, Stuetzer [18] extended his theoretical model to describe the dynamic behavior of an ion-drag pump and presented supporting experimental measurements. Pickard [19]

reexamine the ion-drag pump theoretically and experimentally and obtained new theoretical results for both the static and dynamic cases.

Halpern and Gomer [20, 21] investigated experimentally and theoretically, for various cryogenic liquids, the field emission from tungsten emitters into liquid and field emission from liquids i.e. electron tunneling from the liquid, a phenomenon often called field ionization in the gas phase and Zener breakdown in solids. A simple theoretical model for the field ionization current under the assumption of tunneling from non-interacting individual atoms or molecules was derived and applied to the system. Schmidt [30] treated the electron transfer process from the cathode to the liquid or from the liquid to the anode induced by high electric field strength. He analyzed the influence of the electrode polarity with tip-plane electrode geometry.

Crowley et al. [22] presented a criterion for selecting a working fluid to increase the efficiency and flow rate of EHD pumps. Their analysis was not limited to ion-drag pumping. They concluded that high dielectric constant and low viscosity produce high flow velocities, while low conductivity and mobility promote high efficiency. They also determined that the velocity must be high enough to avoid electrical conduction and mobility losses; however, it can not exceed the limits set by viscosity, turbulence, and electric breakdown.

Bryan and Seyed-Yagoobi [23] experimentally investigated an ion-drag pump in a vertical axisymmetric configuration and various hydrocarbon-base dielectric fluids were studied. The results showed that pumping performance depends on fluid properties,

mostly fluid viscosity and electrical conductivity. They also reported that a decrease in the charge relaxation time causes a decrease in the pump efficiency.

Castaneda [24] developed a general one-dimensional theoretical model for ion-drag pumping and investigated the two modes of ion-drag pumping: the ionization and the emission pumping. Dodecybenzene was used as a working fluid. The pressure generated by the pump was similar for the two modes studied and there was no significant change in the pump efficiency with the change in the mechanism of charge generation. Seyed-Yagoobi et al. [25] improved the one-dimensional theoretical model for the ion-drag pumping by incorporating all three components of the current density in the model. The solutions were presented in non-dimensional form, and the combined effects of the controlling fluid properties and operating conditions were incorporated into three non-dimensional number. The distributions of the charge density and electrical field under various conditions were also provided.

EHD Conduction Pumping

The EHD conduction pumping phenomena has been recently studied, addressed, and clarified by the work of Atten and Seyed-Yagoobi [26] and Jeong and Seyed-Yagoobi [27]. The phenomena of net flow generation in isothermal liquids was erroneously attributed to the electrostriction force (the third term in Eq. (1)) by the majority of the published papers [e.g. 30, 31]. Therefore, very limited work can be found in the literature in regards to the EHD conduction pumping phenomena.

Felici [32] discussed D.C. conduction in liquid dielectrics and described the creation of heterocharges due ionic dissociation in the vicinity of electrodes in the intermediate voltage region where the space charges are usually observed. He further explained that the decrease of the current to voltage ratio due to the increase in voltage clearly shows that the ions are no in equilibrium longer with their parent electrolytes, which emphasizes exactly what happens due to the development of the heterocharges. For the ions that are moving in any volume element, the irreversible generation of ions by dissociation was provided as the basic mechanism. In his other study [33], he mentioned that the electrolysis of any weak electrolyte can provide as strong space charges as any injecting electrode. Therefore, Coulomb forces can exist significantly even if there is absolutely no contribution due to injection. He also discussed the vorticity generation associated with the heterocharges formation in an elongated positive electrode and plane cathode configuration.

Zhakin [29] described the basic conduction processes in dielectric liquids to consider the linear and non-linear deformation of charged interface in a long wave and discussed the general theories on the dissociation and recombination of ion pairs in high electric field. He presented the expression for the recombination rate and the dissociation rate that is dependent on the electric field. He also presented the basic concepts of EHD on the basis of the dissociation-injection model of conductivity.

Pontiga and Castellanos [34] studied the onset of convection for a layer of nonpolar liquid subjected to an adverse thermal gradient and intense electric field. They developed a physicochemical model based on dissociation and injection charge

generation to determine the electrical conductivity. Convective instabilities and overstabilities were predicted as a function of strength of injection and residual conduction. It was also shown that dissociation always plays a stabilizing role.

They later studied the conduction of dielectric liquids doped with salts [35]. The electrical conduction of these liquids was studied using electric-field dependent law for the injection of ions and Onsagar theory for the dissociation of ionic pairs in the bulk. They presented that the injection and the dissociation may contribute very differently to the total current density, depending on the regime of conduction. It has been also shown that the current due to dissociation can constitute significant part of the total current when the intensity of the electric fields is weak or strong. They compared their predictions with experimental results available in the literature. However, their work is primarily focused in the electric conduction phenomena itself, not in EHD phenomena.

Maekawa et al. [36] studied EHD convection in a dielectric liquid subjected to a non-uniform DC electric field experimentally and theoretically. They considered the two types of charge generations, i.e., charge injection from metal electrode into liquid and ion generation by dissociation in liquid. Their theoretical model did not consider the effect of charge dissociation-recombination and convection in the distribution of the positive and negative charges. They also carried out an experiment covering the electrodes with rubber to stop the ion injection from the electrode and proved that convection has been induced in silicon oil.

Jeong and Seyed-Yagoobi [37] investigated the pressure head generated by conduction pumping mechanism theoretically through numerical solutions. The model

presented was for the static case (i.e. no fluid motion) for high-voltage hollow-tube and ground electrodes configuration. The distributions of electric potential, electric field, charge density, and electric body force were provided. The generated pressure as a function of the applied voltage is also presented. Their numerical results confirm the EHD conduction pumping concept theoretically.

In their later study, Jeong and Seyed-Yagoobi [38] presented a non-dimensional theoretical model representing the fluid circulation of an isothermal dielectric liquid in an enclosure generated by EHD conduction mechanism. Numerical results for the distributions of electric potential, electric field, charge density, and electric body forces were presented for different controlling parameters. They concluded that a significant flow circulation/mixing can be achieved within an enclosure using based on EHD conduction phenomenon.

Jeong and Seyed-Yagoobi [39] further investigated experimentally EHD conduction pumping, using R-123 as the working fluid, by using four innovative electrode designs: two different kinds of perforated disks and two other different kinds of porous disks as the high voltage electrode. A ring was used as a ground electrode for the four designs considered. They showed a pressure generation of about 1400 Pa with the 0.2-μm porous disk high-voltage electrode/ring ground electrode design.

Finally, Feng and Seyed-Yagoobi [40] studied the EHD conduction phenomenon for dielectric liquid theoretically as well as experimentally. Their non-dimensional theoretical model was based on the model developed by [26], however, it was normalized using the heterocharge layer thickness as the characteristic length, instead of

the electrode spacing proposed by [26]. This improvement in the model leads to a generalized analytical solution independent of the fluid properties and the applied electric field. They also conducted an experiment to verify their theoretical findings.

CHAPTER IV

ANALYTICAL MODEL*

Theoretical Derivation

The fundamental concept of the model derived in this chapter is based on the analytical model developed by [3] and later extended by [9] to investigate four different electrode configurations for stratified liquid/vapor medium. The presented model investigates the EHD induction pumping of liquid film of insulating liquid in annular configuration which has not been studied previously. The charges responsible for the EHD pumping are assumed to be present only at the liquid vapor interface, where the electric and viscous stresses are in equilibrium, consequently determining the velocity of the liquid/vapor interface. Therefore, this model will be referred to as the "Analytical Model" compared to the one presented in the Chapter V. The model presented in this chapter considers fully developed annular flow of a thin liquid film separated from a vapor by a flat interface in an axisymmetric horizontal tube (see Fig.4.1). In the second part of this chapter the model will be extended to a vertical annular configuration for the purpose of studying the gravitational effect and the stability issues.

As it was mentioned above, the interfacial velocity can be determined by equating the electric and viscous shear stresses at the interface. In evaluating the electric and the viscous shear stresses at the interface, the following assumptions are made,

---

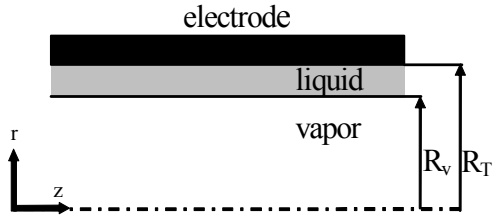

Fig. 4.1 Schematic of the analytical domain

a. the vapor has properties of a vacuum;
b. the electric field is irrotational due to low electric currents in induction pumping applications;
c. the liquid layer exhibits uniform properties limiting the conduction gradient, and thus free changes, to interface;
d. charge transport within the interface due to ion mobility, and surface conduction is negligible;
e. the electric field is axisymmetric and a symmetry boundary condition for the electric potential is applied at the centerline of the tube (i.e. $E_r^v = 0$);
f. flow due EHD induction pumping occurs solely in z-direction;
g. the liquid flow field may be modeled as flow between two infinite concentric cylinders, the outer one being stationary and the inner one moving at the constant speed of the liquid/vapor interface in the z-direction;
h. the flow is fully developed, steady state, laminar (Reynolds number based on hydraulic diameter below 2300), and incompressible;
i. the flow is rotationally symmetric, and does not depend upon θ;

j. the pressure in r-direction is uniform and the pressure gradient in z-direction is constant and independent of the flow velocity;

k. the heat transfer is not present (adiabatic)

The possibility of surface waves due to forces, which may arise from the electric field, gravity, or the surface tension in the radial direction, is neglected. This approximation significantly simplifies the theoretical model allowing for direct analytical solution. In addition, the assumed adiabatic condition implies that the change in the liquid film thickness due to phase change does not exist.

Calculation of the electric shear stress at the liquid/vapor interface involves knowledge of the electric field distribution above and below the interface (i.e. $E_r^l, E_z^l, E_r^v,$ and E_z^v).

The governing differential equations are given by Maxwell's equations

$$\nabla \times \vec{E} = 0 \tag{4.1}$$

and

$$\nabla . \varepsilon \vec{E} = q \tag{4.2}$$

The right hand side of Eq. (4.2) presents the free charges present in the medium due to a conductivity gradient, resulting in an electric field gradient. Since the model considers that electric conductivity gradient and consequently free charges exist only at the liquid/vapor interface, Eq. (4.2) is reduced to

$$\nabla . \varepsilon \vec{E} = 0 \tag{4.3}$$

equations (4.1) and (4.3) have to be solved to obtain the electric field distribution in the analytical domain whereas the charges at the liquid/vapor interface will be accounted for through one of the boundary conditions.

Three cases are considered for this study, each of which will generate a different set of boundary conditions. They are:

1. electric traveling wave generated at a certain radius R_o from the centerline in the vapor layer, conducting plate at the upper boundary; and
2. electric traveling wave generated at the upper boundary, symmetric boundary conditions for the electric field at the centerline (i.e. $E_r^v = 0$);
3. electric traveling wave generated at a certain radius R_o from the centerline in the vapor layer, insulating plate at the upper boundary

The boundary conditions imposed at the interface are identical for all three cases.

The presence of free charges at the interface are accounted for by the first boundary

$$\varepsilon E_r^l - \varepsilon_0 E_r^v = Q \qquad @\ r = R_v \tag{4.4}$$

the continuity of the electric field across the interface in z-direction is the second boundary condition

$$E_z^l - E_z^v = 0 \qquad @\ r = R_v \tag{4.5}$$

The remaining two boundary conditions needed to evaluate the four unknown quantities $E_r^l, E_z^l, E_r^v,$ and E_z^v are specific to each of the three cases studied. While a conducting plate requires that the electric field in z-direction is zero, the symmetry condition

imposes that the electric field in r-direction is zero. The electric traveling wave is assumed to be of a sinusoidal form on the surface where the electrodes are placed as

$$E_z = \mathrm{Re}\left\{ jK\hat{\varphi} \exp\left[j(\omega t - Kz) \right] \right\} \tag{4.6}$$

In the case of the insulating boundary condition (i.e. EC3), a solid plate of thickness (R_s-R_T), permittivity ε_s, and zero-electric conductivity is considered. This plate is grounded from outside. Two more boundary conditions are required at the solid/liquid interface for EC3. One boundary condition requires the continuity of potential on either side of the interface, while the other condition accounts for the surface charges, Qs, respectively

$$\varphi_s = \varphi_l \qquad @\ r = R_T \tag{4.7}$$

$$\varepsilon_s E_r^s - \varepsilon E_r^l = Q_s \qquad @\ r = R_T \tag{4.8}$$

All boundary conditions needed to determine the four unknowns, E_r^l, E_z^l, E_r^v, and E_z^v, are summarized in Table 4.1, for all three electrode configurations. It is evident from Eq. (4.4) that the boundary condition accounting for the free charges at the liquid/vapor interface, introduces an additional unknown quantity, Q. Hence, surface charge distribution is required. Fortunately, the surface charge distribution may be determined using the charge conservation equation

$$\nabla \cdot \vec{J} + \frac{\partial q}{\partial t} = 0 \tag{4.9}$$

And the charge density

$$\vec{J} = \sigma \vec{E} + q\vec{v} \tag{4.10}$$

Table 4.1 Boundary Conditions for the Electric Field

r	**EC1**	**EC2**	**EC3**
	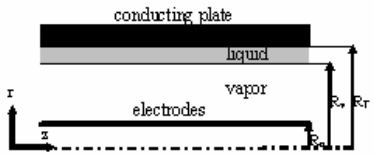	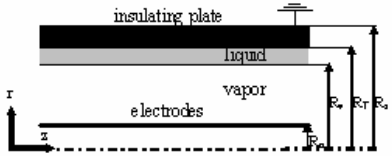	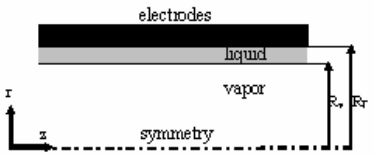
R_S	-	$\varphi_s = 0$	-
R_T	$E_z^l = 0$	$\varphi_s = \varphi_v$	$E_z^l = \mathrm{Re}\left\{jK\hat{\varphi}_e \exp\left[j(\omega t - Kz)\right]\right\}$
R_T	-	$\varepsilon_s E_r^s - \varepsilon E_r^l = Q_s$	-
R_V	$\varepsilon E_r^l - \varepsilon_0 E_r^v = Q$		
R_V	$E_z^v - E_z^l = 0$		
R_0	$E_z^v = \mathrm{Re}\left\{jK\hat{\varphi}_e \exp\left[j(\omega t - Kz)\right]\right\}$	$E_z^v = \mathrm{Re}\left\{jK\hat{\varphi}_e \exp\left[j(\omega t - Kz)\right]\right\}$	-
0	-	-	$E_r^v = 0$

Charge transport due to ion mobility has been neglected in Eq. (4.10). The first term in Eq. (4.10) stands for Ohmic conduction, whereas the second term represents a current due to charge convection. Substituting equation (4.10) into equation (4.9) gives

$$\nabla \cdot (\sigma \vec{E}) + \nabla \cdot (q\vec{v}) + \frac{\partial q}{\partial t} = 0, \tag{4.11}$$

It is assumed that flow occurs solely in z-direction, equation (4.11) becomes

$$\frac{1}{r}\frac{\partial}{\partial r}(r\sigma E_r) + \frac{\partial}{\partial z}(\sigma E_z) + \frac{\partial}{\partial z}(qw) + \frac{\partial q}{\partial t} = 0 \tag{4.12}$$

Since the vapor phase is modeled as a vacuum, then the conductivity of the vapor is taken as zero. In addition, neglecting the surface conduction in z-direction by assuming that surface currents are solely due to convection of free changes within the interface Eq. (4.12) can be integrated across the interface yielding

$$\sigma_l E_r^l = W\frac{\partial Q}{\partial z} + \frac{\partial Q}{\partial t} \tag{4.13}$$

It is noteworthy to be mention that the soul purpose of equation (4.13) is to provide an additional relationship between the electric field and the surface charge distribution. Obviously, if a solution for the surface charge distribution is desired one additional boundary condition and one initial condition would be required. However, this is not the objective of this study, and consequently as it will be shown that the spatial and temporal dependency of the surface charge distribution can be eliminated using the boundary conditions and electric field distributions.

The electrical equations are linear, and hence it is reasonable to look for traveling-electric-field solution. Assuming that the electric traveling wave is of a

sinusoidal form, the solutions for the governing equations given in Eq. (4.1) and Eq. (4.3) for the liquid and the vapor phases, respectively are

$$\vec{E}^{v} = -\nabla\left[\varphi^{v}\exp\left(j(\omega t - Kz)\right)\right]$$

$$\varphi^{v} = -\frac{\left(A^{v}I_0(Kr) + B^{v}K_0(Kr)\right)}{K}$$

$$\vec{E}^{l} = -\nabla\left[\varphi^{l}\exp\left(j(\omega t - Kz)\right)\right]$$

$$\varphi^{l} = -\frac{\left(A^{l}I_0(Kr) + B^{l}K_0(Kr)\right)}{K} \tag{4.14}$$

where the four unknowns A^{v}, B^{v}, A^{l}, and B^{l} are calculated from the above mentioned boundary conditions. It follows immediately from the second boundary condition (Eq. (4.5)) that

$$A^{v} + B^{v}\frac{K_0(KR_v)}{I_0(KR_v)} = A^{l} + B^{l}\frac{K_0(KR_v)}{I_0(KR_v)} \tag{4.15}$$

for all the three cases considered in this study. Herein, the electric field components E_r^{l} and E_r^{v} can be determined. Substituting Eq. (4.14) into the first boundary condition (Eq. (4.4)) and utilizing Eq. (4.12), the terms concerning the surface charge dependency on time and space, introduced by Eq. (4.12), will be cancelled. After some minor mathematical manipulation the following is obtained

$$\left(\frac{\varepsilon}{\varepsilon_0} - \frac{j}{S}\right) = \frac{A^{v}I_1(KR_v) - B^{v}K_1(KR_v)}{A^{l}I_1(KR_v) - B^{l}K_1(KR_v)}\text{ , where }\quad S = \frac{\varepsilon_0(\omega - KW)}{\sigma} \tag{4.16}$$

The values for $A^v, A^l, B^v,$ and B^l can now be computed for EC1 and EC3 using the boundary conditions corresponding to the wall and the centerline (see Table 4.1) and Eq. (4.16). The results are summarized in Tables 4.2 and 4.3.

For EC2, the electric field in the solid is taken as Eq. (4.14)

$$\vec{E}^s = -\nabla\left[\varphi^s \exp\left(j\left(\omega t - Kz\right)\right)\right], \quad \varphi^s = -\frac{\left(A^s I_0\left(Kr\right) + B^s K_0\left(Kr\right)\right)}{K} \tag{4.17}$$

Using the same procedure as in the liquid/vapor interface the charge conservation equation after integration at the solid/liquid interface is

$$\sigma_l E_r^l = \frac{\partial Q_s}{\partial t} \tag{4.18}$$

Note that the interfacial velocity is zero due to the non-slip condition at the liquid/solid interface. The substitution of Eq. (4.17) into the first boundary condition (Eq. (4.7)) will result in expression for the surface charge which can be applied to Eq. (4.18). Upon calculation of the derivatives, it is possible to cancel out the time and dependent term introduced by Eq. (4.18); hence the following expression is obtained

$$\left(\frac{\varepsilon}{\varepsilon_s} - \frac{j\sigma}{\omega\varepsilon_s}\right) = \frac{A^s I_1\left(KR_T\right) - B^s K_1\left(KR_T\right)}{A^l I_1\left(KR_T\right) - B^l K_1\left(KR_T\right)} \tag{4.19}$$

Using the boundary conditions corresponding to the wall and the centerline (see Table 4.1) and Eq. (4.19) the values for $A^v, A^l, B^v,$ and B^l can now be determined for EC2. The results are summarized in Table 4.4.

Evaluating Maxwell's stress tensor

$$\tau_{ij}^{electric} = \varepsilon E_i E_j - \frac{1}{2}\delta_{ij}\varepsilon E_k^2 \tag{4.20}$$

Table 4.2 Electric Field Parameters for EC1

C_1	$\left[\frac{K_0(KR_T)}{I_0(KR_T)}+\frac{K_1(KR_v)}{I_1(KR_v)}\right]$
C_2	$\left[\frac{K_0(KR_v)}{I_0(KR_v)}-\frac{K_0(KR_T)}{I_0(KR_T)}\right]\frac{\left[\frac{K_0(KR_v)}{I_0(KR_v)}+\frac{K_1(KR_v)}{I_1(KR_v)}\right]}{\left[\frac{K_0(KR_v)}{I_0(KR_v)}-\frac{K_0(KR_o)}{I_0(KR_o)}\right]}$
C_3	$\left[\frac{K_0(KR_v)}{I_0(KR_v)}+\frac{K_1(KR_v)}{I_1(KR_v)}\right]$
C_4	$\left[\frac{K_0(KR_v)}{I_0(KR_v)}-\frac{K_0(KR_T)}{I_0(KR_T)}\right]$
C_5	$\frac{\left[\frac{K_0(KR_v)}{I_0(KR_v)}-\frac{K_0(KR_o)}{I_0(KR_o)}\right]I_0(KR_o)}{\left[\frac{K_0(KR_v)}{I_0(KR_v)}+\frac{K_1(KR_v)}{I_1(KR_v)}\right]}\left(\frac{\varepsilon}{\varepsilon_0}C_1+C_4-C_2\right)$
C_6	$\frac{\left[\frac{K_0(KR_v)}{I_0(KR_v)}-\frac{K_0(KR_o)}{I_0(KR_o)}\right]I_0(KR_o)}{\left[\frac{K_0(KR_v)}{I_0(KR_v)}+\frac{K_1(KR_v)}{I_1(KR_v)}\right]}\frac{C_1}{S}$
A^l	$\frac{-K\hat{\varphi}\left[C_5+jC_6\right]}{\left[C_5^2+C_6^2\right]\left[\frac{I_0(KR_T)}{K_0(KR_T)}\right]}$
A^v	$\frac{-K\hat{\varphi}\left[\left(C_5^2+C_6^2\right)+\left(\frac{\varepsilon}{\varepsilon_0}\frac{C_1C_5}{C_3}+\frac{C_1C_6}{SC_3}+\frac{C_4C_5}{C_3}\right)K_0(KR_o)+j\left(\frac{\varepsilon}{\varepsilon_0}\frac{C_1C_6}{C_3}-\frac{C_1C_5}{SC_3}+\frac{C_4C_6}{C_3}\right)K_0(KR_o)\right]}{\left[C_5^2+C_6^2\right]I_0(KR_o)}$
B^l	$\frac{-K\hat{\varphi}\left[C_5-jC_6\right]}{\left[C_5^2+C_6^2\right]}$
B^v	$\frac{K\hat{\varphi}\left[\left(\frac{\varepsilon}{\varepsilon_0}C_1C_5+\frac{C_1C_6}{S}+C_4C_5\right)+j\left(\frac{\varepsilon}{\varepsilon_0}C_1C_6-\frac{C_1C_5}{S}+C_4C_6\right)\right]}{C_3\left[C_5^2+C_6^2\right]}$

Table 4.3 Electric Field Parameters for EC3

C_1	$\dfrac{\left(\dfrac{\varepsilon}{\varepsilon_0}-1\right)}{\left(\dfrac{\varepsilon}{\varepsilon_0}\right)^2+\left(\dfrac{1}{2S}\right)^2}\left\{\dfrac{K_0(KR_v)}{I_0(KR_v)}I_0(KR_T)+\dfrac{K_1(KR_v)}{I_1(KR_v)}K_0(KR_T)\right\}+\dfrac{K_1(KR_v)}{I_1(KR_v)}K_0(KR_T)+K_0(KR_T)$
C_2	$\dfrac{1}{\left[S\left(\dfrac{\varepsilon}{\varepsilon_0}\right)^2+(S)^{-1}\right]}\left\{\dfrac{K_0(KR_v)}{I_0(KR_v)}I_0(KR_T)+\dfrac{K_1(KR_v)}{I_1(KR_v)}K_0(KR_T)\right\}$
C_3	$\left(\dfrac{\varepsilon}{\varepsilon_0}-1\right)^2+\left(\dfrac{1}{S}\right)^2$
A^l	$\dfrac{-K\hat{\varphi}}{\left[C_1^2+C_2^2\right]}\left[\begin{array}{l}\dfrac{1}{C_3}\left(\dfrac{K_0(KR_v)}{I_0(KR_v)}+\dfrac{K_1(KR_v)}{I_1(KR_v)}\right)\left(C_1\left(\dfrac{\varepsilon}{\varepsilon_0}-1\right)+\dfrac{C_2}{S}\right)+C_1\dfrac{K_1(KR_v)}{I_1(KR_v)} \\ +j\left\{\dfrac{1}{C_3}\left(\dfrac{K_0(KR_v)}{I_0(KR_v)}+\dfrac{K_1(KR_v)}{I_1(KR_v)}\right)\left(\dfrac{C_1}{S}-C_2\left(\dfrac{\varepsilon}{\varepsilon_0}-1\right)\right)+C_1\dfrac{K_1(KR_v)}{I_1(KR_v)}\right\}\end{array}\right]$
A^v	$\dfrac{-K\hat{\varphi}\left(\dfrac{K_0(KR_v)}{I_0(KR_v)}+\dfrac{K_1(KR_v)}{I_1(KR_v)}\right)}{\left[C_1^2+C_2^2\right]}\left[\dfrac{1}{C_3}\left(C_1\left(\dfrac{\varepsilon}{\varepsilon_0}-1\right)+\dfrac{C_2}{S}\right)+C_1+j\left\{\dfrac{1}{C_3}\left(\dfrac{C_1}{S}-C_2\left(\dfrac{\varepsilon}{\varepsilon_0}-1\right)\right)-C_2\right\}\right]$
B^l	$\dfrac{-K\hat{\varphi}\left[C_1-jC_2\right]}{\left[C_1^2+C_2^2\right]}$

Table 4.4 Electric Field Parameters for EC2

C_1	$\left[\frac{K_0(KR_v)}{I_0(KR_v)}-\frac{K_0(KR_o)}{I_0(KR_o)}\right]$
C_2	$\left[\frac{K_0(KR_v)}{I_0(KR_v)}+\frac{K_1(KR_v)}{I_1(KR_v)}\right]$
C_3	$\frac{\left[\frac{K_0(KR_s)}{I_0(KR_s)}+\frac{K_1(KR_T)}{I_1(KR_T)}\right]}{\left[\frac{K_0(KR_T)}{I_0(KR_T)}+\frac{K_1(KR_T)}{I_1(KR_T)}\right]\left[\frac{K_0(KR_s)}{I_0(KR_s)}\right]}$
C_4	$\frac{\left[\frac{K_0(KR_s)}{I_0(KR_s)}-\frac{K_0(KR_T)}{I_0(KR_T)}\right]}{\left[\frac{K_0(KR_T)}{I_0(KR_T)}+\frac{K_1(KR_T)}{I_1(KR_T)}\right]\left[\frac{K_0(KR_s)}{I_0(KR_s)}\right]}$
C_5	$\left(\frac{\varepsilon}{\varepsilon_s}\right)\left(\frac{\varepsilon}{\varepsilon_s}-\frac{\theta}{\alpha}\right)+\left(\frac{\sigma_1}{2\omega\varepsilon_s}\right)^2$
C_6	$\frac{\sigma_1}{2\omega\varepsilon_s}\left(\frac{\theta}{\alpha}\right)$
C_7	$\frac{K_0(KR_s)}{I_0(KR_s)}\frac{K_0(KR_T)}{I_0(KR_T)}$
C_8	$\alpha\left[\left(\frac{\varepsilon}{\varepsilon_s}-\frac{\theta}{\alpha}\right)+\left(\frac{\sigma_1}{2\omega\varepsilon_s}\right)^2\right]$
C_9	$\left(\frac{1-F}{H}\right)\left[1-\frac{\varepsilon}{\varepsilon_0}-\frac{B}{A}\right]D-\left(\frac{1-F}{H}\right)\frac{G}{2S}+\frac{\varepsilon}{\varepsilon_0}\left[\frac{K_0(KR_T)}{I_0(KR_T)}+\frac{K_1(KR_v)}{I_1(KR_v)}\right]+\left[\frac{K_0(KR_v)}{I_0(KR_v)}-\frac{K_0(KR_T)}{I_0(KR_T)}\right]\left(1-\frac{B}{A}\right)$
C_{10}	$\left(\frac{1}{2S}\right)\left[\left(\frac{1-F}{H}\right)D-\left[\frac{K_0(KR_T)}{I_0(KR_T)}+\frac{K_1(KR_v)}{I_1(KR_v)}\right]\right]+\left(\frac{1-F}{H}\right)G\left[1-\frac{\varepsilon}{\varepsilon_0}-\frac{B}{A}\right]$

Table 4.4 (Cont.)

A^l	$\dfrac{K\hat{\varphi}\left(\dfrac{B}{A}\right)\left[\dfrac{(1-F)}{H}(RD+CG)-\dfrac{K_0(KR_T)}{I_0(KR_T)}R+j\left(\dfrac{(1-F)}{H}(RG+CD)+\dfrac{K_0(KR_T)}{I_0(KR_T)}C\right)\right]}{\left[R^2+C^2\right]I_0(KR_o)}$
A^v	$\dfrac{-K\hat{\varphi}}{\left[R^2+C^2\right]I_0(KR_o)}\left[\begin{array}{l}\left(R^2+C^2\right)+\\ \left(\dfrac{K_0(KR_o)}{I_0(KR_o)}\right)\left(\left(\dfrac{R^2+C^2}{A}\right)+\dfrac{B}{A^2}\left(R\left[\dfrac{K_0(KR_v)}{I_0(KR_v)}-\dfrac{K_0(KR_T)}{I_0(KR_T)}\right]+\dfrac{CG(1-F)}{AH}\right)\right)\\ +j\left(\dfrac{B}{A}\right)\left(\dfrac{K_0(KR_o)}{I_0(KR_o)}\right)\left(\dfrac{1}{A}\right)\left(\dfrac{RG(1-F)}{H}-C\left[\dfrac{K_0(KR_v)}{I_0(KR_v)}-\dfrac{K_0(KR_T)}{I_0(KR_T)}\right]\right)\end{array}\right]$
B^v	$\dfrac{K\hat{\varphi}}{I_0(KR_o)}\dfrac{\left[R-jC\right]}{\left[R^2+C^2\right]}\left(\dfrac{B}{A}\right)$
B^l	$\dfrac{K\hat{\varphi}\left[\left(R^2+C^2\right)+\dfrac{B}{A}\left(R\left[\dfrac{K_0(KR_v)}{I_0(KR_v)}-\dfrac{K_0(KR_T)}{I_0(KR_T)}\right]+\dfrac{CG(1-F)}{H}\right)+j\dfrac{B}{A}\left(\dfrac{RG(1-F)}{H}-C\left[\dfrac{K_0(KR_v)}{I_0(KR_v)}-\dfrac{K_0(KR_T)}{I_0(KR_T)}\right]\right)\right]}{\left[R^2+C^2\right]I_0(KR_o)A}$

at the liquid/vapor interface, the electric shear stress acting in the z-direction for two dimensional pipe flow, taking into account that $E_z^l = E_z^v$, yields

$$\tau_{rz}^{electric} = (\varepsilon E_r^l - \varepsilon_0 E_r^v)E_z^v \tag{4.21}$$

The time averaged electric surface stress is then,

$$\overline{\tau}_{rz}^{electric} = \frac{1}{4}\left[\hat{E}_z^v\left(\varepsilon\hat{E}_r^{l'} - \varepsilon_o\hat{E}_r^{v'}\right) + \hat{E}_z^{v'}\left(\varepsilon\hat{E}_r^l - \varepsilon_0\hat{E}_r^v\right)\right] \tag{4.22}$$

The peak values of the electric field required in Eq. (4.22) occur, for example, at $z = t = 0$ and are (see Eq. (4.14))

$$\hat{E}_z^v = -jA^vI_0(KR_v) - jB^vK_0(KR_v)$$

$$\hat{E}_r^v = A^v I_1(KR_v) - B^v K_1(KR_v)$$

$$\hat{E}_r^l = A^l I_1(KR_v) - B^l K_1(KR_v) \tag{4.23}$$

The time-averaged electric shear stress is defined as the electric shear stress averaged over the inverse of the frequency and can now be expressed in terms of the electric field parameters given in Tables 4.2, 4.3, and 4.4 as

$$\begin{aligned}\bar{\tau}_{zr}^{electric} = \frac{1}{2} I_0(KR_v) I_1(KR_v) \Bigg[& \varepsilon_0 \left(\frac{K_1(KR_v)}{I_1(KR_v)} + \frac{K_0(KR_v)}{I_0(KR_v)} \right) \left(B_v^C A_v^R - A_v^C B_v^R \right) \\ & + \varepsilon \Bigg(\frac{K_1(KR_v)}{I_1(KR_v)} \left(A_v^C B_l^R - A_v^R B_l^C \right) + \frac{K_0(KR_v)}{I_0(KR_v)} \left(A_l^C B_v^R - A_l^R B_v^C \right) \\ & \left(A_l^C A_v^R - A_v^C A_l^R \right) + \frac{K_1(KR_v)}{I_1(KR_v)} \frac{K_0(KR_v)}{I_0(KR_v)} \left(B_v^C B_l^R - B_l^C B_v^R \right) \Bigg) \Bigg]\end{aligned} \tag{4.24}$$

where the superscript R and C indicate the real and complex coefficient of each parameter. e.g.

$$A_v = A_v^C + A_v^R \tag{4.25}$$

It is assumed that the resulting flow will be laminar. It is important to mention that this model is valid only when the Reynolds number is below 2300. With the electric shear stress acting only at the interface and the pressure gradient, dp/dz assumed to be constant; the fluid motion will be of a combined Couette-Hagen-Poisseuille type and has the following velocity profile

$$\begin{aligned}w(r) = & \frac{1}{4\mu} \frac{dp}{dz} \left(r^2 - R_T^2 \right) + \frac{1}{4\mu} \frac{dp}{dz} \frac{\left(R_v^2 - R_T^2 \right) \left[\ln(R_T) - \ln(r) \right]}{\left[\ln(R_v) - \ln(R_T) \right]} \\ & + \frac{W_{int} \left[\ln(r) - \ln(R_T) \right]}{\left[\ln(R_v) - \ln(R_T) \right]}\end{aligned} \tag{4.26}$$

The viscous shear stress at the interface is then

$$\tau_{zr}^{viscous} = -\mu \left.\frac{dw}{dr}\right|_{r=R_v} = -\frac{R_v}{2}\frac{dp}{dz} + \frac{1}{4}\frac{dp}{dz}\frac{\left(R_v^2 - R_T^2\right)}{R_v\left[\ln\left(R_v\right) - \ln\left(R_T\right)\right]} - \frac{\mu W_{int}}{R_v\left[\ln\left(R_v\right) - \ln\left(R_T\right)\right]} \tag{4.27}$$

Where

$$\left(\frac{dP}{dz}\right) = \left(\frac{dP}{dz}\right)_{internal} + \left(\frac{dP}{dz}\right)_{external} \tag{4.28}$$

Note that the pressure in the radial direction of the liquid film thickness is uniform (assumption j) and the change in the pressure in the axial direction for the motionless vapor phase due to the hydrostatic effect is negligible. These two assumptions in addition to the one that assumes a constant liquid film thickness suggests that the internal pressure gradient in the axial direction, $\left(\frac{dP}{dz}\right)_{internal}$, in the liquid film is zero. On the other hand, the second term in Eq. (4.28) is included to account for the "external" pressure load or gain on the pumping section of EHD system or loop. The external pressure gradient in the z direction in Eq. (4.28) is constant and independent of the flow velocity.

The following relations are now used to non-dimensionalize the equations:

$$W^* = \frac{W}{W_c}, \text{ where } W_c = \frac{\varepsilon_0 K \hat{\varphi}^2}{2\mu}$$
$$\tau_{rz}^* = \frac{\tau_{rz}}{\tau_{rz,c}}, \text{ where } \tau_{rz,c} = \frac{\mu W_c}{\delta} = \frac{\varepsilon_0 K \hat{\varphi}^2}{2\delta} \tag{4.29a}$$
$$\left(\frac{dp}{dz}\right)^* = \left(\frac{dp}{dz}\right) \Big/ \left(\frac{dp}{dz}\right)_c, \text{ where } \left(\frac{dp}{dz}\right)_c = \frac{2\mu W_c}{\delta^2} = \frac{\varepsilon_0 K \hat{\varphi}^2}{\delta^2}$$

$$\sigma^* = \frac{\sigma}{\sigma_c},\ \text{where}\ \ \sigma_c = \varepsilon_0 K W_c = \frac{\varepsilon_0^2 K^2 \hat{\varphi}^2}{2\mu}$$

$$\omega^* = \frac{\omega}{\omega_c},\ \ \text{where}\ \ \omega_c = K W_c = \frac{\varepsilon_0 K^2 \hat{\varphi}^2}{2\mu}$$

$$R_v^* = \frac{R_v}{R_c},\ R_T^* = \frac{R_T}{R_c},\ \delta^* = \frac{\delta}{R_c},\ \ \text{where}\ \ R_c = \frac{1}{K} \qquad (4.29b)$$

$$r^* = \frac{r}{R_c},\ \ \text{where}\ \ R_c = \frac{1}{K}$$

$$z^* = \frac{z}{R_c},\ \ \text{where}\ R_c = \frac{1}{K}$$

$$S^* = \frac{\omega^* - W^*}{\sigma^*},\ \ \varepsilon^* = \frac{\varepsilon}{\varepsilon_0},\ \varepsilon_s^* = \frac{\varepsilon_s}{\varepsilon_0}$$

In a dimensionless form Eq. (4.28) can be written as

$$\left(\tau_{zr}^{\text{viscous}}\right)^* = \left(\frac{dp}{dz}\right)^* \frac{1}{\delta^*}\left[-R_v^* + \frac{1}{2R_v^*}\frac{\left(R_v^2 - R_T^2\right)}{\left[\ln\left(R_v^*\right) - \ln\left(R_T^*\right)\right]}\right] - \frac{W_{int}^* \delta^*}{R_v^*\left[\ln\left(R_v\right) - \ln\left(R_T\right)\right]} \qquad (4.30)$$

As it was stated before, the electric shear stress equals the viscous shear stress at the interface; Eq. (4.30) expands to

$$\left(\tau_{zr}^{\text{viscous}}\right)^* = \left(\tau_{zr}^{\text{electric}}\right)^* = \left(\frac{dp}{dz}\right)^* \frac{1}{\delta^*}\left[-R_v^* + \frac{1}{2R_v^*}\frac{\left(R_v^2 - R_T^2\right)}{\left[\ln\left(R_v^*\right) - \ln\left(R_T^*\right)\right]}\right] - \frac{W_{int}^* \delta^*}{R_v^*\left[\ln\left(R_v\right) - \ln\left(R_T\right)\right]} \qquad (4.31)$$

The solution for the electric shear stress at the interface can be expressed in its non-dimensional form for cases EC1, EC2, and EC3 respectively as

$$\left(\tau_{zr}^{electric}\right)^{*} = \frac{a^{*}\left(S^{*}\right)^{-1}}{\left[b^{*} + \left(S^{*}\right)^{-2} c^{*}\right]} \tag{4.32}$$

$$\left(\tau_{zr}^{electric}\right)^{*} = \frac{a^{*}\left[b^{*}\left(S^{*}\right)^{-1} - c^{*}\right]}{\left[\left(S^{*}\right)^{-2} d^{*} - \left(S^{*}\right)^{-1} e^{*} + g^{*}\right]} \tag{4.33}$$

$$\left(\tau_{zr}^{electric}\right)^{*} = \frac{a^{*}\left[\left(S^{*}\right)^{-1} + S^{*}\left(\varepsilon^{*} - 1\right)^{2}\right]}{\left[S^{*}b^{*} + \left(S^{*}\right)^{-1} c^{*}\right]^{2} + d^{*}} \tag{4.34}$$

the values of the non-dimensional parameters for each of the three cases are listed in Tables 4.5, 4.6, and 4.7, respectively. It needs to be noted that Eqs. (4.32), (4.33), and (4.34) includes the slip coefficient which is itself a function of the non-dimensional interfacial velocity. Hence, these solutions are implicit and non-linear with respect to the interfacial velocity.

Numerical Results

The non-dimensional interfacial velocities depend on the following non-dimensional parameters; angular velocity, electric conductivity, dielectric constant, liquid film thickness, and vapor radius. It also depends on the external pressure gradient Eq. (4.28). The following discussion assumes that the external pressure gradient term is zero merely to provide a fundamental understanding to the theory developed. The effect of the external pressure gradient as well as the gravitational force will be discussed in details in the ‘Stability’ section of this chapter.

Some important observations can be made upon examining Eqs. (4.32) to (4.34) and their coefficients (see Tables 4.5, 4.6, and 4.7). First, the non-dimensional slip coefficient is always positive for both the attraction and the repulsion pumping cases. In attraction pumping, the non-dimensional interfacial velocity never exceeds the non-dimensional synchronous speed, which equals the non-dimensional angular wave velocity, thus causing a positive slip coefficient. However, in repulsion pumping the non-dimensional interfacial velocity is negative, again resulting in a positive slip coefficient. It can be easily concluded from the coefficients of the electric shear stresses, for the three cases considered given in Eqs. (4.32) to (4.34), that only EC3 results in a negative shear stress, thus negative interfacial velocity (see Tables 4.5, 4.6, and 4.7). Therefore, EC1 and EC2 are examples of the attraction pumping since the interfacial velocity is positive (i.e. in the direction of the traveling electric wave). On the other hand, EC3 is an illustration of repulsion pumping since the non-dimensional interfacial velocity is negative, and consequently, in the direction opposite to that of the electric traveling wave.

Additionally, examining the non-dimensional parameters defined in Eqs. (4.29a) and (4.29b) leads to some interesting conclusions. The non-dimensional electric conductivity, σ^*, and the non-dimensional angular velocity ω^* are directly proportional to the square of the electrode wavelength and the inverse square of the applied voltage. They are also proportional to the fluid viscosity. While σ^* has a direct proportionality to the fluid electric conductivity, ω^* is directly proportional to the frequency. Consequently, the effect of doubling the applied voltage can also be attained by either

Table 4.5 Non-Dimensional Parameters for EC1

a^*	$\delta^* I_0\left(R_v^*\right) I_1\left(R_v^*\right) \dfrac{\left[\dfrac{K_0\left(R_T^*\right)}{I_0\left(R_T^*\right)} + \dfrac{K_1\left(R_v^*\right)}{I_1\left(R_v^*\right)}\right]\left[\dfrac{K_0\left(R_v^*\right)}{I_0\left(R_v^*\right)} - \dfrac{K_0\left(R_T^*\right)}{I_0\left(R_T^*\right)}\right]\left[\dfrac{K_0\left(R_v^*\right)}{I_0\left(R_v^*\right)} + \dfrac{K_1\left(R_v^*\right)}{I_1\left(R_v^*\right)}\right]^2}{\left[I_0\left(R_o^*\right)\right]^2\left[\dfrac{K_0\left(R_v^*\right)}{I_0\left(R_v^*\right)} - \dfrac{K_0\left(R_o^*\right)}{I_0\left(R_o^*\right)}\right]^2}$
b^*	$\left\{\varepsilon^*\left[\dfrac{K_0\left(R_T^*\right)}{I_0\left(R_T^*\right)} + \dfrac{K_1\left(R_v^*\right)}{I_1\left(R_v^*\right)}\right] + \left[\dfrac{K_0\left(R_v^*\right)}{I_0\left(R_v^*\right)} - \dfrac{K_0\left(R_T^*\right)}{I_0\left(R_T^*\right)}\right]\left[1 - \dfrac{\left[\dfrac{K_0\left(R_v^*\right)}{I_0\left(R_v^*\right)} + \dfrac{K_1\left(R_v^*\right)}{I_1\left(R_v^*\right)}\right]}{\left[\dfrac{K_0\left(R_v^*\right)}{I_0\left(R_v^*\right)} - \dfrac{K_0\left(R_o^*\right)}{I_0\left(R_o^*\right)}\right]}\right]\right\}^2$
c^*	$\left[\dfrac{K_0\left(R_T^*\right)}{I_0\left(R_T^*\right)} + \dfrac{K_1\left(R_v^*\right)}{I_1\left(R_v^*\right)}\right]^2$

Table 4.6 Non-Dimensional Parameters for EC3

a^*	$-\varepsilon^*\delta^* \dfrac{I_0\left(R_v^*\right) I_1\left(R_v^*\right)}{\left[I_0\left(R_T^*\right)\right]^2}\left[\dfrac{K_0\left(R_v^*\right)}{I_0\left(R_v^*\right)} + \dfrac{K_1\left(R_v^*\right)}{I_1\left(R_v^*\right)}\right]^2$
b^*	$\left(\varepsilon^* - 1\right)\left[\dfrac{K_0\left(R_v^*\right)}{I_0\left(R_v^*\right)} + \dfrac{K_1\left(R_v^*\right)}{I_1\left(R_v^*\right)}\right] + \left(\varepsilon^* - 1\right)^2\left[\dfrac{K_0\left(R_v^*\right)}{I_0\left(R_v^*\right)} + \dfrac{K_0\left(R_T^*\right)}{I_0\left(R_T^*\right)}\right]$
c^*	$\dfrac{K_1\left(R_v^*\right)}{I_1\left(R_v^*\right)} + \dfrac{K_0\left(R_T^*\right)}{I_0\left(R_T^*\right)}$
d^*	$\dfrac{K_0\left(R_v^*\right)}{I_0\left(R_v^*\right)} + \dfrac{K_1\left(R_v^*\right)}{I_1\left(R_v^*\right)}$

Table 4.7 Non-Dimensional Parameters for EC2

C_1^*	$\left[\frac{K_0\left(R_v^*\right)}{I_0(R_v^*)}-\frac{K_0\left(R_o^*\right)}{I_0\left(R_o^*\right)}\right]$
C_2^*	$\left[\frac{K_0\left(R_v^*\right)}{I_0(R_v^*)}+\frac{K_1\left(R_v^*\right)}{I_1\left(R_v^*\right)}\right]$
C_3^*	$\frac{\left[\frac{K_0\left(R_s^*\right)}{I_0(R_s^*)}+\frac{K_1\left(R_T^*\right)}{I_1\left(R_T^*\right)}\right]}{\left[\frac{K_0\left(R_T^*\right)}{I_0(R_T^*)}+\frac{K_1\left(R_T^*\right)}{I_1\left(R_T^*\right)}\right]\left[\frac{K_0\left(R_s^*\right)}{I_0(R_s^*)}\right]}$
C_4^*	$\frac{\left[\frac{K_0\left(R_s^*\right)}{I_0(R_s^*)}-\frac{K_0\left(R_T^*\right)}{I_0\left(R_T^*\right)}\right]}{\left[\frac{K_0\left(R_T^*\right)}{I_0\left(R_T^*\right)}+\frac{K_1\left(R_T^*\right)}{I_1\left(R_T^*\right)}\right]\left[\frac{K_0\left(R_s^*\right)}{I_0(R_s^*)}\right]}$
C_5^*	$\left(\frac{\varepsilon^*}{\varepsilon_s^*}\right)\left(\frac{\varepsilon^*}{\varepsilon_s^*}\mathrm{C}_4^*-\mathrm{C}_3^*\right)+\mathrm{C}_4^*\left(\frac{\sigma_l^*}{2\omega^*\varepsilon_s^*}\right)^2$
C_6^*	$\frac{\sigma_l^* C_3^*}{2\omega^*\varepsilon_s^*}$
C_7^*	$\frac{I_0\left(R_s^*\right)}{K_0(R_s^*)}\frac{K_0\left(R_T^*\right)}{I_0\left(R_T^*\right)}$
C_8^*	$\left[\left(\frac{\varepsilon^*}{\varepsilon_s^*}C_4^*-C_3^*\right)+\left(\frac{C_4^*\sigma_l^*}{2\omega^*\varepsilon_s^*}\right)^2\right]$

Table 4.7 (Cont.)

a*	$\dfrac{\delta^* I_0\left(R_v^*\right) I_1\left(R_v^*\right) C_2^{*2}}{\left[I_0\left(R_o^*\right)\right]^2 C_1^{*2}}$
b*	$-\left(\dfrac{1-C_7^*}{C_8^*}\right)^2 C_6^{*2}\left(1-\varepsilon^* \dfrac{K_1\left(R_v^*\right)}{I_1\left(R_v^*\right)}\right)-$ $\left(\dfrac{K_0\left(R_v^*\right)}{I_0(R_v^*)}-\dfrac{K_0\left(R_T^*\right)}{I_0\left(R_T^*\right)}+\left(\dfrac{1-C_7^*}{C_8^*}\right)C_5^*\right)\left(\left(\dfrac{1-C_7^*}{C_8^*}\right)C_5^*-\left[\dfrac{K_1\left(R_v^*\right)}{I_1(R_v^*)}+\dfrac{K_0\left(R_T^*\right)}{I_0\left(R_T^*\right)}\right]\right)$
c*	$\left(\dfrac{1-C_7^*}{C_8^*}\right)C_6^*\left\{\begin{array}{c}\left(\dfrac{1-C_7^*}{C_8^*}\right)C_5^*\left(\varepsilon^* \dfrac{K_1\left(R_v^*\right)}{I_1\left(R_v^*\right)}\left(1-\varepsilon^*-\dfrac{C_2^*}{C_1^*}\right)\right) \\ +\varepsilon^* \dfrac{K_1\left(R_v^*\right)}{I_1\left(R_v^*\right)}\left(\varepsilon^*\left[\dfrac{K_1\left(R_v^*\right)}{I_1(R_v^*)}+\dfrac{K_0\left(R_T^*\right)}{I_0\left(R_T^*\right)}\right]+\left[\dfrac{K_0\left(R_v^*\right)}{I_0(R_v^*)}-\dfrac{K_0\left(R_T^*\right)}{I_0\left(R_T^*\right)}\right]\left(1-\dfrac{C_2^*}{C_1^*}\right)-1\right)\end{array}\right\}$
d*	$\left(\dfrac{1-C_7^*}{C_8^*}\right)^2 C_6^{*2}+\left(\left(\dfrac{1-C_7^*}{C_8^*}\right)C_5^*-\left[\dfrac{K_1\left(R_v^*\right)}{I_1(R_v^*)}+\dfrac{K_0\left(R_T^*\right)}{I_0\left(R_T^*\right)}\right]\right)^2$
e*	$2C_6^*\left(\left(\dfrac{1-C_7^*}{C_8^*}\right)\left(1-\dfrac{C_2^*}{C_1^*}\right)\left[\dfrac{K_1\left(R_v^*\right)}{I_1(R_v^*)}+\dfrac{K_0\left(R_v^*\right)}{I_0\left(R_v^*\right)}\right]\right)$
g*	$\left\{\left(\dfrac{1-C_7^*}{C_8^*}\right)C_5^*\left(1-\varepsilon^*-\dfrac{C_2^*}{C_1^*}\right)+\varepsilon^*\left[\dfrac{K_1\left(R_v^*\right)}{I_1(R_v^*)}+\dfrac{K_0\left(R_T^*\right)}{I_0\left(R_T^*\right)}\right]+\left[\dfrac{K_0\left(R_v^*\right)}{I_0(R_v^*)}-\dfrac{K_0\left(R_T^*\right)}{I_0\left(R_T^*\right)}\right]\left(1-\dfrac{C_2^*}{C_1^*}\right)\right\}^2$ $+\left\{\left(\dfrac{1-C_7^*}{C_8^*}\right)C_6^*\left(1-\varepsilon^*-\dfrac{C_2^*}{C_1^*}\right)\right\}^2$

reducing fluid conductivity, or viscosity, or frequency by a factor of four, or by cutting the wavelength in half. The dimensionless radius R_v^* and the dimensionless liquid film thickness δ^*, which can be suitably expressed as a percentage of the total radius R_T^* to represent different operating conditions, are inversely proportional to the electrode wavelength.

In order to determine the range of significance for each parameter, a relatively wide range of real fluids are considered. These fluids include fluids of great interest for many engineering applications such as refrigerants R123, R134a, R404A, and R404C. Additionally, fluids that mainly feature good performance characteristics in EHD pumps [22] and cover a wide range of conductivity, viscosity and dielectric constant such as Sun #4, transformer oil, and Aroclor 1232 are also included. The thermophysical and electrical properties of the refrigerants as a function of temperature are given in [41], while [22] was consulted for the property values of the remaining fluids. In the analytical solutions presented here, the ratio between the total radius of the tube and the wavelength is varied from 0.1 and 1, with the total radius varying from 0.005 m to 0.015 m. The liquid film thickness is varied from 1% to 10% of the total radius, which corresponds to the expected range of a thin film in an annular regime. It is noteworthy to mention that the parameters are varied over a range corresponding to stable pumping, i.e. when only one of the solutions is real, while the others are imaginary.

In attraction pumping, i.e. EC1 and EC2, an increase in the liquid film thickness will lead to an increase in the interfacial velocity. This is due to the fact that the viscous shear stress decreases as the film thickness height increases, while the contending interfacial electric shear stress becomes greater as the interface moves closer to the electrode located at a radius R_o from the centerline of the pipe. Also, when the radius of the electrode increases the interfacial electric shear stress increases due to the closeness of the electrode to the free charges at the interface. From this analogy, it is clear that the highest velocity could be obtained if the interface is placed infinitesimally close to the

electrode or vise versa. However, the constraints at hand are as follows: firstly, due to the nature of an annular regime the liquid film thickness is very small (i.e. not more than 10%-20% of the total radius), which eliminates the option of increasing the film thickness to become infinitesimally close to the electrode. Secondly, increasing R_o brings the electrode close to the interface, though, great caution must be exercised to the vertical electric forces acting on the surface charges, as well as surface waves due to fluid motion. These two may cause the liquid to get in contact with the electrode even if the thickness of the film is relatively small, thus leading to a breakdown of the presumed boundary conditions. Bridge of the liquid to the electrode was experimentally observed by Melcher [3]. Even if the latter is preventable, increasing R_o will force the electrode to act as an obstacle to the flow, hence changing the flow condition, which is practically undesirable. The situation is different for EC3 (repulsion pumping), since both the viscous and electric shear stresses acting at the interface will decrease with an increase in the liquid film thickness.

Equation (4.31) representing the viscous shear stress was solved along with the electric shear stress equation for all the cases considered using “Maple software solver”, in order to obtain the interfacial velocity.

Figure 4.2 shows the relations between the non-dimensional angular frequency of the electric wave and the interfacial liquid film velocity for EC1 and EC2. The subscripts of the label entries, e.g. “30%”, indicate the electrode radius as a percentage of the total radius. A higher percentage value indicates that the electrode is closer to the interface,

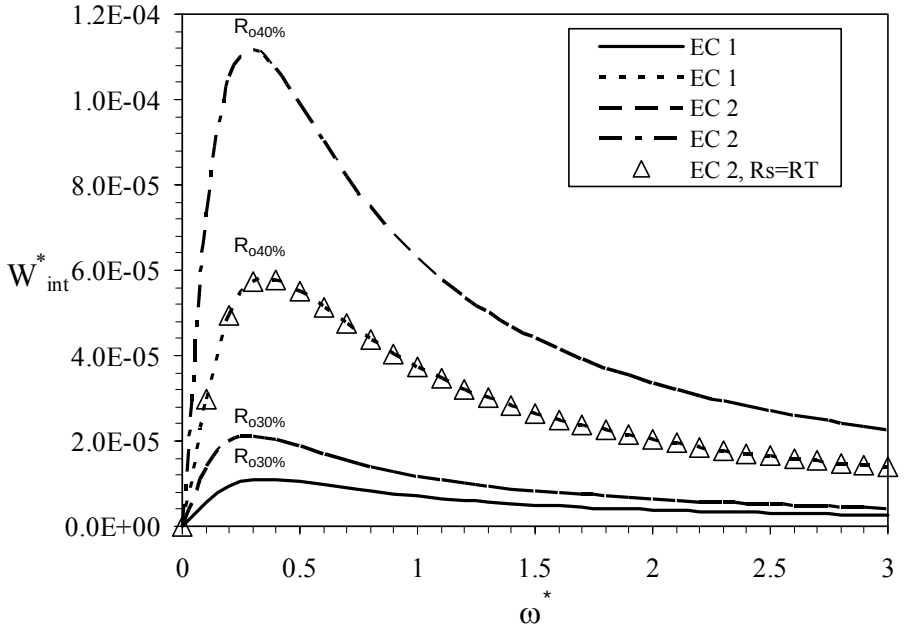

Fig. 4.2 Dependency of interfacial velocity on electric wave angular velocity for two electrode radius for EC1 and EC2 (R^*_T=7, σ^*=4, ε^*=5) (Note: subscripts indicate electrode radius in percent of total radius.)

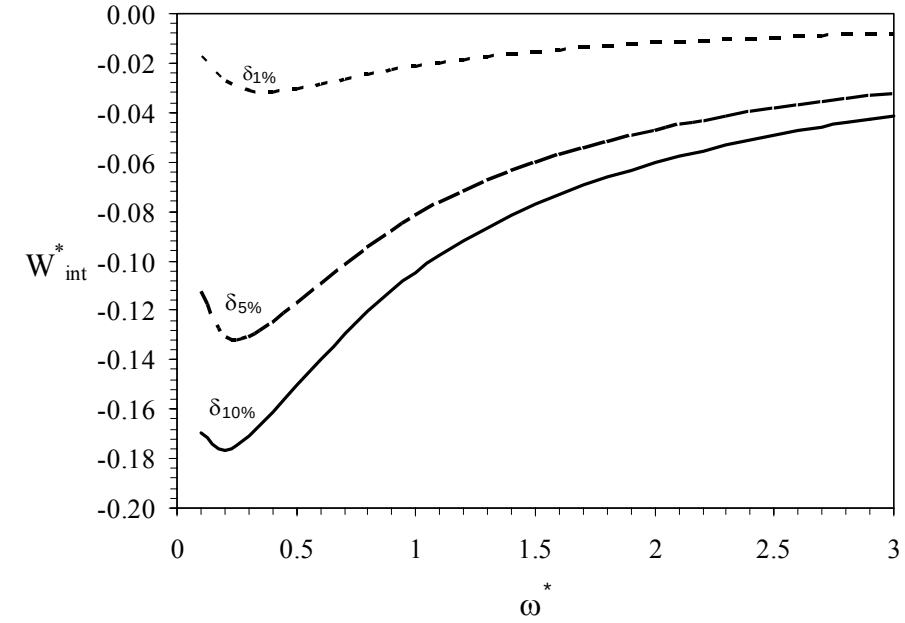

Fig. 4.3 Dependency of interfacial velocity on electric wave angular velocity for EC3 (R^*_T=7, σ^*=4, ε^*=5) (Note: subscripts indicate liquid film thickness in percent of total radius.)

thus the higher interfacial velocity. On the other hand, Fig. 4.3 illustrates the same relations for EC3. The subscripts of the label entries, e.g. “1%”, indicate the liquid film thickness as a percentage of the total radius. Despite the values for the fixed parameters, an optimum value of an angular electric wave frequency for all three cases does exist. When the angular electric wave frequency is very small, the electric shear acting at the interface is small and the interface velocity must be small as well. Conversely, when the angular frequency becomes too large, charges at the interface are not capable to follow the electric wave effectively due to the limiting electric conductivity of the fluid, resulting in a small velocity as well. The velocities obtained with EC2 are greater than those attained with EC1. However, EC2 and EC1 should collapse on one curve as the thickness of the insulated plate in EC2 approaches zero. The same conclusion was reported by Brand and Seyed-Yagoobi [16].

An increase in the liquid film thickness leads to an increase from 1% to 10% in the interfacial velocity as shown in Figs. 4.2 and 4.3. For the repulsion pumping, however, such an increase, as described earlier, is not necessarily always reflected by a higher interfacial velocity. A full description of the situation may be provided through Figs. 4.4 and 4.5. These figures indicate that due to the no-slip condition at the wall (i.e. when $\delta^*=0$), the viscous forces become noticeably higher as the liquid film approaches infinitesimally small values, hence the interfacial velocities converge to a value of zero. For attraction pumping, Fig. 4.4 shows that as the liquid film increases initially, the interfacial velocity increases gradually. When the liquid film grows further, the interface gets closer to the electrode and experiences a stronger electric field. This allows the free

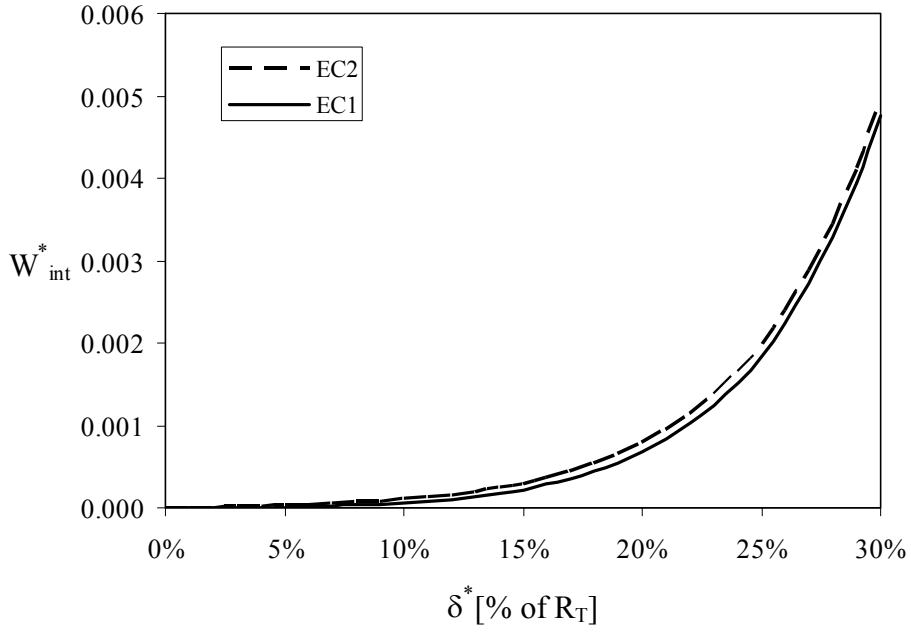

Fig. 4.4 Dependency of interfacial velocity on liquid film thickness for EC1 and EC2 (R^*_T=7, σ^*=4, ε^*=5, ω^*=0.4)

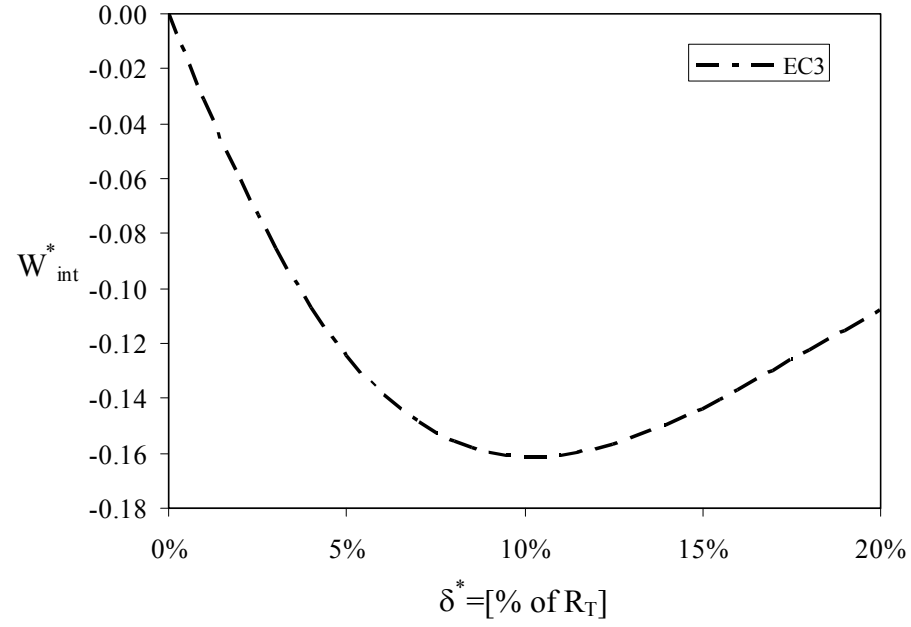

Fig. 4.5 Dependency of interfacial velocity on liquid film thickness for EC3 (R^*_T=7, σ^*=4, ε^*=5, ω^*=0.4)

charges at the interface to follow the electric wave more closely; consequently a higher velocity is attained. As illustrated in Fig. 4.5, in repulsion pumping mode, there is an optimum liquid film thickness yielding the highest interfacial velocity under given operating conditions. After this optimum value and as the interface moves away from the wall the viscous shear stress become weaker, however, the electric shear stress becomes weaker as well as it approaches the imposed insulating boundary condition (due to symmetry) at the centerline of the pipe, thus a smaller interfacial velocity is obtained.

It is noteworthy to mention that Figs. 4.4 and 4.5 were generated using a fixed value of non-dimensional electric conductivity. If a higher non-dimensional electric conductivity is elected, the interfacial velocity will increase at lower liquid film thickness for EC1 and EC2. This is due to the fact that the free charges in these two cases relax to the interface at reduced field strengths, and the interfacial velocity will be relatively high even at low liquid thickness. On the contrary, when a fluid with lower non-dimensional electric conductivity is chosen, the increase in the interfacial velocity will be deferred until the electric field become stronger, i.e. higher liquid thickness is reached. This implies that the interface has to be placed very close to the electrode in order to experience a sufficiently strong electric field, and therefore producing significant pumping. In the case of repulsion pumping Fig. 4.5, if a lower non-dimensional conductivity is selected, the liquid, which is more insulating in this case, will act as a shield between the interface and the electric wave at the wall. In order to reach an optimum interaction between the electric field and the surface charges the

interface needs to move closer to the interface. Consequently, the point of the optimum interfacial velocity (Fig. 4.5) now will shift to a lower liquid film thickness.

Figures 4.6 and 4.7 are typical examples for the influence of non-dimensional conductivity on interfacial velocity. For all three configurations considered, an optimum conductivity level exists. If the conductivity level is small, no charges relax to the interface and hence no interaction with the electric wave is possible. However, in a fluid with large conductivity, the charges can relax instantaneously from one point on the interface to another, resulting in a perpendicular electric field with minimal electric shear [3]. As shown in Fig. 4.7 for EC3, the electric conductivity must increase as the interface moves away from the electrode to overcome the decrease in electric field's strength at the interface.

Finally, the significance of the dielectric constant ε^* is shown in Figs. 4.8 and 4.9. Since dielectric constants with values below one have no physical significance, only dielectric constants with values of one and higher are considered. In attraction mode pumping, Fig. 4.8 shows that the interfacial velocity is reduced as the dielectric constant is increased, while an optimum value for the dielectric constant exists for the repulsion mode pumping. This can be explained through the mathematical solutions of the interfacial velocity, Eqs. (4.32), (4.33), and (4.34), with their appropriate parameters listed in Tables 4.5, 4.6, and 4.7. In the attraction mode, ε^* appeared only in the denominator, therefore a reduction in the interfacial velocity as the non-dimensional permittivity increases is expected. On the other hand, the solutions for the repulsion pumping show ε^* in both the numerator and denominator, thus optimum value is

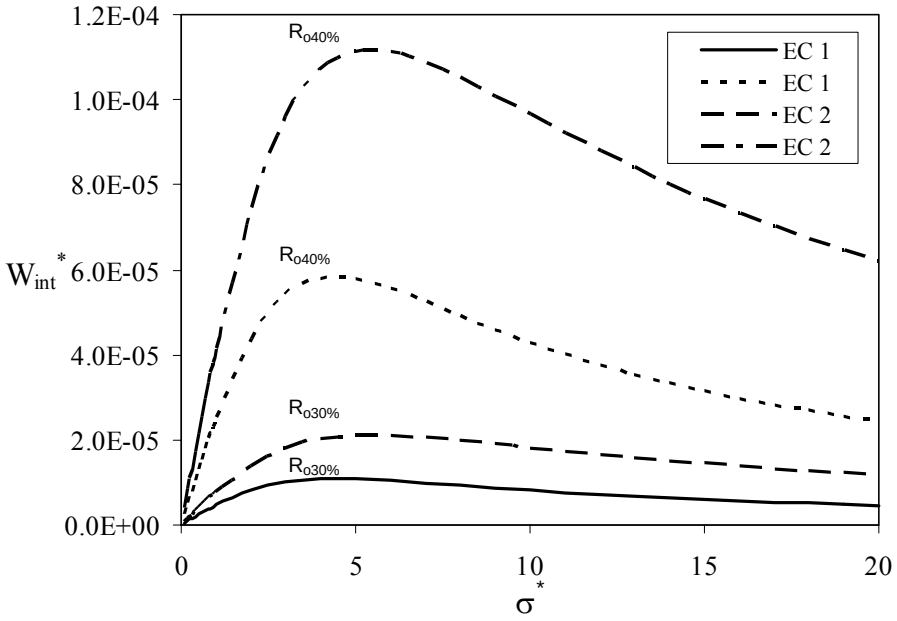

Fig. 4.6 Influence of conductivity on interfacial velocity for EC1 and EC2 (R^*_T=7, ε^*=5, ω^*=0.4) (Note: subscripts indicate electrode radius in percent of total radius.)

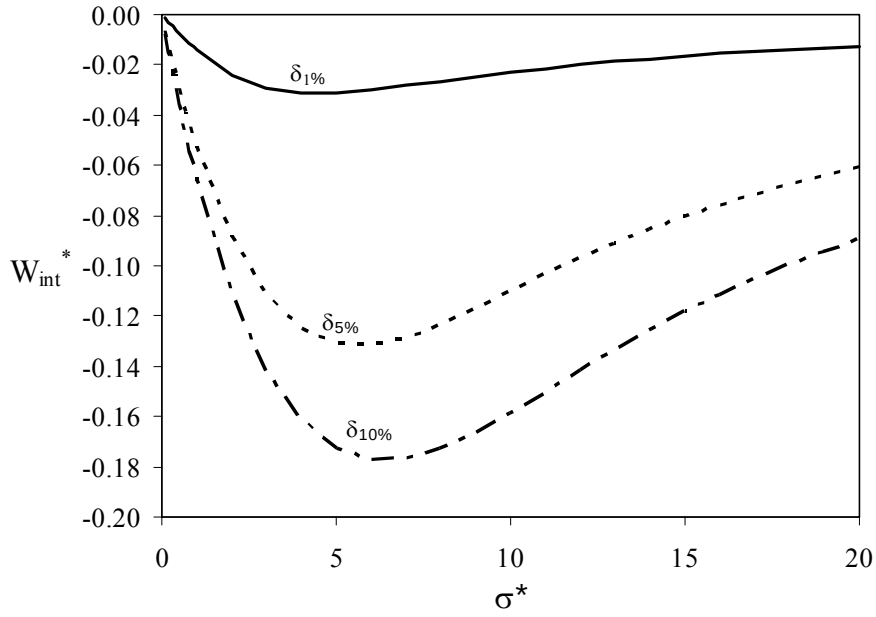

Fig. 4.7 Influence of conductivity on interfacial velocity for EC3 (R^*_T=7, ε^*=5, ω^*=0.4) (Note: subscripts indicate liquid film thickness in percent of total radius.)

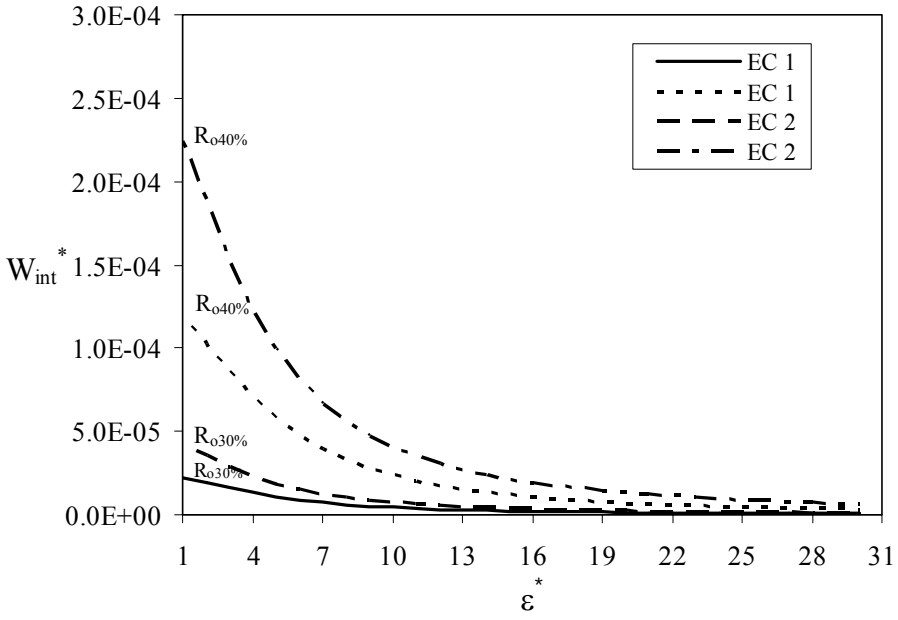

Fig. 4.8 Influence of dielectric constant on interfacial velocity for EC1 and EC2 (R^*_T=7, σ^*=4, ω^*=0.4) (Note: subscripts indicate electrode radius in percent of total radius.)

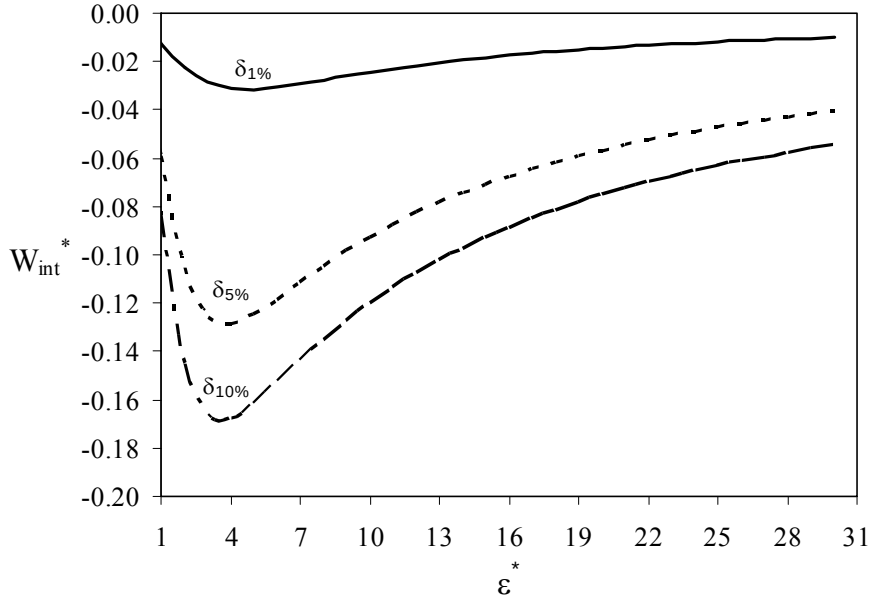

Fig. 4.9 Influence of dielectric constant on interfacial velocity for EC3 (R^*_T=7, σ^*=4, ω^*=0.4) (Note: subscripts indicate liquid film thickness in percent of total radius.)

expected.

Stability

A sudden drop in pump output or even alternating flow direction is among the signs of unstable induction pump. This may depend on the geometry, electric parameters, fluid properties, and external load applied to the system. Obviously, it is necessary to design and operate an induction pump which is free from such unreliable behavior. Melcher [2] graphically illustrated the deriving electric shear stress and the retarding viscous shear stress versus the interfacial velocity. These plots provided an easily accessible way to understand the characteristics of EHD induction pump operation. He ob-served stable (one operating point) and unstable (two or three operating points) pump operations and determined the corresponding operating conditions. Crowley [5] relied on this stress diagram to establish criteria for stable operation of both attraction and repulsion mode pumps. This investigation assumed an overly simplified expression for the electric shear stress, but nonetheless provided valuable tool for the prediction of pump behavior. In a recent study by Wawzyniak and Seyed-Yagoobi [10], quantitative values were given, allowing for simple characterization of stable or unstable pump behavior based on non-dimensional values of electric conductivity, dielectric constant, and non-dimensional liquid and vapor heights for both attraction and repulsion mode pumps . In recent work by Brand and Seyed-Yagoobi [16], EHD induction pump of a dielectric micro condensation film in an external horizontal configuration was investigated experimentally. Bi-directional flow

was observed for the first time due to instability of EHD induction pumping. It was also observed that by increasing the frequency, the flow became unidirectional. They were able to explain qualitatively the observed bi-directional flow followed by unidirectional flow with frequency increase using the theoretical work presented in [10].

This section investigates the EHD induction pumping of liquid film in vertical annular configuration Fig. 4.10. The core objective of this section is to analytically analyze the effect of the external load (i.e. pressure gradient and gravity) on the stability of EHD induction pumping of liquid film in vertical annular configuration for the more practical case of repulsion mode induction pumping (i.e. EC3). Even though the geometry considered in this section is in vertical configuration, the solution for the electric shear stress for EC3 obtained in the previous section Eq. (4.34) is still applicable. However, the non-dimensional viscous shear stress, with the gravitational term included, is given below

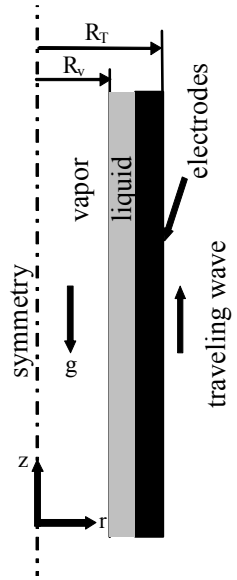

Fig. 4.10 Schematic of the vertical analytical domain

$$\left(\tau_{zr}^{viscous}\right)^{*} = \frac{1}{2\delta^{*}}\left(\left(\frac{dp}{dz}\right)^{*}_{external} - G^{*}\right)\left[-2R_{v}^{*} + \frac{1}{R_{v}^{*}}\frac{\left(R_{v}^{2} - R_{T}^{2}\right)}{\left[\ln\left(R_{v}^{*}\right) - \ln\left(R_{T}^{*}\right)\right]}\right] - \frac{W_{int}^{*}\delta^{*}}{R_{v}^{*}\left[\ln\left(R_{v}\right) - \ln\left(R_{T}\right)\right]} \tag{4.35}$$

Combining Eq. (4.34) and (4.35), with the parameters from Table 4.7, and substitution of the slip coefficient, yields

$$W_{int}^{*5} + A_{1}^{*} * W_{int}^{*4} + A_{2}^{*} * W_{int}^{*3} + A_{3}^{*} * W_{int}^{*2} + A_{4}^{*} * W_{int}^{*} + A_{5}^{*} = 0 \tag{4.36}$$

where

$$A_{1}^{*} = \left(4\omega^{*} - C_{1}^{*}C_{2}^{*}\right) \tag{4.37}$$

$$A_{2}^{*} = -2\omega^{*2} - 4\omega^{*}C_{1}^{*}C_{2}^{*} + \frac{\left(2b^{*}c^{*} + d^{*}\right)\sigma^{*2}}{b^{*2}} - \frac{a^{*}\sigma^{*}\left(\varepsilon^{*2} - 1\right)^{2}C_{1}^{*}}{b^{*2}} \tag{4.38}$$

$$A_{3}^{*} = -4\omega^{*3} + 2\omega^{*2}C_{1}^{*}C_{2}^{*} - 2\omega^{*}\frac{\left(2b^{*}c^{*} + d^{*}\right)\sigma^{*2}}{b^{*2}} + 3\omega^{*}\frac{a^{*}\sigma^{*}C_{1}^{*}\left(\varepsilon^{*2} - 1\right)^{2}}{b^{*2}} - \frac{\left(2b^{*}c^{*} + d^{*}\right)\sigma^{*2}C_{1}^{*}C_{2}^{*}}{b^{*2}} \tag{4.39}$$

$$A_{4}^{*} = \omega^{*4} + 4\omega^{*3}C_{1}^{*}C_{2}^{*} + \omega^{*2}\frac{\left(2b^{*}c^{*} + d^{*}\right)\sigma^{*2}}{b^{*2}} - \left(\frac{3a^{*}\omega^{*2}\sigma^{*}C_{1}^{*}\left(\varepsilon^{*2} - 1\right)^{2}}{b^{*2}}\right) + 2\omega^{*}\frac{\left(2b^{*}c^{*} + d^{*}\right)\sigma^{*2}C_{1}^{*}C_{2}^{*}}{b^{*2}} + \frac{c^{*2}\sigma^{*4}}{b^{*2}} - \frac{a^{*}\sigma^{*3}C_{1}^{*}}{b^{*2}} \tag{4.40}$$

$$A_{5}^{*} = -\omega^{*4}C_{1}^{*}C_{2}^{*} - \omega^{*2}\frac{\left(2b^{*}c^{*} + d^{*}\right)\sigma^{*2}C_{1}^{*}C_{2}^{*}}{b^{*2}} - \frac{c^{*2}\sigma^{*4}C_{1}^{*}C_{2}^{*}}{b^{*2}} + \frac{a^{*}\omega^{*}\sigma^{*3}C_{1}^{*}}{b^{*2}} + \frac{a^{*}\omega^{*3}\sigma^{*2}C_{1}^{*}\left(\varepsilon^{*2} - 1\right)^{2}}{b^{*2}} \tag{4.41}$$

and

$$C_1^* = \frac{\delta^*}{R_v^*\left[\ln\left(R_v^*\right) - \ln\left(R_T^*\right)\right]} \tag{4.42}$$

$$C_2^* = \frac{1}{2\delta^*}\left[\left(\frac{dP}{dz}\right)_{externel}^{*} - G^*\right]\cdot\left[-2R_v^* + \frac{\left(R_v^{*2} - R_T^{*2}\right)}{R_v^*\left(\ln\left(R_v^*\right) - \ln\left(R_T^*\right)\right)}\right] \tag{4.43}$$

a^* has a negative value, while the values of b^*, c^*, and d^* are always positive. It is important to mention that Eq. (4.43) represents the coupled effect of gravitational force density and external pressure gradient on the viscous shear stress. This implies that, as expected, the effect of the gravitational force density can be incorporated in the pressure gradient effect. Both effects can be treated as one, signified by the net difference.

The formulation given above Eq. (4.36) demonstrates that there could be in fact not one solution for the interfacial velocity, but five. With the right combination of the aforementioned parameters and electric properties, one real solution for the interfacial velocity could exist, while the other four solutions would be imaginary. The results presented in this chapter so far are only for cases where only one of the solutions is real. On the other hand, other combinations of the operating parameters could yield three real solutions for the interfacial velocity (negative, positive, or null) along with two imaginary solutions. There are even situations under which attraction pumping, i.e. positive velocities can be realized with a repulsion mode pumping. Finally, there are evident contradictions where induction pumping is generated without applying an electric traveling wave (i.e. real solutions at $\omega^* = 0$). Obviously, this is not feasible; they are solely unacceptable mathematical roots of the above non-linear equation.

Plotting the dimensionless viscous (Eq. (4.35)) and electric shear (Eq. (4.34)) stresses as a function of the non-dimensional interfacial velocity in what is so called, force curves [3], [5], and [10], is a valuable tool to understand and qualitatively evaluate the instability phenomenon. Figure 4.11 displays the electric shear stress as a function of the interfacial velocity with the same electrical properties, but for two different liquid thicknesses. Since the interface happens to be closer to the electrode at a smaller liquid film thickness, a higher electric shear stress is expected. Figure 4.9 also presents the viscous shear stress for three different pressure gradients, -0.03, 0, and +0.03, in the presence of negative gravitational effect (i.e. G*= -0.09) to demonstrate the influence of the coupled effect of pressure gradient and gravitational force density on the pump performance. Negative gravitational effect corresponds to the direction of gravity in the terrestrial applications (see Fig. 4.10). The non-dimensional pressure gradient of 0.03 corresponds to the dimensional pressure gradient of 914 Pa/m for R-123 as the working fluid at 25 ^{o}C along with λ= 7.0 mm and φ= 1380 V. On the other hand, the non-dimensional gravitational effect was chosen to have the same order of magnitude as the external pressure gradient to allow for the comparison of both effects. The non-dimensional gravitational effect of 0.09 (g=2.0 m/s^2) considered in this study corresponds to applications where the gravitational acceleration is less than the terrestrial gravitational acceleration at the same operating conditions. The three curves have a linear trend with the same slope for fixed geometric parameters and fluid properties. The results presented in Fig. 4.11 in the presence of gravitational effect can be easily extended to exclude the gravitational effect (for outer space applications). For instance,

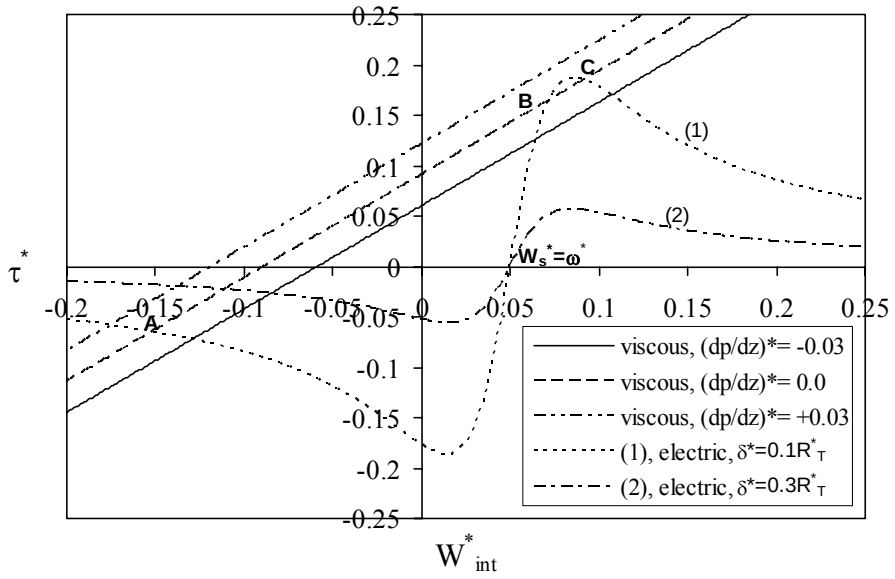

Fig. 4.11 Dimensionless viscous shear stress and electric shear stress as a functions of the dimensionless interfacial velocity (R^*_T=7, σ^*=0.2, ε^*=5, ω^*=0.05, G^*=-0.09)

Fig. 4.11 represents the dimensionless viscous and electric shear stresses in the absence of the gravitational effect (G*=0) for three different external pressure gradients of +0.06, +0.09, and +0.12.

As previously mentioned, whenever there is equilibrium between the electric shear stress and the retarded viscous shear stress, solutions of the interfacial velocities exist. These points of equilibrium, thus the interfacial velocities, manifest themselves in the intersections between the electric shear stress and the viscous shear stress curves as shown in Fig. 4.11. These points of intersections will be referred to as the operating points of the pump.

When only one operating point exists, pump operation is called stable. Otherwise, the operation is referred to as unstable [3]. For zero and negative pressure gradient, at a

liquid thickness of 10%, three operating points do exist, denoting unstable pump. However, for positive pressure gradient, only one operating point exists, indicating stable pump operation. In spite of the pressure gradient effect, at a liquid thickness of 30%, stable operations always exist (Fig. 4.11, curve 2). At all pressure gradients considered (i.e. $\left(\frac{dp}{dz}\right)^*_{externel}$ = -0.03, 0, +0.03) negative interfacial velocity exists, as curve 2 in Fig. 4.11 reveals. An operating point is stable if and only if [5], [9]

$$\frac{\partial\left(\tau_{rz}^{electric}\right)^*}{\partial W^*} < \frac{\partial\left(\tau_{rz}^{viscous}\right)^*}{\partial W^*} \tag{4.44}$$

That is why of the three operating points (A, B, and C) possible in the absence of an external pressure gradient, A and C are stable, while B is unstable as shown in curve 1 in Fig. 4.11. At operating point B, if a perturbing force makes the interfacial velocity decrease slightly in magnitude, the viscous will force dominate the electric force. As a result, the pump will resume its operation stability at a lower stable point of operation (point A). On the other hand, if a similar perturbing force makes the interfacial velocity increase in magnitude slightly, the electric force will dominate the viscous force and will tend to return the pump to its operation at the higher stable speed possible (point C). For more details on such behavior see [3].

The following discussion is carried out using the case of zero gravitational force and pressure gradient as an example. Important comments can be made upon examination of Eq. (4.36) and curve 1 in Fig. 4.11. The electric shear stress is a

function of the difference between the non-dimensional angular velocity and the non-dimensional interfacial velocity,

$$\left(\tau_{rz}^{electric}\right)^{*} = \text{function}\left(\omega^{*} - W^{*}\right) \tag{4.45}$$

When electric wave and interface charges move at the same velocity, the dimensionless interfacial velocity equals the dimensionless angular velocity (i.e. $W_s^{*}=\omega^{*}$) [10]. At this point, the interfacial velocity reaches the synchronous speed limit and the electric shear stress equals to zero, as shown in Fig. 4.11. If the dimensionless electric wave angular velocity is altered (by changing the frequency), the dimensionless electric shear stress curves in Fig. 4.11 would simply shift as a whole to the left or to the right, such that it intersects the W_{int}^{*} axis at the dimensionless electric wave angular velocity. Based on the above information, one can prove by visual examination that a frequency exists for the positive pressure gradients shown in curve 1 of Fig. 4.11, which will cause the pump to be unstable. Consequently, operation of a repulsion-mode pump at any frequency is always stable if

$$\left.\frac{\partial\left(\tau_{rz}^{electric}\right)^{*}}{\partial W^{*}}\right|_{max} < \frac{\partial\left(\tau_{rz}^{viscous}\right)^{*}}{\partial W^{*}} \tag{4.46}$$

This criterion was established in [5] and used in [10]. The maximum positive electric shear stress slope for repulsion pumping occurs at the synchronous speed illustrated in [5], [10].

$$\left(\omega^{*} - W^{*}\right) = 0 \tag{4.47}$$

Taking the derivative of the electric shear stress (Eq. (4.34)) with respect to the velocity, and then substitution of Eq. (4.47) in the resultant equation yield

$$\left.\frac{\partial\left(\tau_{rz}^{electric}\right)^{*}}{\partial W^{*}}\right|_{max} = -\frac{a^{*}}{\sigma^{*}C^{*2}} \tag{4.48}$$

This guarantees stable operation can always be achieved independent of frequency and external load only if

$$-\frac{a^{*}}{\sigma^{*}c^{*2}} < \frac{\delta^{*}}{R_{v}^{*}\left[\ln\left(R_{T}^{*}\right)-\ln\left(R_{v}^{*}\right)\right]} \tag{4.49}$$

The values of the non-dimensional parameter, a^{*} and c^{*}, are negative and positive, respectively, for the repulsion pumping cases (see Table 4.7). The guaranteed stability criteria for repulsion mode pumping depends on the non-dimensional conductivity, and the parameters a^{*} and c^{*}, which in turn are a function of the non-dimensional liquid thickness, vapor radius, total radius, and the dielectric constant. The stability criteria for repulsion pumping obtained by [10] shows a similar dependency on the dielectric constant and electric conductivity to the one in Eq. (4.49) except for the geometric parameters, which account for the curvature effect in this study. Equation (4.49) also indicates that stable pump operation is guaranteed as long as the maximum electric shear stress slope is smaller than the viscous shear stress slope (see Eq. (4.46)) in spite of the electric wave angular velocity or the external load. In an actual EHD induction pump, the total radius will often be fixed. However, the liquid film thickness, hence the vapor radius, can be changed. In addition, it is relatively difficult to change the dielectric

constant compared to the electric conductivity. Therefore, the guaranteed stability of an induction pump is only a matter of non-dimensional electric conductivity and liquid film thickness as shown in Fig 4.12. Combinations of non-dimensional conductivity and liquid film thickness above the curve will provide the guaranteed stable performance, while combinations below the curve will cause unstable operation. However, for a given unstable pump operation (i.e. three operating points) in the presence of external load, the operation can be stabilized (i.e. yielding only one operation point) by increasing the electric wave angular velocity by simply increasing the frequency above a certain threshold value as shown in the following paragraph.

Figure 4.13 presents the dependency of non-dimensional interfacial velocity on non-dimensional electric wave angular velocity for various external pressure gradients corresponding to stable and unstable cases in the presence of the gravitational effect. Figure 4.13 was generated by equating Eq. (4.34) and Eq. (4.35) at different electric wave angular velocity. The two different cases of repulsion pumping, at a non-dimensional angular velocity of 0.05, gravitational force of -0.09, and three different pressure gradients, presented in Fig. 4.11 are incorporated into Fig. 4.13. The non-dimensional interfacial velocities resulting from the equilibrium between viscous and electric shear stresses (points of intersections) in Fig. 4.11 at the same value of non-dimensional angular velocity match those included in Fig. 4.13. At a given angular velocity, the curve is termed stable when only one interfacial velocity is possible (curves 1-3), while it is rendered unstable when more than one velocity is possible (curves 4, 5, and 6).

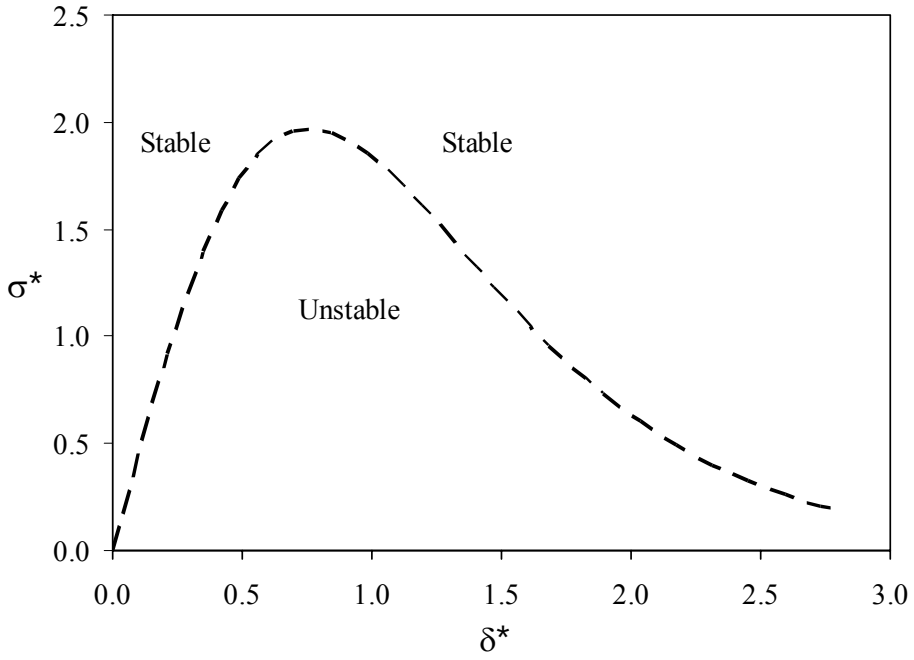

Fig. 4.12 Stability map for dimensionless conductivity and liquid film thickness; the region above the curve is stable (R^*_T=7, ε^*=5)

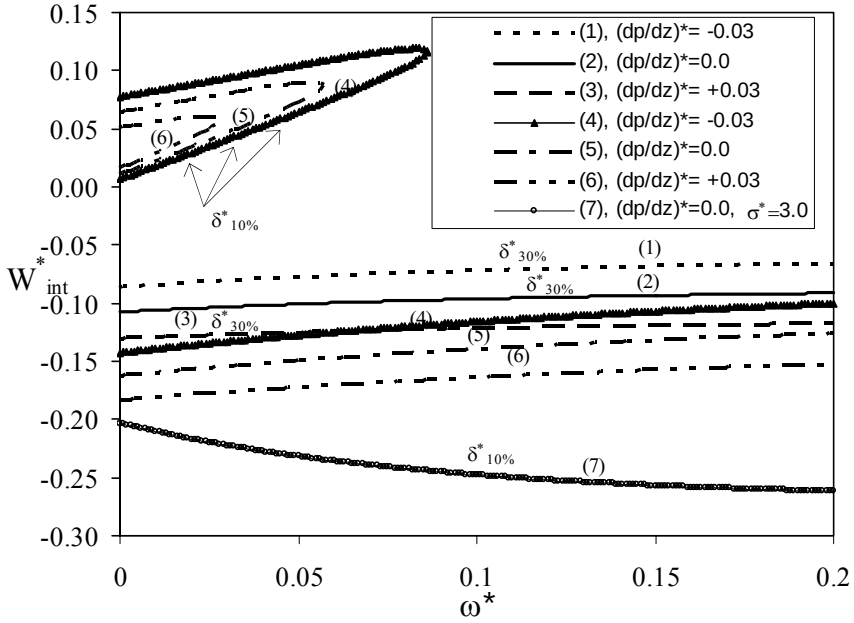

Fig. 4.13 Dependency of interfacial velocity on electric wave angular velocity with two sets of liquid film thickness (R^*_T=7, σ^*=0.2, ε^*=5.0, G^*= -0.09)

In the repulsion pumping mode, the interfacial velocity acts in the opposite direction of the traveling wave. Therefore, under the conditions illustrated in Fig. 4.10, the positive pressure gradient and the negative gravitational force favor the motion of the interfacial velocity; while a negative pressure gradient opposes the gravitational force and the motion of the interfacial velocity, resulting in a lower interfacial velocity. Consequently, besides resulting in a higher interfacial velocity, it is expected that the electric wave angular velocity threshold for the positive pressure gradient to be smaller than that for the negative and zero pressure gradients regardless of the value of the dimensionless gravitational force density (see Fig. 4.13). Figure 4.14 shows that as the magnitude of the dimensionless gravitational force density (G*) decreases the electric wave angular velocity threshold increases. It is evident from Fig. 4.14 that the gravitational force density assists the stabilization of the pump operation.

Figure 4.13 indicates that three solutions for the equilibrium interfacial velocity (two positive and one negative) appear for dimensionless angular velocity less than 0.086 (electric wave angular velocity threshold) for all three pressure gradients at the liquid film thickness of 10% of the total radius. Whereas, only one negative solution appears for higher electric wave angular velocity than 0.086, meaning that the pump is unstable below a given angular velocity threshold and stable beyond it.

Closer look at the unstable cases gives insight into the mechanisms of a pump enduring instability. It is significant to note that for unstable cases, the pump may have one meta-stable point (where the viscous shear stress slope is greater than the electric shear stress slope) at a positive interfacial velocity and one at a negative interfacial

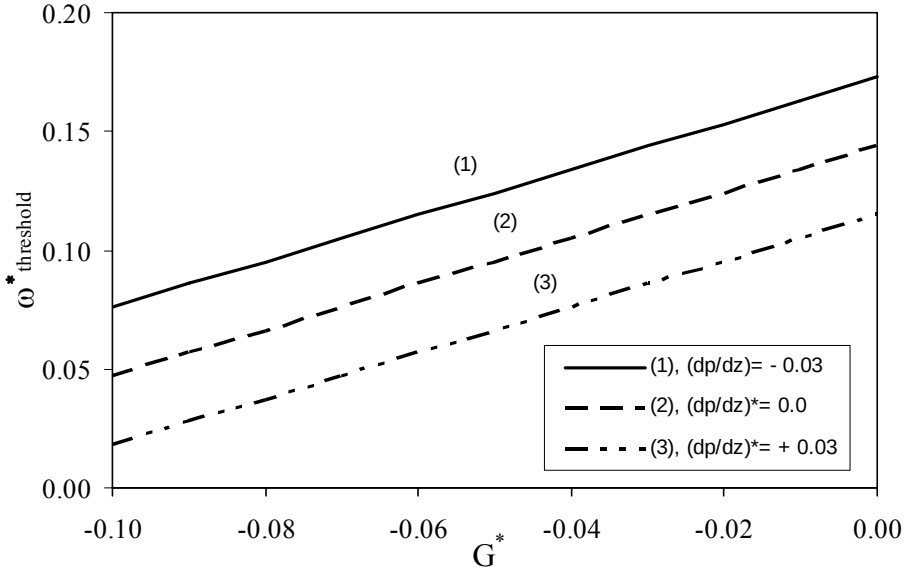

Fig. 4.14 Dependency of electric wave angular velocity threshold on gravitational force density (R^*_T=7, σ^*=0.2, ε^*=5.0, δ^*=0.1R^*_T)

velocity. This could lead not only in inconsistency in the pump operation, velocity jumps or drops, but it could also result in changing the pumping direction. For example, in the absence of pressure gradient (Fig.4.13, curve 5), for the non-dimensional angular velocity ranging from zero to approximately 0.057, the interfacial velocity may assume any one of the three possible values. Upon increasing the non-dimensional angular velocity past a value of about 0.057, the interfacial velocity will have only one negative solution; in this case the pump will operate in its expected direction. A further increase in frequency leads to gradual decrease of stable interfacial velocity as is common in induction devices [10]. Note that the stable operation criterion given by Eq. (4.49) is based on Eq. (4.46) where the "maximum" slope of the electric shear stress was assumed to be less than the slope of the viscous shear stress. This resulted in an assured stability

criteria, independent of the traveling electric wave frequency. However, as presented above, there are operating conditions that locally yield lower slope for the electric shear stress (not the maximum) than for the viscous shear stress, which could result in stable pump operation by increasing the traveling electric wave frequency beyond the corresponding threshold frequency.

It is very clear from Fig. 4.12 that the combination between the dimensionless electric conductivity of 0.2 and a liquid film thickness of 10% of the total radius (i.e. $\delta^* = 0.7$) leads to unstable pump behavior. With the help of Fig 4.12, curve 5 in Fig. 4.13 can be stabilized by increasing the non-dimensional electric conductivity from 0.2 to 3.0 while keeping the value of the liquid film thickness the same. It is also clear from curve 7 in Fig. 4.13 that this not only avoids the unreliable behavior of the pump, but also improves the performance of the pump [10]. For liquid film thickness of 30% of the total radius, only one negative solution appears for the entire range of the electric wave angular velocity.

CHAPTER V

NUMERICAL MODEL*

The model derived in this chapter is an improvement of the model presented in the previous chapter. However, only the most practical case studied in the preceding chapter will be discussed here (EC3). The Numerical Model considers a two-dimensional developing annular flow of a thin liquid film in an axisymmetric vertical tube (see Fig. 5.1). The liquid film is separated from the vapor by a flat interface. Boundary condition of electric traveling wave is imposed in the liquid film adjacent the wall of the tube while symmetric boundary condition for the electric field is imposed at the tube centerline (i.e. $E_r^v = 0$). In addition to the charges, and therefore electric shear stress, at the liquid/vapor interface the Numerical Model considers charges throughout the bulk of the liquid film. Due to an electric conductivity gradient in the liquid film, charge induction takes place. This gradient may exist as a result of a temperature gradient, which is a consequence of viscous dissipation, Joule heating, or cooling or heating of the boundaries. The following assumptions are made with regards to the electric shear stress and liquid film flow field are.

a. the vapor has properties of a vacuum;
b. the electric field is irrotational due to low electric currents in induction pumping applications;

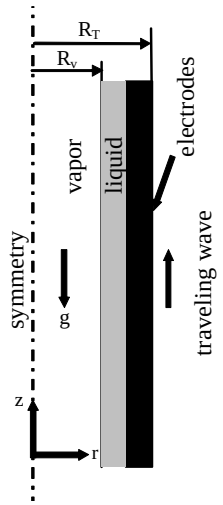

Fig. 5.1 Schematic of the analytical domain

c. all fluid properties in the liquid layer are temperature dependent (volumetric charge induction will occur in the bulk);

d. charge transport within the interface due to ion mobility, surface conduction, and bulk conduction in z-direction are negligible;

e. the flow is two-dimensional and in vertical configuration;

f. the flow field may be modeled as flow between two concentric cylinders, the outer one being stationary and the inner one moving at the constant speed of the liquid/vapor interface in the z-direction;

g. the flow is steady state, laminar, incompressible , but not fully developed;

h. the flow is rotationally symmetric, i.e., the variable do not depend upon θ;

i. the electric field is axisymmetric;

j. the pressure in r-direction is uniform, the pressure gradient in z-direction is constant and independent of the flow velocity;

k. The model neglects all forces in radial direction and therefore the possibility of surface waves and resulting in flat liquid/vapor interface.

Governing Equations

The continuity equation is

$$\nabla.\left(\rho\bar{v}\right)=0 \tag{5.1}$$

For an incompressible flow with constant density, it reduces to

$$\nabla.\bar{v}=0 \tag{5.2}$$

The conservation of momentum, or Navier-Stokes, equation is

$$\rho\frac{D\bar{v}}{Dt}=-\nabla p-\nabla.\tau_{ij}+\rho g+\bar{f}_e \tag{5.3}$$

The flow is assumed to be steady state and incompressible. The electric force in z-direction acting on a plane with normal r can be expressed as

$$f_{e,z}=\frac{1}{r}\frac{\partial}{\partial r}\left\langle r\tau_{e,rz}\right\rangle+\frac{1}{r}\frac{\partial}{\partial\theta}\left\langle\tau_{e,\theta z}\right\rangle+\frac{\partial}{\partial z}\left\langle\tau_{e,zz}\right\rangle\ , \tag{5.4}$$

Since the electric field is axisymmetric and the change in the time averaged electric shear stress in the flow direction is small, the last two terms become negligible. Therefore, the equation (5.4) becomes

$$f_{e,z}=\frac{1}{r}\frac{\partial}{\partial r}\left\langle r\tau_{e,rz}\right\rangle \tag{5.5}$$

Now the momentum equation in the axial direction becomes

$$\rho\left(u\frac{\partial w}{\partial r}+w\frac{\partial w}{\partial z}\right)=-\frac{dp}{dz}-\nabla.\tau_{ij}+\rho g+\frac{1}{r}\frac{\partial}{\partial r}\left\langle r\tau_{e,rz}\right\rangle \tag{5.6}$$

Since the flow is axisymmetric $\tau_{z\theta}$ can be neglected and τ_{ij} simplifies to only on term, τ_{rz} and τ_{zz}, which is equal to

$$\tau_{rz} = -\mu\left(\frac{\partial w}{\partial r} + \frac{\partial u}{\partial z}\right) \tag{5.7}$$

$$\tau_{zz} = -2\mu\frac{\partial w}{\partial z} \tag{5.8}$$

Equation (5.6) becomes

$$\rho\left(u\frac{\partial w}{\partial r} + w\frac{\partial w}{\partial z}\right) = -\frac{dp}{dz} + \frac{1}{r}\frac{\partial}{\partial r}\left(\mu r\frac{\partial w}{\partial r} + \mu r\frac{\partial u}{\partial z}\right) + \frac{\partial}{\partial z}\left(2\mu\frac{\partial u}{\partial z}\right) + \rho g + \frac{1}{r}\frac{\partial}{\partial r}\left\langle r\tau_{e,rz}\right\rangle \tag{5.9}$$

The momentum equation in the r-direction is

$$\rho\left(u\frac{\partial u}{\partial r} + w\frac{\partial u}{\partial z}\right) = -\frac{dp}{dr} - [\frac{1}{r}\frac{\partial}{\partial r}(r\tau_{rr}) - \frac{\tau_{\theta\theta}}{r} + \frac{\partial\tau_{rz}}{\partial z}] \tag{5.10}$$

where the electrical forces are ignored (see the assumptions). The stress tensor in equation (2.8) is defined as follows

$$\tau_{rr} = -\mu\left(2\frac{\partial u}{\partial r} - \frac{2}{3}\nabla.\bar{v}\right) = -2\mu\frac{\partial u}{\partial r} \tag{5.11}$$

$$\tau_{\theta\theta} = -\mu\left(2\left(\frac{1}{r}\frac{\partial v}{\partial\theta} + \frac{u}{r}\right) - \frac{2}{3}\nabla.\bar{v}\right) = -2\mu\frac{u}{r} \tag{5.12}$$

$$\tau_{rz} = -\mu\left(\frac{\partial w}{\partial r} + \frac{\partial u}{\partial z}\right) \tag{5.13}$$

Substituting the shear stresses into equation (5.10) gives

$$\rho\left(u\frac{\partial u}{\partial r}+w\frac{\partial u}{\partial z}\right)=-\frac{dp}{dr}-\{-\frac{1}{r}\frac{\partial}{\partial r}\left(2\mu r\frac{\partial u}{\partial r}\right)+2\mu\frac{u}{r^2}-\frac{\partial}{\partial z}\left(\mu\left[\frac{\partial w}{\partial r}+\frac{\partial u}{\partial z}\right]\right)\} \tag{5.14}$$

The full energy equation including viscous dissipation and Joule heating is given as

$$\rho c_p\frac{DT}{Dt}=k\nabla^2T+\mu\Phi+\sigma\vec{E}^2-T\left(\frac{\partial p}{\partial T}\right)_\rho\left(\nabla.\bar{v}\right) \tag{5.15}$$

From the continuity equation, the last term in the above equation is zero. Then equation (5.15) becomes

$$u\frac{\partial T}{\partial r}+w\frac{\partial T}{\partial z}=\frac{k}{\rho c_p}\frac{1}{r}\frac{\partial}{\partial r}\left(r\frac{\partial T}{\partial r}\right)+\frac{\sigma E^2}{\rho c_p} \tag{5.16}$$

under the assumption of steady-state, incompressible flow, and negligible viscous dissipation. The second derivative of T in z-direction is neglected since it is much smaller than in r-direction.

The irrotational electric field is governed by Maxwell's equations

$$\nabla\times\vec{E}=0 \tag{5.17}$$

and

$$\nabla.\varepsilon\vec{E}=q \tag{5.18}$$

The electric field may be expressed as

$$\vec{E}=-\nabla\phi \tag{5.19}$$

Under the assumption of constant permittivity, Poisson's equation is obtained

$$\nabla^2\phi=-\frac{q}{\varepsilon} \tag{5.20}$$

Additionally, equations for charge conservation and charge density are given below, respectively,

$$\nabla.\vec{J} + \frac{\partial q}{\partial t} = 0 \tag{5.21}$$

$$\vec{J} = \sigma\vec{E} + q\vec{v} \tag{5.22}$$

Substituting Eqs. (5.20) and (5.22) into (5.21), the result after some manipulation is

$$\varepsilon\frac{\partial}{\partial t}\left[\nabla^2\phi\right] + \nabla.\left[\sigma\nabla\phi + \varepsilon\vec{v}\nabla^2\phi\right] = 0 \tag{5.23}$$

For the electric potential, φ. The solution is separable in time and space and of form

$$\phi(r,z,t) = \sum_{m=-\infty}^{\infty}\sum_{n=-\infty}^{\infty}\Psi_m(r,z)\Theta_n(t) \tag{5.24}$$

The function $\Theta_n(t)$ is periodic with respect to time and can be expressed as the Fourier series

$$\Theta_n(t) = c_n \exp\left[j\omega_n t\right] , \tag{5.25}$$

where the electric angular wave (i.e. $\omega_n = 2n\pi f$), while space the function $\psi_m(r,z)$ can be represented as

$$\Psi_m(r,z) = C(r)Z_m(z) \tag{5.26}$$

Here, $Z_m(z)$ is periodic with respect to z can be expressed as

$$Z_m(z) = c_m \exp\left[-jK_m z\right] \tag{5.27}$$

where $K_m = \frac{2m\pi}{\lambda}$, giving the electric potential as

$$\phi(r,z,t) = \sum_{m=-\infty}^{\infty}\sum_{n=-\infty}^{\infty} c_m c_n\, C(r)\exp\left[\, j\left(\omega_n t - K_m z\right)\right] \tag{5.28}$$

Substituting Eq. (5.28) in to Eq. (5.23) and taking into consideration that $\frac{\partial \sigma}{\partial z} \cong 0$ due to the negligibly small temperature variation in z-direction and that $\nabla . \vec{v} = 0$ (Eq. (5.2)), yields

$$\left[\sigma + j\varepsilon\left(\omega_n - wK_m\right)\right]\frac{1}{r}\frac{d}{dr}\left(r\frac{dC}{dr}\right) + \frac{d\sigma}{dr}\frac{dC}{dr} - \left[\sigma + j\varepsilon\left(\omega_n - wK_m\right)\right]K_m^2 C = 0 \qquad (5.29)$$

Eq. (5.29) represents the governing equation for the electric potential. For this study, only the first harmonics (i.e. m= n= 1) will be retained.

Subsequently, the electric shear stress and the Joule heating need to be expressed in terms of the electric potential. The time-averaged shear stress as given by [42] is

$$\overline{\tau}_{e,rz} = \frac{\varepsilon}{2}\mathrm{Re}\left(E_z E_r^{'}\right) \qquad (5.30)$$

$$E_r = -\frac{\partial \phi}{\partial r} \quad \text{and} \quad E_z = -\frac{\partial \phi}{\partial z} \qquad (5.31)$$

where Re stands for the real value of the complex term and ‘ for its complex conjugate. With Eq. (5.28), the time-averaged shear stress becomes,

$$\overline{\tau}_{e,rz} = \frac{\varepsilon}{2}\mathrm{Re}\left(-jKC\frac{dC^{'}}{dr}\right) \qquad (5.32)$$

The Joule heating may be calculated from

$$\sigma\vec{E}^2 = \sigma\left[\left(\frac{\partial \phi}{\partial z}\right)^2 + \left(\frac{\partial \phi}{\partial r}\right)^2\right] \qquad (5.33)$$

or

$$\sigma\vec{E}^2 = \frac{1}{2}\sigma\left[K^2|C|^2 + \left|\frac{dC}{dr}\right|^2\right] \qquad (5.34)$$

where $\left|\ \right|$ stand for the magnitude of a complex number.

Interfacial Electric Shear Stress Boundary Condition

The interfacial electric shear stress, which is a necessary the boundary equations to the above set of equations can be obtained as follows,

Evaluating Maxwell's stress tensor

$$\tau_{ij}^{electric} = \varepsilon E_i E_j - \frac{1}{2}\delta_{ij}\varepsilon E_k^2 \tag{5.35}$$

at the liquid/vapor interface the electric shear stress in the z-direction for 2-d pipe flow

$$\tau_{rz}^{electric} = (\varepsilon E_r^l - \varepsilon_0 E_r^v)E_z^v \tag{5.36}$$

where $E_z^l = E_z^v$ is applied . The time averaged electric shear stress at the interface becomes (see Eq. (4.22)),

$$\overline{\tau}_{rz}^{electric} = \frac{1}{4}\left[\hat{E}_z^v\left(\varepsilon\hat{E}_r^{l'} - \varepsilon_o\hat{E}_r^{v'}\right) + \hat{E}_z^{v'}\left(\varepsilon\hat{E}_r^l - \varepsilon_0\hat{E}_r^v\right)\right] \tag{5.37}$$

The electric field distribution in the vapor phase can be calculated by letting

$$\vec{E}^v = -\nabla\left[\varphi^v \exp\left(j(\omega t - Kz)\right)\right]$$

$$\varphi^v = -\left(A^v I_0(Kr) + B^v K_0(Kr)\right) \tag{5.38}$$

The boundary conditions at the interface are

$$E_z^v - E_z^l = 0 \qquad @\, r = R_v \tag{5.39}$$

and

$$\varepsilon E_r^l - \varepsilon_0 E_r^v = Q \qquad @\, r = R_v \tag{5.40}$$

While the symmetrical boundary condition at the centerline of the pipe is

$$E_r^v = 0 \quad @\, r = 0 \tag{5.41}$$

Finally, the electric traveling wave imposed at the electrodes gives the following boundary condition

$$E_z = \mathrm{Re}\left\{ jK\hat{\varphi} \exp\left[j(\omega t - Kz) \right] \right\} \tag{5.42}$$

The electric field in z-direction at the interface is

$$E_z^l\Big|_{r=R_v} = -\frac{\partial \varphi}{\partial z}\Big|_{r=R_v} = jK\,C\big|_{r=R_v} \exp\left[j(\omega t - Kz) \right] \tag{5.43}$$

and

$$E_z^v\Big|_{r=R_v} = -\frac{\partial \varphi}{\partial z}\Big|_{r=R_v} = -jK \exp\left[j(\omega t - Kz) \right]\left(A^v I_0(R_v K) + B^v K_0(R_v K) \right) \tag{5.44}$$

These two equations may be combined with the first boundary condition (Eq. (5.39)) to obtain

$$-\left(A^v I_0(R_v K) + B^v K_0(R_v K) \right) = C\big|_{r=R_v} \tag{5.45}$$

Similarly, the electric field in r-direction at the interface is

$$E_r^l\Big|_{r=R_v} = -\frac{\partial \varphi}{\partial r}\Big|_{r=R_v} = -\frac{dC}{dr}\Big|_{r=R_v} \exp\left[j(\omega t - Kz) \right] \tag{5.46}$$

and

$$E_r^v\Big|_{r=R_v} = \exp\left[j(\omega t - Kz) \right]\left(A^v K I_1(R_v K) - B^v K K_1(R_v K) \right) \tag{5.47}$$

This may be combined with the second boundary condition (Eq. (5.40)) to produce

$$-\varepsilon_0 \exp\left[\,j\left(\omega t - Kz\right)\right]\left(A^{v} K I_1\left(R_v K\right) - B^{v} K K_1\left(R_v K\right)\right)$$
$$-\varepsilon \left.\frac{dC}{dr}\right|_{r=R} \exp\left[\,j\left(\omega t - Kz\right)\right] = Q \tag{5.48}$$

Substituting Eq. (5.22) into Eq. (5.21) yields

$$\nabla.\left(\sigma \vec{E}\right) + \nabla.\left(q\vec{v}\right) + \frac{\partial q}{\partial t} = 0 \tag{5.49}$$

It is assumed that flow occurs solely in z-direction, equation (2.46) becomes

$$\frac{1}{r}\frac{\partial}{\partial r}\left(r\sigma E_r\right) + \frac{\partial}{\partial z}\left(\sigma E_z\right) + \frac{\partial}{\partial z}\left(qw\right) + \frac{\partial q}{\partial t} = 0 \tag{5.50}$$

The conductivity of the vapor is taken as zero, since the vapor phase is modeled as a vacuum. Furthermore, presuming that surface currents are due solely to convection of free changes within the interface, i.e. surface conduction in z-direction is negligible; Eq. (5.50) can be integrated across the interface to yield

$$-\sigma_l E_r^{l} = w\frac{\partial Q}{\partial z} + \frac{\partial Q}{\partial t} \tag{5.51}$$

Here we assume the velocity w in z-direction at the interface is constant.

From Eqs. (5.46), (5.48), and (5.51) after cancellation of the time dependent term we get

$$-\sigma \left.\frac{dC}{dr}\right|_{r=R_v} = j\left[\varepsilon_0 K\left(A^{v} I_1(KR_v) - B^{v} K_1(KR_v)\right) + \varepsilon \left.\frac{dC}{dr}\right|_{r=R_v}\right]\left[\omega - wK\right] \tag{5.52}$$

Rearrange results in

$$\frac{j}{S}\left.\frac{dC}{dr}\right|_{r=R_v} = \frac{\varepsilon}{\varepsilon_0}\left.\frac{dC}{dr}\right|_{r=R_v} + K\left[A^{v} I_1(KR_v) - B^{v} K_1(KR_v)\right] \tag{5.53}$$

where

$$S = \frac{\varepsilon_0 (\omega - wK)}{\sigma}$$

Upon the application of Eq. (5.41) $K_1(0) \to \infty$, thus $B^v = 0$ must be zero in order to have a bounded solution. Therefore, Eq. (5.45) yields

$$A^v = \frac{-C\big|_{r=R_v}}{I_0(KR)} \tag{5.54}$$

Using (5.54) into (5.53) results,

$$\left.\frac{dC}{dr}\right|_{r=R_v} = \frac{+KC\big|_{r=R_v} \dfrac{I_1(KR_v)}{I_0(KR_v)}\left(\dfrac{\varepsilon}{\varepsilon_0} + \dfrac{j}{S}\right)}{\left(\dfrac{1}{S}\right)^2 + \left(\dfrac{\varepsilon}{\varepsilon_0}\right)^2} \tag{5.55}$$

The peak values of the electric fields required to determine the electric interfacial shear stress, based on Eqs. (5.44), (5.46) and (5.47), respectively are

$$\hat{E}_z^v = -jA^v K I_0(KR_v) \tag{5.56}$$

$$\hat{E}_r^v = A^v K I_1(KR_v) \tag{5.57}$$

$$\hat{E}_r^l = -\left.\frac{dC}{dr}\right|_{r=R_v} \tag{5.58}$$

Substitution of these last three equations into Eq. (5.37) yields

$$\overline{\tau}_{rz}^{electric} = \frac{1}{2} K I_0(KR_v) \varepsilon \left[A^R \left(\left.\frac{dC}{dr}\right|_{r=R_v} \right)^C - A^C \left(\left.\frac{dC}{dr}\right|_{r=R_v} \right)^R \right] \tag{5.59}$$

The superscripts R and C again indicate the real and complex coefficients of a complex number. The coefficient A has been determined in Eq. (5.54) so that the interfacial shear

stress may be written as

$$\bar{\tau}_{rz}^{electric} = \frac{1}{2} K\varepsilon \left[C^C \left(\left. \frac{dC}{dr} \right|_{r=R_v} \right)^R - C^R \left(\left. \frac{dC}{dr} \right|_{r=R_v} \right)^C \right] \tag{5.60}$$

Substituting Eq. (5.55) into Eq. (5.60) yields after simplification

$$\bar{\tau}_{rz}^{electric} = -\frac{\frac{\varepsilon K^2}{4S} \frac{I_1(KR_v)}{I_0(KR_v)}}{\left(\frac{1}{S}\right)^2 + \left(\frac{\varepsilon}{\varepsilon_0}\right)^2} \left[\left(C^R\right)^2 + \left(C^C\right)^2 \right] \tag{5.61}$$

All Cs are evaluated at $r = R_v$.

Additional Boundary Conditions

For the momentum equations, the non-slip boundary conditions at the wall are

$$u = w = 0 \qquad @ \qquad r = R_T \tag{5.62}$$

The assumption that the liquid/vapor interface is flat

$$u = 0 \qquad @ \qquad r = R_v \tag{5.63}$$

The balance of viscous and electric shear stresses at the liquid/vapor interface

$$-\mu \frac{\partial w}{\partial r} = \tau_{e,rz}^{int} \qquad @ \qquad r = R_v \tag{5.64}$$

with $\tau_{e,rz}^{int}$ being given in Eq. (5.61). In addition, a zero velocity in r-direction is imposed at the pipe inlet and outlet

$$u = 0 \qquad @ \qquad z = 0,\ z = L \tag{5.65}$$

this implies that $\frac{\partial u}{\partial r} = 0$ at $z = 0$ and $z = L$. Therefore, from continuity equation

$$\frac{\partial w}{\partial z} = 0 \qquad @ \qquad z = 0,\ z = L \tag{5.66}$$

For the energy equation heat transfer gain or loss through pipe wall or across the interface are accounted for by the following two boundary conditions

$$-k\frac{\partial T}{\partial r} = q''_{wall} \qquad @ \qquad r = R_T \tag{5.67}$$

and

$$-k\frac{\partial T}{\partial r} = q''_{interface} \qquad @ \qquad r = R_v \tag{5.68}$$

In addition, the temperature profile at the pipe entrance is specified as

$$T(r) \quad @ \quad z=0 \tag{5.69}$$

Finally, the two boundary conditions are the electric potential at the electrode

$$C = \hat{\varphi}_e \qquad @ \qquad r = R_T \tag{5.70}$$

and the requirement that the electric field be zero at the centerline due to the symmetry (Eq. (5.41)). For the electric potential at the interface (Eq. (5.55))

$$\left|\frac{dC}{dr}\right| = \frac{-KC\big|_{r=R_v}\dfrac{I_1(KR_v)}{I_0(KR_v)}\left(\dfrac{\varepsilon}{\varepsilon_0}+\dfrac{j}{S}\right)}{\left(\dfrac{1}{S}\right)^2+\left(\dfrac{\varepsilon}{\varepsilon_0}\right)^2} \qquad @ \qquad r = R_v \tag{5.71}$$

Non-Dimensionalization

The governing equations and boundary conditions are non-dimensionalized using the following dimensionless fluid properties,

$$\mu^* = \frac{\mu}{\mu_{bo}},\ \rho^* = \frac{\rho}{\rho_{bo}},\ c_p^* = \frac{c_p}{c_{pbo}},\ k^* = \frac{k}{k_{bo}},\ \sigma^* = \frac{\sigma}{\sigma_{bo}},\ \varepsilon^* = \frac{\varepsilon}{\varepsilon_c} \tag{5.72}$$

where

$$\varepsilon_c = \frac{\sigma_{bo}\rho_{bo}\delta^2}{\mu_{bo}} = \frac{\varepsilon_0}{N_e}$$

Length scales are as follows

$$z^* = \frac{z}{\delta},\quad r^* = \frac{r}{\delta},\quad R_v^* = \frac{R_v}{\delta},\quad R_T^* = \frac{R_T}{\delta},\quad L^* = \frac{L}{\delta} \tag{5.73}$$

and the dimensionless electric parameters are given below

$$E^* = \frac{E}{E_c},\ \text{where}\ E_c = \frac{\hat{\varphi}_e}{\delta}$$

$$C^* = \frac{C}{\hat{\varphi}_e},\ C'^* = \frac{C'}{\hat{\varphi}_e}$$

$$K^* = \frac{K}{K_c},\quad \text{where}\ K_c = \frac{1}{\delta}$$

$$\omega^* = \frac{\omega}{\omega_c},\quad \text{where}\ \omega_c = \frac{\mu_{bo}}{\rho_{bo}\delta^2}$$

$$S^* = \frac{S}{N_e^*},\quad \text{where}\ N_e^* = \frac{\mu_{bo}}{\rho_{bo}\delta^2}\frac{\varepsilon_0}{\sigma_{bo}}$$

$$\tau_{e,rz}^* = \frac{\tau_{e,rz}}{\tau_{e,rz_c}},\ \text{where}\ \tau_{e,rz_c} = \frac{\rho_{bo}\sigma_{bo}\hat{\varphi}_e^2}{2\mu_{bo}} \tag{5.74}$$

and finally, dimensionless flow parameters defined as follows

$$u^* = \frac{u}{u_c}, \quad \text{where} \quad u_c = \frac{\mu_{bo}}{\rho_{bo}\delta}$$

$$w^* = \frac{w}{w_c}, \quad \text{where} \quad w_c = \frac{\mu_{bo}}{\rho_{bo}\delta}$$

$$p^* = \frac{p}{p_c}, \quad \text{where} \quad p_c = \frac{\mu_{bo}^2}{\rho_{bo}\delta^2}$$

$$T^* = \frac{T}{T_c}, \quad \text{where} \quad T_c = \frac{\sigma_{bo}\hat{\varphi}_e^2}{\mu_{bo}c_{pbo}} = \frac{2\mu_{bo}\sigma_{bo}M_e^*}{\varepsilon_o c_{pbo}\rho_{bo}} \tag{5.75}$$

Then the momentum, energy, electric potential, time averaged shear stress, and Joule heating equations (Eqs. (5.9), (5.14), (5.16), (5.29), (5.32), and (5.34), respectively) become

$$\rho^*\left(u^*\frac{\partial w^*}{\partial r^*} + w^*\frac{\partial w^*}{\partial z^*}\right) = -\frac{dp^*}{dz^*} + \frac{1}{r^*}\frac{\partial}{\partial r^*}\left(\mu^* r^*\frac{\partial w^*}{\partial r^*} + \mu^* r^*\frac{\partial u^*}{\partial r^*}\right) + \frac{\partial}{\partial z^*}\left(2\mu^*\frac{\partial w^*}{\partial z^*}\right) + \frac{M_e}{N_e}\frac{1}{r^*}\frac{\partial}{\partial r^*}\left\langle r^*\tau_{e,rz}^*\right\rangle \tag{5.76}$$

$$\rho^*\left(u^*\frac{\partial u^*}{\partial r^*} + w^*\frac{\partial u^*}{\partial z^*}\right) = -\frac{dp^*}{dr^*} + \frac{1}{r^*}\frac{\partial}{\partial r^*}\left(2\mu^* r^*\frac{\partial u^*}{\partial r^*}\right) - \frac{2\mu^* u^*}{r^{*2}} + \frac{\partial}{\partial z^*}\left(\mu^*\left(\frac{\partial w^*}{\partial r^*} + \frac{\partial u^*}{\partial z^*}\right)\right) \tag{5.77}$$

$$\left(u^*\frac{\partial T^*}{\partial r^*} + w^*\frac{\partial T^*}{\partial z^*}\right) = \frac{k^*}{\rho^* c_p^*}\frac{1}{Pr_{bo}}\frac{1}{r^*}\frac{\partial}{\partial r^*}\left(r^*\frac{\partial T^*}{\partial r^*}\right) + \frac{\sigma^* E^*}{\rho^* c_p^*} \tag{5.78}$$

$$\left[\sigma^* + j\varepsilon^*\left(\omega_n^* - w^* K_m^*\right)\right]\frac{1}{r^*}\frac{d}{dr^*}\left(r^*\frac{dC^*}{dr^*}\right) + \frac{d\sigma^*}{dr^*}\frac{dC^*}{dr^*} - \left[\sigma^* + j\varepsilon^*\left(\omega_n^* - w^* K_m^*\right)\right]K_m^{*2}C^* = 0 \tag{5.79}$$

$$\overline{\tau}_{e,rz}^{*} = \varepsilon^{*}\,\mathrm{Re}\left(-jK^{*}C^{*}\frac{dC^{'*}}{dr^{*}}\right) \tag{5.80}$$

$$\sigma^{*}\overline{E}^{*2} = \frac{1}{2}\sigma^{*}\left[K^{*2}\left|C^{*}\right|^{2} + \left|\frac{dC^{*}}{dr^{*}}\right|^{2}\right] \tag{5.81}$$

The non-dimensional slip coefficient is

$$S^{*} = \frac{\omega^{*} - K^{*}w^{*}}{\sigma^{*}} \tag{5.82}$$

to simplify Eqs. (5.79)- (5.81) it is convenient to express the complex electric potential as

$$C^{*} = C^{*R} + jC^{*C} \tag{5.83}$$

Substitution of Eq. (5.83) into (5.79) leads to

$$\begin{aligned}&\left[\sigma^{*} + j\varepsilon^{*}\left(\omega^{*} - w^{*}K_{m}^{*}\right)\right]\frac{1}{r^{*}}\frac{d}{dr^{*}}\left(r^{*}\left(\frac{dC^{*R}}{dr^{*}} + j\frac{dC^{*C}}{dr^{*}}\right)\right) + \frac{d\sigma^{*}}{dr^{*}}\left[\frac{dC^{*R}}{dr^{*}} + j\frac{dC^{*c}}{dr^{*}}\right]\\ &-\left[\sigma^{*} + j\varepsilon^{*}\left(\omega^{*} - w^{*}K_{m}^{*}\right)\right]K_{m}^{*2}\left[C^{*R} + jC^{*C}\right] = 0\end{aligned} \tag{5.84}$$

The equation for the real term is then

$$\begin{aligned}&\frac{1}{r^{*}}\frac{d}{dr^{*}}\left(r^{*}\frac{dC^{*R}}{dr^{*}}\right) - \frac{\varepsilon^{*}\left(\omega^{*} - w^{*}K_{m}^{*}\right)}{\sigma^{*}}\frac{1}{r^{*}}\frac{d}{dr^{*}}\left(r^{*}\frac{dC^{*c}}{dr^{*}}\right) + \frac{1}{\sigma^{*}}\frac{d\sigma^{*}}{dr^{*}}\frac{dC^{*R}}{dr^{*}}\\ &-K_{m}^{*2}C^{*R} + \frac{K_{m}^{*2}\varepsilon^{*}\left(\omega^{*} - w^{*}K_{m}^{*}\right)}{\sigma^{*}}C^{*C} = 0\end{aligned} \tag{5.85}$$

or

$$\begin{aligned}&\frac{1}{r^{*}}\frac{d}{dr^{*}}\left(r^{*}\frac{dC^{*R}}{dr^{*}}\right) - \varepsilon^{*}S^{*}\frac{1}{r^{*}}\frac{d}{dr^{*}}\left(r^{*}\frac{dC^{*c}}{dr^{*}}\right) + \frac{1}{\sigma^{*}}\frac{d\sigma^{*}}{dr^{*}}\frac{dC^{*R}}{dr^{*}}\\ &-K_{m}^{*2}C^{*R} + K_{m}^{*2}\varepsilon^{*}S^{*}C^{*C} = 0\end{aligned} \tag{5.86}$$

While that for the complex terms is

$$\frac{1}{r^*}\frac{d}{dr^*}\left(r^*\frac{dC^{*C}}{dr^*}\right)+\frac{\varepsilon^*\left(\omega^*-w^*K_m^*\right)}{\sigma^*}\frac{1}{r^*}\frac{d}{dr^*}\left(r^*\frac{dC^{*R}}{dr^*}\right)+\frac{1}{\sigma^*}\frac{d\sigma^*}{dr^*}\frac{dC^{*C}}{dr^*}$$
$$-K_m^{*2}C^{*C}-\frac{K_m^{*2}\varepsilon^*\left(\omega^*-w^*K_m^*\right)}{\sigma^*}C^{*R}=0 \tag{5.87}$$

or

$$\frac{1}{r^*}\frac{d}{dr^*}\left(r^*\frac{dC^{*C}}{dr^*}\right)+\varepsilon^*S^*\frac{1}{r^*}\frac{d}{dr^*}\left(r^*\frac{dC^{*R}}{dr^*}\right)+\frac{1}{\sigma^*}\frac{d\sigma^*}{dr^*}\frac{dC^{*C}}{dr^*}$$
$$-K_m^{*2}C^{*C}-K_m^{*2}\varepsilon^*S^*C^{*R}=0 \tag{5.88}$$

The electric shear stress (Eq. (5.80)) becomes

$$\bar{\tau}_{e,rz}^*=\varepsilon^*K^*\left[C^{*C}\frac{dC^{*R}}{dr^*}-C^{*R}\frac{dC^{*C}}{dr^*}\right] \tag{5.89}$$

Finally, the Joule heating (Eq. (5.81)) changes to

$$\sigma^*\bar{E}^{*2}=\frac{1}{2}\sigma^*\left[K^{*2}\left[\left(C^{*R}\right)^2+\left(C^{*C}\right)^2\right]+\left[\left(\frac{dC^{*R}}{dr^*}\right)^2+\left(\frac{dC^{*C}}{dr^*}\right)^2\right]\right] \tag{5.90}$$

The corresponding dimensionless boundary conditions for the momentum equations are

$$u^*=0\quad @\quad r^*=R_T^* \tag{5.91}$$

$$w^*=0\quad @\quad r^*=R_T^* \tag{5.92}$$

$$u^*=0\quad @\quad r^*=R_v^* \tag{5.93}$$

$$-\mu^*\frac{\partial w^*}{\partial r^*}=-\frac{M_e\varepsilon^*K^{*2}\dfrac{I_1\left(K^*R_v^*\right)}{I_0\left(K^*R_v^*\right)}\left[\left(C^{*C}\right)^2+\left(C^{*R}\right)^2\right]}{\left[\dfrac{1}{S^*}+S^*\varepsilon^{*2}\right]}\quad @\quad r^*=R_v^* \tag{5.94}$$

$$u^* = 0 \quad @ \quad z^* = 0,\ z^* = L^* \tag{5.95}$$

$$\frac{\partial w^*}{\partial z^*} = 0 \quad @ \quad z^* = 0,\ z^* = L^* \tag{5.96}$$

Equation (5.94) expresses the balance of viscous and electric shear stresses at the interface (Eqs. (5.61) and (5.64)). For the energy equation, the dimensionless boundary conditions are

$$-k\frac{\partial T^*}{\partial r^*} = \frac{Pr_{bo}\,\delta}{\sigma_{bo}\hat{\varphi}_e^2} q''_{wall} \qquad @ \quad r^* = R_T^* \tag{5.97}$$

$$-k\frac{\partial T^*}{\partial r^*} = \frac{Pr_{bo}\,\delta}{\sigma_{bo}\hat{\varphi}_e^2} q''_{interface} \quad @ \quad r^* = R_v^* \tag{5.98}$$

The imposed dimensionless temperature profile at the channel entrance becomes

$$T^*\left(r^*\right) = \frac{\mu_{bo} c_{pbo}}{\sigma_{bo}\hat{\varphi}_e^2} T\left(r\right) \qquad @ \quad z^* = 0 \tag{5.99}$$

The dimensionless boundary conditions for the electric potential equation are

$$C^* = 1 \ @ \quad r^* = R_T^* \tag{5.100}$$

$$\frac{\partial C^*}{\partial r^*} = + \frac{N_e K^* C^* \dfrac{I_1\left(K^* R_v^*\right)}{I_0\left(K^* R_v^*\right)}\left(\varepsilon^* + \dfrac{j}{S^*}\right)}{\varepsilon^{*^2} + \left(\dfrac{1}{S^*}\right)^2} \quad @ \quad r^* = R_v^* \tag{5.101}$$

Decomposition of the last equation yields to the following real and complex terms, respectively

$$\frac{\partial C^{R*}}{\partial r^*} = + \frac{N_e K^* \dfrac{I_1\left(K^* R_v^*\right)}{I_0\left(K^* R_v^*\right)} \left(C^{*R} \varepsilon^* - \dfrac{C^{*C}}{S^*} \right)}{\varepsilon^{*2} + \left(\dfrac{1}{S^*} \right)^2} \quad @ \quad r^* = R_v^* \tag{5.102}$$

$$\frac{\partial C^{C*}}{\partial r^*} = + \frac{N_e K^* \dfrac{I_1\left(K^* R_v^*\right)}{I_0\left(K^* R_v^*\right)} \left(C^{*C} \varepsilon^* + \dfrac{C^{*R}}{S^*} \right)}{\varepsilon^{*2} + \left(\dfrac{1}{S^*} \right)^2} \quad @ \quad r^* = R_v^* \tag{5.103}$$

Numerical Methods

A finite element code was developed using the finite element software Fastflo Version 3.0 (developed at CSIRO Mathematical and Information Sciences) to solve the governing equations iteratively. Each iteration starts by updating all the fluid properties based on the temperature of the last step. Following that the electric shear stress (Eq. (5.89)) is computed entirely from the results of the previous iteration.

$$\overline{\tau}_{e,rz_n}^* = \varepsilon_{n-1}^* K^* \left[C_{n-1}^{*C} \frac{dC_{n-1}^{*R}}{dr^*} - C_{n-1}^{*R} \frac{dC_{n-1}^{*C}}{dr^*} \right] \tag{5.104}$$

The momentum equations for the new flow field are then solved using the penalty method. The continuity equation (Eq. (5.2))

$$\nabla . \overline{v}_n^* = 0 \tag{5.105}$$

In the penalty method, one a fictitious representation for the pressure in the continuity equation, namely

$$p_n^* = \text{Pen}\nabla.\vec{v}_n^* \tag{5.106}$$

and therefore,

$$\nabla p_n^* = \text{Pen}\nabla\left(\nabla.\vec{v}_n^*\right) \tag{5.107}$$

If Pen is large, then Eq. (5.105) is forced to be small, therefore satisfying the continuity equation

The momentum equation is formulated as

$$\rho_{n-1}^*\vec{v}_{n-1}^*.\left(\nabla\vec{v}_n^*\right) = -\nabla p_n^* + \nabla.\left(2\mu_{n-1}\boldsymbol{D}_n^*\right) + \frac{\text{Me}}{\text{Ne}}\left(0, \frac{1}{r^*}\frac{\partial}{\partial r^*}\left(r^*\bar{\tau}_{rz_n}^*\right)\right) \tag{5.108}$$

where $\boldsymbol{D}_n^*$ is the deformation tensor as a function of flow field velocities in cylindrical coordinates. The expansion of this tensor was shown in Eq. (5.76) and Eq. (5.77) for the axial and radial components, respectively. The deformation tensor was left in the above equation without expansion to allow for the illustration of the numerical methods in compact form. Substituting Eq. (5.107) into Eq. (5.108) allows

$$\rho_{n-1}^*\vec{v}_{n-1}^*.\left(\nabla\vec{v}_n^*\right) = \text{Pen}\nabla\left(\nabla.\vec{v}_n^*\right) + \nabla.\left(2\mu_{n-1}\boldsymbol{D}_n^*\right) + \frac{\text{Me}}{\text{Ne}}\left(0, \frac{1}{r^*}\frac{\partial}{\partial r^*}\left(r^*\bar{\tau}_{rz_n}^*\right)\right) \tag{5.109}$$

Separating the pressure gradient in Eq. (5.109) into an external and an internal component by adding a constant normal stress permits for the simulation of an external pressure gradient (see chapter IV).

$$\rho^*_{n-1}\vec{v}^*_{n-1}.\left(\nabla\vec{v}^*_n\right) = \mathrm{Pen}\nabla\left(\nabla.\vec{v}^*_n\right) + \nabla.\left(2\mu_{n-1}\boldsymbol{D}^*_n\right) + \frac{\mathrm{Me}}{\mathrm{Ne}}\left(0, \frac{1}{r^*}\frac{\partial}{\partial r^*}\left(r^*\bar{\tau}^*_{rz_n}\right)\right) - \left[0, \left(\frac{dp}{dz}\right)_{\mathrm{external}}\right] \tag{5.110}$$

The electric potential equations (Eqs. (5.86) and (5.88)) are discretized as follows

$$\frac{1}{r^*}\frac{d}{dr^*}\left(r^*\frac{dC^{*R}_n}{dr^*}\right) - \varepsilon^*_{n-1}S^*_n\frac{1}{r^*}\frac{d}{dr^*}\left(r^*\frac{dC^{*C}_{n-1}}{dr^*}\right) + \frac{1}{\sigma^*_{n-1}}\frac{d\sigma^*_{n-1}}{dr^*}\frac{dC^{*R}_{n-1}}{dr^*} - K^{*2}_m C^{*R}_n + K^{*2}_m\varepsilon^*_{n-1}S^*_n C^{*C}_{n-1} = 0 \tag{5.111}$$

and

$$\frac{1}{r^*}\frac{d}{dr^*}\left(r^*\frac{dC^{*C}_n}{dr^*}\right) + \varepsilon^*_{n-1}S^*_n\frac{1}{r^*}\frac{d}{dr^*}\left(r^*\frac{dC^{*R}_{n-1}}{dr^*}\right) + \frac{1}{\sigma^*_{n-1}}\frac{d\sigma^*_{n-1}}{dr^*}\frac{dC^{*C}_{n-1}}{dr^*} - K^{*2}_m C^{*C}_n - K^{*2}_m\varepsilon^*_{n-1}S^*_n C^{*R}_{n-1} = 0 \tag{5.112}$$

where

$$S^*_n = \frac{\omega^* - K^* w^*_n}{\sigma^*_{n-1}} \tag{5.113}$$

The Joule heating (Eq. (5.90) is calculated from

$$\left(\sigma^*\bar{E}^{*2}\right)_n = \frac{1}{2}\sigma^*_{n-1}\left[K^{*2}\left[\left(C^{*R}_n\right)^2 + \left(C^{*C}_n\right)^2\right] + \left[\left(\frac{dC^{*R}_n}{dr^*}\right)^2 + \left(\frac{dC^{*C}_n}{dr^*}\right)^2\right]\right] \tag{5.114}$$

discretizing the energy equation yields

$$\rho^*_{n-1}c^*_{p_{n-1}}\left(\vec{v}^*_n.\nabla T^*_n\right) = \frac{1}{\mathrm{Pr}_{b0}}\nabla.\left(K_{n-1}\nabla T^*_n\right) + \left(\sigma^*\vec{E}^{*2}\right)_n \tag{5.115}$$

The interfacial boundary conditions resulting from the electric and shear stress balance (Eq. (5.94)) can be expressed as

$$-\mu_{n-1}^{*}\frac{\partial w_{n}^{*}}{\partial r^{*}} = -\frac{M_e \varepsilon_{n-1}^{*} K^{*2}\dfrac{I_1\left(K^{*}R_v^{*}\right)}{I_0\left(K^{*}R_v^{*}\right)}\left[\left(C_{n-1}^{*C}\right)^2+\left(C_{n-1}^{*R}\right)^2\right]}{\left[\dfrac{1}{S_n^{*}}+S_n^{*}\varepsilon_{n-1}^{*2}\right]} \quad @ \quad r^{*}=R_v^{*} \tag{5.116}$$

where

$$S_n^{*} = \frac{\omega^{*}-K^{*}w_{n-1}^{*}}{\sigma_{n-1}^{*}} \tag{5.117}$$

Lastly, the boundary conditions for the electric field at the interface are formulated as

$$\frac{\partial C_n^{*R}}{\partial r^{*}} = +\frac{N_e K^{*}\dfrac{I_1\left(K^{*}R_v^{*}\right)}{I_0\left(K^{*}R_v^{*}\right)}\left(C_{n-1}^{*R}\varepsilon_{n-1}^{*}-\dfrac{C_{n-1}^{*C}}{S_n^{*}}\right)}{\varepsilon_{n-1}^{*2}+\left(\dfrac{1}{S_n^{*}}\right)^2} \quad @ \quad r^{*}=R_v^{*} \tag{5.118}$$

$$\frac{\partial C_n^{*C}}{\partial r^{*}} = +\frac{N_e K^{*}\dfrac{I_1\left(K^{*}R_v^{*}\right)}{I_0\left(K^{*}R_v^{*}\right)}\left(C_{n-1}^{*C}\varepsilon_{n-1}^{*}+\dfrac{C_{n-1}^{*R}}{S_n^{*}}\right)}{\varepsilon_{n-1}^{*2}+\left(\dfrac{1}{S_n^{*}}\right)^2} \quad @ \quad r^{*}=R_v^{*} \tag{5.119}$$

The rest of the boundary conditions are imposed based on values of the current iteration. At the beginning of the calculation all the initial values for the non-dimensional velocities and electric field potentials are set to zero However, the initial value of the non-dimensional temperature is assumed to be the non-dimensional average entrance temperature. To maximize the number of parameters using values of current

iteration rather than the preceding iteration the computations are carried out in the following order:

1. update the fluid properties
2. update the electric shear stress
3. solve the momentum equations for the current flow field
4. solve the potential equation
5. update Joule heating
6. solve energy equation for the current temperature distribution

Comparison of Numerical Model and Analytical Model

Analytical Comparison

The comparison of the governing equations of the Numerical Model derived in this chapter to that of the Analytical Model presented in the preceding chapter implies that there are three main points which underline when the Numerical Model departs from the simplified assumptions of the Analytical Model. These points are as follows

1. the inclusion of the bulk shear stress (Eq. (5.80)) in the momentum equation (Eq. (5.76)
2. the dependency of the electric potential (Eqs. (5.86) and (5.88)) on the local values of the main velocity component, electric conductivity, electric permittivity as well as the electric conductivity gradient

3. determining the temperature field by solving the energy equation (Eq. (5.78)) in the presence of the Joule heating (Eq. (5.81)) accounting for the appropriate boundary conditions (Eqs. (5.97)- (5.99)).

Obviously all of these effects were neglected in the Analytical Model based on the assumption that the temperature is constant throughout the domain. The intent here is to analytically examine if the governing equations for the electric potential of the Numerical Model will reduce to those stated in the Analytical Model under the assumption of constant temperature and, therefore, constant fluid properties.

The equations for the electric potential were derived from Eq. (5.79)

$$\left[\sigma^* + j\varepsilon^*\left(\omega_n^* - w^* K_m^*\right)\right]\frac{1}{r^*}\frac{d}{dr^*}\left(r^*\frac{dC^*}{dr^*}\right) + \frac{d\sigma^*}{dr^*}\frac{dC^*}{dr^*} - \left[\sigma^* + j\varepsilon^*\left(\omega_n^* - w^* K_m^*\right)\right]K_m^{*2}C^* = 0 \tag{5.120}$$

if the electric conductivity is constant and the pump is not operating at synchronous speed (i.e. $S^* \neq 0$), which can not be attained by a real pump, then Eq. (5.120) reduces to

$$\frac{1}{r^*}\frac{d}{dr^*}\left(r^*\frac{dC^*}{dr^*}\right) - K_m^{*2}C^* = 0 \tag{5.121}$$

the above equation can also be decomposed to

$$\frac{1}{r^*}\frac{d}{dr^*}\left(r^*\frac{dC^{R^*}}{dr^*}\right) - K_m^{*2}C^{R^*} = 0 \tag{5.122}$$

$$\frac{1}{r^*}\frac{d}{dr^*}\left(r^*\frac{dC^{C^*}}{dr^*}\right) - K_m^{*2}C^{C^*} = 0 \tag{5.123}$$

which have the following solutions, respectively

$$C^{*R} = A^{R} I_0\left(K_m^* r^*\right) + B^{R} K_0\left(K_m^* r^*\right) \tag{5.124}$$

and

$$C^{*C} = A^{C} I_0\left(K_m^* r^*\right) + B^{C} K_0\left(K_m^* r^*\right) \tag{5.125}$$

The aforementioned solutions are identical to those in the Analytical Model. Predictably, these solutions have to be valid even after the decomposition of the electric potential equation (Eq. (5.79)) into its real and imaginary components (Eqs. (5.86) and (5.88)). This can be confirmed by examining Eqs. (5.86) and (5.88) with the assumption of constant electric conductivity

$$\frac{1}{r^*}\frac{d}{dr^*}\left(r^* \frac{dC^{*R}}{dr^*}\right) - K_m^{*2} C^{*R} - \varepsilon^* S^* \frac{1}{r^*}\frac{d}{dr^*}\left(r^* \frac{dC^{*c}}{dr^*}\right) + K_m^{*2} \varepsilon^* S^* C^{*C} = 0 \tag{5.126}$$

$$\frac{1}{r^*}\frac{d}{dr^*}\left(r^* \frac{dC^{*C}}{dr^*}\right) - K_m^{*2} C^{*C} + \varepsilon^* S^* \frac{1}{r^*}\frac{d}{dr^*}\left(r^* \frac{dC^{*R}}{dr^*}\right) - K_m^{*2} \varepsilon^* S^* C^{*R} = 0 \tag{5.127}$$

The first two terms in Eqs. (5.126) and (5.127) can be dropped since the solutions given in Eqs. (5.124) and (5.125) satisfy them respectively yielding

$$-\varepsilon^* S^* \frac{1}{r^*}\frac{d}{dr^*}\left(r^* \frac{dC^{*c}}{dr^*}\right) + K_m^{*2} \varepsilon^* S^* C^{*C} = 0 \tag{5.128}$$

$$\varepsilon^* S^* \frac{1}{r^*}\frac{d}{dr^*}\left(r^* \frac{dC^{*R}}{dr^*}\right) - K_m^{*2} \varepsilon^* S^* C^{*R} = 0 \tag{5.129}$$

Elimination of the non-zero electric permittivity and slip coefficient result into equations identical to Eqs. (5.122) and (5.123), consequently, having similar solutions to (Eqs. (5.124) and (5.125)). This indeed demonstrates that the governing equations for the electric potentials of the Numerical Model reduce to those stated in the Analytical Model.

It is also important to show that the resulting electric potentials will not lead to any bulk shear stress. This is true if and only if the contribution of the electric shear stress $\frac{1}{r^*}\frac{\partial}{\partial r^*}\left(r^*\tau_{e,rz}^*\right)$ in the momentum equation (Eq. (5.76)) is zero.

Recall,

$$\overline{\tau}_{e,rz}^* = \varepsilon^* K_m^* \left[C^{*C} \frac{dC^{*R}}{dr^*} - C^{*R} \frac{dC^{*C}}{dr^*} \right] \tag{5.130}$$

The solutions of the electric potential distribution under the assumption of constant temperature are given in Eqs. (5.124) and (5.125). And its derivative can be determined as

$$\frac{dC^{*R}}{dr^*} = K_m^* A^R I_0\left(K_m^* r^*\right) - K_m^* B^R K_1\left(K_m^* r^*\right) \tag{5.131}$$

$$\frac{dC^{*C}}{dr^*} = K_m^* A^C I_0\left(K_m^* r^*\right) - K_m^* B^C K_1\left(K_m^* r^*\right) \tag{5.132}$$

resulting in

$$\overline{\tau}^{*}_{e,rz} = \varepsilon^{*} K^{*}_{m} \left\{ \begin{array}{l} \left[A^{C} I_0\left(K^{*}_{m} r^{*}\right) + B^{C} K_0\left(K^{*}_{m} r^{*}\right) \right] \\ \left[K^{*}_{m} A^{R} I_0\left(K^{*}_{m} r^{*}\right) - K^{*}_{m} B^{R} K_1\left(K^{*}_{m} r^{*}\right) \right] \end{array} \right\} - \varepsilon^{*} K^{*}_{m} \left\{ \begin{array}{l} \left[A^{R} I_0\left(K^{*}_{m} r^{*}\right) + B^{R} K_0\left(K^{*}_{m} r^{*}\right) \right] \\ \left[K^{*}_{m} A^{C} I_0\left(K^{*}_{m} r^{*}\right) - K^{*}_{m} B^{C} K_1\left(K^{*}_{m} r^{*}\right) \right] \end{array} \right\} \tag{5.133}$$

rearranging

$$\overline{\tau}^{*}_{e,rz} = \varepsilon^{*} K^{*2}_{m} \left[A^{R} B^{C} - B^{R} A^{C} \right] \left[I_0\left(K^{*}_{m} r^{*}\right) K_1\left(K^{*}_{m} r^{*}\right) + K_0\left(K^{*}_{m} r^{*}\right) I_1\left(K^{*}_{m} r^{*}\right) \right] \tag{5.134}$$

the electric shear stress in the momentum equation is given by

$$\frac{1}{r^{*}} \frac{\partial}{\partial r^{*}} \left(r^{*} \tau^{*}_{e,rz} \right) = \frac{\partial \tau^{*}_{e,rz}}{\partial r^{*}} + \frac{\tau^{*}_{e,rz}}{r^{*}} \tag{5.135}$$

from Eq. (5.134)

$$\frac{\overline{\tau}^{*}_{e,rz}}{r^{*}} = \frac{\varepsilon^{*}}{r^{*}} K^{*2}_{m} \left[A^{R} B^{C} - B^{R} A^{C} \right] \left[I_1\left(K^{*}_{m} r^{*}\right) K_0\left(K^{*}_{m} r^{*}\right) + K_1\left(K^{*}_{m} r^{*}\right) I_0\left(K^{*}_{m} r^{*}\right) \right] \tag{5.136}$$

utilizing the relations

$$I'_1\left(K^{*}_{m} r^{*}\right) = K^{*}_{m} I_0\left(K^{*}_{m} r^{*}\right) - \frac{1}{r^{*}} I_1\left(K^{*}_{m} r^{*}\right) \tag{5.137}$$

$$K'_1\left(K^{*}_{m} r^{*}\right) = -K^{*}_{m} K_0\left(K^{*}_{m} r^{*}\right) - \frac{1}{r^{*}} K_1\left(K^{*}_{m} r^{*}\right) \tag{5.138}$$

the radial derivative of the electric shear stress can be presented as

$$\frac{\partial \overline{\tau}^{*}_{e,rz}}{\partial r^{*}} = -\frac{\varepsilon^{*}}{r^{*}} K^{*2}_{m} \left\{ \begin{array}{l} \left[A^{R} B^{C} - B^{R} A^{C} \right] \\ \left[I_1\left(K^{*}_{m} r^{*}\right) K_0\left(K^{*}_{m} r^{*}\right) + K_1\left(K^{*}_{m} r^{*}\right) I_0\left(K^{*}_{m} r^{*}\right) \right] \end{array} \right\} \tag{5.139}$$

which leads to

$$\frac{1}{r^*}\frac{\partial}{\partial r^*}\left(r^*\tau^*_{e,rz}\right)=\frac{\partial\tau^*_{e,rz}}{\partial r^*}+\frac{\tau^*_{e,rz}}{r^*}=0 \tag{5.140}$$

consequently, substantiating that the contribution of the electric shear stress in the momentum equation is zero.

Finally, it can be concluded that under the assumption of constant temperature, the equations of the Numerical Model reduce to those developed for the Analytical Model. However, it is obvious from (Eq. (5.90)) that any imposed non-zero electric field will result into finite non-zero Joule heating. Hence it is important to note that the assumption of constant temperature requires that the unavoidable Joule heating to be neglected or found to be of insignificant magnitude.

Numerical Comparison

In order to ensure that the results generated by the computer program for the Numerical Model are under the assumption of constant temperature the following adjustments must be incorporated in the computer program:

1. uniform temperature is specified at the tube entrance
2. the heat fluxes at the tube's wall and interface are set to a value of zero

In addition, the Joule heating term is forced to be zero to permit for the reduction of the Numerical Model to the Analytical Model as it was shown in the preceding section of this chapter. The computer code for the Numerical Model is devised in away that uses

actual dimensional input values and converts them to non-dimensional numbers. For given values of peak voltage, wavelength, viscosity, and density, the dimensional values of liquid film thickness and vapor radius, electric conductivity, frequency, permittivity, and pressure gradient were selected. This process is essential since the input parameters used to non-dimensionlize the governing equations and their solutions for the two models are different. The comparison presented in this section is carried out using the non-dimensional numbers introduced in the previous chapter for the Analytical Model. Moreover, assuming constant temperature throughout the domain sets the value of the non-dimensional electric conductivity of the Numerical Model to unity since ($\sigma^* = \frac{\sigma}{\sigma_{b0}}$). This assumption also suggests an adjustment to the non-dimensional electric permittivity to ensure that the same value of electric permittivity is used in both models. The relationships for the permittivity for Numerical Model and Analytical Model respectively are

$$\left(\varepsilon^*\right)_{\text{advanced}} = \frac{\varepsilon}{\varepsilon_0}\,\text{Ne} \tag{5.141}$$

$$\left(\varepsilon^*\right)_{\text{simple}} = \frac{\varepsilon}{\varepsilon_0} \tag{5.142}$$

combining the above two equations yields

$$\left(\varepsilon^*\right)_{\text{advanced}} = \left(\varepsilon^*\right)_{\text{simple}}\,\text{Ne} \tag{5.143}$$

A comparison of the results generated by the two models in the absence of the external pressure gradient is given in Fig. 5.2. The curve displayed corresponds to results

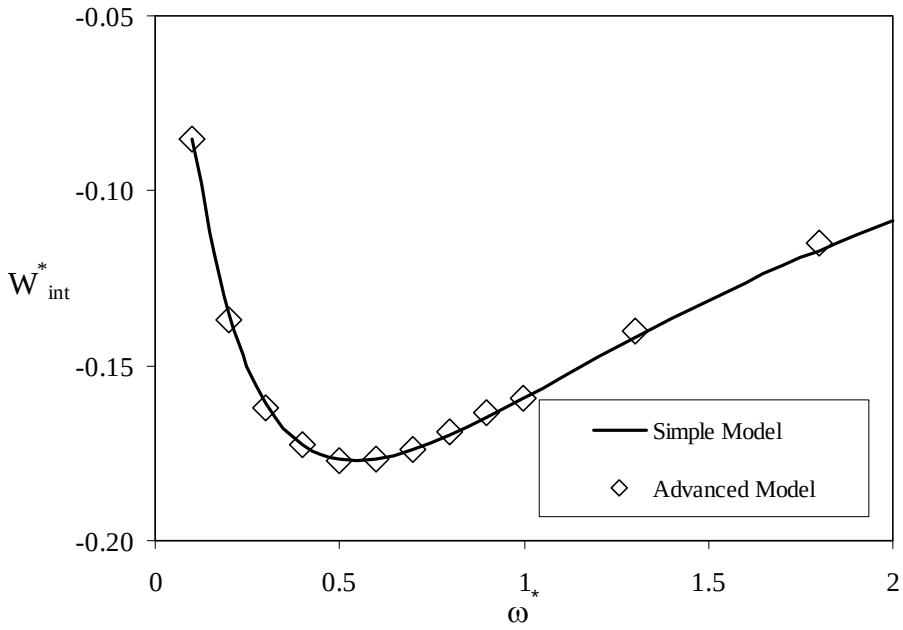

Fig. 5.2 Comparison of Numericaland Analytical Model without pressure gradient (R^*_T=7, σ^*=4, ε^*=5, δ^*=0.1R^*_T)

obtained by the Analytical Model. On the other hand the points correspond to numerical results for the Numerical Model. The points for Numerical Model are carried out using grid of 20x20. For the case of $\omega^* = 0.2$ and $\delta^* = 0.1R_T^*$, to ensure grid independence computations were carried out using grids of 2x2, 5x5, 10x10, 20x20, and 50x50. Convergence was achieved for all grids and the residuals of the non-dimensional velocities, potentials, and temperatures were less than 10^{-5}. The absolute difference between the two models ranged from -0.007% (50x50 grid) to 1.11% (2x2 grid) and it was 0.0034% (20x20 grid). Comparisons between the two models in the presence of pressure gradient are also shown in Fig. 5.3 using 20x20 grid. All residuals also did fall below 10^{-5} and the discrepancy for the 20x20 grid is ranged between 0.2% and 0.5%

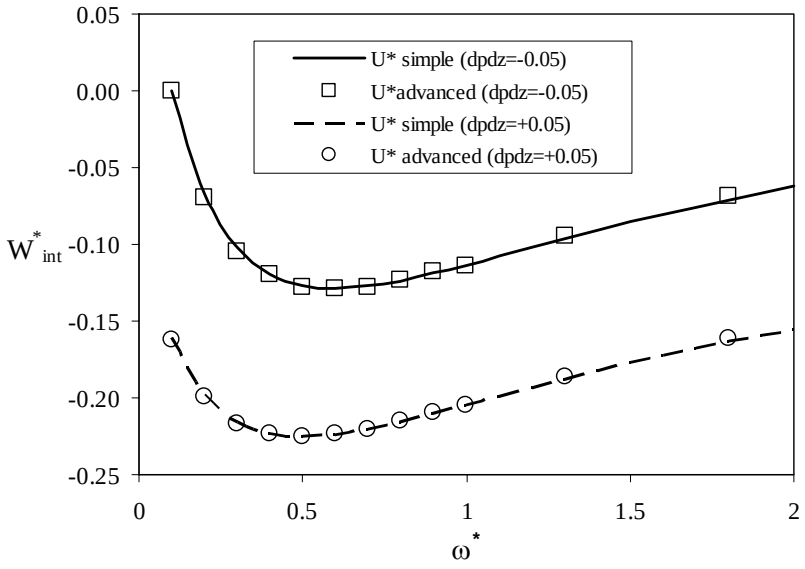

Fig. 5.3 Comparison of Numericaland Analytical Model with pressure gradient (R^*_T=7, σ^*=4, ε^*=5, δ^*=0.1R^*_T)

depending on the values of the frequency and/or whether the pressure gradient is positive or negative.

The excellent agreement between the numerical results of the Numerical Model and the Analytical Model verifies that the numerical technique used in the computer code for the Numerical Model is correct, and thus validates the numerical results of it.

External Stratified Liquid/Vapor Medium Over a Solid Cylinder

The main purpose of this section is to extend the existing Numerical Model of vertical internal annular configuration to the EHD induction pumping of stratified liquid/vapor medium over a radially large horizontal cylinder (see Fig. 5.4). This should serve as another mean to validate the existing Numerical Model. By letting the radius of

the cylinder go to infinity for a small liquid film thickness, the extended model should reduce to that of EHD induction pumping of stratified liquid/vapor medium in a channel [9] in Cartesian coordinates.

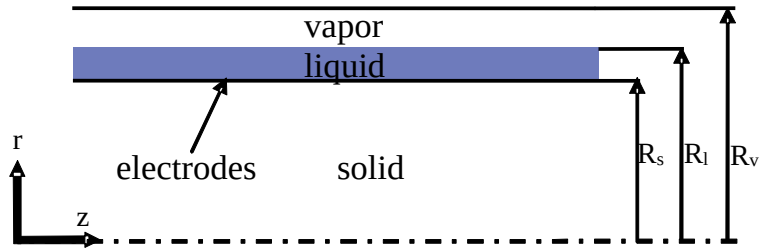

Fig. 5.4 Schematic of the horizontal external analytical domain

Besides it is a horizontal configuration, the formulation of this problem differs from the one for the annular configuration introduced earlier in two main points:

1. the vapor phase is in top of the liquid phase, which in turn change the boundary conditions at the interface with a negative sign
2. the gravitational force is acting perpendicular to the interface, which is neglected due to the assumption that the all forces normal to the interface are neglected resulting in a flat interface

Taking these two main differences into consideration yields the following dimensionless boundary conditions for the momentum, energy, and electric potentials equations, respectively

$$u^* = 0 \quad @ \quad r^* = R_s^* \tag{5.144}$$

$$w^* = 0 \quad @ \quad r^* = R_s^* \tag{5.145}$$

$$u^* = 0 \quad @ \quad r^* = R_l^* \tag{5.146}$$

$$\mu^* \frac{\partial w^*}{\partial r^*} = -\frac{M_e \varepsilon^* K^{*2} D^* \dfrac{I_1\left(K^* R_l^*\right)}{I_0\left(K^* R_l^*\right)}\left[\left(C^{*C}\right)^2 + \left(C^{*R}\right)^2\right]}{\left[\dfrac{1}{S^*} + S^* \varepsilon^{*2}\right]} \quad @ \quad r^* = R_l^* \tag{5.147}$$

where

$$D^* = \frac{\left[\dfrac{K_1\left(K^* R_v^*\right)}{I_1\left(K^* R_v^*\right)} - \dfrac{K_1\left(K^* R_l^*\right)}{I_1\left(K^* R_l^*\right)}\right]}{\left[\dfrac{K_0\left(K^* R_l^*\right)}{I_0\left(K^* R_l^*\right)} + \dfrac{K_1\left(K^* R_v^*\right)}{I_1\left(K^* R_v^*\right)}\right]} \tag{5.148}$$

$$u^* = 0 \quad @ \quad z^* = 0, \; z^* = L^* \tag{5.149}$$

$$\frac{\partial w^*}{\partial z^*} = 0 \quad @ \quad z^* = 0, \; z^* = L^* \tag{5.150}$$

For the energy equation, the dimensionless boundary conditions are

$$-k \frac{\partial T^*}{\partial r^*} = \frac{Pr_{bo}\,\delta}{\sigma_{bo} \hat{\varphi}_e^2} q''_{wall} \quad @ \quad r^* = R_s^* \tag{5.151}$$

$$-k \frac{\partial T^*}{\partial r^*} = \frac{Pr_{bo}\,\delta}{\sigma_{bo} \hat{\varphi}_e^2} q''_{interface} \quad @ \quad r^* = R_l^* \tag{5.152}$$

The imposed dimensionless temperature profile at the channel entrance becomes

$$T^*\left(r^*\right)=\frac{\mu_{bo}c_{pbo}}{\sigma_{bo}\hat{\varphi}_e^2}T\left(r\right) \qquad @ \quad z^*=0 \tag{5.153}$$

The dimensionless boundary conditions for the electric potential equation are

$$C^*=1 \ @ \quad r^*=R_s^* \tag{5.154}$$

$$\frac{\partial C^*}{\partial r^*}=+\frac{N_e K^* C^* D^* \dfrac{I_1\left(K^*R_l^*\right)}{I_0\left(K^*R_l^*\right)}\left(\varepsilon^*+\dfrac{j}{S^*}\right)}{\varepsilon^{*^2}+\left(\dfrac{1}{S^*}\right)^2} \quad @ \quad r^*=R_l^* \tag{5.155}$$

Decomposition of the last equation yields to real and complex terms respectively

$$\frac{\partial C^{R*}}{\partial r^*}=+\frac{N_e K^* D^* \dfrac{I_1\left(K^*R_l^*\right)}{I_0\left(K^*R_l^*\right)}\left(C^{*^R}\varepsilon^*-\dfrac{C^{*^C}}{S^*}\right)}{\varepsilon^{*^2}+\left(\dfrac{1}{S^*}\right)^2} \quad @ \quad r^*=R_l^* \tag{5.156}$$

$$\frac{\partial C^{C*}}{\partial r^*}=+\frac{N_e K^* D^* \dfrac{I_1\left(K^*R_l^*\right)}{I_0\left(K^*R_l^*\right)}\left(C^{*^C}\varepsilon^*+\dfrac{C^{*^R}}{S^*}\right)}{\varepsilon^{*^2}+\left(\dfrac{1}{S^*}\right)^2} \quad @ \quad r^*=R_l^* \tag{5.157}$$

where D^* is expressed as in Eq. (5.148).

In the external Numerical Model presented, the ratio between the solid radius and the film thickness is taken to be ($\frac{R_s}{\delta}=1000$ and 10000), with dimensional film thicknesses of (1.0 mm and 0.1 mm) respectively. The vapor thickness considered is equal to that of the liquid film thickness. For these two large values of the solid radius the curvature effect become insignificant and thus allow for the comparison between the external

Numerical Model and the one presented by [9] for stratified liquid/vapor medium in a channel. Figures 5.5 and 5.6 illustrate the comparisons between the non-dimensional interfacial velocities as a function of non-dimensional wave number, of the two different models for liquid film thicknesses of (1.0 mm and 0.1 mm) respectively. The excellent agreement between the two models also demonstrates the accuracy of the

Numerical Results

The factors controlling the performance of a two-phase flow EHD induction pump fall can be summarized in the following three categories:

I. Thermal

a. entrance temperature profile

b. heat flux at wall of the pipe and interface; q''_{wall}, $q''_{interface}$

c. transport properties of the working fluid; ρ, μ, k, c_p

II. Electrical

a. applied voltage; $\hat{\varphi}$

b. frequency; f

c. wavelength, λ

d. electrical properties of the working fluid, ε, σ

III. Physical

a. external load or pressure drop

b. liquid film thickness, vapor radius, the length and the radius of the pumping section

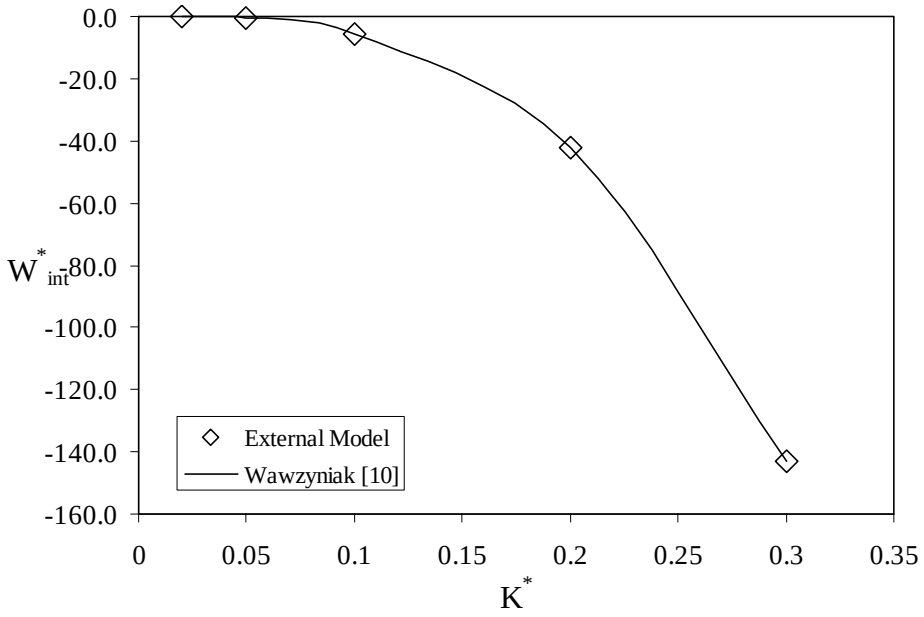

Fig. 5.5 Comparison of Numericalexternal Model with [10] (R_s=1000, σ^*=4, ε^*=5)

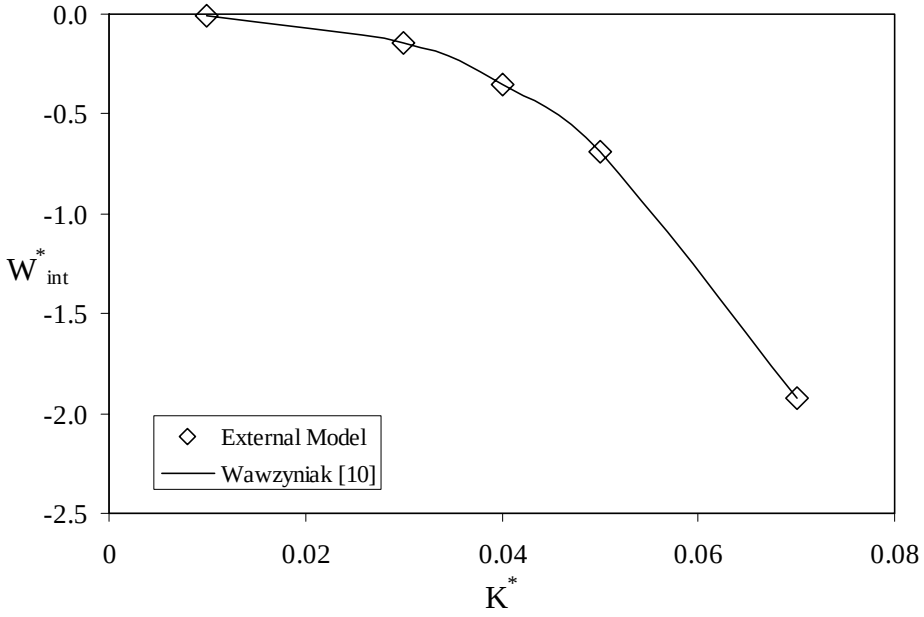

Fig. 5.6 Comparison of Numericalexternal Model with [10] (R_s=10000, σ^*=4, ε^*=5)

The effect of the above parameters on a vertical induction pump is discussed in this section. Since the transport and the electrical properties of any working fluid to be considered in this study are function of temperature and require temperature dependent relations a dimensionless parametric study is conducted using refrigerant R123 as reference working fluid. The thermophysical and the electrical properties of the working fluid (R-123) are function of temperature. While [41] was consulted for the electrical properties, the thermophysical properties were taken from NIST (Refprop Version 6.01). Three different temperature profiles at the entrance corresponding to a uniform profile of 20 ^{o}C (Profile No. 1), and a two linear temperature profiles with an average temperature of 20 ^{o}C (Profile No. 2) and 22.0 ^{o}C (Profile No. 3), respectively, are considered. On the other hand the heat fluxes at the wall of the tube and at the interface are taken as zero because no phase change is taking place as it was justified in the assumptions.

The effect of the parameters such as the applied voltage $\hat{\varphi}$, electric wave angular velocity ω, wave number K, the vapor radius R_v, and gravity are investigated through the following dimensionless parameters M_e^*, ω^*, K^*, R_V^*, G^* respectively. Each of these parameters is studied separately while the others are maintained constant. Since the working fluid is fixed, the electric permittivity through ε^* and the electric conductivity σ^* through N_e^* will not be varied to accommodate for different working fluids, however, they are function of temperature. To account for the effect of the liquid film thickness two base cases corresponding to two different liquid film thicknesses of 10% and 33 % of the total radius of the pipe are considered.

The dimensional and the non-dimensional parameters of the two base cases are given in Tables 5.1 and 5.2. The effect of the external pressure load or gain on the pumping section of EHD system or loop is also studied. This pressure load, which plays a critical role in operating the EHD pump, is present in the liquid film only, for example, due to the existence of other EHD pumping sections and upstream and downstream connecting lines. In general a negative pressure gradient is a favorable load that assists the pumping, whereas the positive gradient is unfavorable and is expected to work against the pumping direction. However, in the results presented the opposite is true since the pump is operating in repulsion mode (i.e. negative velocity). It is noteworthy to mention that the assumption No. j along with the assumption of constant film thickness imply that the internal pressure gradient in the axial direction in the liquid film in the EHD pumping section is zero. Hence, the external pressure load or gain is the only term left in the momentum equation and it is an input parameter.

Table 5.1 Base Cases in Dimensional Form for R-123

	R_v (mm)	δ (mm)	$\hat{\varphi}$ (V)	λ (mm)	f (Hz)
Case 1	12.6	1.4	501	4.4	19.0
Case 2	9.34	4.66	501	9.8	19.0

Table 5.2 Base Cases in Non-Dimensional Form for R-123 at 20^oC

	R_v^*	δ^*	N_e^*	M_e^*	K^*	ω^*
Case 1	9.0	1.0	6.0e-05	7000	2.0	720
Case 2	2.0	1.0	5.4e-06	7000	3.0	8000

In each of the following figures four cases are compared: 1) numerical solutions with a uniform temperature profile at the entrance and the Joule heating is set to zero; 2) numerical solutions with a uniform temperature profile at the entrance (Profile No. 1) and the Joule heating present; 3) numerical solutions with a linear temperature profile at the entrance (Profile No. 2) resulting in 21.0 ^{o}C at the pipe wall and 19.0 ^{o}C at the liquid/vapor interface, and producing an average entrance temperature of 20.0 ^{o}C; 4) numerical solutions with a linear temperature profile at the entrance (Profile No. 3) resulting in 25.0 ^{o}C at the pipe wall and 19.0 ^{o}C at the liquid/vapor interface, and producing an average entrance temperature of 22.0 ^{o}C. While the first two cases are presented to study the effect of the Joule heating on the pump performance, the last two are presented to illustrate the effect of the temperature gradient coupled with Joule heating on the pump performance. Computations were carried out on a domain with dimensionless liquid height and axial length of one and twenty, respectively, on a 20x100 grid. The parameters are varied over a range corresponding to stable operation of EHD induction pumping. The stability criteria were discussed in the previous chapter (chapter IV).

When the film thickness is larger, the electric shear stresses are smaller because the dominant induced charges at the liquid/vapor interface are far away from the electrodes. This is why the results for Case 1 show higher mass fluxes than those of Case 2. It is noteworthy to mention that the effect of the temperature gradient is more noticeable when the generated velocity falls in the lower range of the Reynolds number (~<600).

For this reason the numerical results produced for the film thickness of 33 % of the total radius of the pipe responded more positively to the effect of temperature gradient.

Figures 5.7 and 5.8 display the dimensionless mass flux as a function of the dimensionless electric wave number, which is inversely proportional to the wave length, for Case 1 and 2, respectively. The dimensionless mass flux is calculated at the pipe exit by integrating $\rho^* w^*$ over the dimensionless liquid film thickness. The behavior of all the four curves presented in Figs. 5.7 and 5.8 are similar. The mass flux rises to its peak by increasing the electric wave number and then slowly starts to decrease. The reason of such behavior is that at large wave number (i.e., short wave length), the electric force is limited to a smaller space and the electric field is confined to the vicinity of the electrodes, in effect limiting its penetration depth into the liquid film, resulting in a lower mass flux. In addition, slip coefficient Eq. (5.82), which is the measure for the lag between the traveling electric wave and the charges induced in the liquid film at the interface, is small. This also means that large wave numbers correspond to small wave speeds. On the other hand, at small wave numbers (i.e., long wave length) the distances between the electrodes are long; hence the electric field is not confined to the pipe resulting in small electric shear stress, therefore, small mass flow rate. Furthermore, at a given frequency and very small wave numbers the slip coefficient grows too large again producing small electric shear stress Eq. (5.82).

Figures 5.7 and 5.8 also reveal that the inclusion of the Joule heating is insignificant regardless of the value of the wave number. This is due to the proportionality of the Joule heating to the electric conductivity which, under the

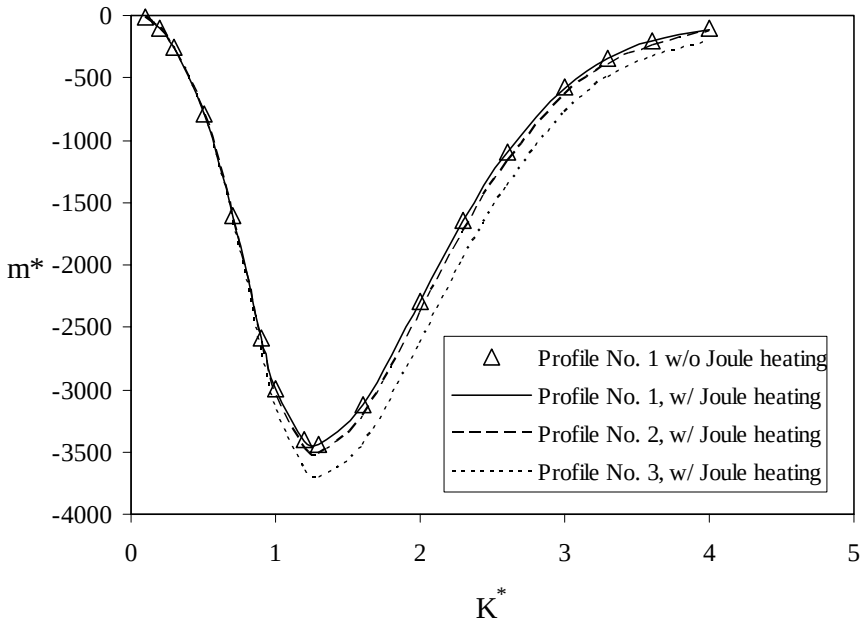

Fig. 5.7 Dimensionless mass flux as a function of dimensionaless electric wave number for Case 1

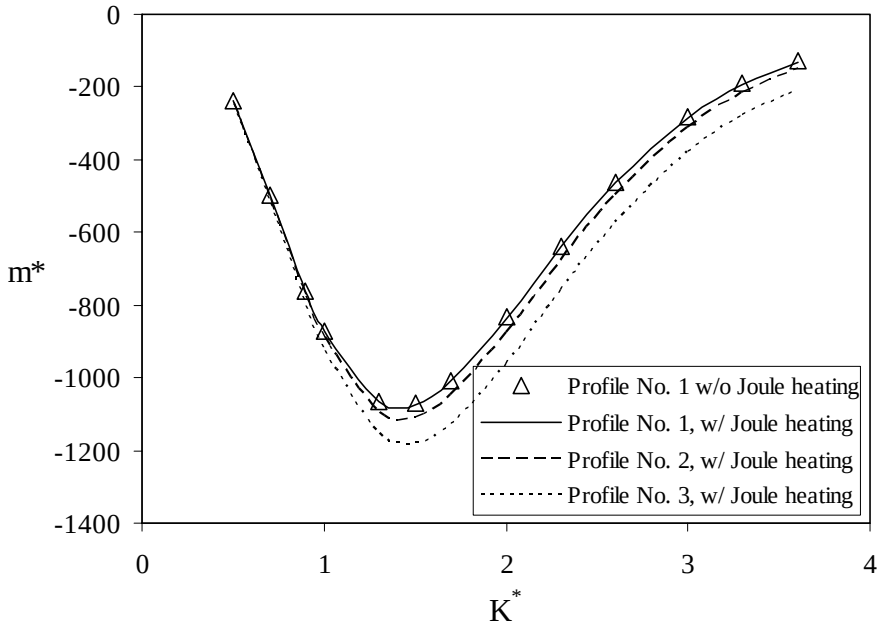

Fig. 5.8 Dimensionless mass flux as a function of dimensionaless electric wave number for Case 2

operating conditions considered, is of order 10^{-8}. However, the presence of the temperature gradient (Profiles No. 2 and 3) becomes significant only at the wave number is greater than unity. At larger wave numbers, the bulk electric shear stress within the liquid film is responsible for the increase in the mass flow rate. This is due to the fact that the electric shear stress is proportional to the square of the wave number. In addition, the electric shear stress is a function of the electric conductivity gradient. A greater temperature gradient gives a greater conductivity gradient. Therefore, as can be seen from Figs. 5.9 and 5.10, the electric shear stress is the largest with Profile No. 3, which in turns gives the highest mass flux. Note that the electric shear stress is the largest close to the electrodes where the electric field is the strongest. Fig. 5.7 also shows that as the wave number increases, the inclusion of the temperature Profiles No. 2 and 3 yields higher mass flow rate compared to the case of Profile No. 1. For example, at wave number of 2.0 the mass flow flux with temperature Profiles No. 2 and 3 increased by 4% and 14.5%, respectively. With the wave number of 4.0, the mass flux increased by 19% and 88% with Profiles No. 2 and 3, respectively.

The effect of the electric wave angular velocity on the mass flux is presented in Figs. 5.11 and 5.12. In light of the slip coefficient, it is obvious that the mass flux has analogous dependency on the electric wave angular velocity as it has on the wave number. As the frequency increases, the mass flow rate increases until it reaches a critical value, and then it falls gradually with further increase in the frequency. It is noteworthy to mention that this critical value of the angular velocity is lower with higher wavelength (i.e. small wave number). The trend shown in Fig. 5.11 and 5.12 depict the

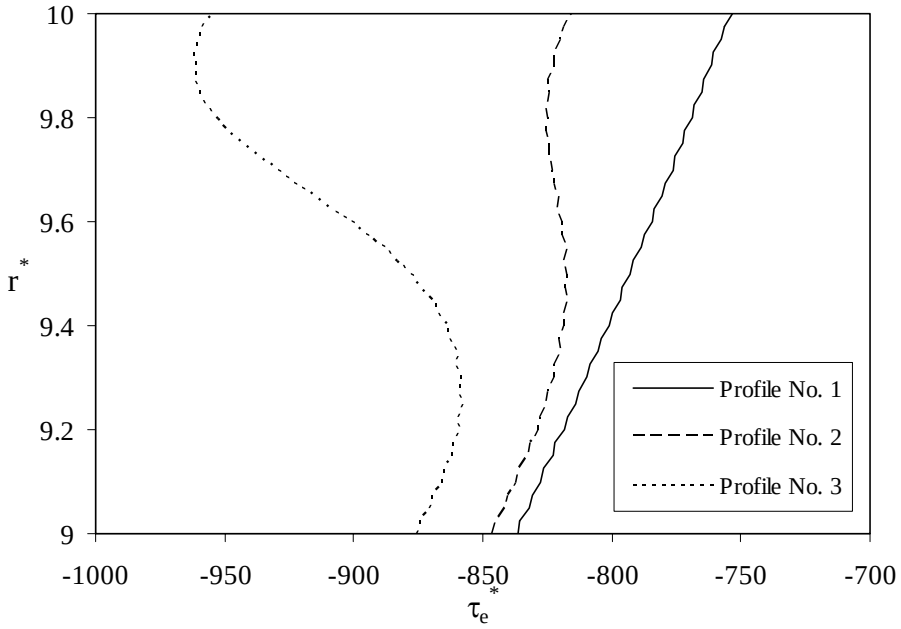

Fig. 5.9 Dimensionless electric shear stress dustribution at the entrance for Case 1

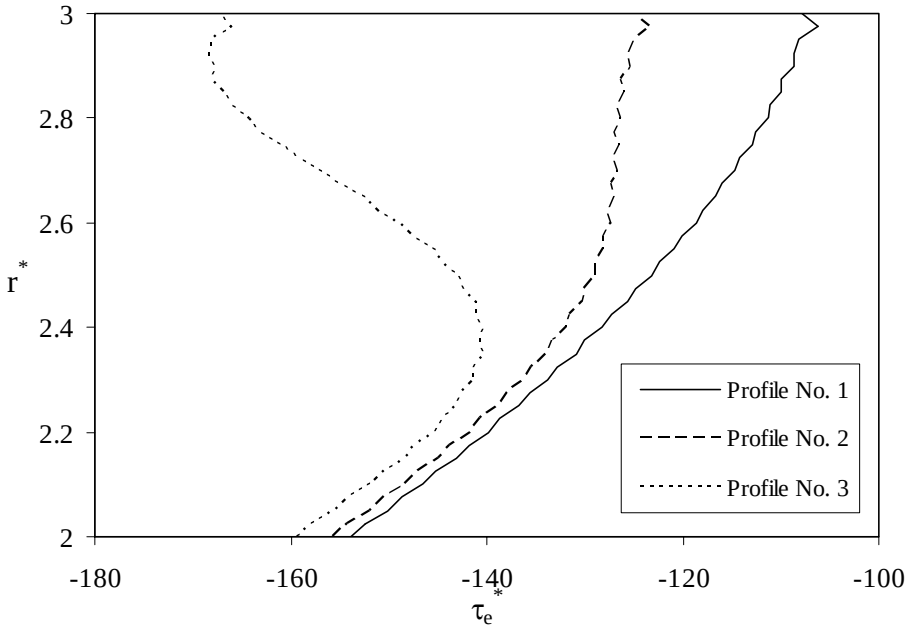

Fig. 5.10 Dimensionless electric shear stress dustribution at the entrance for Case 2

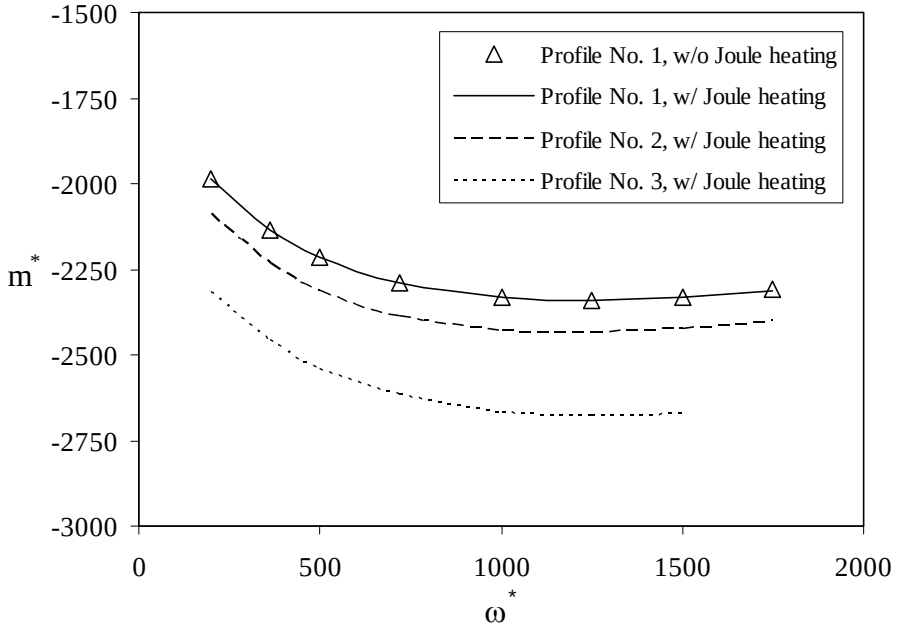

Fig. 5.11 Dimensionless mass flux as a function of electric wave angular velocity for Case 1

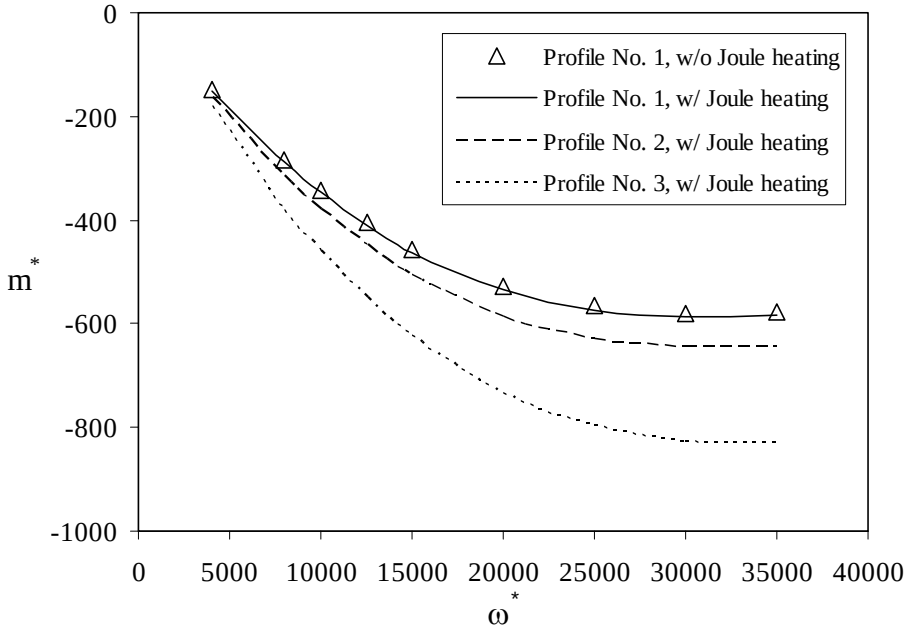

Fig. 5.12 Dimensionless mass flux as a function of electric wave angular velocity for Case 2

role of the electric shear stress within the liquid film. Figure 5.11 indicates an increase in the mass flux compared to the case of Profile No. 1 of about 4.7% and 15% for Profiles No. 2 and 3, respectively. These values are approximately constant for the range of frequency considered here.

The influence of M_e^*, which is proportional to the square of the applied voltage, is shown in Figs. 5.13 and 5.14 for the two Cases considered, respectively. The mass flux increases with increasing M_e^* as expected. For example (see Fig. 5.13), at M_e^* of 7000 Profiles No. 2 and 3 result in an increase in the mass flux of about 4% and 12%, respectively. On the other hand, Fig. 5.14 shows an increase in the mass flux of about 9% and 32% by Profiles No. 2 and 3, respectively , at the same value of M_e^*. In addition, Fig. 5.14 reveals that for high values of M_e^* (grater than 10000), inclusion of Joule heating alone can enhance the mass flux. It was not possible to observe the same from Fig. 5.13 because it was not feasible to increase M_e^* beyond a value of 10000 as it will result in Reynolds number above 2500 (i.e. transient-turbulent flow regime).

Figures 5.15 and 5.16 illustrate the effect of the inclusion of the Joule heating on the electric shear distribution for two different levels of M_e^*. Besides that higher M_e^* will result in a higher electric shear stress effect (Eq. (5.94)), Fig. 5.16 shows an increase of about 11% in the value of electric shear stress near the wall due to the Joule heating. However, Fig. 5.15 shows same electric shear stress distributions (with and with Joule heating) throughout most of the bulk, thus insignificant effect of the Joule heating. It is also important to note that the upper limit of the applied voltage is constrained by the breakdown strength of the fluid at a given wavelength.

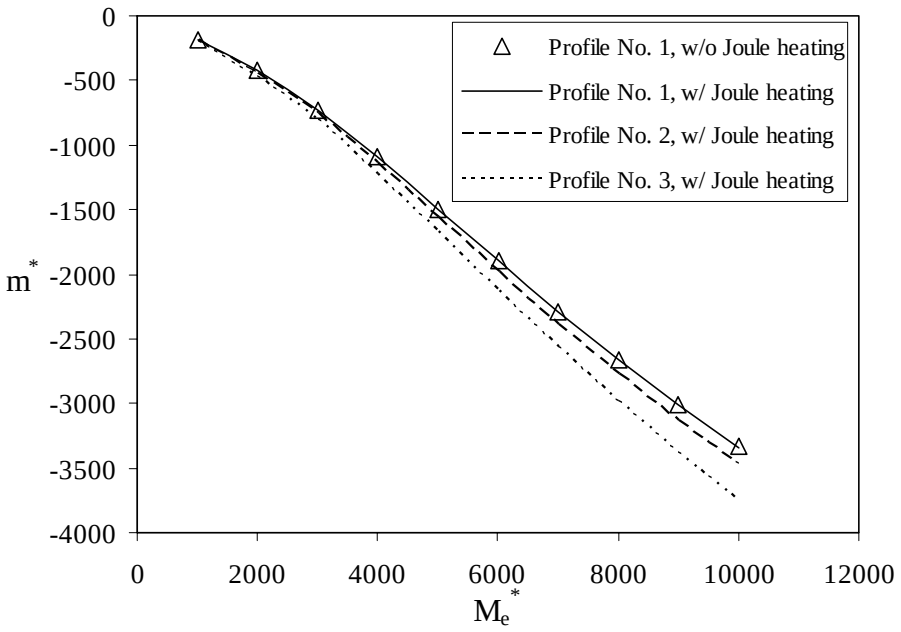

Fig. 5.13 Dimensionless mass flux as a function of M_e^* number for Case 1

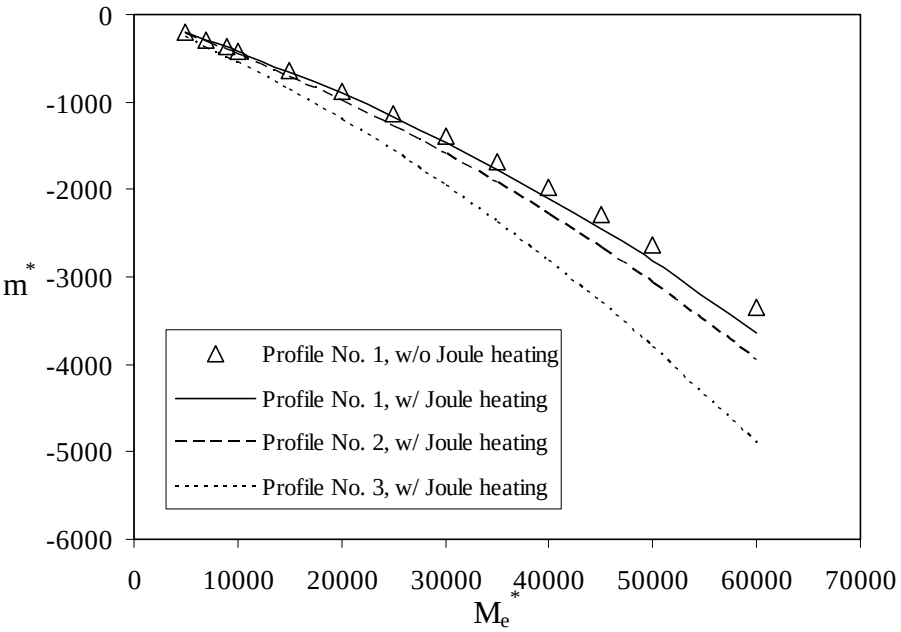

Fig. 5.14 Dimensionless mass flux as a function of M_e^* number for Case 2

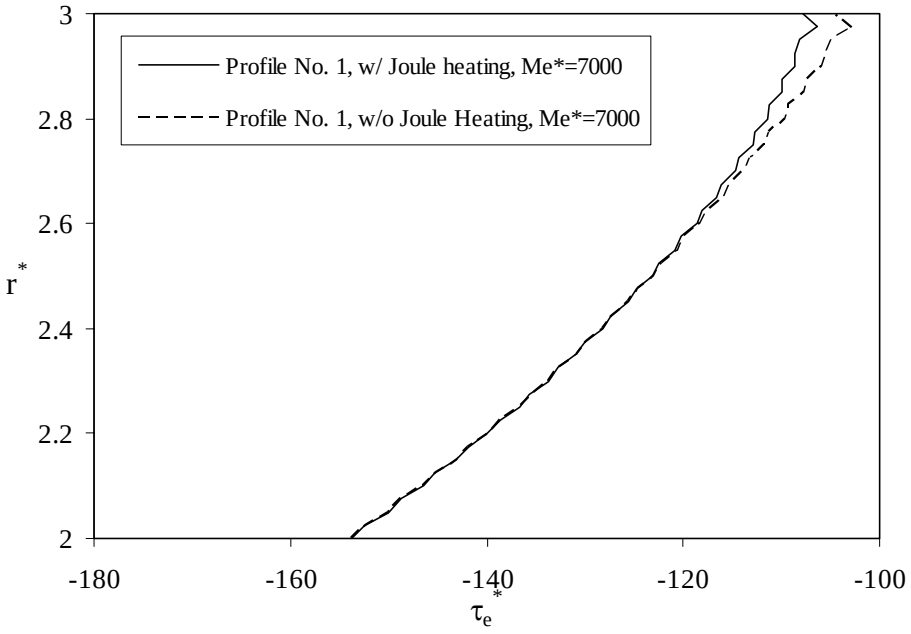

Fig. 5.15 Dimensionless electric shear stress distribution at the entrance Case 2 (M_e^*=7000)

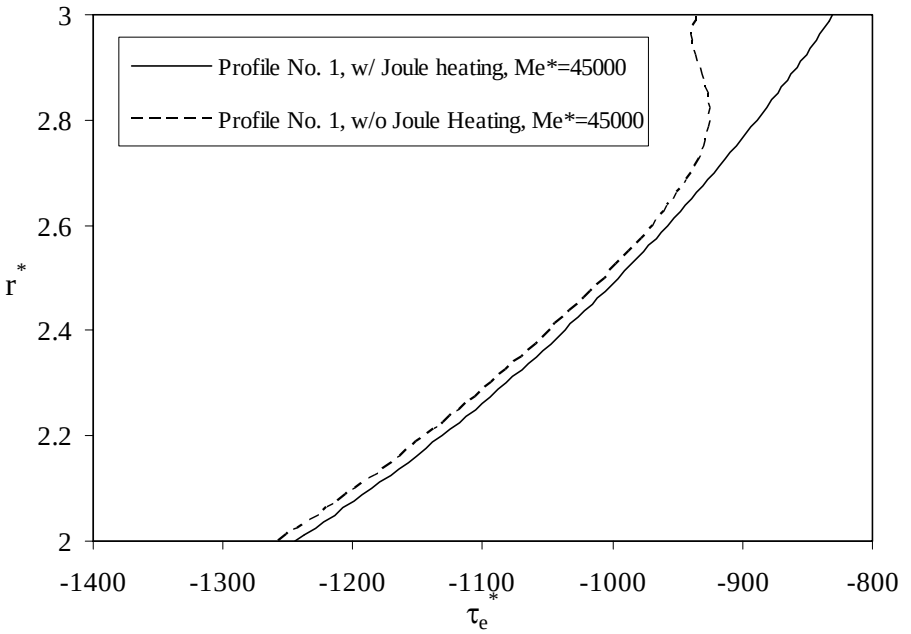

Fig. 5.16 Dimensionless electric shear stress distribution at the entrance Case 2 (M_e^*=45000)

Figures 5.17 and 5.18 present the mass flux as a function of the dimensionless vapor radius for Case 1 and 2, correspondingly. The liquid film thickness is kept constant. Varying the vapor radius only and keeping the liquid film thickness fixed is identical to varying the pipe diameter. For example, for case 1 with R_v^* of 9.0, the dimensionless liquid film thickness is 1.0 resulting in the tube dimensionless radius of 10.0 (implying that the film thickness is 10% of the total radius). However, if R_v^* is 1.0 and the dimensionless liquid film thickness is 1.0 the tube dimensionless radius becomes 2.0 implying that the film thickness is 50% of the total radius. Similar conclusions can be made about case 2. Figures 5.17 and 5.18 state that the inclusion of the Joule heating only results in negligible effect on the mass flux under the operating conditions considered. According to Figs. 5.17 and 5.18, the mass flux initially increases with R_v^* and then it reaches an asymptotic value. This is primarily because the influence of the symmetry boundary condition at pipe centerline diminishes as R_v^* increases. While profile No. 2 results in an increase in the mass flow rate of about 4.5% and 9% for cases 1 and 2, respectively, profile No. 3 produces an increase of about 15% and 31%. These values are approximately constant for the range of vapor radius considered in this study. The exception is for profile No. 3 at Rv^* of 1.0 where it generates an increase of 52% and 37% for cases 1 and 2, respectively.

The dependency of the mass flux on the external pressure gradient is shown in Figs. 5.19 and 5.20 for the two cases considered, respectively. The external load plays a crucial role in operating the EHD pump. Generally a negative pressure is a favorable load which speeds the pumping, whereas the positive pressure gradient is unfavorable

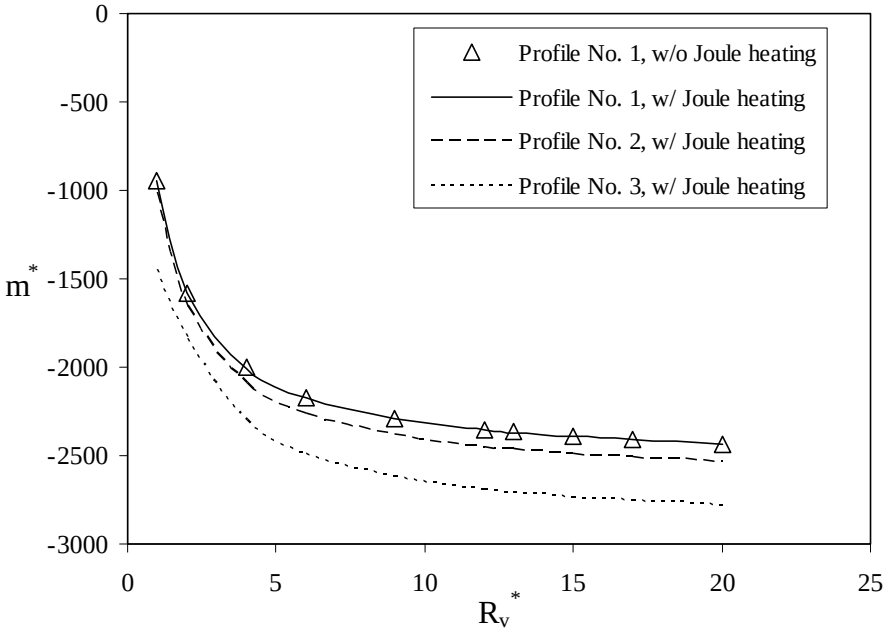

Fig. 5.17 Dimensionless mass flux as a function of dimensionless vapor radius for Case 1

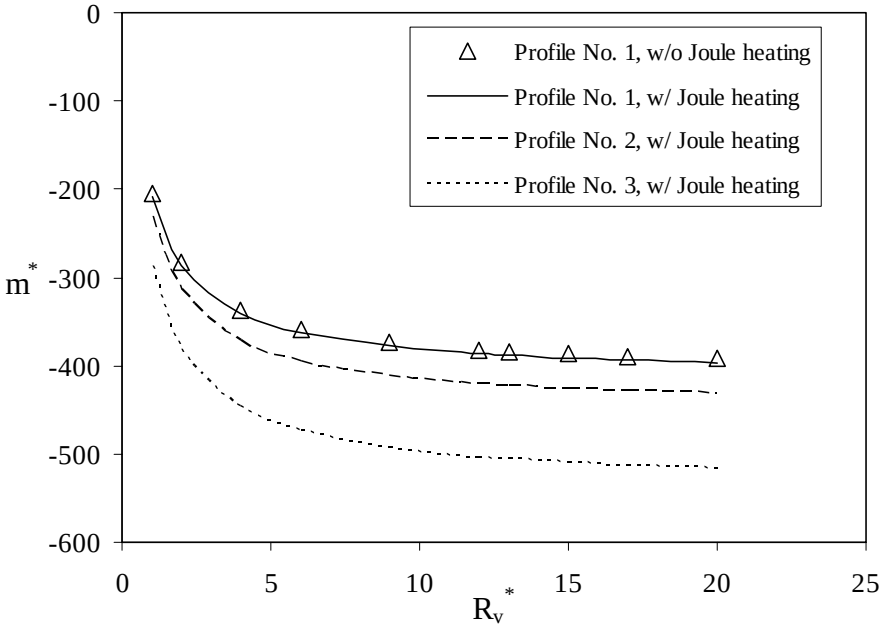

Fig. 5.18 Dimensionless mass flux as a function of dimensionless vapor radius for Case 2

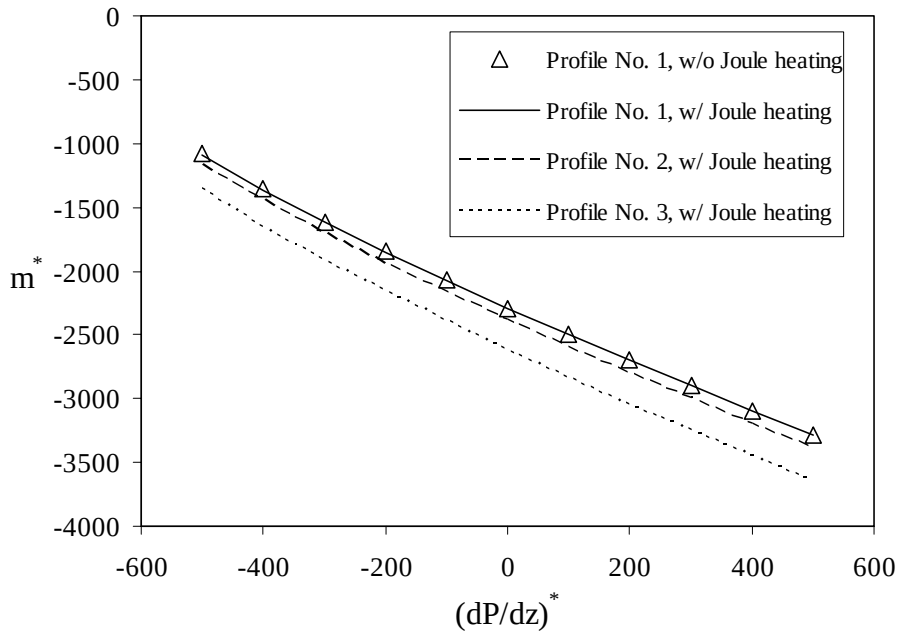

Fig. 5.19 Dimensionless mass flux as a function of dimensionless pressure gradient for Case 1

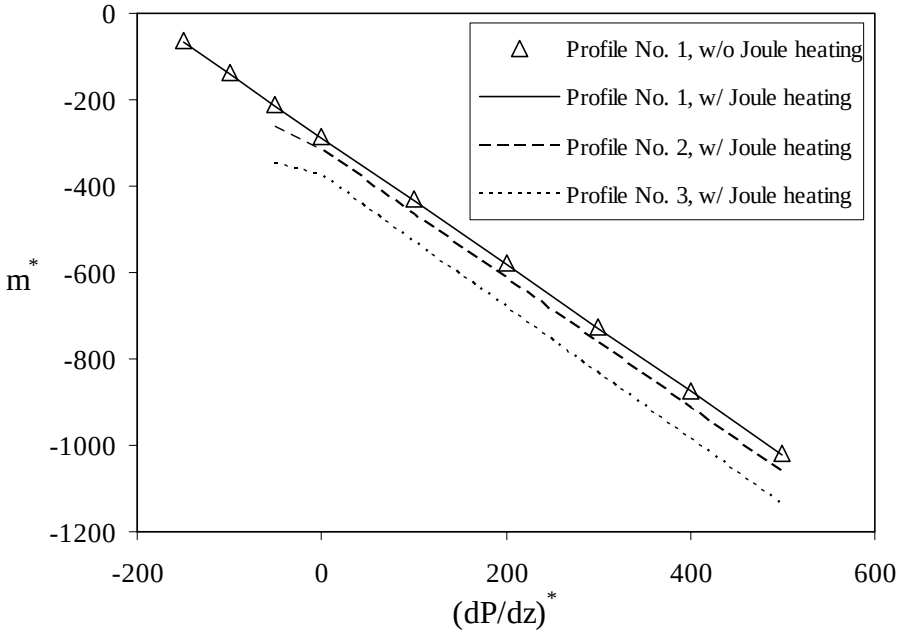

Fig. 5.20 Dimensionless mass flux as a function of dimensionless pressure gradient for Case 2

and tends to lower the velocity. However, in the results presented here the opposite is true since the pump is operating in repulsion mode resulting in the fluid flow in the negative z-direction (see Fig. 5.1). The curves are almost linear (properties are temperature dependent) for all three profiles for the two cases. As an example, according to Fig. 5.19, Profiles No. 2 and 3 enhance the mass flux for dimensionless pressure gradient of -500 by about 7% and 25%, respectively, compared to Profile No. 1. Fig. 5.20 presents the results for the negative pressure gradient up to -150 for Profile No. 1 and -50 for Profiles No. 2 and 3. The reason is that decreasing the external negative pressure gradient further results in a bi-directional flow or a flow in the opposite direction (in positive z-direction). This behavior will be explained further in light of the velocity distribution. Nonetheless, Profiles No. 2 and 3 result in an increase in the mass flux of about 23% and 62%, respectively, at pressure gradient of -50 compared to Profile No. 1. This enhancement decreases as the pressure gradient increases.

To further explain the effect of the external pressure gradient on the pump performance, the actual velocity profiles at the entrance of the pipe for the three temperature profiles and selected pressure gradients are presented in Figs. 5.21-5.27 and Figs. 5.28-5.34 cases 1 and 2, respectively. In these figures, the velocity profiles are subjected to the effects of the electric shear stress as well as the external pressure gradient. The effect of the electric shear stress alone (i.e. zero pressure gradient, Figs. 5.21 and 5.28) on the velocity profile results in a negative velocity distribution, as expected for EHD pump operating in repulsion mode. The positive external pressure gradient is expected to assist the electric shear stress resulting in a higher negative

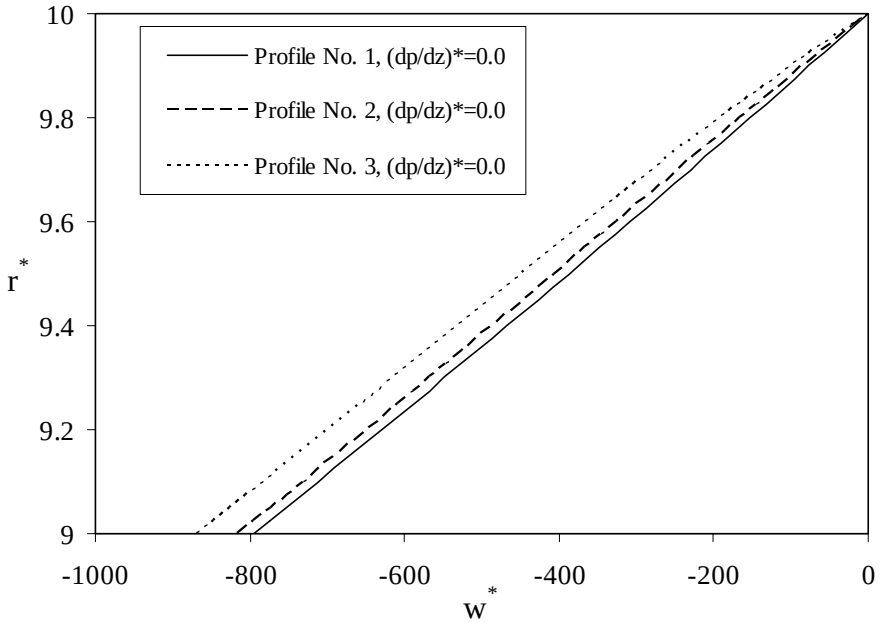

Fig. 5.21 Dimensionless velocity profile at the pipe entrance for $(dp/dz)^*=0.0$ for Case 1

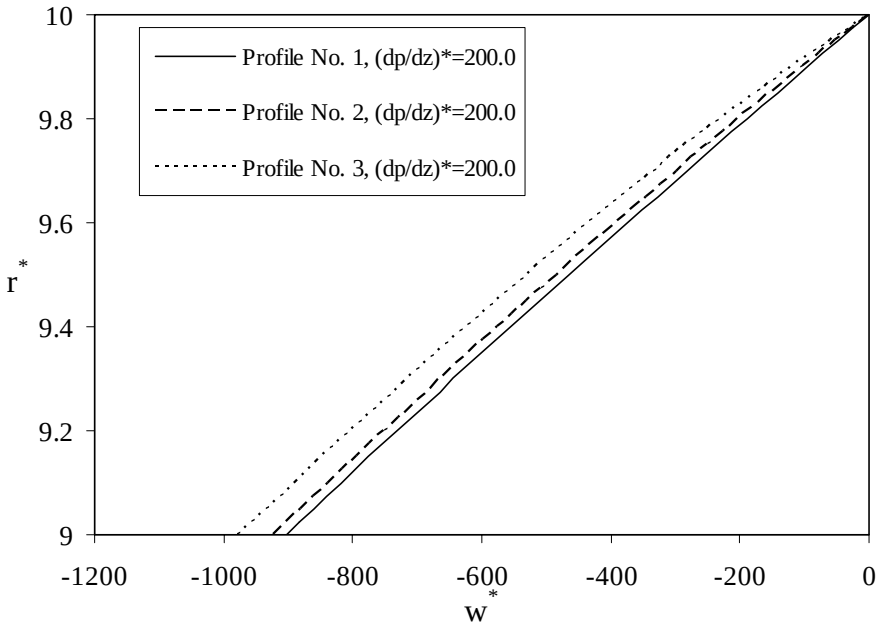

Fig. 5.22 Dimensionless velocity profile at the pipe entrance for $(dp/dz)^*=200.0$ for Case 1

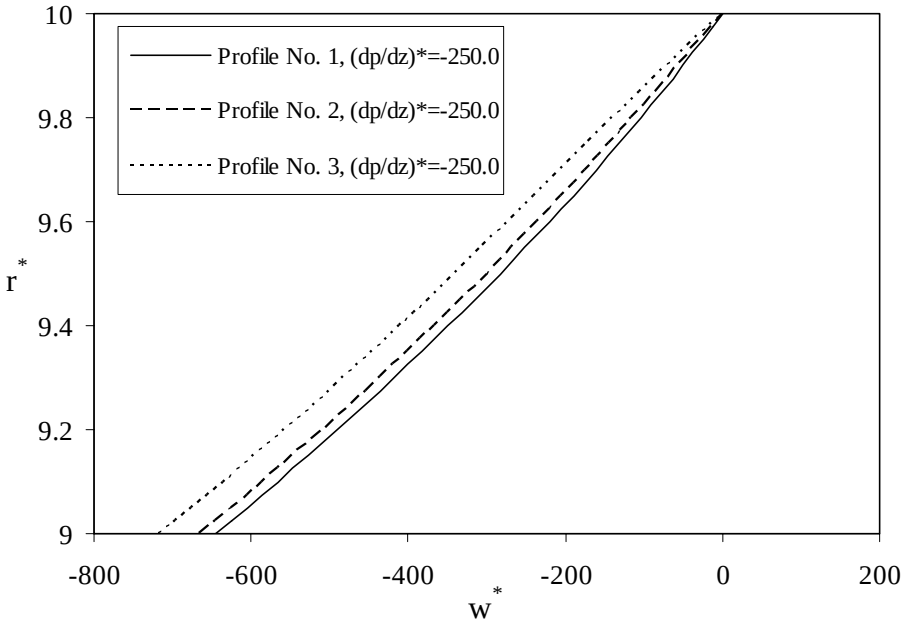

Fig. 5.23 Dimensionless velocity profile at the pipe entrance for $(dp/dz)^*$=-250.0 for Case 1

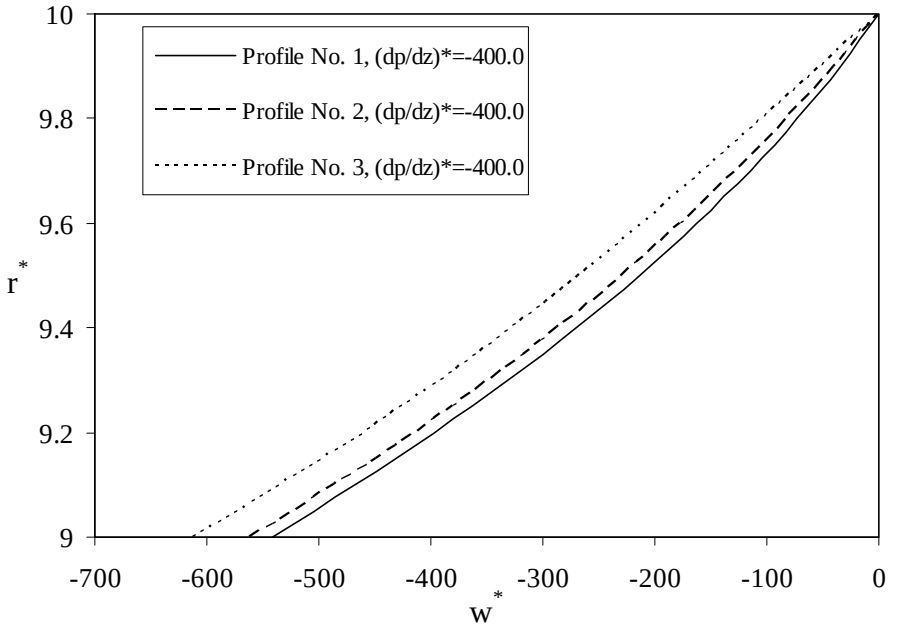

Fig. 5.24 Dimensionless velocity profile at the pipe entrance for $(dp/dz)^*$=-400.0 for Case 1

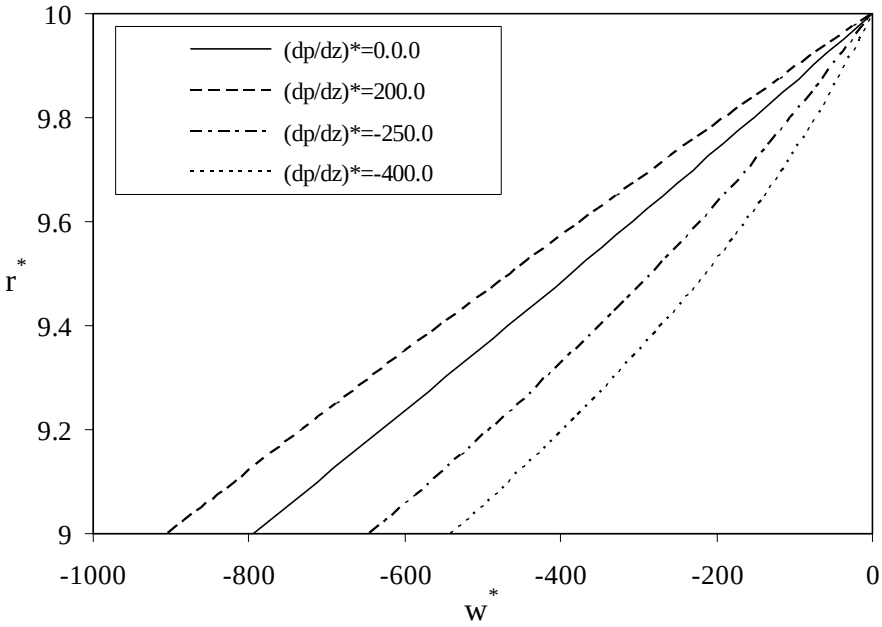

Fig. 5.25 Dimensionless velocity profile at the pipe entrance for Profile No. 1 for Case 1

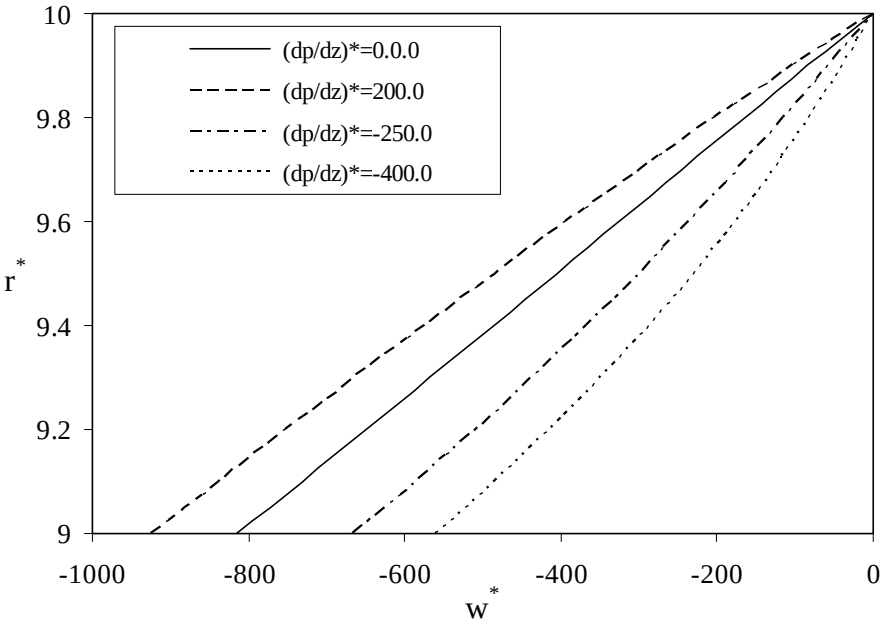

Fig. 5.26 Dimensionless velocity profile at the pipe entrance for Profile No. 2 for Case 1

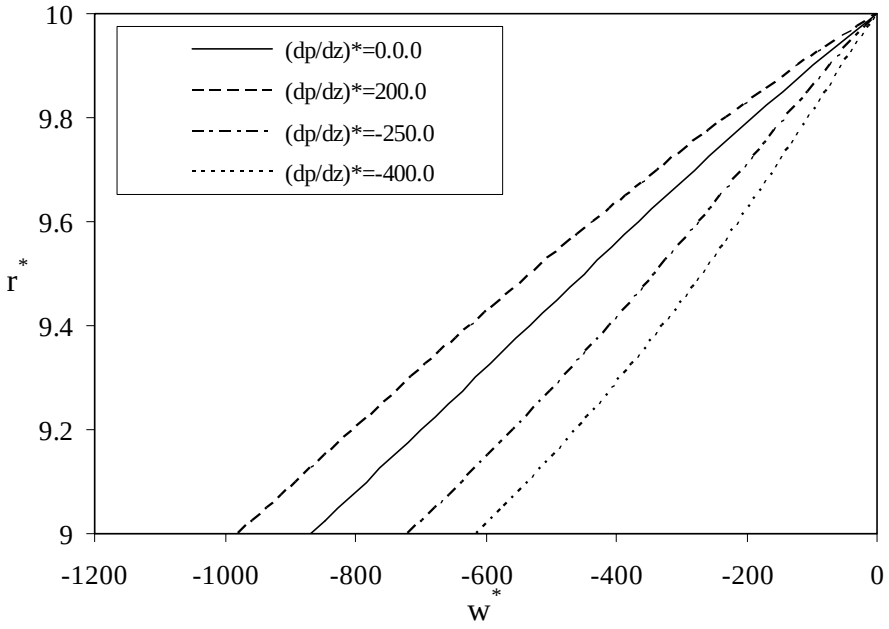

Fig. 5.27 Dimensionless velocity profile at the pipe entrance for Profile No. 3 for Case 1

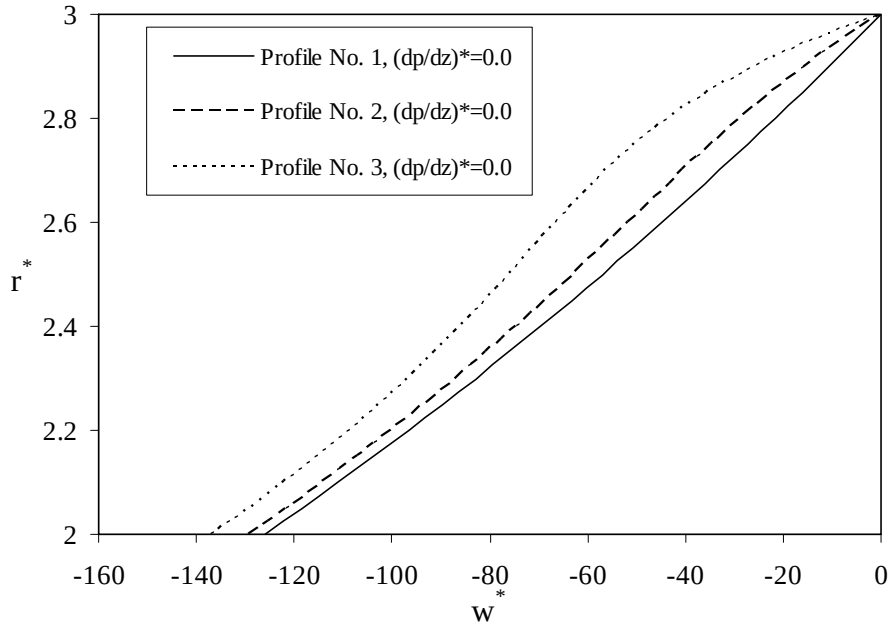

Fig. 5.28 Dimensionless velocity profile at the pipe entrance for $(dp/dz)^*=0.0$ for Case 2

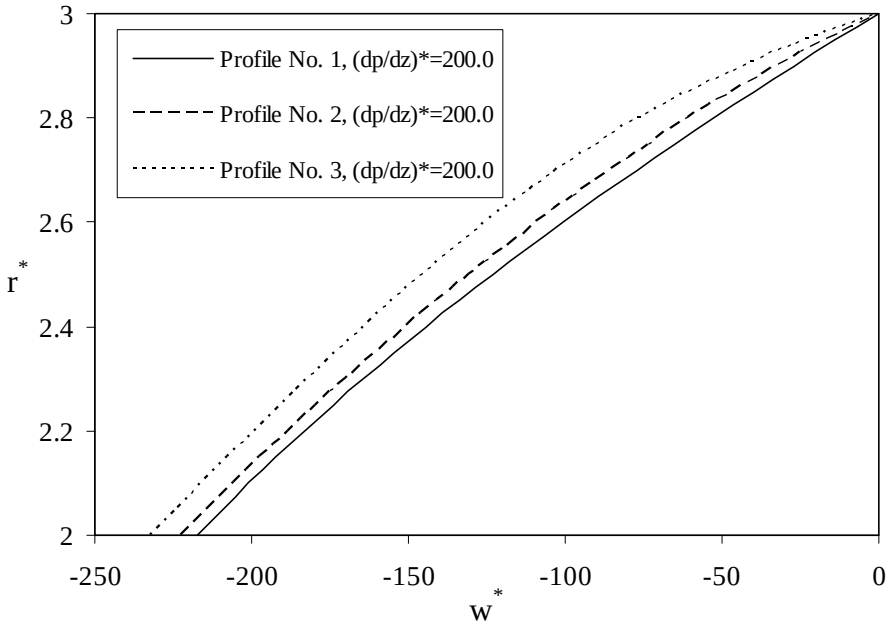

Fig. 5.29 Dimensionless velocity profile at the pipe entrance for $(dp/dz)^*$=200.0 for Case 2

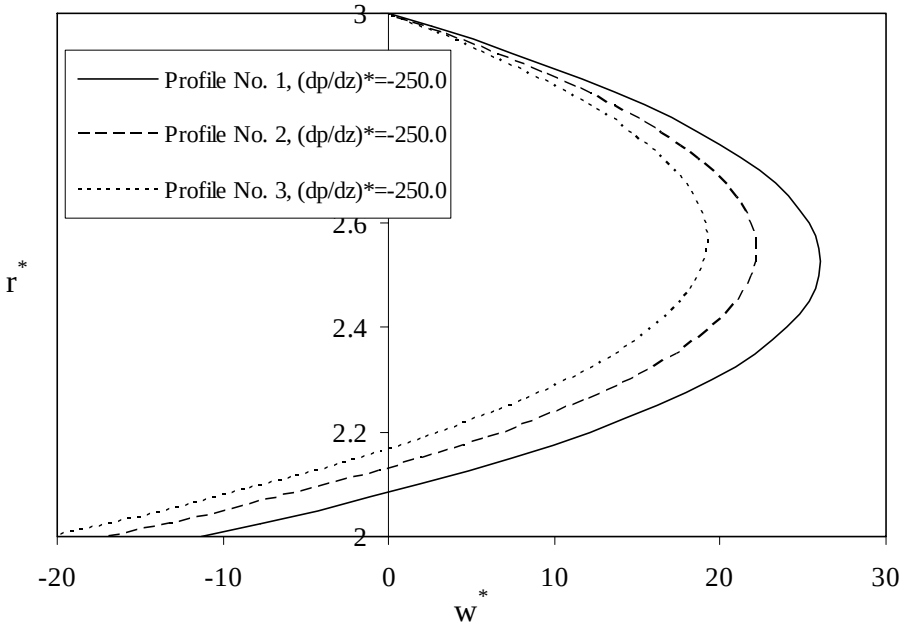

Fig. 5.30 Dimensionless velocity profile at the pipe entrance for $(dp/dz)^*$=-250.0 for Case 2

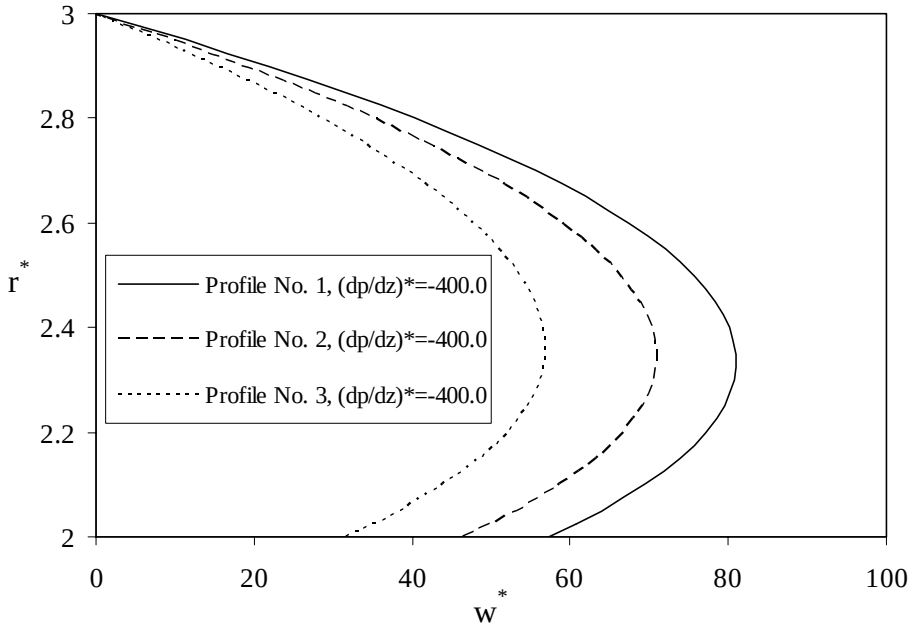

Fig. 5.31 Dimensionless velocity profile at the pipe entrance for $(dp/dz)^*$=-400.0 for Case 2

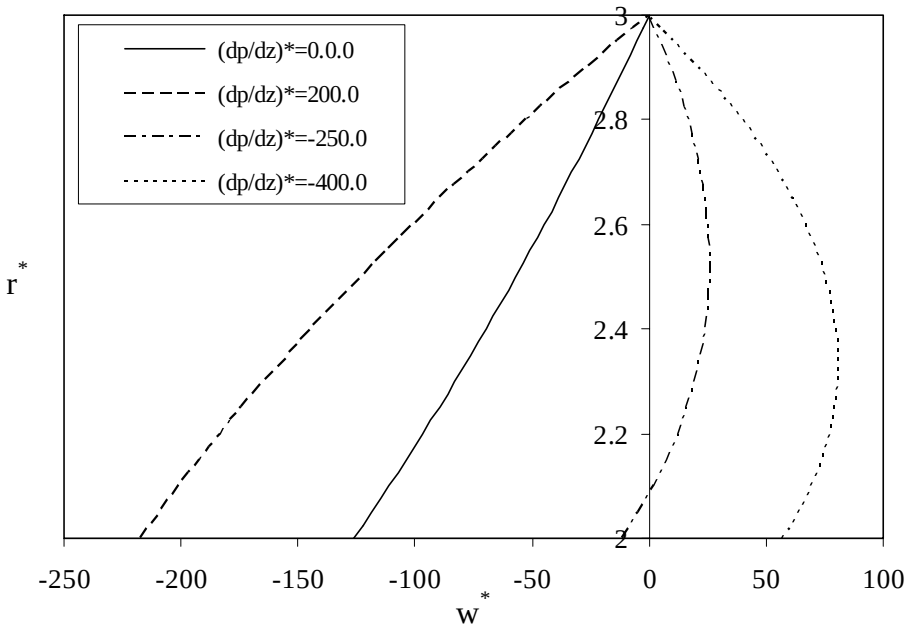

Fig. 5.32 Dimensionless velocity profile at the pipe entrance for Profile No. 1 for Case 2

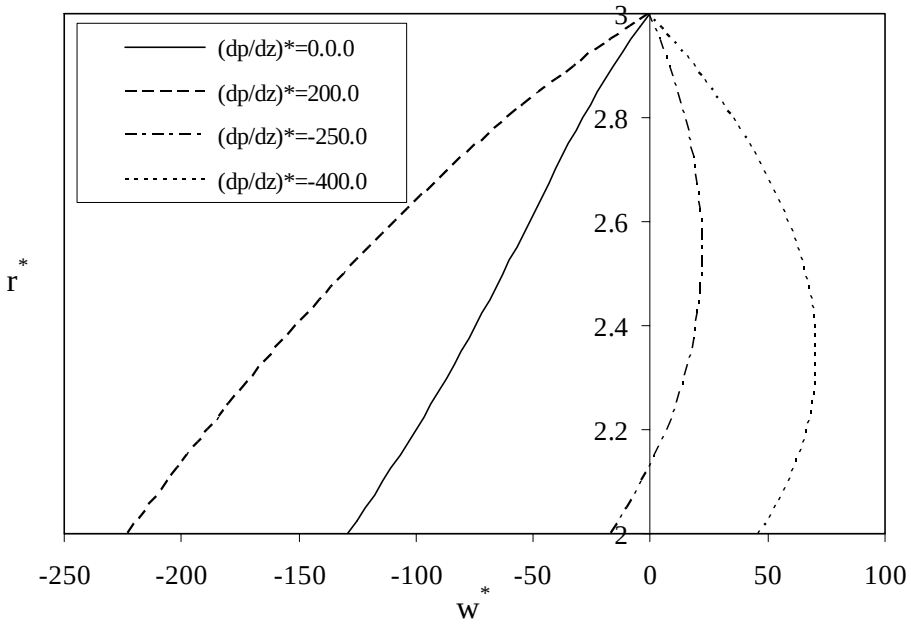

Fig. 5.33 Dimensionless velocity profile at the pipe entrance for Profile No. 2 for Case 2

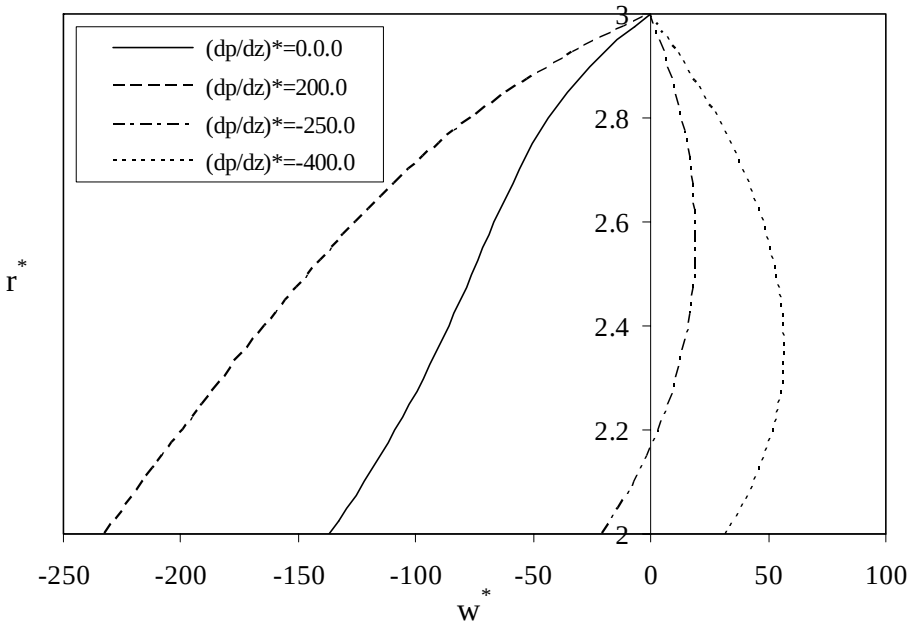

Fig. 5.34 Dimensionless velocity profile at the pipe entrance for Profile No. 3 for Case 3

velocity (Figs. 5.22 and 5.29). However, when the external pressure gradient is negative, the overall effect depends on the dominant force. If the electric shear stress is dominant then negative velocity profile should result (Figs. 5.23 and 5.24). If the electric shear stress and the negative pressure gradient are comparable, then the velocity profile could be bi-directional as illustrated in Fig. 5.30. When the negative pressure is dominant, then the velocity profile is expected to be solely in the positive z-direction (see Fig. 5.31). Bi-directional liquid film flow, in general, is not desirable and in designing an EHD pump, the load should not exceed its limit in order to prevent this occurrence.

It is evident from Figs. 5.21-5.27 for case 1 that all the external pressure gradients considered resulted in a negative velocity profile, which means that the electric shear stress is dominant compared to the external load. However, as the external pressure gradient changes from positive (200) towards negative (-400) the resulting velocity at the interface as well as through the bulk decreases (Figs. 5.25-5.27). This is because when the load is negative the electric shear stress finds it more difficult to overcome its effect, therefore lower velocity is generated. Figures 5.21-5.24 present almost similar trends with the exception that the velocity profile is more convex in the case of positive pressure gradient and more concave for the cases with negative pressure gradients.

In the absence of the external load, Fig. 5.28 presents that for profiles No. 1 and No. 2 the velocity profile gently increases towards its maximum at the interface. However, the velocity profile for profile No. 3 increases rapidly close to the wall and moves toward its maximum at the interface with nearly constant slop over the lower half of the liquid film. Which indicates that the electric shear stress is the largest close to the

wall where the electrodes are placed (i.e. electric field is the strongest). For a positive external load as in Fig. 5.29, the velocity profiles become more convex as the pressure gradient assist the electric shear stress producing larger velocity. It is interesting to notice that in the upper portion of Fig. 5.30, which presents results for bi-directional flow, that profile No. 3 with the largest electric shear stress produces the smallest positive velocity. That is because the electric shear stress is unable to overcome the strong applied negative external pressure gradient which tends to move the flow in the opposite direction.

Finally, Figs. 5.35 and 5.36 present the effect of the gravitational force on the mass flux for cases 1 and 2, respectively. Note that a dimensionless wave number of 0.5 was chosen instead of 2.0 to allow for wider variation of the gravitational force before the results reach values corresponding to the region of transition-turbulent. Here, the wave number of 0.5 corresponds to a wave length of 17.6 mm. Figures 5.35 and 5.36 show that the gravitational force accelerates the flow, thus enhances the mass flow rate. Another observation is that the gravitational force, as it grows larger, dominates the electric shear stress. Thus, the presence of temperature profiles within the liquid has practically no effect on the resultant liquid film mass flow rate.

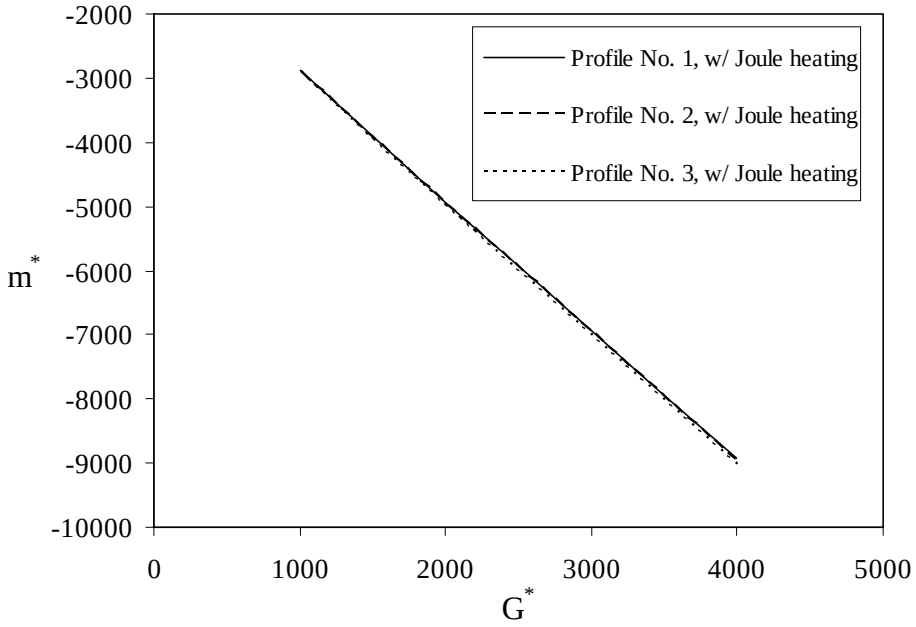

Fig. 5.35 Dimensionless mass flux as a function of dimensionless gravitational force for Case 1 (K*=0.5)

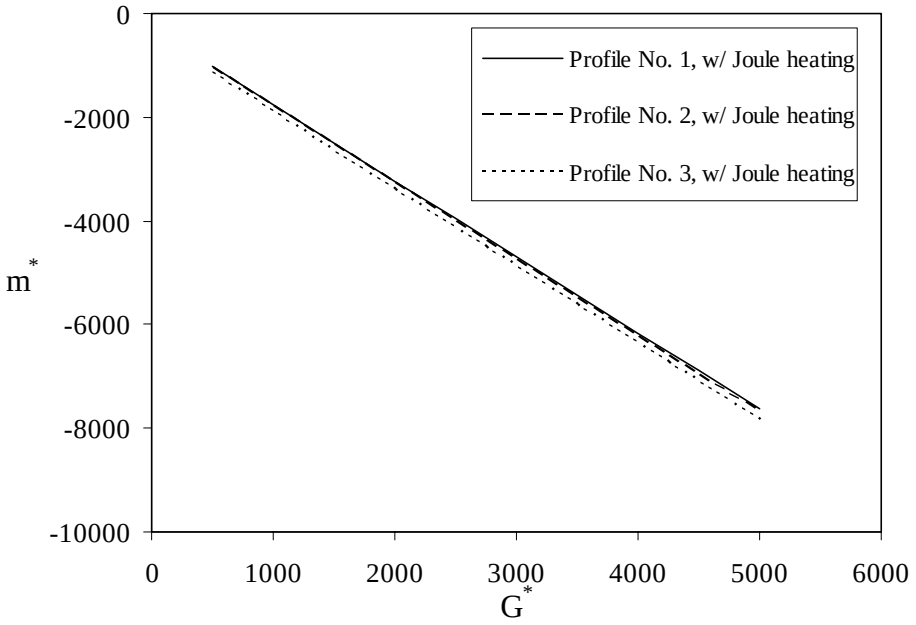

Fig. 5.36 Dimensionless mass flux as a function of dimensionless gravitational force for Case 2

CHAPTER VI

THEORETICAL MODEL OF EHD CONDUCTION PUMPING

Introduction

The general shape of the current (I) versus voltage (V) curve for a wide range of the applied voltage is highly non-linear and can be roughly divided into three different regions. Figure 6.1 presents the general shape of current-voltage characteristics for a dielectric liquid [43].

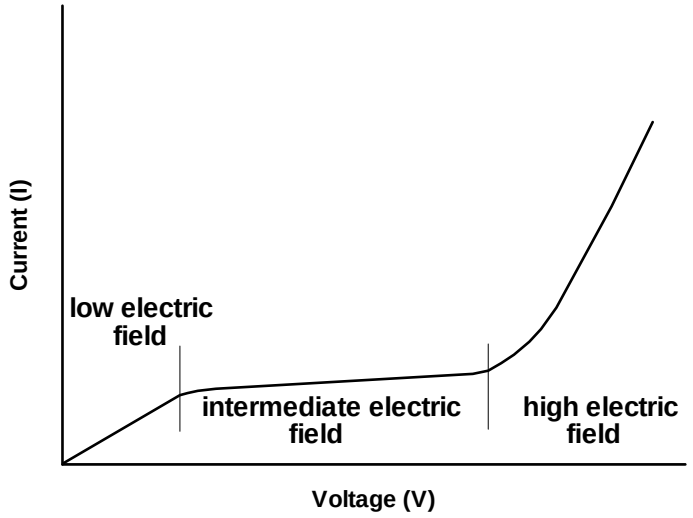

Fig. 6.1 Current (I) – voltage (V) characteristics for a dielectric liquid

In the low electric field regime, linear behavior is observed mainly due to dissolved electrolytic impurities [32]. If the liquid contains a very small number of ions (for instance, due to impurities), ions of opposite polarity in the liquid will be attracted

by the electrostatic charges on the solid surface. The re-arrangement of the charges on the solid surface and the balancing charges in the liquid is called the electrical double layer.

As a result of the electrostatic interaction, the ionic concentration near the solid surface is higher than that in the bulk liquid far away from it. Immediately next to the solid surface, ions are strongly attracted to the solid surface and immobile forming what is called the compact layer. This layer is normally about 0.5 nm thick. From the compact layer to the uniform bulk liquid, the ionic concentration gradually reduces to that of bulk liquid. Ions in this region are affected less by the electrostatic interaction and are mobile. This layer is called the diffuse layer of the electrical double layer. The thickness of the diffuse layer depends on the bulk ionic concentration and electrical properties of the liquid [44]. At this low electric field regime, the conduction is attributable to the impurities of ions and to positive and negative ions formed as a result of the self-dissociation of liquid carrier molecules. Dissociation and recombination are in dynamic equilibrium,

$$A^+B^- \leftrightarrow A^+ + B^- \tag{6.1}$$

When the applied electric field exceeds a certain value (approximately 1 kV/cm, depending on the liquid characteristics) the rate of dissociation exceeds that of the recombination and it continues to increase at higher electric fields. Consequently, away from the diffuse layer, there is a non-equilibrium layer where the dissociation-recombination reactions are not in equilibrium [29].

The conduction mechanism in this regime is mainly caused by the ionic dissociation and the formation of heterocharges, i.e., charges having the opposite polarity from that of the adjacent electrode. The I versus V behavior in this regime is sub-ohmic showing only a slightly increased current with increased voltage. The thickness of this heterocharge layer is proportional to the corresponding relaxation time of the working fluid and depends on the applied electric field. This regime is directly related to conduction pumping mechanism. As shown in Fig. 2.4, the attraction between the electrodes and the charges within the heterocharge layer induces a fluid motion near the electrode from the liquid side to the electrode side. With this particular electrode configuration, only the motion around the high voltage electrode can contribute to the net axial flow. This is because the net axial motion around the ring ground electrode is almost canceled because of the symmetrical electrode configuration.

The high electric field region (on the order of 10^4 kV/m, depending on the liquid characteristics, electrode material), is characterized by very steep rise of current with an increase in the voltage. This steep increase in the current is due to the injection of ions from the electrodes into the liquid. This phenomenon is mainly controlled by the electrochemical reactions at the electrode-liquid interface and therefore depends critically on the composition and geometry of the electrodes [45]. Beyond this electric field level, the ion-drag pumping mechanism will be dominant.

Single Phase Flow Generation in a Plane Channel

The first model for generation of hydrodynamic pressure through EHD conduction appeared in [26], where approximate analytical solutions were provided for parallel plate and point-plane electrode configurations. A numerical model for pressure generation in a round pipe fitted with a hollow-tube electrode was presented in [37]. However neither of these models accounted for the EHD flow generated. Later, Jeong and Seyed-Yagoobi [38] theoretically and numerically studied the circulation in an enclosure generated by EHD conduction mechanism.

This section investigates, theoretically, EHD conduction in geometry capable of providing a net flow. The main motivation behind this study is to develop a fundamental understanding for the conduction pumping mechanism and to confirm the concept through the numerical calculations. The numerical results are of a great value for the proper electrode design. This problem was preliminarily investigated by Datta [46]. However, inappropriate boundary conditions were imposed at the channel wall for the electric field as well as for the positive and negative charges. These boundary conditions will be discussed in the section of boundary conditions and corrected boundary conditions for electric filed, positive charge, and negative charge will be provided.

The EHD conduction pumping shows a great promise for various micro-gravity and terrestrial applications. For instance, EHD conduction pump can be used to enhance and/or to control the heat transfer in phase change thermal devices such as heat pipes, capillary pumped loops, condensers, and evaporators.

Figure 6.2 illustrates the geometry considered for the flow generation (side view).

The dielectric liquid is contained between two parallel plates whose spanwise dimensions (into and out of the plane paper) are very much larger than the width between the plates. This flow geometry will henceforth termed channel. The high voltage (HV) electrode is in the form of a rectangular block (of the same spanwise dimension as the channel), that also acts as an obstacle to any flow generated in the channel. The ground electrode is in the form of a plate embedded on the wall of the channel.

Governing Equations

The theoretical model is developed based on the following assumptions [38].

a. The state is steady,
b. the model is two-dimensional,
c. fluid is incompressible and single phase,
d. the flow generated is laminar,
e. the dielectric liquid is isothermal
f. no injection is present on the electrodes' surfaces,
g. mobility for the positive and negative ions is the same ($b_+ = b_- = b$),
h. diffusion coefficient for positive ions and negative ions are the same ($D_+ = D_- = D(= bk_BT/e)$),

In the case of incompressible fluid, the continuity equation is expressed as,

$$\nabla \cdot \vec{U} = 0 \tag{6.2}$$

The momentum equation with electric body force due to Coulomb force reduces to

$$\rho\left((\vec{U}\cdot\nabla)\vec{U}\right) = -\nabla P + \mu\nabla^2\vec{U} + (p-n)\vec{E} \tag{6.3}$$

The electric field with space charge can be calculated from the Gauss' law of Maxwell's equations

$$\nabla\cdot(\varepsilon\vec{E}) = q\,,\ \vec{E} = -\nabla\phi\,,\ \ q = (p-n) \tag{6.4}$$

where p and n are the positive and negative charge density , respectively. The charge carriers are determined from the dissociation-recombination process expressed by Eq. (6.1) and are governed by the following charge conservation equations with the above assumptions,

$$\nabla\cdot\left(bp\vec{E} + p\vec{U} - D\nabla p\right) = k_d N - k_r pn\,, \tag{6.5}$$

$$\nabla\cdot\left(-bn\vec{E} + n\vec{U} - D\nabla n\right) = k_d N - k_r pn \tag{6.6}$$

where N is the concentration of neutral species. The terms in the left-hand side of Eqs. (6.5) and (6.6) represent three different components for the charge current density (J). The first term is the conduction term that results due to mobility in presence of electric field. This term signifies electromigration flux of the species of charge q (p for A^+ and n for B^-). The second term is the convective flux due to the generated EHD flow. The third term is the flux due to diffusion across concentration gradients of the charged species.

The corresponding boundary conditions and geometric parameters for the numerical calculation are shown in Fig. 6.2.

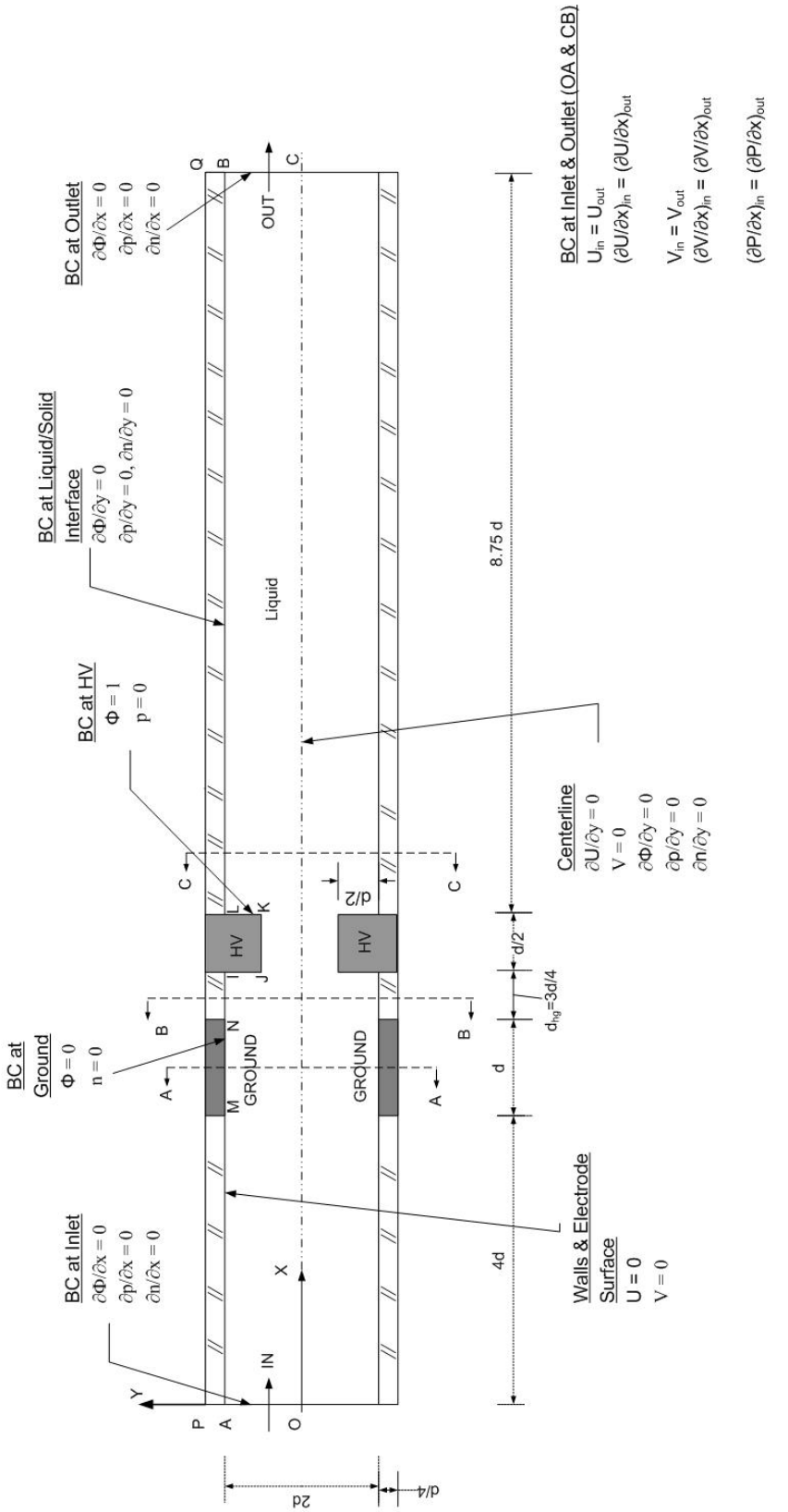

Fig 6.2 Boundary conditions and geometric parameters for single phase medium

Non-Dimensionalization

The governing equations and boundary conditions are non-dimensionalized with the following dimensionless parameters [38],

$$P^* = \frac{P}{\mu^2 / \rho d_{hg}^2},\ x^* = \frac{x}{d_{hg}},\ y^* = \frac{y}{d_{hg}},\ p^* = \frac{p}{n_{eq}},\ n^* = \frac{n}{n_{eq}},$$

$$q^* = \frac{q}{n_{eq}},\ \vec{E}^* = \frac{\vec{E}}{V/d_{hg}},\ \phi^* = \frac{\phi}{V},\ \vec{U}^* = \frac{\vec{U}}{bV/d_{hg}} = \frac{U}{u_e}$$

where $u_e (= bV/d)$ is mobility limit and n_{eq} is the negative charge density at thermodynamic equilibrium. n_{eq} is expressed as $n_{eq} = \sqrt{k_{d0} N / k_r}$ since the following relation is satisfied at thermodynamic equilibrium

$$k_{d0} N = k_r p_{eq} n_{eq} = k_r n_{eq}^2 \tag{6.7}$$

where k_{d0} is the dissociation rate constant when no electric field is present. Based on the Onsager's field-enhanced dissociation model [47], the dissociation rate constant, k_d, with the local electric field magnitude, and is expressed as $k_d = k_{d0} F(\omega) = k_{d0} I_1(2\omega)/\omega$.

Here, $\omega = \left[\frac{e^3 |E|}{4\pi\varepsilon k_B^2 T^2} \right]^{1/2}$ and I_1 is first order modified Bessel function of first kind. In the limit as the absolute value of electric field tends to zero (i.e. $\omega \to 0$), the dissociation rate coefficient is electric field independent. With the electric field dependent dissociation rate coefficient (i.e. ω > 0.0), F (ω) becomes larger than 1.0, resulting in $k_d > k_{d0}$. The recombination rate constant is independent of the electric field and is

assumed to satisfy $k_r = 2b/\varepsilon$ which is the upper bound given by Langevin [48]. The dimensionless form of Eqs. (6.2) to (6.6) are;

$$\nabla^* \cdot \vec{U}^* = 0 \tag{6.8}$$

$$\left((\vec{U}^* \cdot \nabla^*)\vec{U}^*\right) = -\left(\frac{1}{Re_{ehd}}\right)^2 \nabla^* P^* + \left(\frac{1}{Re_{ehd}}\right)\nabla^{*2}\vec{U}^* + M\left(p^* - n^*\right)\vec{E} \tag{6.9}$$

$$\nabla^* \cdot \vec{E}^* = C_o(p^* - n^*),\ \vec{E}^* = -\nabla^*\phi^*, \tag{6.10}$$

$$\nabla^* \cdot (p^*\vec{E}^* + p^*\vec{U}^*) - \alpha\nabla^{*2}p^* = 2C_o(F(\omega) - p^*n^*), \tag{6.11}$$

$$-\nabla^* \cdot (n^*\vec{E}^* - n^*\vec{U}^*) - \alpha\nabla^{*2}n^* = 2C_o(F(\omega) - p^*n^*) \tag{6.12}$$

Four dimensionless parameters appear in the above dimensionless equations and are given by

$$Re_{ehd} = \frac{\rho u_e d_{hg}}{\mu}, \tag{6.13}$$

$$M = \frac{n_{eq}d_{hg}^2}{\rho b^2 V} = \frac{\varepsilon C_o}{\rho b^2}, \tag{6.14}$$

$$C_o = \frac{n_{eq}d_{hg}^2}{\varepsilon V}, \tag{6.15}$$

$$\alpha = \frac{D}{bV} \tag{6.16}$$

The parameter C_o which is the dimensionless n_{eq} can also be viewed as half the ratio of the ionic transit time (t_T) to the charge relaxation time (τ). The ionic transit time corresponds to the required time for a charged particle to travel the distance between the electrodes with a velocity of bE (mobility limit). The charge relaxation time

represents the time during which a charged particle maintains its charge in a medium. The parameter C_o can be expressed as;

$$C_o = \frac{n_{eq} d_{hg}^2}{\varepsilon V} = \frac{1}{2}\frac{(2bn_{eq})d_{hg}^2}{b\varepsilon V} = \frac{1}{2}\frac{\sigma d_{hg}^2}{b\varepsilon V} \propto \frac{1}{2}\frac{d_{hg}^2 / bE}{\varepsilon/\sigma} = \frac{1}{2}\frac{t_T}{\tau} \tag{6.17}$$

M is determined when C_o and the fluid properties of the working fluid are given. Re_{ehd} is the electric Reynolds number and depends on the applied voltage. The parameter α is also dependent on the applied voltage. The mobility b is related to the diffusivity D through the Nernst-Einstein relationship $\frac{D}{b} = \frac{k_B T}{e}$. Therefore, α can be estimated as $\alpha = \frac{D}{bV} = \frac{k_B T}{eV} \approx \frac{1}{40V}$, which implies that for a high voltage level the contribution of charge diffusion flux to the current density can be negligible. However, α thus, the diffusion component of the current conservation is kept in the calculations presented in this study. Consequently, C_o and the applied voltage are the input parameters in the numerical calculations if the fluid properties and geometric parameters are set. Equations (6.9), (6.10), (6.11), and (6.12) are strongly coupled together and should be solved interactively.

Boundary Conditions

Due to the symmetry of the problem, only the upper half-plane in Fig. 6.2 is labeled for describing the boundary conditions. The flow field boundary conditions at the inlet (OA) and outlet (CB) should provide a mathematical closure to the problem, while preserving the essential nature of the flow as one solely due to the EHD

conduction phenomenon occurring near the electrodes. Therefore, no flow can be specified at the inlet (OA) of the domain a priori. Additionally, the flow should be free from end-effects at both the inlet (OA) and the outlet (CB). Furthermore, the overall force balance in the problem can be predefined to be one between the EHD force and the fluidic resistance of the channel with no external pressure difference maintained between the inlet and the outlet.

The aforementioned conditions can be satisfied by applying periodic boundary conditions on the primary and the secondary velocities, as well as for the pressure along with allowing the distances upstream (AM) and downstream (JB) the high voltage electrode large enough for flow to reach fully developed conditions at both ends.

The dimensionless periodic boundary conditions at the inlet and the outlet require:

$$u^*_{in} = u^*_{out}, \left(\frac{\partial u^*}{\partial x}\right)_{in} = \left(\frac{\partial u^*}{\partial x}\right)_{out},$$

$$v^*_{in} = v^*_{out}, \left(\frac{\partial v^*}{\partial x^*}\right)_{in} = \left(\frac{\partial v^*}{\partial x^*}\right)_{out},$$

and

$$\left(\frac{\partial P^*}{\partial x^*}\right)_{in} = \left(\frac{\partial P^*}{\partial x^*}\right)_{out}$$

since the inlet and the outlet are far enough from the zone of the electrodes, the boundary conditions at the inlet and the outlet for potential, positive charge, and negative charge are as follows:

$$\frac{\partial \phi^*}{\partial x^*} = \frac{\partial p^*}{\partial x^*} = \frac{\partial n^*}{\partial x^*} = 0$$

the boundary conditions in dimensionless forms at high voltage electrode and ground electrode, respectively are as follows

$$p^* = 0,\ u^* = 0,\ \ v^* = 0,\ \phi^* = 1.0$$

and

$$n^* = 0,\ u^* = 0,\ \ v^* = 0,\ \phi^* = 0.0$$

the symmetry conditions ;

$$\left(\frac{\partial u^*}{\partial y^*}\right) = 0,\ v^* = 0,$$

and

$$\frac{\partial \phi^*}{\partial y^*} = \frac{\partial p^*}{\partial y^*} = \frac{\partial n^*}{\partial y^*} = 0$$

It is noteworthy to mention that Datta [46] assumed that no charge density existed at the liquid/solid interface on the part of the channel wall that was not grounded. As a result of this assumption he came to an inappropriate conclusion and imposed the positive and the negative charges to be zero at the channel wall. Equations (6.5) and (6.6) do not admit such conditions. In the context of the present formulation, there is no way to avoid electromigration of the charge toward the channel wall and no way to remove the charge from the wall. Hence, the positive and negative charge density can not be imposed to be zero at the wall and should be determined as part of the solution. In addition, at the liquid/solid interface [46], $\varepsilon_s E_y^s - \varepsilon_l E_y^l = 0$ is imposed for the jump of the normal

component of the electric displacement at the wall. For the aforementioned reasons this boundary condition can not be imposed at the liquid/solid interface. Moreover, representing the jump in the normal component of the electric displacement in terms of the electric permittivity seems to be accurate when AC voltage is applied. However, in the present study where DC voltage is applied it seems more reasonable to represent such a jump in terms of the electric conductivity. For a stationary flow at the liquid/solid interface and DC limit [49] the jump of the normal component of the electric displacement can be reduced to $\sigma_s E_y^s - \sigma_l E_y^l = 0$. The electric conductivity of the solid for a perfectly insulating material is much less than that for R-123. Thus, $E_y^l = \frac{\partial \varphi}{\partial y} = 0$ appears to be the correct boundary condition at the liquid side of the channel wall. Charge would accumulate at the wall during an initial transient until this condition is satisfied.

The correct boundary conditions for the electric field as well as the positive and negative charges on the channel wall are as follows, respectively;

$$\frac{\partial \phi^*}{\partial y^*} = \frac{\partial p^*}{\partial y^*} = \frac{\partial n^*}{\partial y^*} = 0$$

Single Phase Flow Generation in a Plane Channel with Minimum Drag Electrodes

In this section, EHD conduction is studied for the first time in geometry with minimum drag electrodes capable of providing a net flow. The minimum drag electrodes give minimal drag to the flow. In micro-scale this is important as there may be a

significant hindrance to the flow if the electrode is in the path of the fluid flow. Therefore, the concept of minimum drag electrodes allows for micro-scale fluid flow. From manufacturing point of view, it is easy to fabricate micro and macro devices with electrodes embedded in the channel wall.

The theoretical model and boundary conditions presented in the previous section are applicable to the case of EHD conduction pumping with minimum drag electrodes. The boundary conditions and the geometric parameters are summarized in Fig. 6.3.

EHD Conduction Pumping of Stratified Liquid/Vapor Medium

The theoretical model is developed based on the following assumptions:

a. The state is steady,
b. the model is two-dimensional,
c. fluid is incompressible and single phase,
d. the flow generated is laminar,
e. the dielectric liquid is isothermal,
f. flat liquid/vapor interface
g. constant liquid film thickness (no phase change)
h. vacuum properties for the vapor
i. no injection is present on the electrodes' surfaces,
j. mobility for the positive and negative ions is the same ($b_+ = b_- = b$),
k. diffusion coefficient for positive ions and negative ions are the same ($D_+ = D_- = D(= bk_BT/e)$),

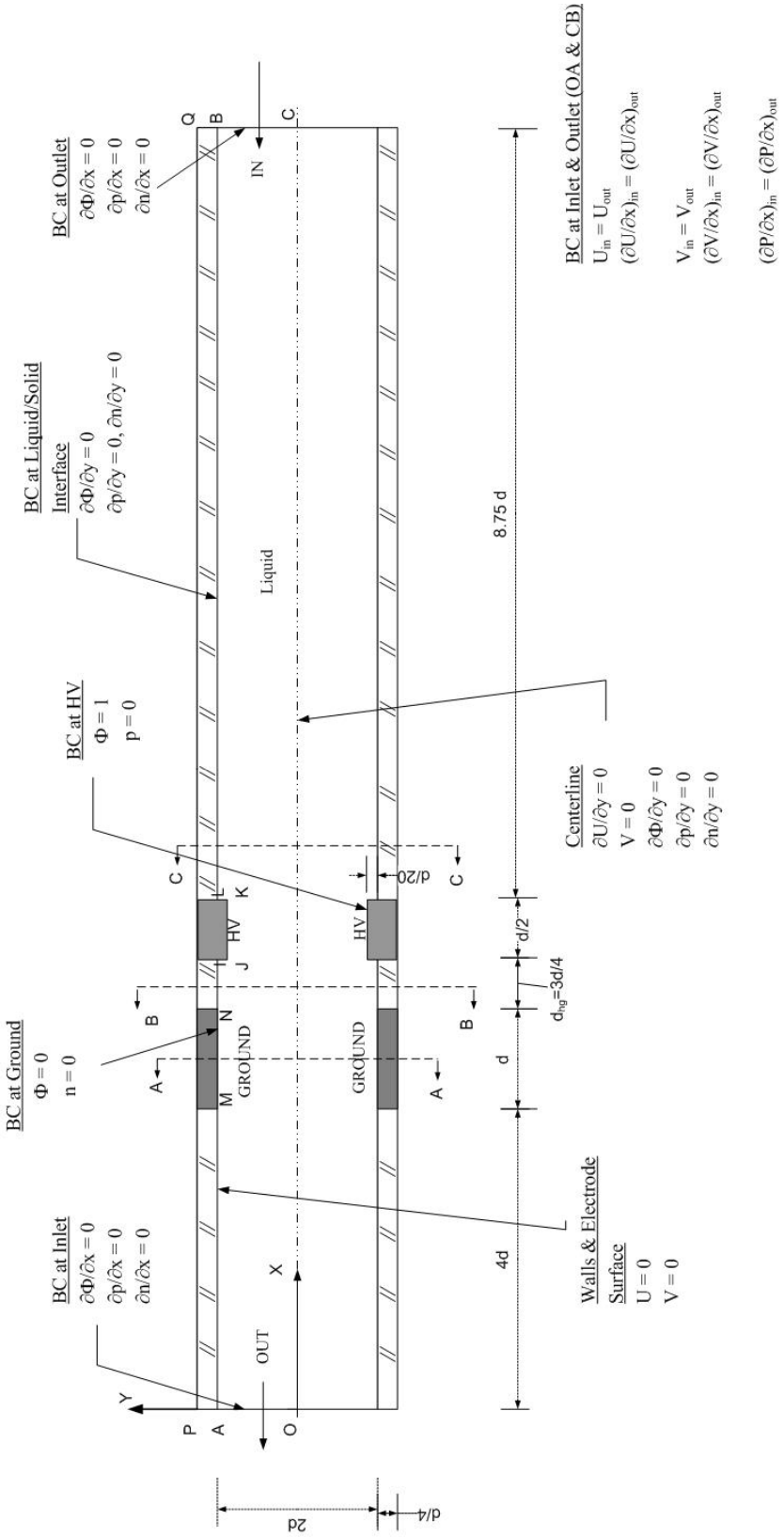

Fig. 6.3 Boundary conditions and geometric parameters for single phase medium with Minimum Drag Electrodes

In this case, the liquid film is solely pumped due to EHD conduction phenomenon. The mathematical formulation for pumping the liquid film is similar to that of single phase liquid presented in the previous section. However, the treatment of the boundary conditions at the liquid/vapor interface makes this problem substantially different from that of a single phase liquid. The boundary conditions and the geometric parameters are summarized in Fig. 6.4. Both high voltage and ground electrodes are placed at the channel wall. The high voltage (HV) electrode is in the form of a rectangular block, of the same spanwise dimension as the channel, which also acts as an obstacle to the flow generated in the channel. The ground electrode is in the form of a plate embedded on the wall of the channel.

The vapor is assumed to be motionless and the liquid film is solely pumped due to EHD conduction. Therefore, the following boundary conditions are imposed for the velocity field at the liquid/vapor interface

$$\left(\frac{\partial u^*}{\partial y^*}\right) = 0\,,\ v^* = 0\,,$$

Away from the electrodes and the heterocharge layers, the charges are in equilibrium and positive and negative charges are equal. In the electroneutral core (including the liquid/vapor interface), the following boundary condition is imposed

$$p^* = n^* = 1.0$$

This aforementioned boundary condition at the liquid/vapor interface is only appropriate when the interface is assumed to be away from the heterocharge layers allowing for the region of electroneutrality in the liquid film away from the heterocharge layers. If the

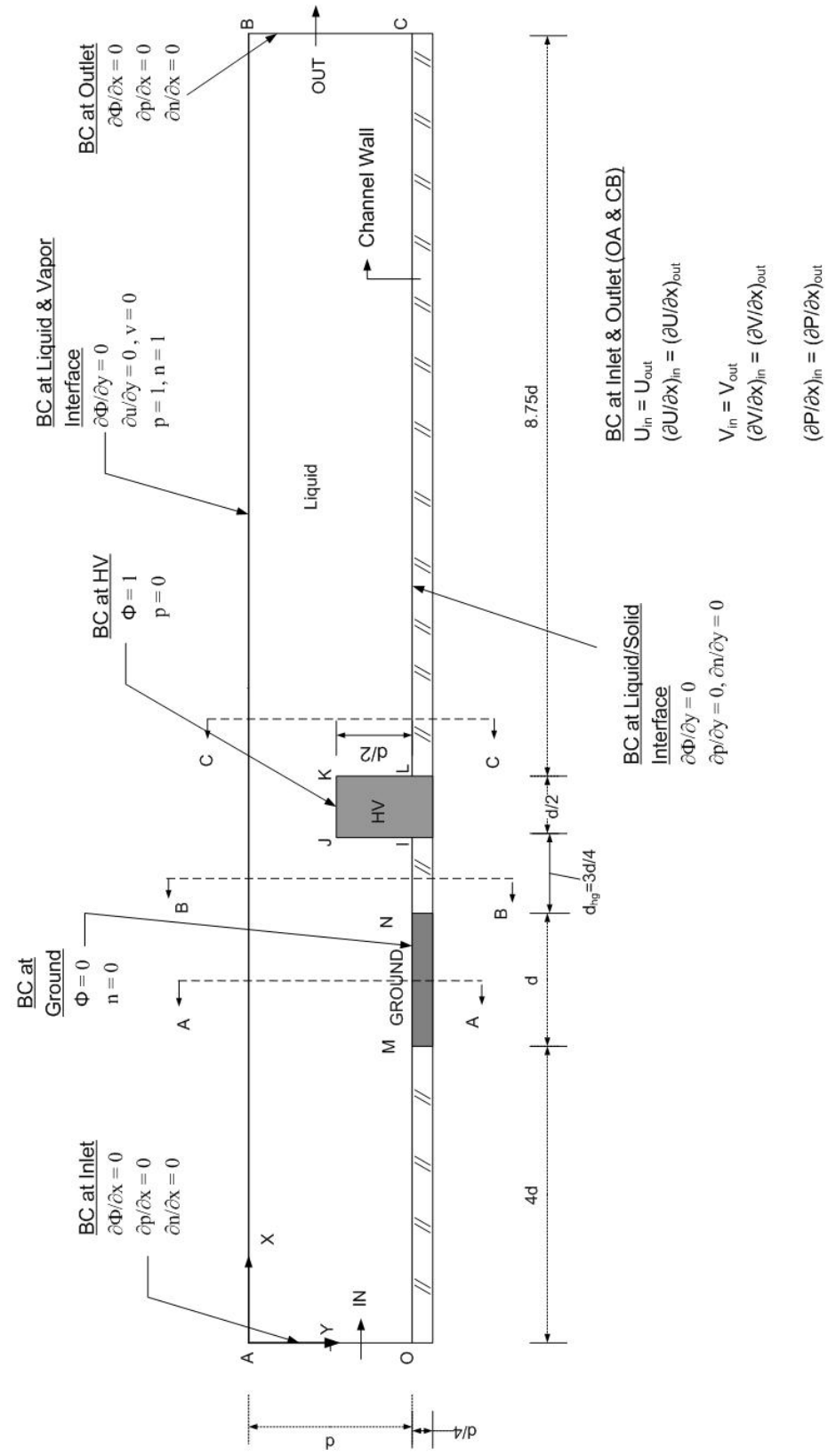

Fig. 6.4 Boundary conditions and geometric parameters for stratified liquid/vapor medium

liquid film is thin and the electrodes are long then the above boundary condition could be inappropriate. For the two cases considered here, the liquid film is thick enough to allow for the electroneutral region to exit close to the liquid/vapor interface. Assuming the electric conductivity of the vapor to be zero, the jump of the normal component of the electric field at the liquid/vapor interface (in the DC limit) suggests the following boundary condition

$$\frac{\partial \phi^*}{\partial y^*} = 0$$

This theoretical model and boundary conditions are applicable to the case of EHD conduction pumping with zero drag (i.e. flushed) electrodes of liquid film in stratified liquid/vapor medium. The boundary conditions and geometric parameters are summarized in Fig. 6.5.

Numerical Methods

For discretization of the governing equations, finite volume method was used [50]. The discretization equations were solved iteratively by the line-by-line application of the tri-diagonal matrix algorithm. Central difference scheme was applied to the Gauss' law and upwind scheme based on the electric field direction, was applied to the charge conservation equations. The momentum equations were solved using the SIMPLE algorithm [50]. Owing to the geometric symmetry, only upper half domain was solved for the cases considered single phase. As a convergence criterion, $\max\left|\frac{\phi_{i,j}^{k+1} - \phi_{i,j}^{k}}{\phi_{i,j}^{k+1}}\right| \le 10^{-4}$

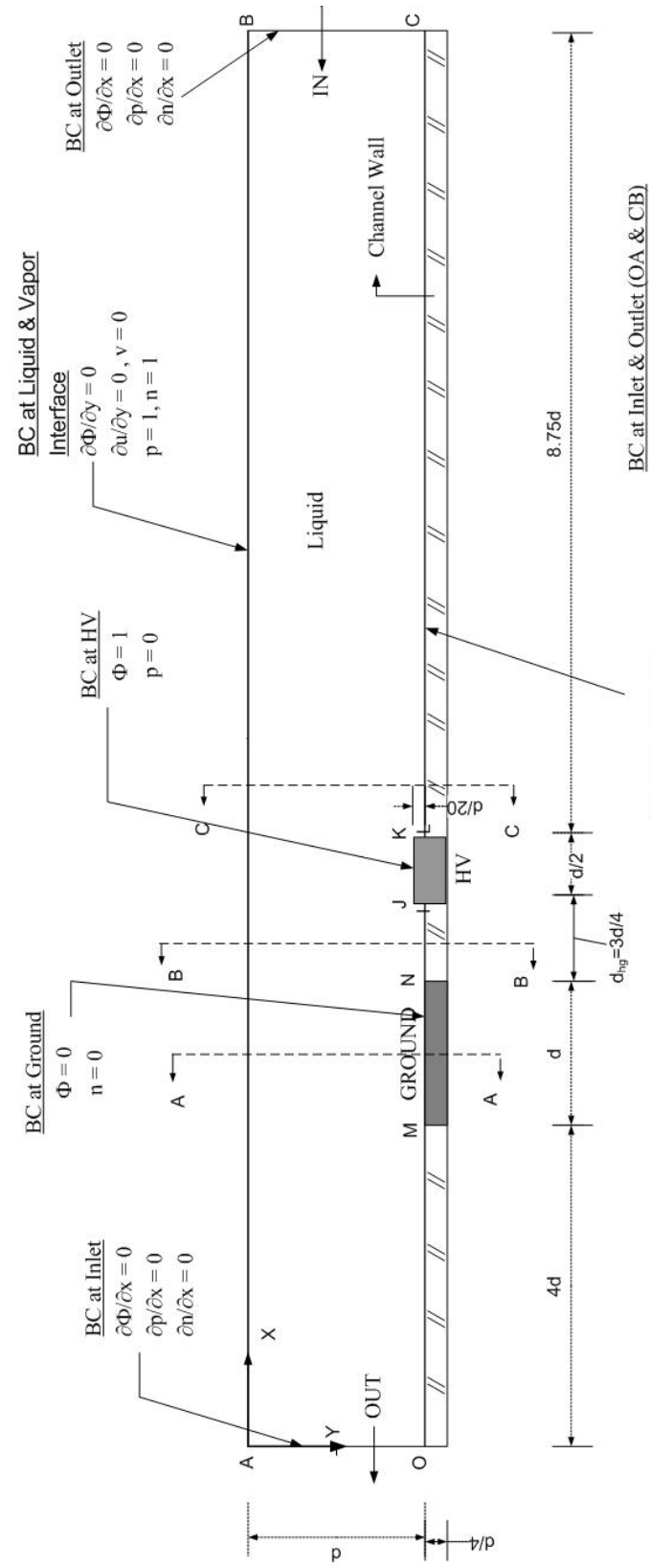

Fig. 6.5 Boundary conditions and geometric parameters for stratified liquid/vapor medium with Minimum Drag Electrodes

was used for all parameters except for the cases considered the minimum drag electrodes design $\max\left|\frac{\phi_{i,j}^{k+1}-\phi_{i,j}^{k}}{\phi_{i,j}^{k+1}}\right| \le 10^{-3}$ was used for the convergence of the velocities.

Numerical Results

Numerical results are obtained for the aforementioned electrode configurations. A net flow generation was observed for the four cases considered in this study. The length scale, d (Figs. 6.2-6.5) is assumed to be 2.5 cm, resulting in an inter-electrode axial gap (d_{hg}) of 1.875 cm. This inter-electrode gap is relatively large compared to the typical values used in the experiments [40]. It was necessary to assume an inter-electrode gap of order of centimeter because values with a smaller order of magnitude caused divergence in the numerical solutions. This can be attributed to the increased electric field strength in the inter-electrode region and hence increased magnitude of field enhanced dissociation term F (ω) which amplifying the nonlinearities. This problem could have been potentially resolved if more refined grids were used in the inter-electrode region. However, this would have increased the computational time significantly. Despite the relatively large value of the inter-electrode gap used in this study, the numerical results presented here prove the concept of the net flow generation using conduction phenomenon. A smaller gap is expected to result in higher body-force, thus higher net flow. The properties of the working dielectric liquid (i.e. R-123) considered in this work are given in Table 6.1. It is important to note that the electrical conductivity, σ, of R-123 shows a wide range of variation because of its sensitivity to the concentration levels of

chemical species that are not monitored during its production. Therefore, a value of 4.7×10^{-11} S/m was chosen for this particular study as shown in Table 6.1. With the specified working fluid and inter-electrode axial gap, and at 2 kV applied potential, the value of C_0 is 2.0 which corresponds to the limit of transition from quasi-Ohmic conduction to saturation. The corresponding non-dimensional parameters M and Re_{ehd} are 24.28 and 359.42, respectively.

Table 6.1 Properties for R-123

Electrical permittivity (F/m)	42.43×10^{-12}
Electrical conductivity (S/m)	4.7×10^{-11}
Density (kg/m^3)	1459.0
Dynamic Viscosity (Pa•s)	4.087×10^{-4}
Mobility ($m^2/V•s$)	4.894×10^{-8}

For all the figures generated the x-axis and the y-axis were normalized using the half width of the channel (d). The location of the normal planes selected for the presented profiles are shown in Figs. 6.2 to 6.5. The plane AA is at x/d=4.5d and passes through the center of the ground electrode. The plane BB is at x/d=5.4d and passes through the axial gap between the ground and HV electrodes. The plane CC downstream of HV electrode is at x/d=6.6d.

Single Phase Flow Generation in a Plane Channel

Figures 6.6 to 6.11 present the contours of the electric field components, net charge density, and electric body-force components.

Figures 6.6 and 6.7 illustrate the x-component of the electric field (E_x) and y-component of the electric field (E_y), respectively. The electric field distribution in Fig. 6.6 also shows features originating from the geometrical arrangement of electrodes and the boundary conditions of Fig. 6.2. The values of E_x on the surface of the HV electrode adjacent to the ground electrode (IJ) are higher than that on the opposite side of the HV electrode (LK). This feature and the difference in direction of E_x between the

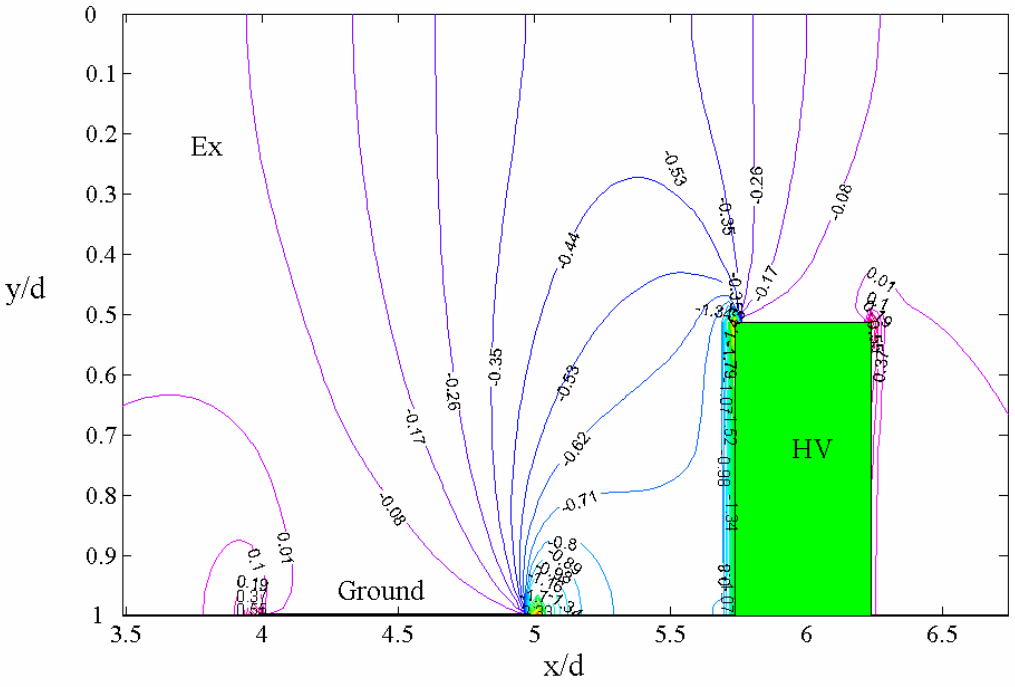

Figure 6.6 Contours of streamwise electric field (Single phase)

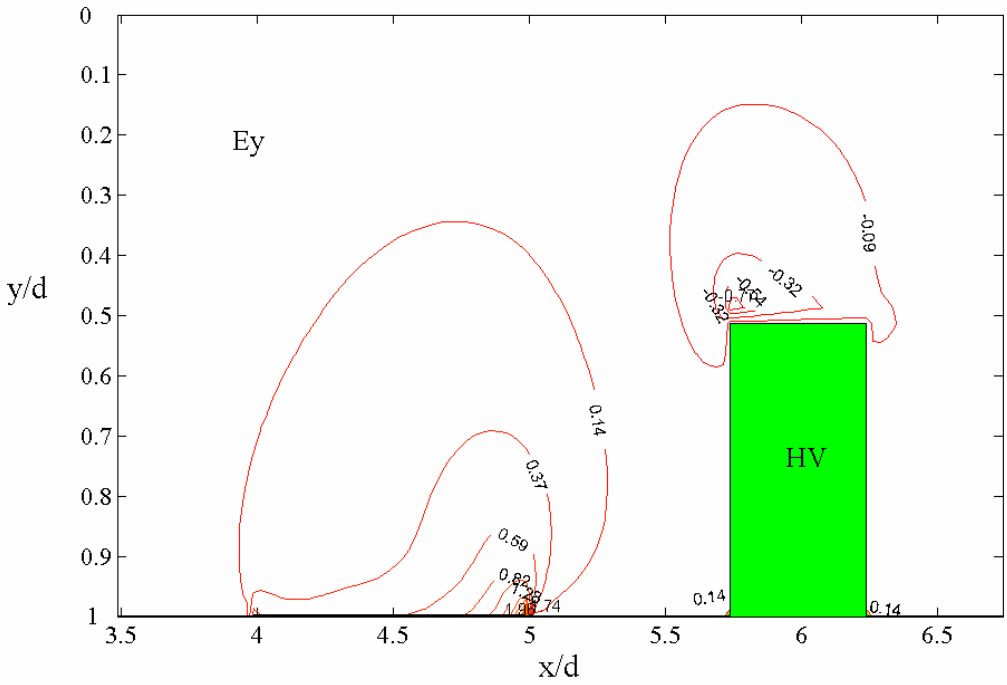

Figure 6.7 Contours of normal electric field (Single phase)

two opposite surfaces of the HV electrode play an important role in determining the downstream direction of the net streamwise force $\int\!\!\int M(p-n)E_x\,dV$ on the control volume. Because of its proximity to the HV electrode, the edge of the ground electrode (N) has larger absolute values of E_x than the one on the opposite edge (M). The inter-electrode region is characterized by moderately high absolute values for both E_x and E_y (see Figs. 6.6 and 6.7), and hence a high electric field magnitude ($|\vec{E}|$). This will cause the field-enhanced dissociation effect [47] to increase the yield of the opposite charges in the heterocharge layers close to the electrodes and lead to higher charge density levels (both positive and negative) in the inter-electrode region.

The net charge density $(p-n)$ distribution near the HV and the ground electrodes are shown in Figs. 6.8 and 6.9, respectively. While net negative charge densities are observed near the surface of the HV electrode, net positive charge densities are observed near the ground electrode. The heterocharge layer is thicker on the surface of the HV electrode facing the ground electrode. Consequently, higher values of negative charge densities are observed in this side of the HV electrode. This characteristic plays an important role in determining the downstream direction of the net streamwise force $\int\!\!\int M(p-n)E_x\,dV$ on the control volume. The positive heterocharge layer on the ground electrode is a significant source of normal body force $M(p-n)E_y$, directed toward the surface.

Figures 6.10 and 6.11 present the contours of the streamwise electric body-force $M(p-n)E_x$ and those of the normal electric body-force density $M(p-n)E_y$, respectively. Large positive values of the streamwise body-force occur near the edge of the HV electrode adjacent to the ground electrode (IJ). However, negligible negative values are observed on the edge away from the ground electrode (LK). The significant difference in the values of the streamwise body-force in the opposite sides of the HV electrode is due to the high magnitude of electric field ($|\vec{E}|$) in the inter-electrode region resulting in a higher value of E_x and due to an increase in dissociation. Therefore higher values of streamwise body-force $M(p-n)E_x$ are expected in this region.

As a consequence of the above streamwise body-force distribution, liquid will be carried from the region upstream of the HV electrode (surface IJ) toward the region

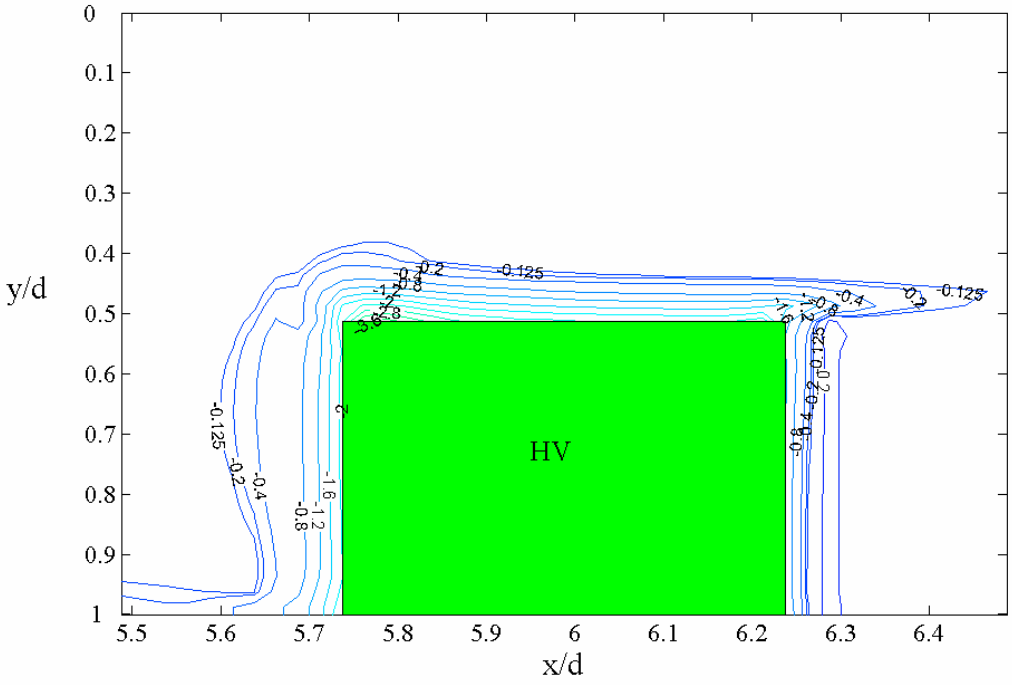

Figure 6.8 Contours of net charge density around the HV electrode (Single phase)

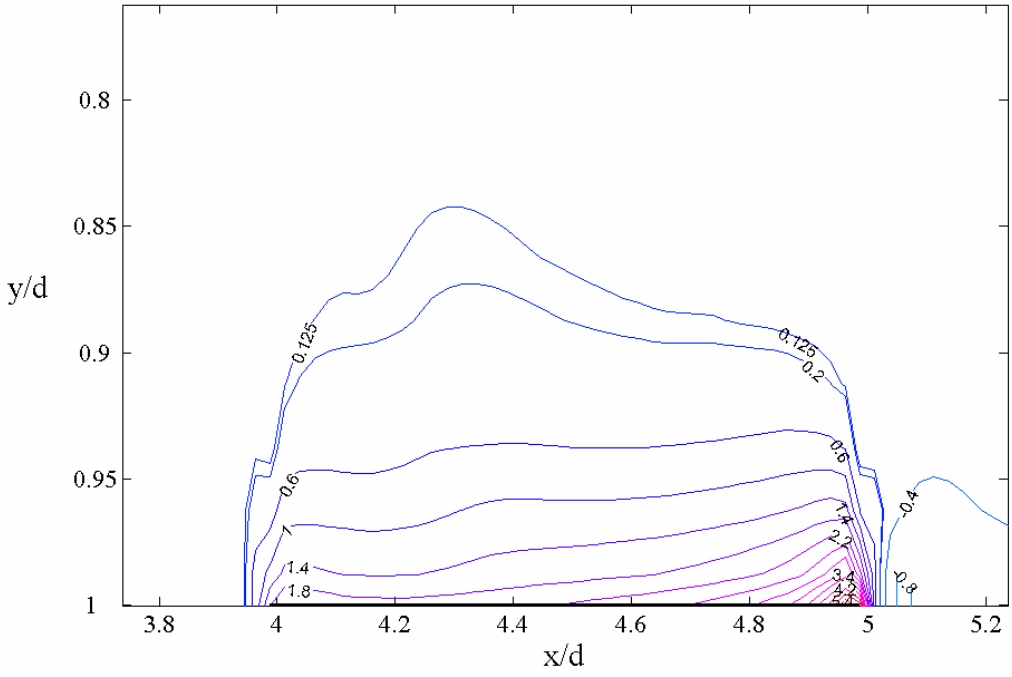

Figure 6.9 Contours of net charge density around the ground electrode (Single phase)

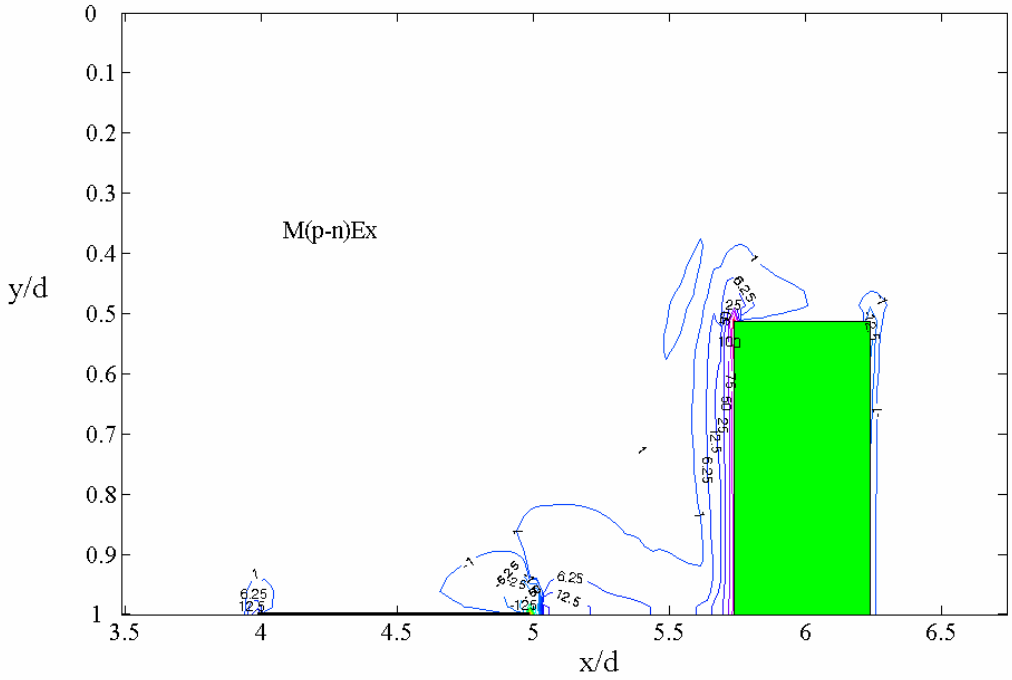

Figure 6.10 Contours of streamwise body-force (Single phase)

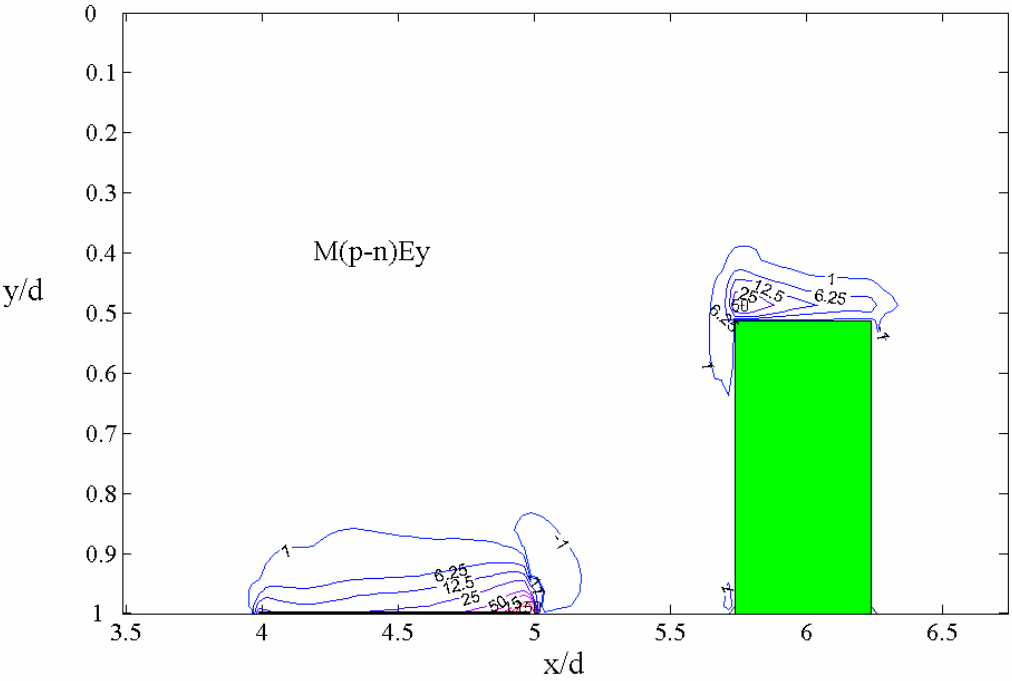

Figure 6.11 Contours of normal body-force (Single phase)

downstream of the HV electrode (surface LK). Locally, the generated flow is parallel to the upper surface of the HV electrode (JK) and directed from J to K. This locally generated motion is responsible for a systematic motion of fluid from the inlet OA to outlet BC as depicted by Fig. 6.12 by the open-ended streamlines starting from inlet and ending at the outlet. At the ground electrode the streamwise body-force $M(p-n)E_x$ is significant only at the side near the HV electrode (N).

One significant vortex is observed near the ground electrode as shown in Fig. 6.12. While the net streamwise body-force $M(p-n)E_x$ at N is negative, the normal component of the body-force $M(p-n)E_y$ is toward the ground electrode leading to anti-clockwise circulation (see Fig. 6.13). This direction of the circulation suggests the existence of a reversed flow (i.e. flow in a negative direction). The reversed flow is

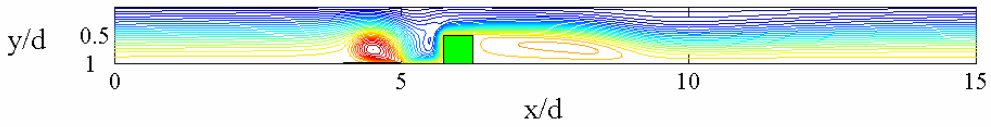

Figure 6.12 Streamlines (Single phase)

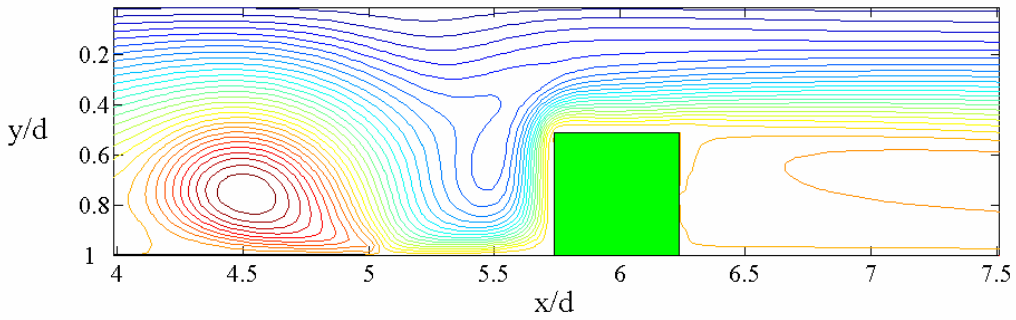

Figure 6.13 Streamlines enlarged near the electrodes (Single phase)

carried by the inertia of the liquid to the surface of the ground electrode. However, at the surface of the ground electrode, the streamwise electric field component has to be zero on an isopotential surface parallel to the streamwise direction, thus zero streamwise body-force along the ground electrode (except at its both ends M and N). Consequently, both the extent and the volume of the reversed flow are limited. Furthermore, instead of a systematic reversed flow, a vortex due to the normal component of the electric body-force $M(p-n)E_y$ was formed.

Figure 6.11 also presents a relatively high positive normal electric body-force $M(p-n)E_y$ in the upper left corner of the HV electrode (J). This positive normal body-

force in addition to the high positive streamwise body-force at the same corner (J) are responsible for pulling the liquid towards the corner, hence towards the positive direction. The flow is following the normal stagnation pattern in the immediate vicinity of corner (J). As it was mentioned previously, the streamwise body-force in the surface of the HV electrode away from the ground electrode (LK) is insignificant; therefore detachment of flow from the surface (LK) is expected. Consequently, the circulation shown in Fig. 6.12 downstream the HV electrode represents the expected wake of any flow past an obstacle.

Figure 6.14 shows the net charge density profiles at the planes described in Fig. 6.2. The profile at x/d = 4.5 has a net positive charge for y/d > 0.80 due to the closeness of the ground electrode. For y/d < 0.8 (outside the heterocharge layers), Fig. 6.14 indicates a zero net charge density. The profile at x/d = 5.4 has a net negative charge density for y/d > 0.80 due to the closeness of the HV electrode. However, for 0.4 < y/d < 0.8, the profile at x/d = 5.4 lies outside the heterocharge layers of the HV electrode, hence a small net positive charge density is observed, followed by a zero net charge density when y/d < 0.4. The profile at x/d = 6.6 lies outside the heterocharge layers downstream the HV electrode; therefore zero net charge is observed throughout the bulk of the fluid except close to the upper corner of the HV electrode (K) where a slightly net negative charge density exists. This is merely due the extension of the HV heterocharge layers in the vicinity of HV electrode, specifically around (K) as shown in Fig. 6.8.

Figure 6.15 shows the profiles of the body-force component in the x-direction $M(p-n)E_x$. As expected for a profile lying in the inter-electrode gap close to

the HV electrode, the profile at x/d = 5.4 has a positive streamwise body-force for y/d < 0.8. This plays an important role in the generation of the flow patterns illustrated in Fig. 6.12. The streamwise forces on the other planes x/d = 4.5 and x/d = 6.6 are not of significant magnitude. The body force at the centerline (y/d = 0) for all profiles presented in Fig. 6.15 approaches zero as the values of the positive and negative charge densities approach unity in the equilibrium region outside the heterocharge layers.

Figures 6.16 and 6.17 show the profiles for primary (U) and secondary (V) velocities, respectively. The periodic boundary conditions imposed in this study sets the inlet (IN) and outlet (OUT) profiles of U and V in Figs. 6.16 and 6.17 into values that are identical, but not specified a priori. The profiles presented in Fig. 6.16 for U correspond to the flow structures shown in the streamlines (Figs. 6.12 and 6.13). For example, in profile x/d = 4.5 (in the middle of the ground electrode) the U velocity is negative in the region 0.75 <y/d < 1.0 near the ground electrode and positive in the region 0 <y/d < 0.75. This corresponds to the counter-clockwise circulation near the ground electrode in Figs. 6.12 and 6.13. In the inter-electrode axial gap, x/d = 5.4, the U velocity profile presents a positive values throughout the bulk of the liquid except in the region 0.5 <y/d < 0.6 where a small negative values are observed. These negative values correspond to the weak circulation indicated in Figs. 6.12 and 6.13. On the other hand, the maximum positive values are observed close to the wall where the interaction between the two electrodes is expected to be the maximum. Finally, the profile in x/d = 6.6 shows a reversed flow in the region 0.6 <y/d < 1.0 due to the existence of the separation region downstream the HV electrode. As shown in Fig. 6.17 the normal

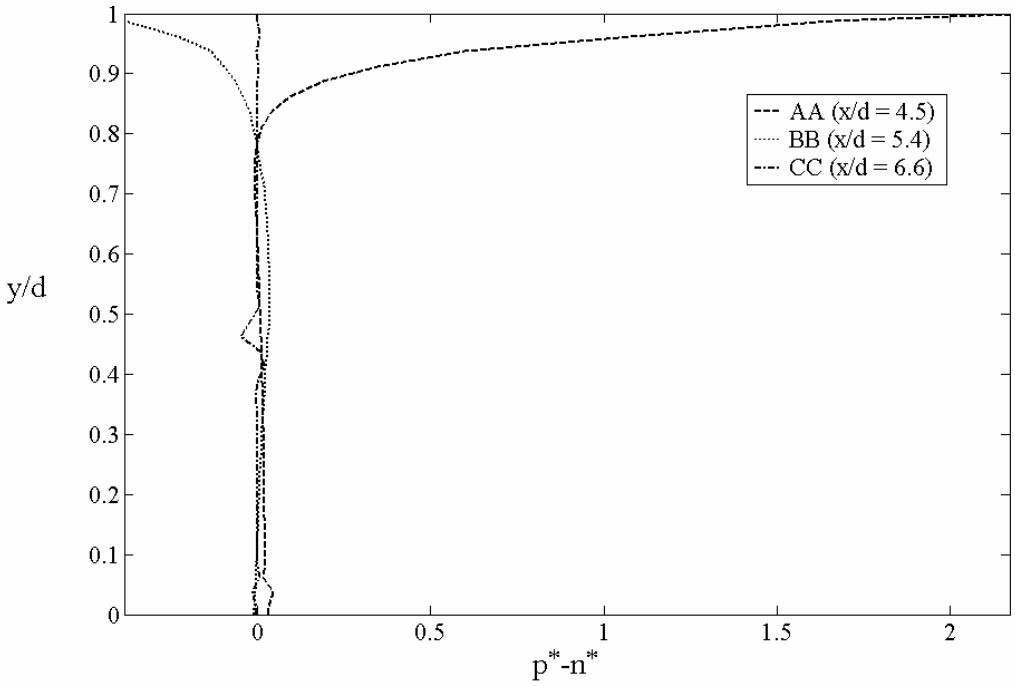

Figure 6.14 Net charge density profiles (Single phase)

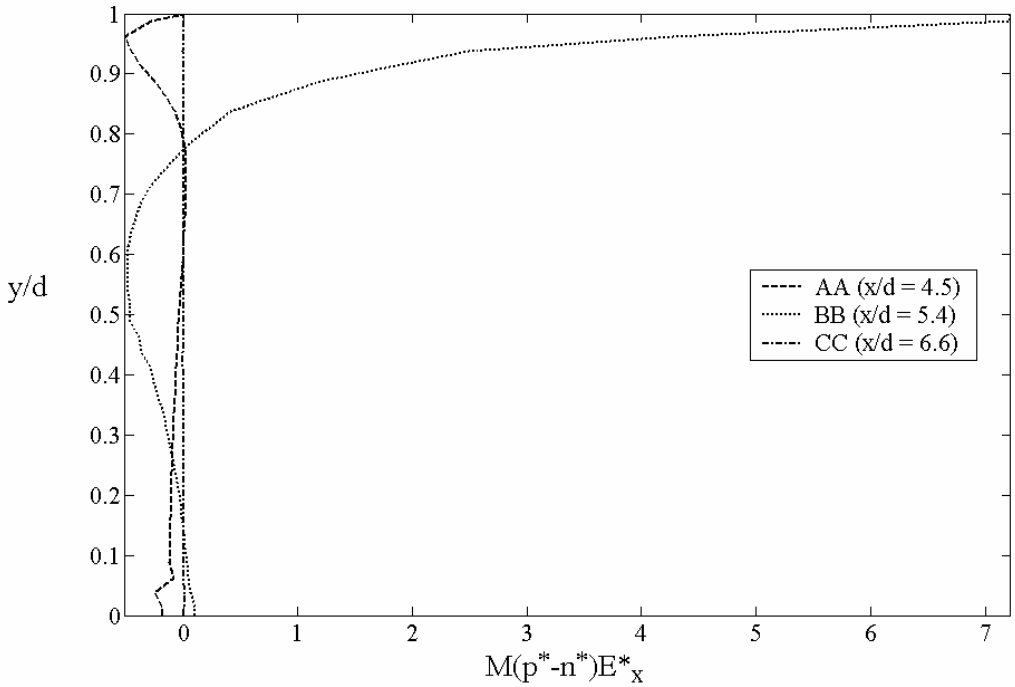

Figure 6.15 Streamwise body-force profiles (Single phase)

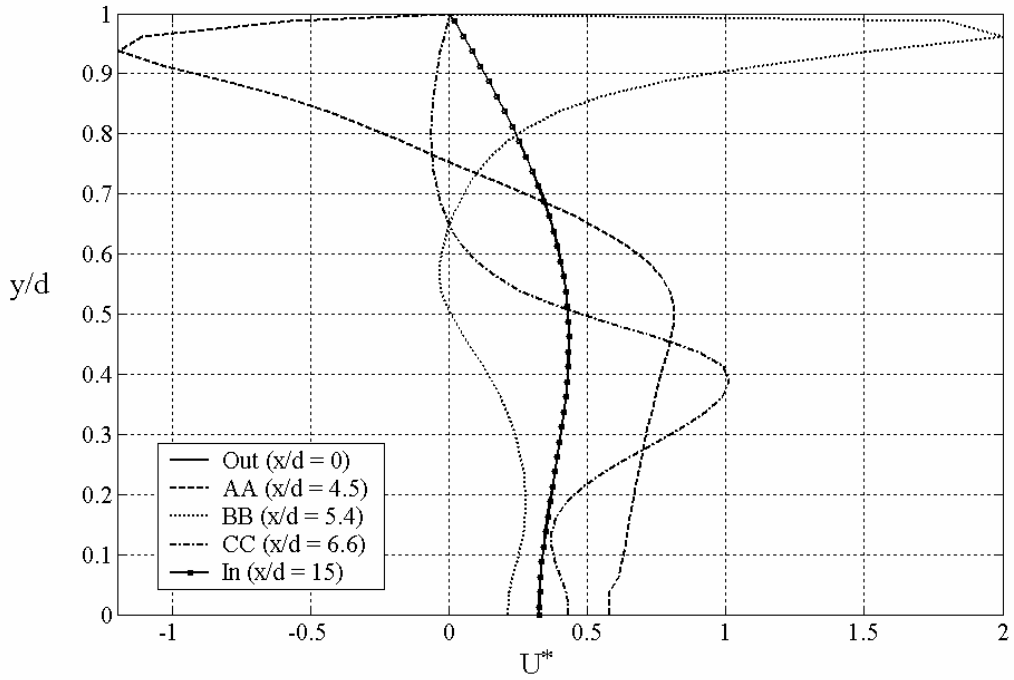

Figure 6.16 Streamwise velocity profiles (Single phase)

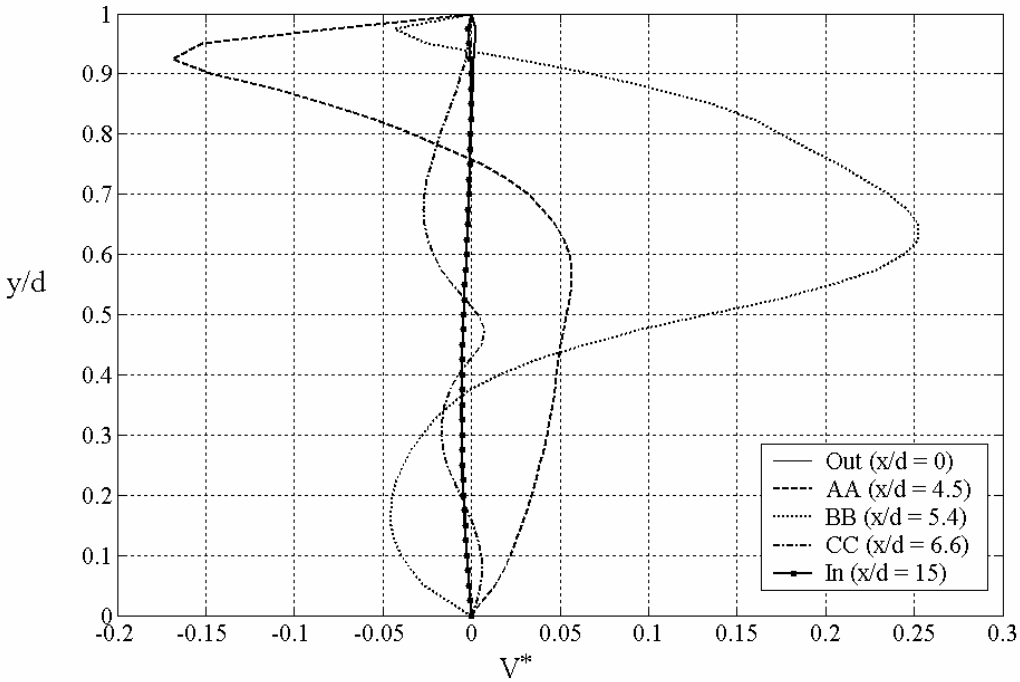

Figure 6.17 Normal velocity profiles (Single phase)

velocity (V) profile is significant on the ground electrode (AA) and in the inter-electrode gap (BB), but not quite significant in the plane located downstream of the HV electrode (CC) indicating the low strength of the wake-like circulation in Fig. 6.13. The inlet and the outlet profiles indicate a secondary velocity close to zero. This implies that the distance upstream and downstream the electrodes are large enough to allow for flow development. The flow development and the imposed periodic boundary condition allow the net flow generation to be interpreted as solely due to the conduction mechanism.

The numerical results presented in this section confirm the net flow generation in positive x-direction with conduction mechanism in a channel configuration. For the electrode geometry shown in Fig. 6.2, the applied voltage is 2kV and the inter-electrode axial gap is taken as 1.875 cm. For this particular configuration and under the aforementioned operating conditions the dimensionless average velocity generated at the channel exist is 0.4. In order to dimensionalize the velocity at the channel exit a nominal electric field of $1.0 \mathrm{X} 10^{5}$ V/m based on the aforementioned applied voltage and inter-electrode gap is used. This results in dimensional velocity of 2.1 mm/s at the exit of the channel, which corresponds to anywhere along the channel.

Single Phase Flow Generation in a Plane Channel with Minimum Drag Electrodes

Numerical results are obtained for the minimum drag electrode configuration as illustrated in Fig. 6.3. The results indicate that there is a net flow generated with its direction from the HV electrode toward the ground electrode (i.e. negative x-direction) due to the associated lengths selected for this study.

Figures 6.18 and 6.19 illustrate the x-component of the electric field (E_x) and y-component of the electric field (E_y), respectively. The electric field distribution in Fig. 6.18 also shows features originating from the geometrical arrangement of electrodes and the boundary conditions of Fig. 6.3. The values of E_x on the surface of the HV electrode adjacent to the ground electrode (IJ) are higher than those on the opposite side of the HV electrode (LK). This difference in magnitude of E_x between the two opposite surfaces of the HV electrode play an important role in determining the downstream directon of the net streamwise force $\iint M(p-n)E_x \, dV$ on the control volume. Because of its proximity to the HV electrode, the edge of the ground electrode (N) has larger absolute values of E_x than the one on the opposite edge (M). The inter-electrode region is characterized by moderately high absolute values for both E_x and E_y (see Figs. 6.18 and 6.19), and hence a high electric field magnitude ($|\vec{E}|$). This will cause the field-enhanced dissociation effect [47] to increase the yield of the opposite charges in the heterocharge layers close to the electrodes and lead to higher charge density levels (both positive and negative) in the inter-electrode region.

The net charge density $(p-n)$ distribution near the HV and the ground electrodes are shown in Figs. 6.20 and 6.21, respectively. While net negative charge densities are observed near the surface of the HV electrode, net positive charge densities are observed near the ground electrode. The heterocharge layer is thicker on the surface of the HV electrode facing the ground electrode. Consequently, higher values of negative charge

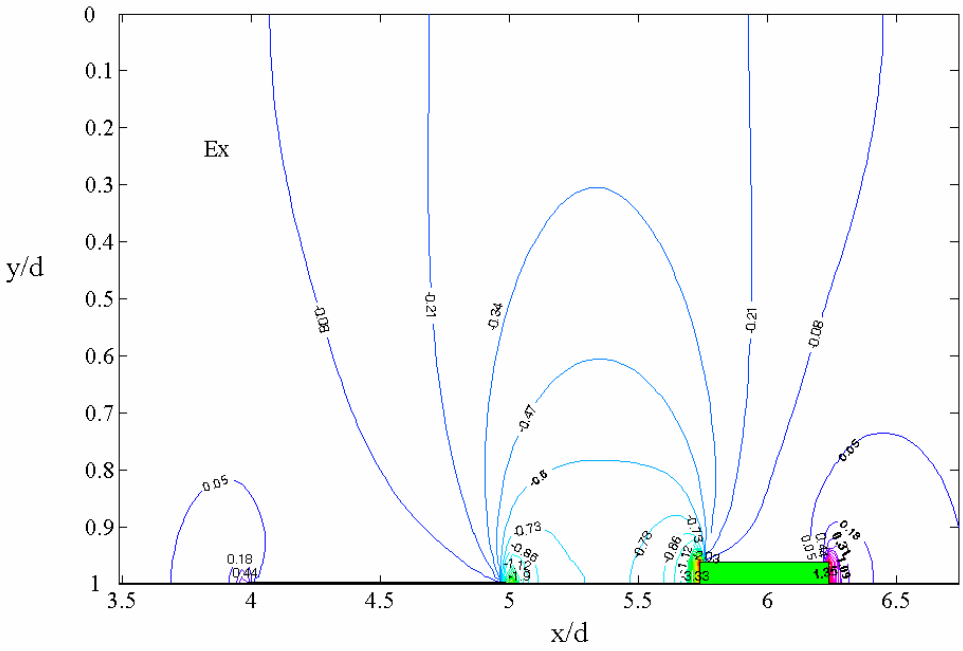

Figure 6.18 Contours of streamwise electric field (Single phase with minimum drag electrodes)

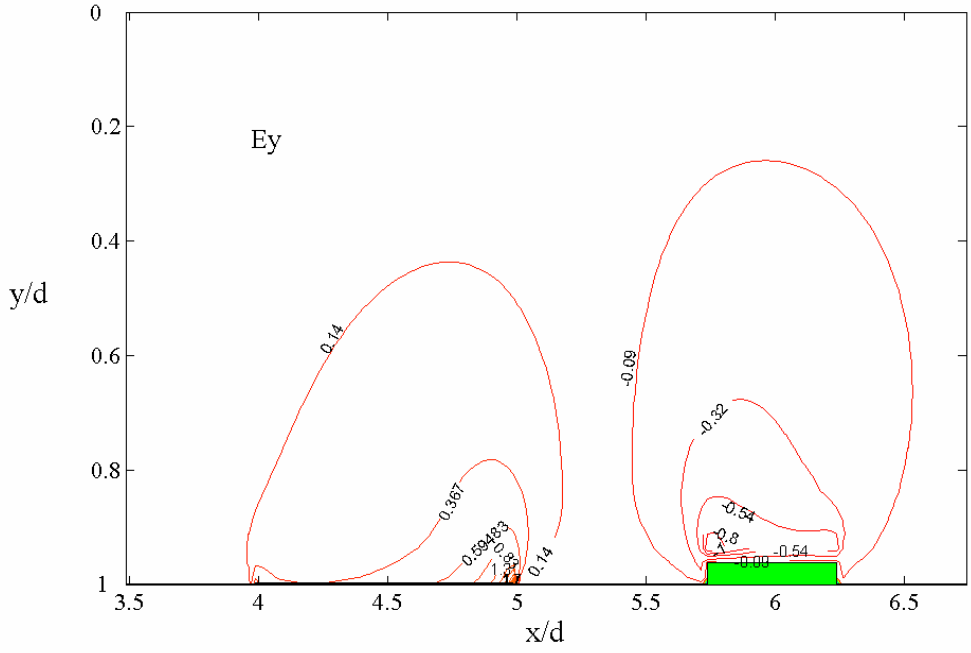

Figure 6.19 Contours of normal electric field (Single phase with minimum drag electrodes)

densities are observed in this side of the HV electrode. This characteristic plays an important role in determining the downstream direction of the net streamwise force $\int\int M(p-n)E_x \, dV$ on the control volume. The positive heterocharge layer on the ground electrode is a significant source of normal body force $M(p-n)E_y$, directed toward the surface. It is noteworthy to mention that the heterocharge layers thickness of both the HV and the ground electrodes is of the same order of magnitude. This feature is a result of the electrode configuration considered (see Fig. 6.3) and it is believed to be the source of the net body-force responsible for generating a net flow in the negative x-direction.

Figures 6.22 and 6.23 present the contours of the streamwise electric body-force density, $M(p-n)E_x$, and the normal electric body-force density, $M(p-n)E_y$, respectively. Large positive values of the streamwise body-force occur near the edge of the HV electrode adjacent to the ground electrode (IJ). Furthermore, small positive values are observed on the edge away from the ground electrode (LK). The significant difference in the values of the streamwise body-force in the opposite sides of the HV electrode is due to the high magnitude of electric field, $|\vec{E}|$, in the inter-electrode region resulting in a higher value of E_x and is due also to an increase in dissociation rate. Therefore higher values of streamwise body-force $M(p-n)E_x$ are expected in this region. At the ground electrode large negative values of the streamwise body-force $M(p-n)E_x$ occur at the side near the HV electrode (N). However, negligible positive values are observed on the edge away from the HV electrode (M). It is evident that the

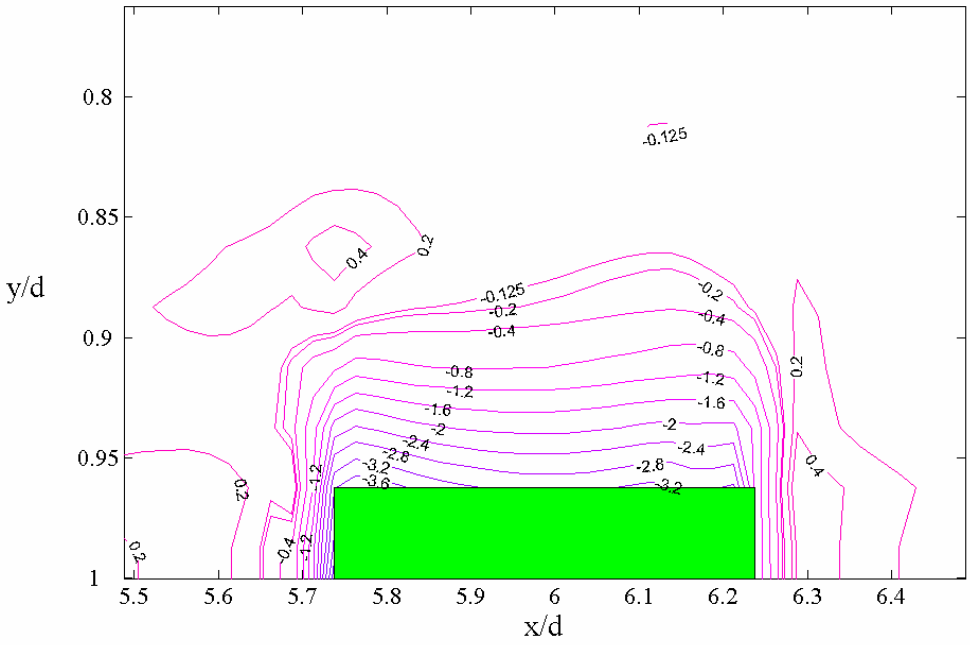

Figure 6.20 Contours of net charge density around the HV electrode (Single phase with minimum drag electrodes)

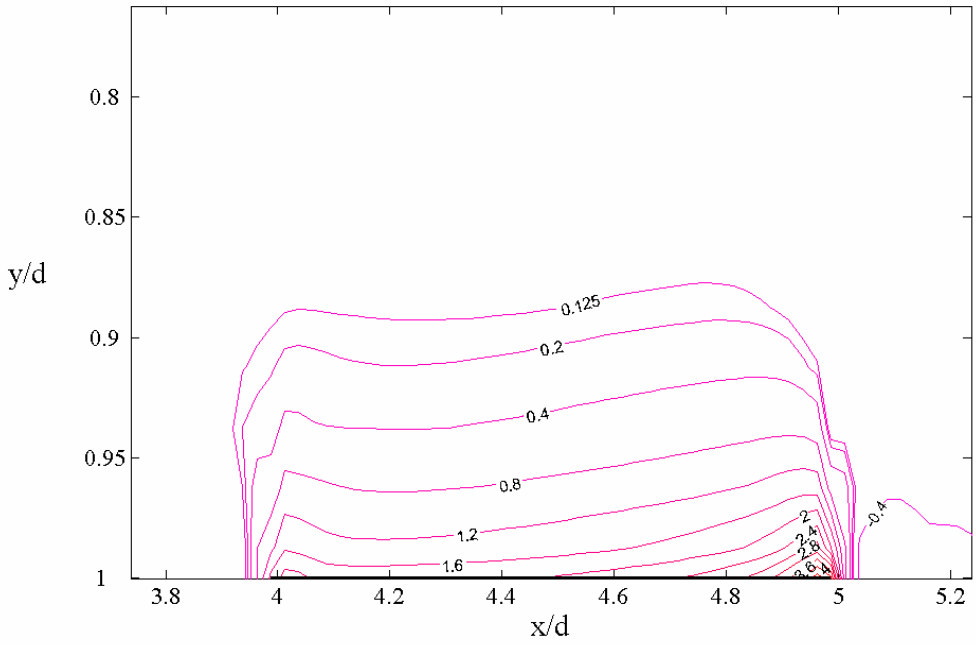

Figure 6.21 Contours of net charge density around the ground electrode (Single phase with minimum drag electrodes)

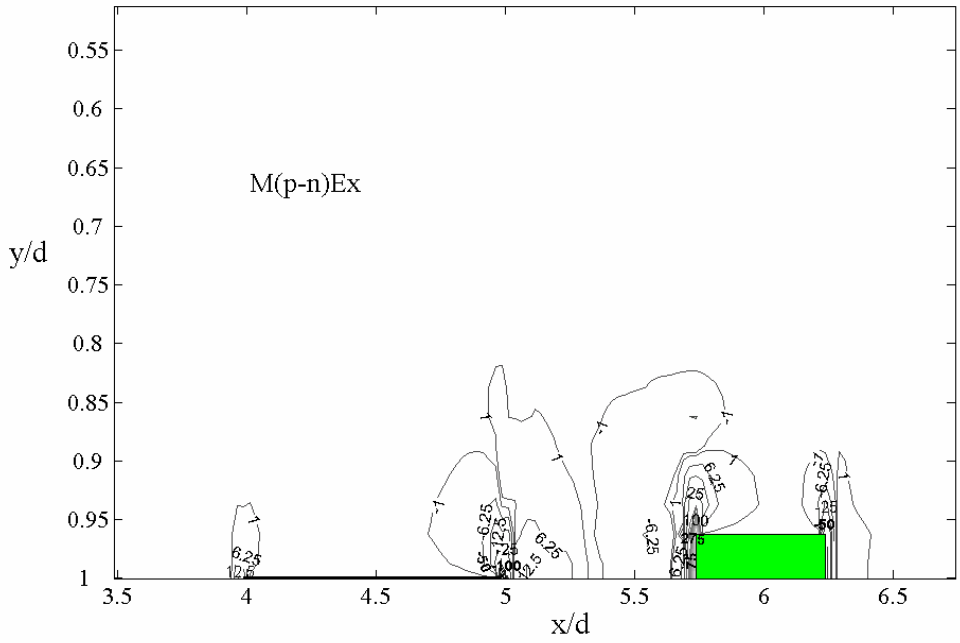

Figure 6.22 Contours of streamwise body-force (Single phase with minimum drag electrodes)

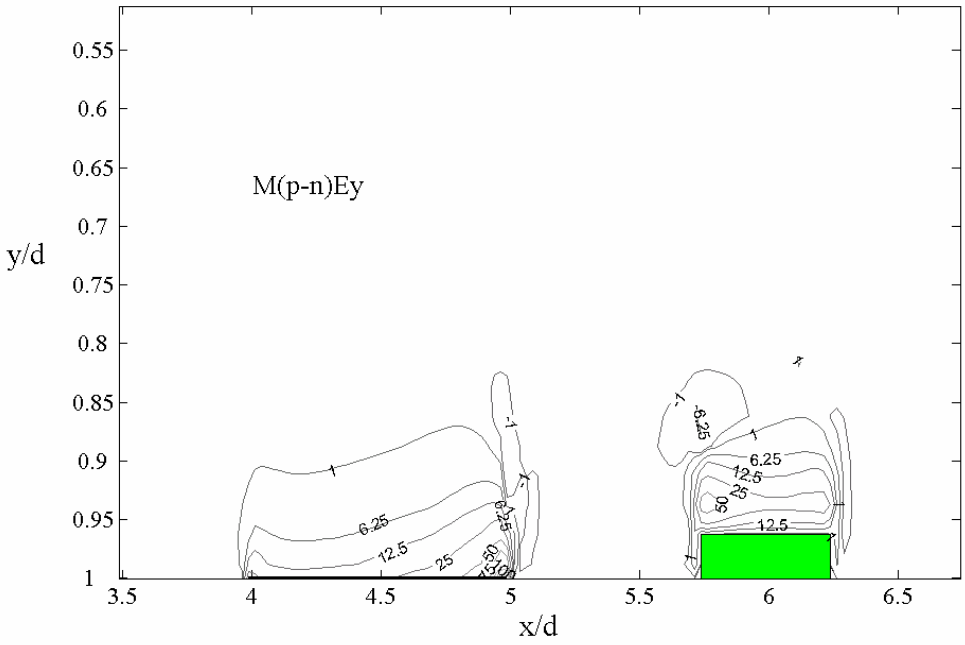

Figure 6.23 Contours of normal body-force (Single phase with minimum drag electrodes)

geometry of the electrode considered in this section (Fig. 6.3) affected the body-force distribution in a way different than the electrode geometry considered in the previous section (Fig. 6.2). This effect can be noticed in the sign of the streamwise body-force in the side of the HV electrode away from the ground electrode (LK).

As a consequence of the above streamwise body-force distribution, a net body force is generated in the inter-electrode region causing the liquid to be carried from the region downstream (with respect to positive x-direction illustrated in Fig. 6.3) of the HV electrode (surface LK) toward the region upstream of the HV electrode (surface IJ). This would be responsible for a systematic motion of fluid from the inlet BC to outlet OA as depicted in Fig. 6.24 by the open-ended streamlines starting from inlet and ending at the outlet.

It is important to emphasize that the generated net flow is in the negative x-direction. Therefore, when the term reversed flow is used in the following discussion it indicates a flow in the positive x-direction (i.e. opposite to the direction of the generated flow). In addition, the terms upstream and downstream are used with respect to the generated flow direction (i.e. negative x-direction).

Two significant vortices are observed near the HV and the ground electrodes as shown in Fig. 6.25. The streamwise body-force $M(p-n)E_x$ on the edge (J) of the HV electrode is positive and the normal component of the body-force $M(p-n)E_y$ is toward the HV electrode leading to clockwise circulation (see Fig. 6.25). This direction of the circulation suggests the existence of a reversed flow (i.e. flow in a positive direction). The reversed flow is carried by the inertia of the liquid to the surface of the HV

electrode. However, at the surface of the HV electrode, the streamwise electric field component has to be zero on an isopotential surface parallel to the streamwise direction, thus zero streamwise body-force along the HV electrode (except at its both ends IJ and LK). Consequently, both the extent and the volume of the reversed flow are limited. Furthermore, instead of a systematic reversed flow, a vortex due to the normal component of the electric body-force $M(p-n)E_y$ is formed.

On the other hand, the net streamwise body-force, $M(p-n)E_x$, at N on the ground electrode is negative, whereas the normal component of the body-force, $M(p-n)E_y$, is toward the ground electrode leading to anti-clockwise circulation (see Fig. 6.25).

Figure 6.25 indicates that the flow is not following the normal stagnation pattern in the immediate vicinity of corner (L) at the upstream surface of the HV electrode. This is due to the positive streamwise body-force $M(p-n)E_x$ acting on the side of the HV away from the ground electrode (LK), which tends to repel the flow away from the electrode, thus causing a wake region. In addition, for any flow past an obstacle detachment of the flow downstream from the surface is expected. While Fig. 6.25 does support such expectation, reattachment of the flow downstream the HV electrode happens soon after a small wake region. This is because the high positive streamwise body-force $M(p-n)E_x$ acting on the surface (IJ) of the HV electrode is responsible for pulling the liquid towards the surface (IJ), hence diminishing the propagation of the wake region. Furthermore, the anti-clockwise circulation near the ground electrode and the high negative values of the streamwise body-force $M(p-n)E_x$ at the edge of the

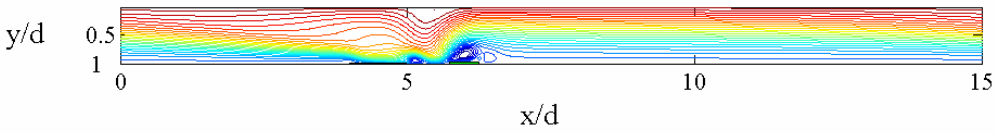

Figure 6.24 Streamlines (Single phase with minimum drag electrodes)

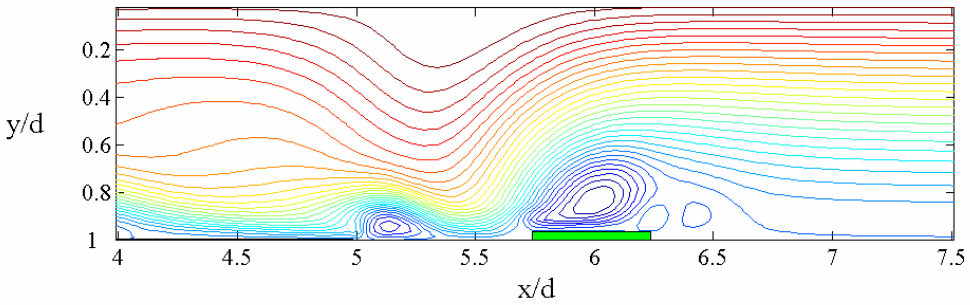

Figure 6.25 Streamlines enlarged near the electrodes (Single phase with minimum drag electrodes)

ground electrode facing the HV electrode (N) cause the flow to accelerate in the inter-electrode region. Consequently, chances for detachment to occur are eliminated.

Figure 6.26 shows the net charge density profiles at the planes described in Fig. 6.3. The profile at x/d = 4.5 has a net positive charge for y/d > 0.80 due to the closeness of the ground electrode. For y/d < 0.8 (outside the heterocharge layers), Fig. 6.26 indicates a zero net charge density. The profile at x/d = 5.4 has a very small net positive charge density for y/d > 0.75 as it falls in the inter-electrode region outside the concentrated heterocharge layers of both electrodes. However, for y/d < 0.75, the profile at x/d = 5.4 lies outside the heterocharge layers of the HV electrode, hence zero net charge density is observed. The profile at x/d = 6.6 lies outside the heterocharge layers downstream the HV electrode; therefore zero net charge is observed throughout the bulk of the fluid.

Figure 6.27 shows the profiles of the body-force component in the x-direction $M(p-n)E_x$. As expected for a profile lying in the inter-electrode gap close to the HV electrode, the profile at x/d = 5.4 has a negative streamwise body-force for y/d >0.7. The highest value of streamwise body-force is observed at y/d = 0.96 which is at the same level of the upper surface of the HV electrode, where the interaction between the two electrodes are expected to be maximum. This negative streamwise body-force plays an important role in the generation of the flow patterns illustrated in Fig. 6.25. The streamwise forces on the other planes x/d = 4.5 and x/d = 6.6 are not of significant magnitude. The body force at the centerline (y/d = 0) for all profiles presented in Fig.

6.27 approaches zero as the values of the positive and negative charge densities approach unity in the equilibrium region outside the heterocharge layers.

Figures 6.28 and 6.29 show the profiles for primary (U) and secondary (V) velocities, respectively. The periodic boundary conditions imposed in this study sets the inlet (IN) and outlet (OUT) profiles of U and V in Figs. 6.28 and 6.29 into values that are identical, but not specified a priori. The profiles presented in Fig. 6.28 for U correspond to the flow structures shown in the streamlines (Figs. 6.24 and 6.25). For example, in profile x/d = 4.5 (in the middle of the ground electrode) the U velocity is negative throughout the bulk of the liquid with its maximum in the region $0.8 < y/d < 1.0$ near the ground electrode. This corresponds to the accelerated flow near the ground electrode in Figs. 6.24 and 6.25. In the inter-electrode axial gap, x/d = 5.4, the U velocity profile presents a negative values throughout the bulk of the liquid; however, as we move away from the wall of the channel the negative U velocity decreases. Moreover, the maximum negative values are observed close to the wall where the interaction between the two electrodes is expected to be the maximum. Finally, the profile in x/d = 6.6 shows a reversed flow in the region very close to the wall due to the existence of the separation region upstream the HV electrode. As shown in Fig. 6.29 the normal velocity (V) profile is significant in the inter-electrode gap (BB), but not quite significant in the planes located on the ground electrode (AA) and upstream of the HV electrode (CC) indicating the low strength of the wake-like circulation in Fig. 6.25. The inlet and the outlet profiles indicate a secondary velocity close to zero. This implies that the distance upstream and downstream the electrodes are large enough to allow for flow

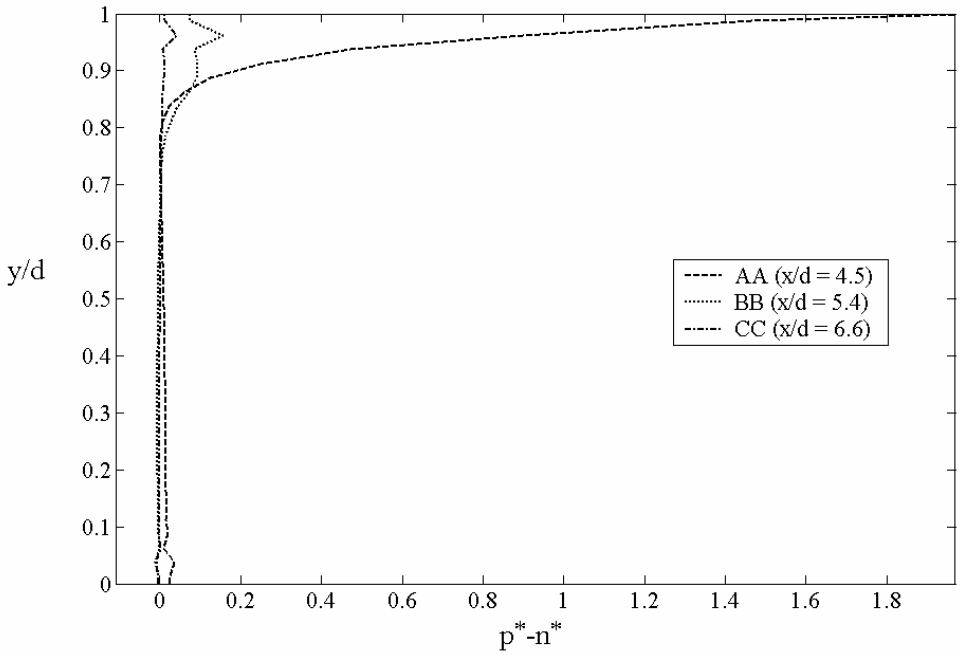

Figure 6.26 Net charge density profiles (Single phase with minimum drag electrodes)

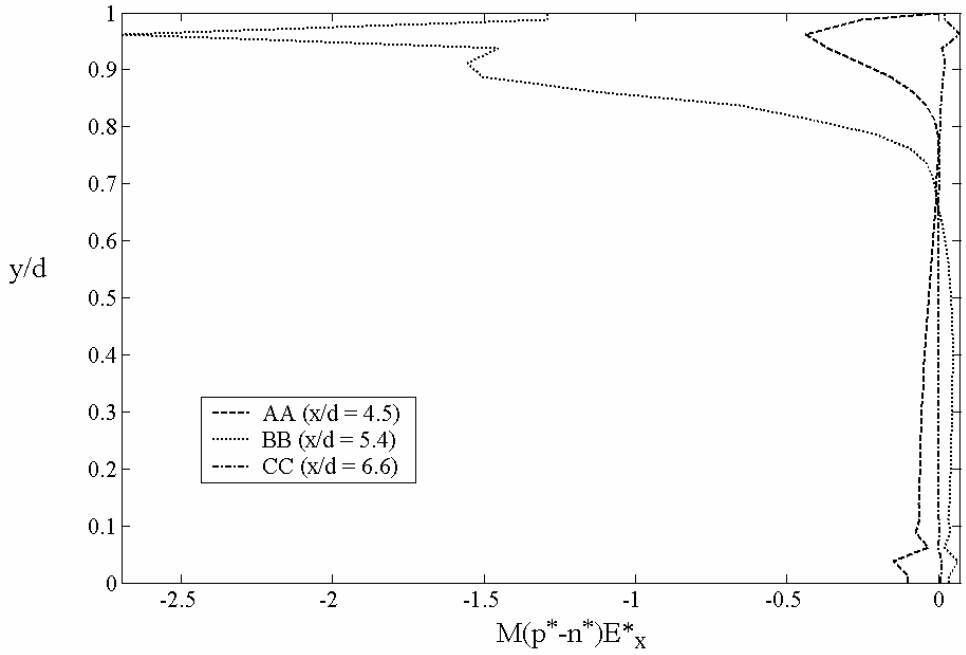

Figure 6.27 Streamwise body-force profiles (Single phase with minimum drag electrodes)

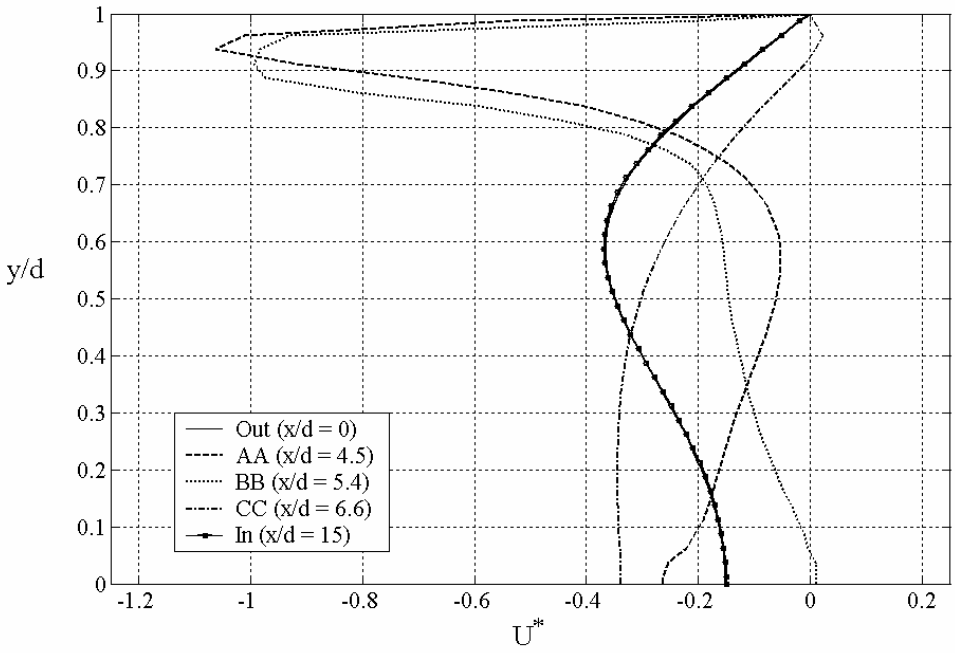

Figure 6.28 Streamwise velocity profiles (Single phase with minimum drag electrodes)

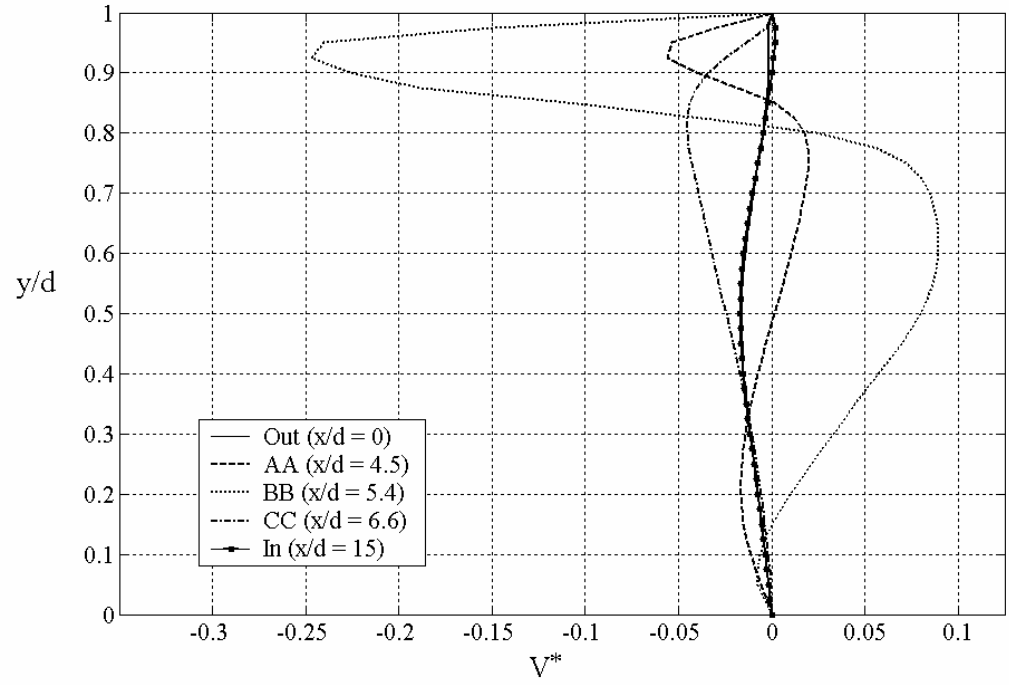

Figure 6.29 Normal velocity profiles (Single phase with minimum drag electrodes)

development. The flow development and the imposed periodic boundary condition allow the net flow generation to be interpreted as solely due to the conduction mechanism.

In summery, the two electrode designs considered in this study resulted in two different flow field as well as net flow in two different directions. The negative net flow generated by the minimum drag electrode design is due to the associated height of the HV electrode selected in this study.

EHD Conduction Pumping of Stratified Liquid/Vapor Medium

Numerical results considering the aforementioned two electrode designs for stratified liquid/vapor medium are obtained. Figures 6.30 to 6.41 represent the numerical results for the electrode design shown in Fig. 6.4. Furthermore, Figs. 6.42 to 6.53 present the numerical results generated for the minimum drag electrode design. All the numerical results generated exhibits similar behaviors to the results presented in the previous section for single phase. This is can be explained in the light of the imposed boundary conditions at the interface (for two-phase flow) and at the centerline (single phase flow), respectively. At the interface, away from the electrodes and the heterocharge layers, the charges are in equilibrium and positive and negative charges are equal. Therefore, a boundary condition for positive and negative charges equal to unity was imposed at the interface. For the single phase case the normal derivative of the positive and negative charges at the centerline of the channel is set to zero due to the geometrical symmetry. However, due to the liquid film thickness considered in this study the symmetry boundary condition for the positive and the negative charge density

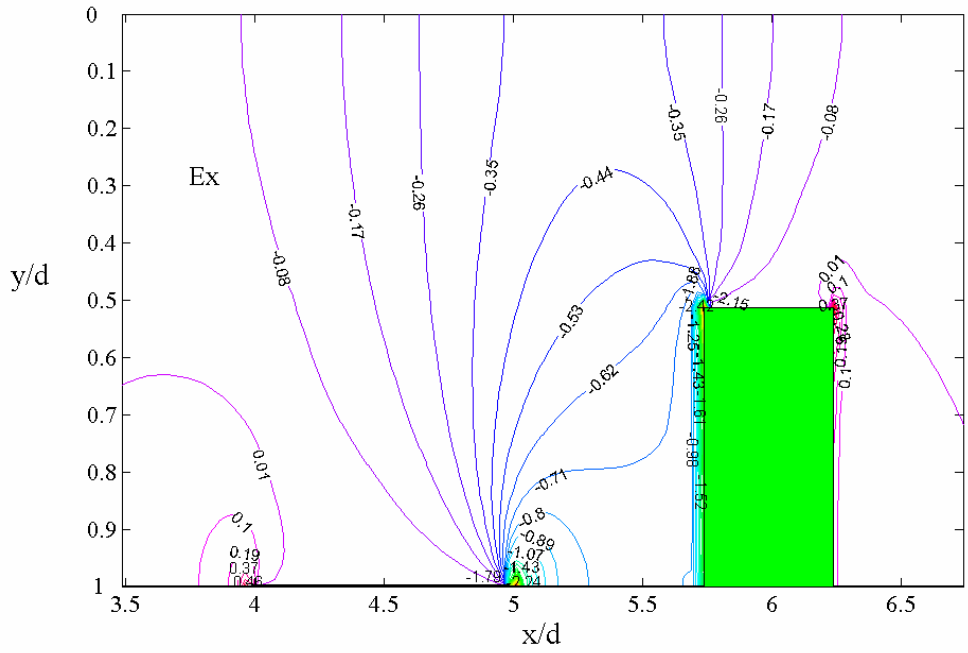

Figure 6.30 Contours of streamwise electric field (Stratified liquid/vapor medium)

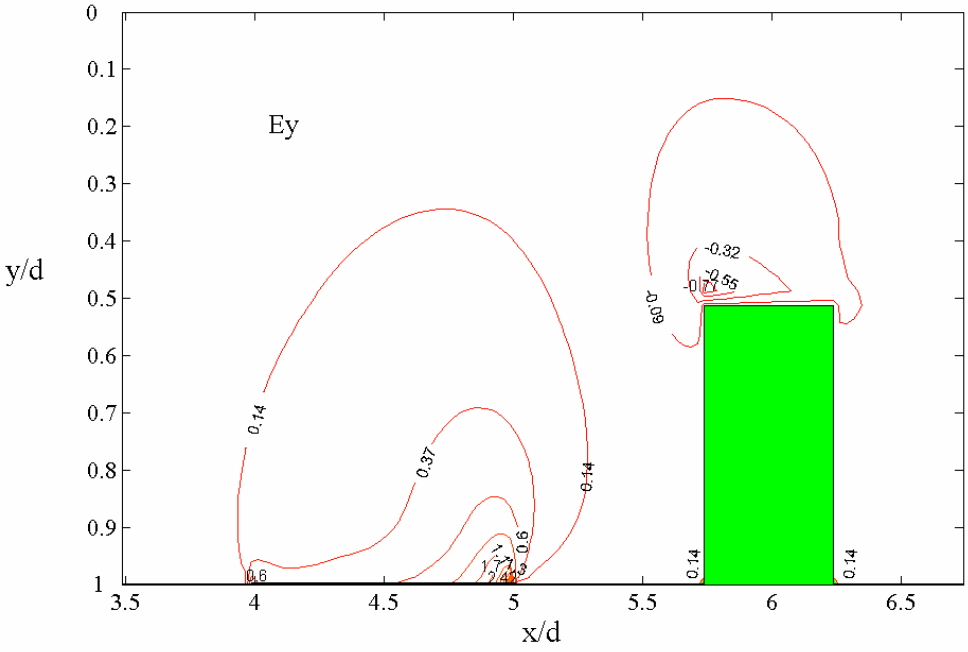

Figure 6.31 Contours of normal electric field (Stratified liquid/vapor medium)

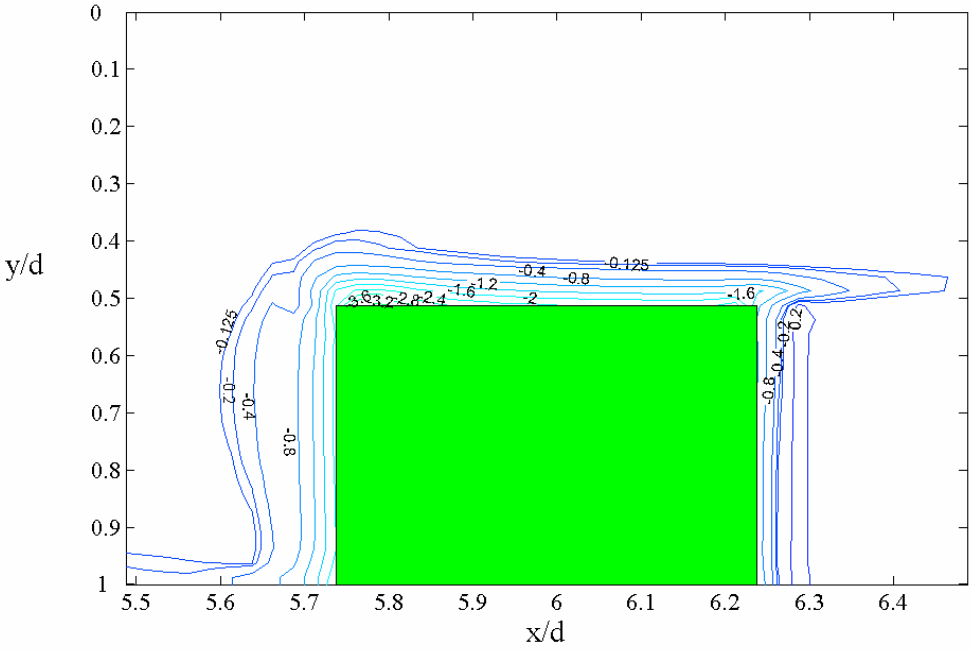

Figure 6.32 Contours of net charge density around the HV electrode (Stratified liquid/vapor medium)

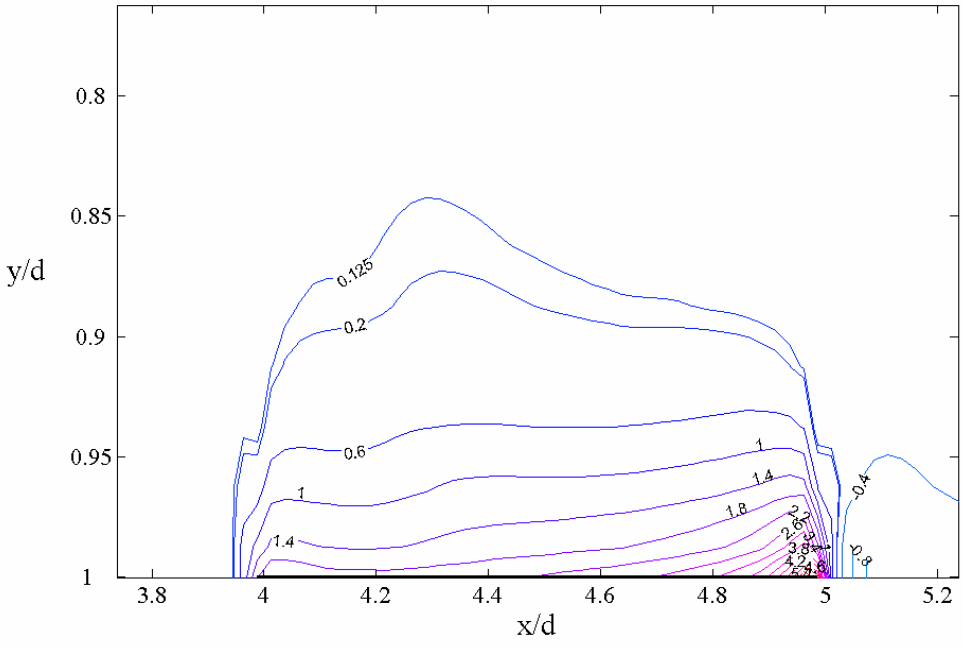

Figure 6.33 Contours of net charge density around the ground electrode (Stratified liquid/vapor medium)

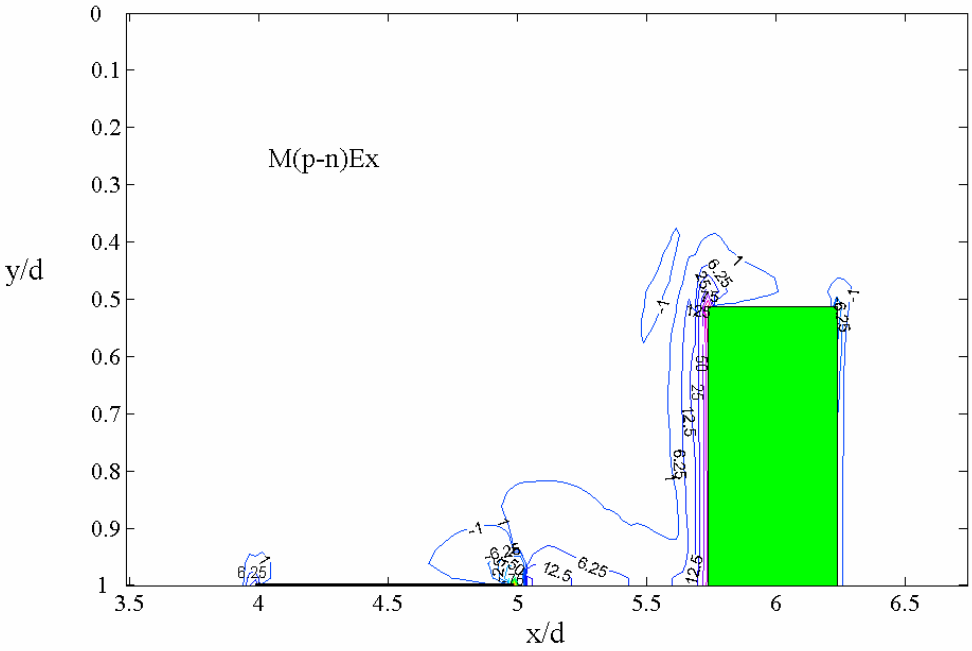

Figure 6.34 Contours of streamwise body-force (Stratified liquid/vapor medium)

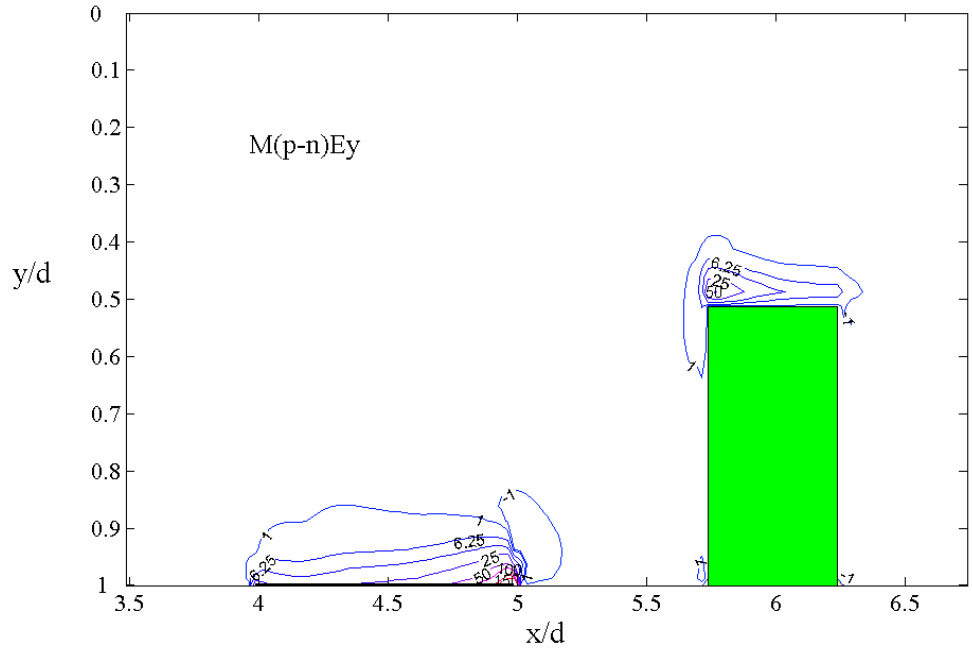

Figure 6.35 Contours of normal body-force (Stratified liquid/vapor medium)

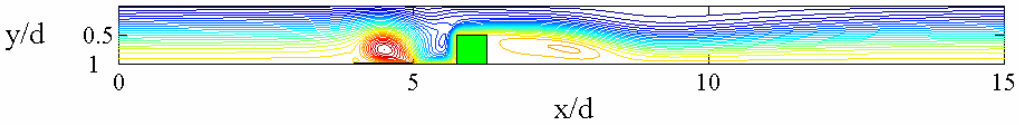

Figure 6.36 Streamlines (Stratified liquid/vapor medium)

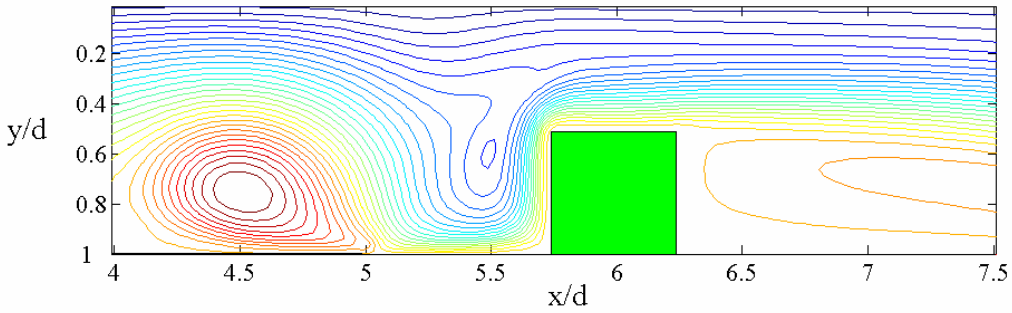

Figure 6.37 Streamlines enlarged near the electrodes (Stratified liquid/vapor medium)

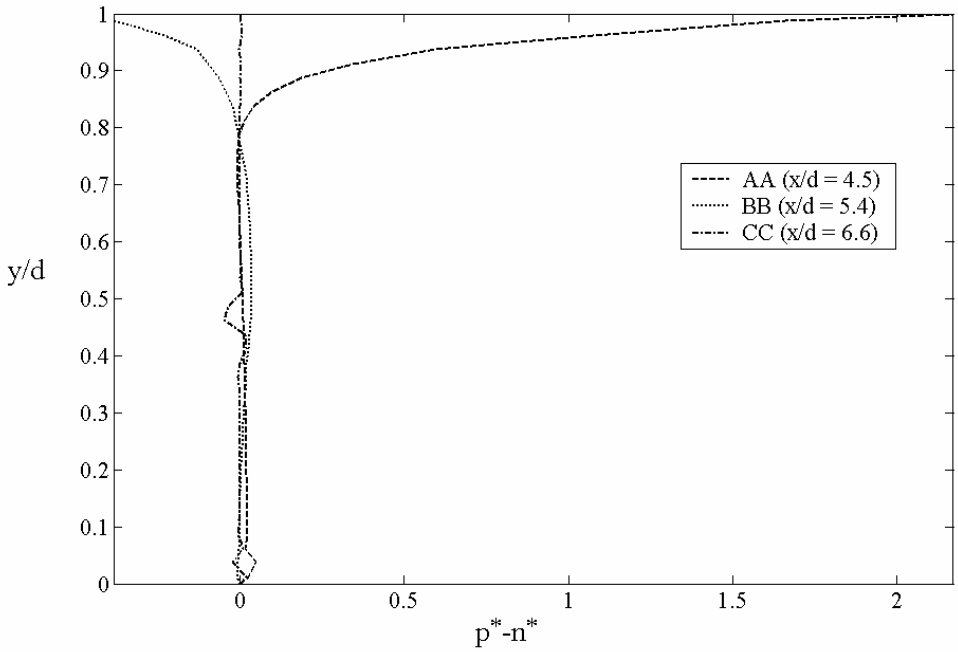

Figure 6.38 Net charge density profiles (Stratified liquid/vapor medium)

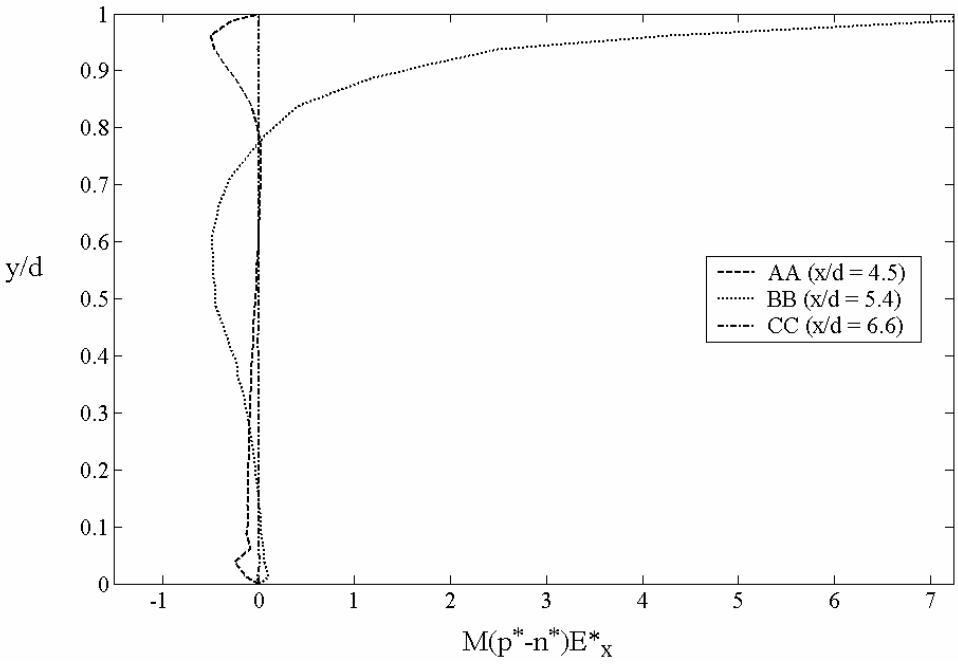

Figure 6.39 Streamwise body-force profiles (Stratified liquid/vapor medium)

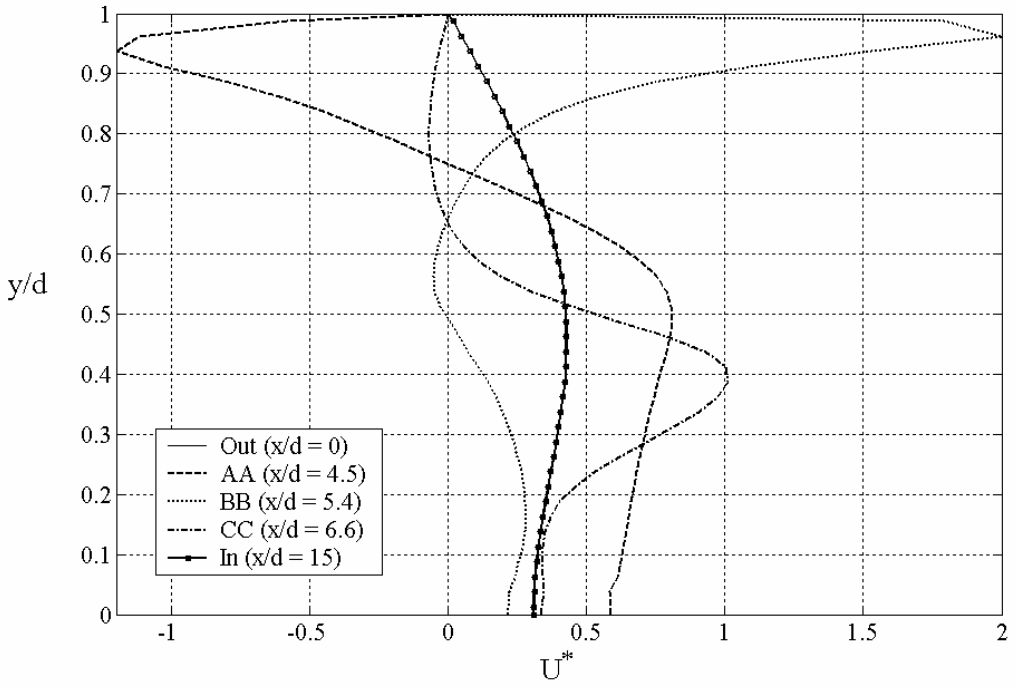

Figure 6.40 Streamwise velocity profiles (Stratified liquid/vapor medium)

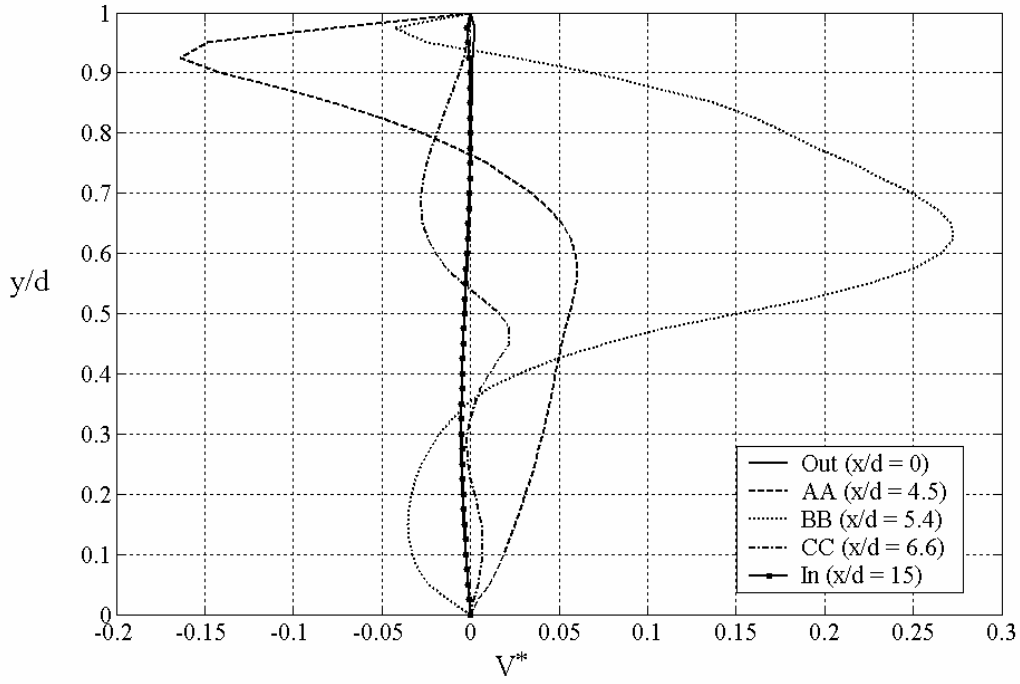

Figure 6.41 Normal velocity profiles (Stratified liquid/vapor medium)

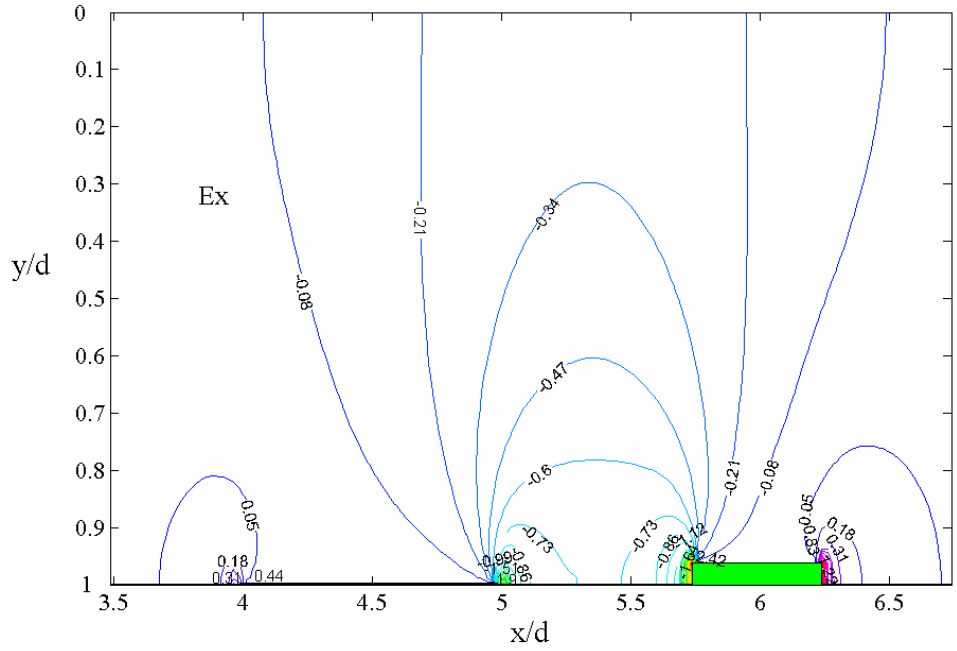

Figure 6.42 Contours of streamwise electric field (Stratified liquid/vapor with minimum drag electrodes)

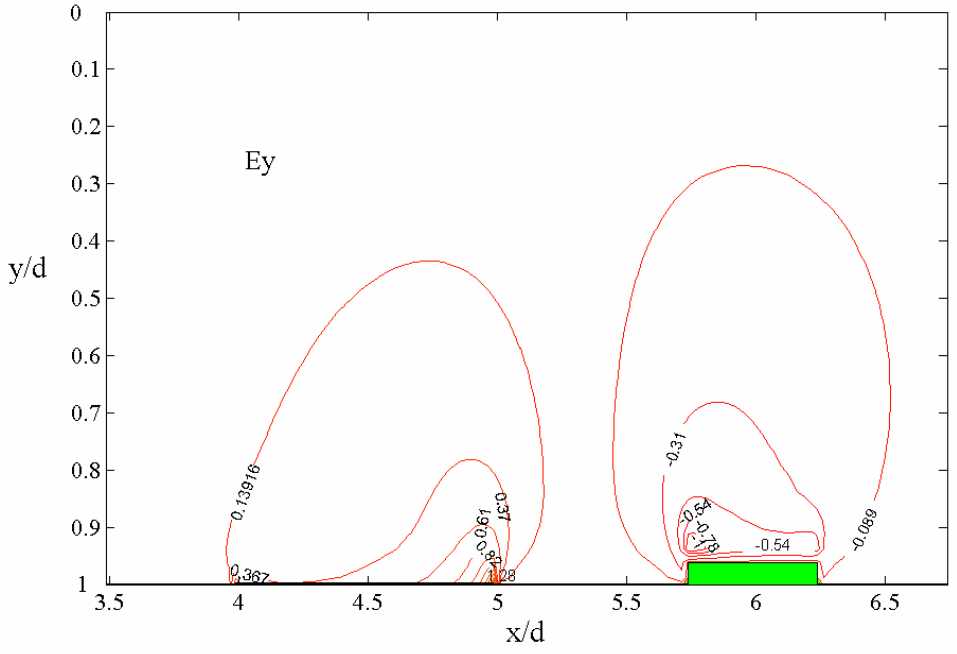

Figure 6.43 Contours of nomal electric field (Stratified liquid/vapor with minimum drag electrodes)

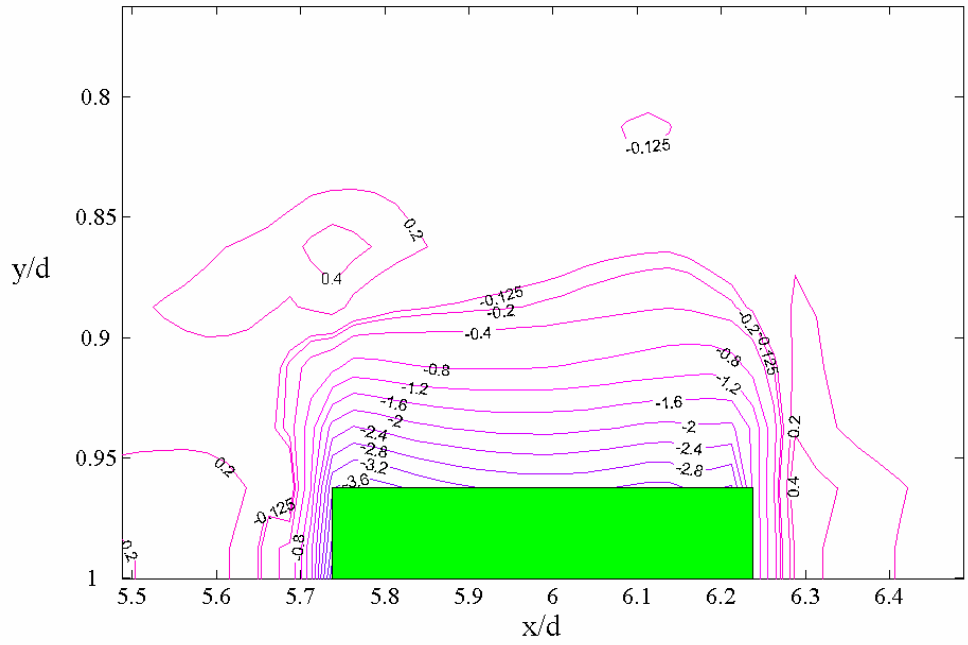

Figure 6.44 Contours net charge density around the HV electrode (Stratified liquid/vapor with minimum drag electrodes)

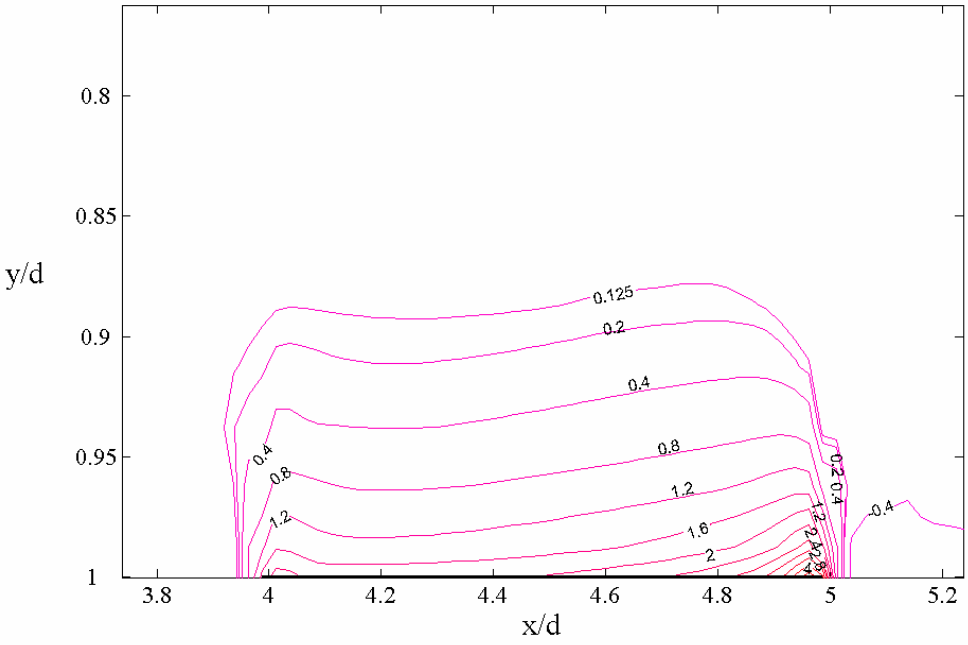

Figure 6.45 Contours net charge density around the ground electrode (Stratified liquid/vapor with minimum drag electrodes)

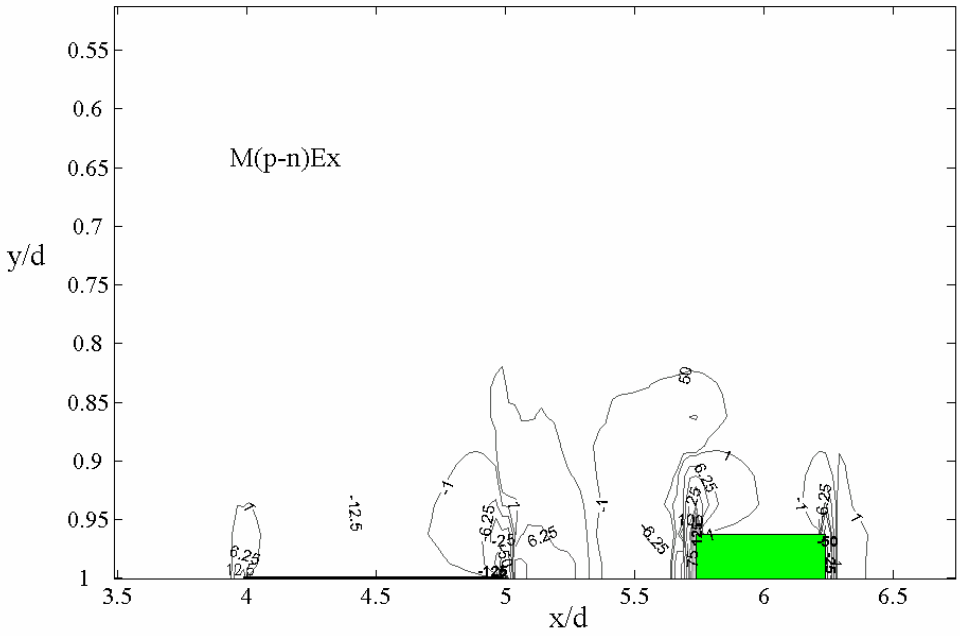

Figure 6.46 Contours of streamwise body-force (Stratified liquid/vapor with minimum drag electrodes)

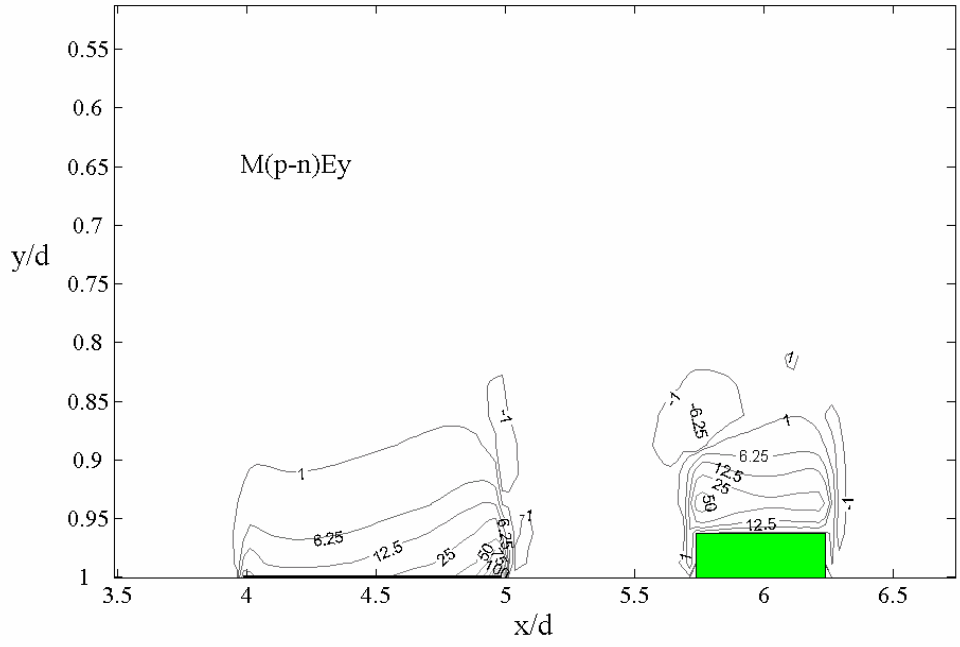

Figure 6.47 Contours of normal body-force (Stratified liquid/vapor with minimum drag electrodes)

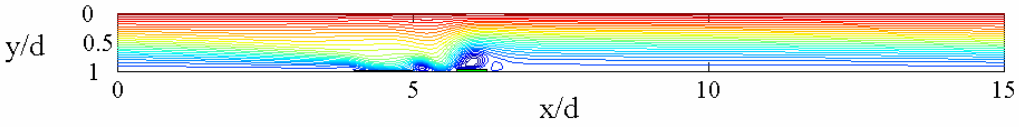

Figure 6.48 Streamlines (Stratified liquid/vapor with minimum drag electrodes)

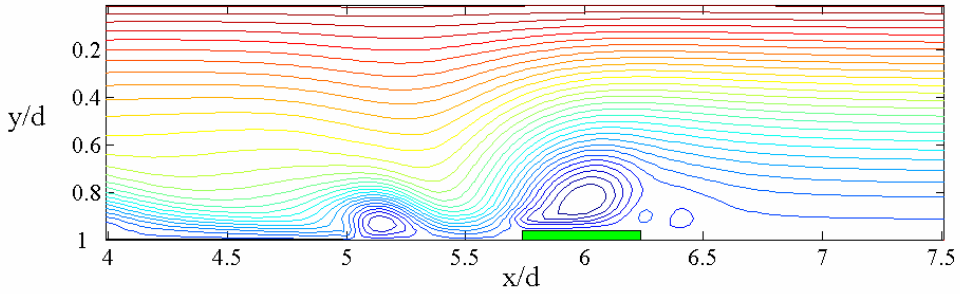

Figure 6.49 Streamlines enlarged near the electrodes (Stratified liquid/vapor with minimum drag electrode)

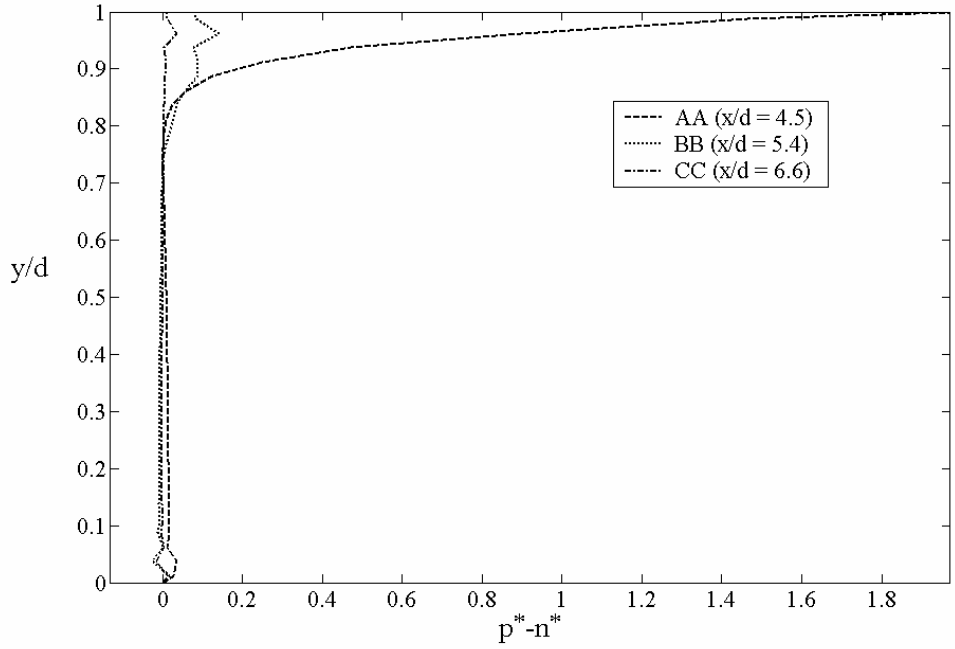

Figure 6.50 Net charge density profiles (Stratified liquid/vapor with minimum drag electrodes)

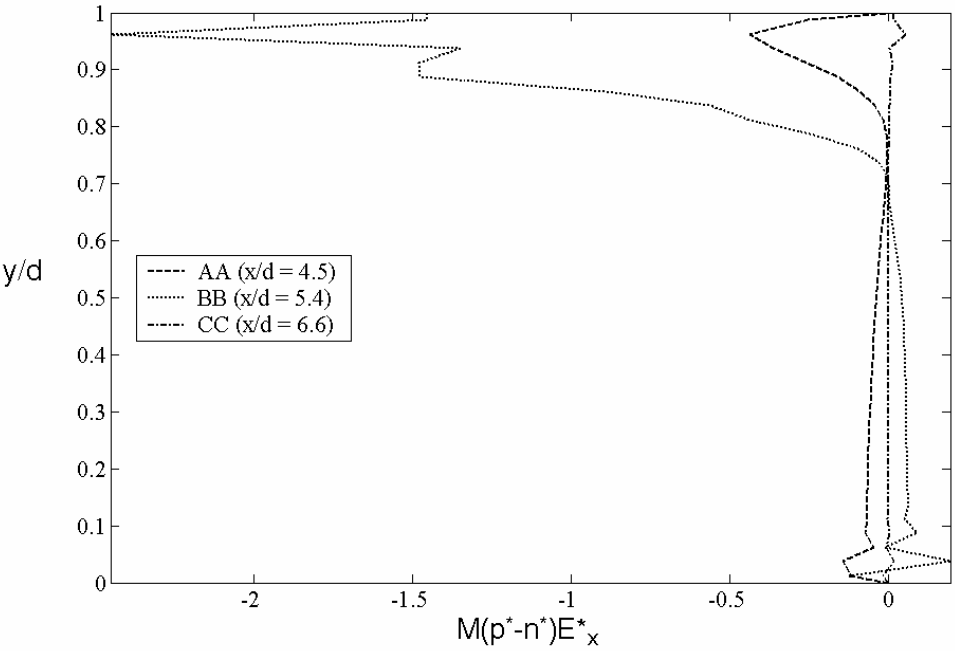

Figure 6.51 Streamwise body-force profiles (Stratified liquid/vapor with minimum drag electrodes)

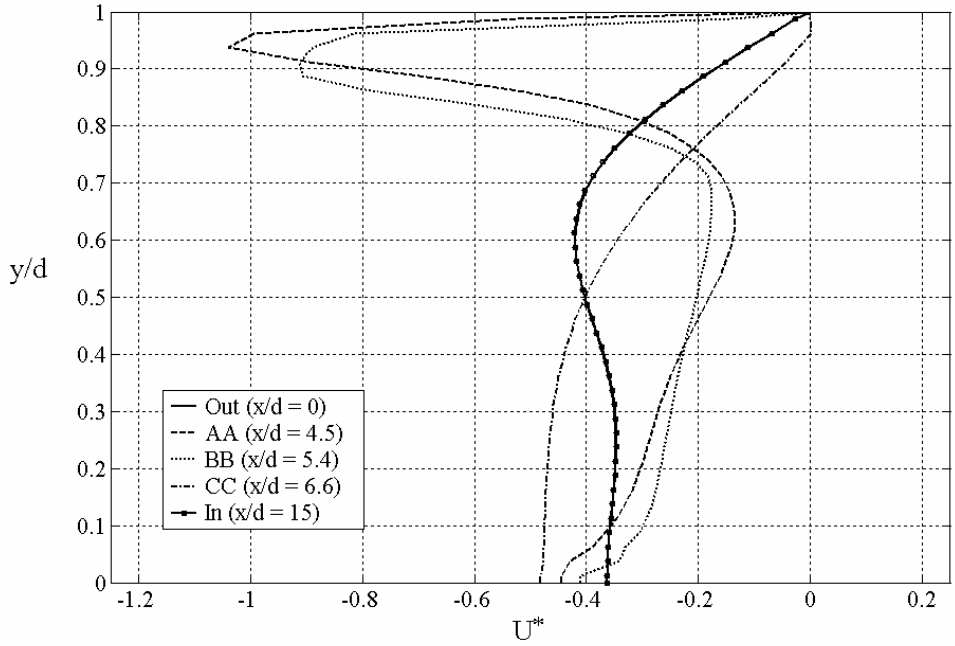

Figure 6.52 Streamwise velocity profiles (Stratified liquid/vapor with minimum drag electrodes)

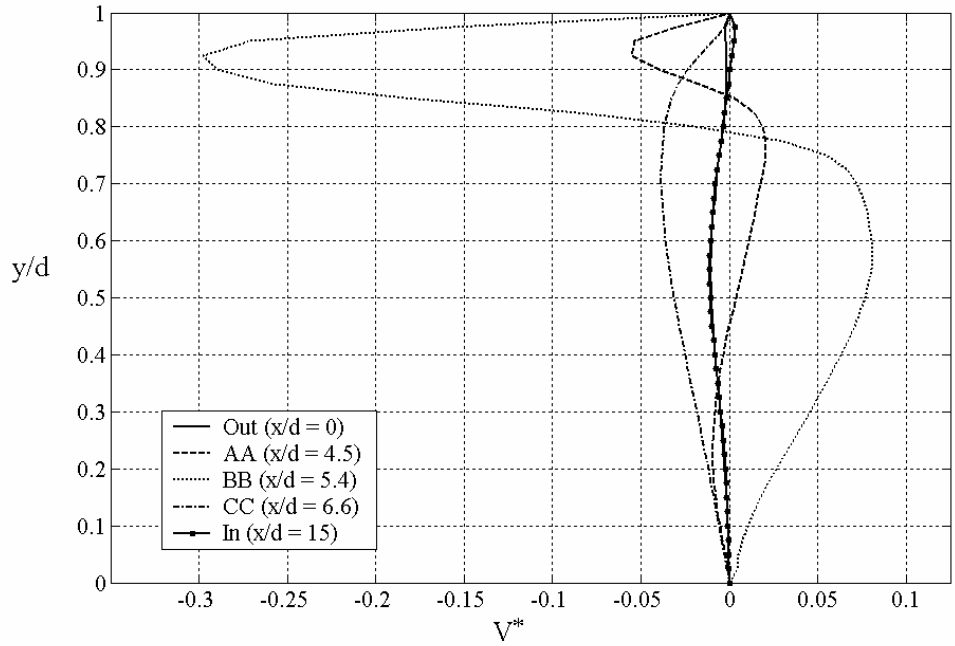

Figure 6.53 Normal velocity profiles (Stratified liquid/vapor with minimum drag electrodes)

imposed at the centerline resulted in asymptotic value of one away from the electrodes and the heterocharge layers. Consequently, identical results to the stratified liquid/vapor medium for the two electrode designs were generated. The exception is for the streamwise velocity profiles U where different values for the dimensionless average velocity at the channel exist are generated. At this stage it is not clear if the difference is due to the imposed boundary conditions or numerical artifacts.

CHAPTER VII

CONCLUSIONS AND RECOMMENDATIONS

Conclusions

The main focus of this research has been to provide an in-depth fundamental understanding for EHD induction and conduction pumping mechanisms. For this purpose theoretical and numerical studies for both cases were conducted.

EHD Induction Pump

EHD induction pumping of liquid film in an annular vertical and horizontal configuration was studied theoretically as well as numerically. A non-dimensional model accounting only for electric shear stress at the liquid/vapor interface for three electrode configurations of attraction and repulsion pumping modes was developed (i.e. Analytical Model) for horizontal configuration. For the Analytical Model the effects of the non-dimensional parameters on the non-dimensional interfacial velocity were studied to illustrate the pump performance at different operating conditions. The non-dimensional parameters were determined to be the angular electric wave velocity, electric conductivity, dielectric constant, vapor radius, and liquid film thickness.

The relations between the non-dimensional angular electric wave velocity and the interfacial liquid film velocity were presented. An optimum value of an angular electric wave velocity exists for all three electric configurations considered. When the angular electric wave velocity is small, the electric shear stress acting at the interface is small too; therefore small interfacial velocity is generated. On the other hand, if the angular

electric wave velocity becomes too large, charges at the interface are unable to follow the electric wave effectively, resulting again in a small interfacial velocity.

The dependency of the interfacial velocity on the non-dimensional electric conductivity showed a similar trend (i.e. an optimum conductivity level exists for all three configurations considered). If the conductivity level is too small, no charges relax to the interface and hence no interaction with the electric wave is possible. However, in a liquid with high electric conductivity, the charges are allowed to move freely into positions directly aligned against the oppositely or similarly charged electrodes, resulting in a perpendicular electric field with no electric shear.

In attraction pumping mode, the interfacial velocity reduces as the dielectric constant increases, while an optimum value for the dielectric constant do exist for the repulsion mode pumping.

The attraction and repulsion pumping responded differently to the changes on the vapor radius and liquid film thickness. For the attraction pumping, as the liquid film thickness increases (i.e. the interfaces moves closer to the electrodes) the electric shear stress at the interface becomes stronger, however, the effect of the viscous shear stress becomes weaker, and therefore an increase in the interfacial velocity was observed. On the contrary, as the interface moves away from the surface, where the electrodes are placed, reduction in the electric shear as well as the retarding viscous shear stress is experienced by the interface. Consequently, there is an optimum liquid film thickness yielding the highest interfacial velocity. However, due to the nature of the annular

regime the liquid film thickness is small (i.e. not more than 10% to 20% of the total radius); therefore the above discussions are limited to this range.

Form this study, it was concluded that the repulsion pumping mode is the most practical configuration, and consequently the Analytical Model was extended to a vertical configuration to study the stability of EHD induction pumping of liquid film in vertical annular configuration in the presence of gravity. The pump operation is called stable when only one real solution exists, whereas when more than one real solution exists the pump is termed unstable. A guaranteed stability criterion for repulsion mode pumping was determined. The criterion depends on the non-dimensional conductivity, non-dimensional liquid thickness, vapor radius, total radius, and dielectric constant. Because it is relatively difficult to change the dielectric constant of a working fluid compared to the electric conductivity, and since in an actual EHD induction pump the total radius is often fixed, therefore the guaranteed stability of an induction pump depends on the non-dimensional electric conductivity and liquid film thickness. A stability map for non-dimensional conductivity and liquid film thickness was generated. It was also concluded that for a given unstable pump operation in the presence of external load, the operation can be stabilized by increasing the electric wave angular velocity by simply increasing the frequency above a certain threshold value. It was found that as the magnitude of the non-dimensional gravitational force density decreases, the electric wave angular velocity threshold increases. This implies that the gravitational force density assists the stabilization of the pump operation.

A Numerical Model was developed for EHD induction pumping of liquid film in vertical annular configuration accounting for the electric shear stress at the liquid/vapor interface as well as through the bulk of the liquid film. Charges are induced in the bulk due to electric conductivity gradient arising from a gradient of temperature across the liquid film. The Numerical Model was compared to the Analytical Model and it was extended for external configuration for comparison with the model developed by [9] for stratified liquid/vapor medium. Excellent agreement between both models was achieved.

A parametric study was conducted (for R-123) to evaluate the significance of the bulk effects in comparison to the interfacial effect for four cases: 1) a uniform temperature profile at the entrance and the Joule heating is set to zero; 2) a uniform temperature profile at the entrance (Profile No. 1) and the Joule heating present; 3) a linear temperature profile at the entrance (Profile No. 2) resulting in 21.0 ^{o}C at the pipe wall and 19.0 ^{o}C at the liquid/vapor interface, and producing an average entrance temperature of 20.0 ^{o}C; 4) numerical solutions with a linear temperature profile at the entrance (Profile No. 3) resulting in 25.0 ^{o}C at the pipe wall and 19.0 ^{o}C at the liquid/vapor interface, and producing an average entrance temperature of 22.0 ^{o}C. While the first two cases were presented to study the effect of the Joule heating on the pump performance, the last two were presented to illustrate the effect of the temperature gradient coupled with Joule heating on the pump performance. The parametric study was presented for both thin and thick film thickness, reflecting realistic thicknesses for pure pumping applications of a liquid/vapor vertical annular configuration.

The numerical results indicated that for the electric conductivity and voltage level of interest, including the Joule heating proved to be insignificant. In addition, the results showed that higher mass flow rate can be achieved by increasing the voltage, pipe diameter, fluid temperature, and also by increasing the positive external pressure gradient (note that, in this study the pump operated in repulsion mode). On the other hand, negative external pressure load, at certain level and beyond, yielded flow reversal or bi-directional flow, which is potentially undesirable. The entrance temperature profile played an important role in the operation of the pump and it is effect is more noticeable closer to the wall, where the electrodes are positioned. It was also observed that the effect of the temperature profile on the induced charges is more significant when the film thickness is thicker (i.e. viscous effect is weaker). In addition, it was shown that the bulk effects play a significant role at high non-dimensional wave number (i.e. smaller wavelength). It was concluded that the gravitational force could easily dominate the effect of the electric shear stress.

EHD Conduction Pump

The EHD pumping based on conduction phenomenon was theoretically and numerically investigated to illustrate the generation of net flow in a channel for single phase as well as a stratified liquid/vapor medium. The governing equations for the theoretical model of conduction pumping mechanism were developed and the numerical solutions were presented in dimensionless forms to illustrate the effects of the controlling parameters on the generated flow. The electric potential, electric field,

charge density, electric body force, and velocity distributions in the region between the two electrodes were presented. The numerical results confirmed the presence of net flow generation based on the EHD conduction phenomenon. In addition, an innovative electrode design of having electrodes embedded in the channel walls, utilizing EHD conduction phenomenon, was theoretically and numerically demonstrated to generate net flow.

Recommendations

A number of simplifying assumptions were made during the development of the Analytical and Numerical Models for EHD induction pumping presented in this study. A more comprehensive model would have to account for the presence of surface waves at the interface. In addition, in the presence of a phase change the change in the liquid film thickness should be included. Turbulent effects need to be incorporated in order to allow for more precise agreement between the experimental observations available in the literature and theoretical model. Additionally, the stability analysis was conducted based on isothermal cases. However, consideration of temperature effect in the stability analysis could improve the model. Nevertheless, the presented models provide very valuable tools to design EHD induction pump. The stability analysis presented provides a mean to fundamentally understand the erratic behavior of the EHD induction pump operation and to improve the pump performance. However, a more inclusive model will provide a more accurate tool for the electrode design.

In the EHD conduction side more research is needed on the parameters determining the performance of the pump. Parametric study including the electrical and thermophysical properties of the working fluid as well as the geometric parameters of the electrode will be a valuable addition. Investigating two-phase EHD conduction pumping with respect to the phase change and presence of heat transfer and temperature gradient is also needed. This will serve as a valuable source to select optimum working fluids and improve the electrode design for EHD conduction pump. Nevertheless, the work presented in this study proves and confirms the EHD conduction phenomena.

REFERENCES

[1] Castellanos, A., 1998, "Basic Concepts and Equations in Electrohydrodynamics," *Electrohydrodynamics,* edited by A. Castellanos, Springer, New York, pp. 2-19.

[2] Melcher, J.R., 1981, *Continuum Electromechanics*, MIT Press, Cambridge, MA

[3] Melcher, J. R., 1966, "Traveling-Wave Induced Electroconvection," Physics of Fluids, **9**(8), pp. 1548-1555.

[4] Crowley, J.M., 1980, "The Efficiency of Electrohydrodynamic Pumps in the Attraction Mode," Journal of Electrostatics, **8**, pp. 171-181.

[5] Crowley, J.M., 1983, "Stability of EHD Induction Pumps," *IEEE-IAS Annual Meeting*, Mexico City, Mexico, pp. 1149-1153.

[6] Melcher, J.R., and Firebaugh, M.S., 1967, "Traveling-Wave Bulk Electroconvection Induced across a Temperature Gradient," Physics of Fluids, **10**(6), pp. 1178-1185.

[7] Kuo, B.S., Chato, J.C., and Crowley, J.M., 1984, "Temperature Induced Electrohydrodynamic Pumping in Horizontal Pipes," ASME Journal of Heat Transfer, **106**, pp.78-84.

[8] Seyed-Yagoobi, J., Chato, J. C., Crowley, J. M., and Krein, P. T., 1989, "Induction Electrohydrodynamic Pump in a Vertical Configuration, Part 2 - Experimental Study," ASME Journal of Heat Transfer, **111**, pp. 670-674.

[9] Wawzyniak, M. and Seyed-Yagoobi, J., 1999, "An Analytical Study of Electrohydrodynamic Induction Pumping of a Stratified Liquid/Vapor Medium," IEEE Transactions on Industry Applications, **35**(1), pp. 231-239.

[10] Wawzyniak, M. and Seyed-Yagoobi, J., 1999, "Stability of Electrohydrodynamic Induction Pumping of a Stratified Liquid/Vapor Medium in the Presence of an External Load," IEEE Transactions on Industry Applications, **35**(5), pp. 1211-1217.

[11] Wawzyniak, M. and Seyed-Yagoobi, J., 2001, "Electrohydrodynamic Induction Pumping of a Stratified Liquid/Vapor Medium in the Presence of Volumetric and Interface Electric Charges," IEEE Transactions on Industry Applications, **37**(4), pp. 950-958.

[12] Brand, K and Seyed-Yagoobi, J., 2002, Effect of Electrode Configuration on Electrohydrodynamic Induction Pumping of a Stratified Liquid/Vapor Medium," IEEE Transactions on Industry Applications, **38**(2), pp. 389-400.

[13] Kervin, D.J., Crowley, J.M., Krein, P., and Chato, J.C., 1981, “Parametric Studies of a Large Thermal EHD Induction Pump,” *Conference Record, IEEE-Industry Applications Society Annual Meeting*, New York, pp. 1015-1020.

[14] Seyed-Yagoobi, J., Chato, J. C., Crowley, J. M., and Krein, P. T., 1989, “Induction Electrohydrodynamic Pump in a Vertical Configuration, Part 1 - Theory,” ASME Journal of Heat Transfer, **111**, pp. 664-669.

[15] Wawzyniak, M., Seyed-Yagoobi, J., and Morrison, G.L., 2000, "An Experimental Study of Electrohydrodynamic Induction Pumping of a Stratified Liquid/Vapor Medium," ASME Journal of Heat Transfer, **122**, pp. 200-203.

[16] Brand, K. and Seyed-Yagoobi, J., 2003, “Experimental Study of Electrohydrodynamic Induction Pumping of a Dielectric Micro Liquid Film in External Horizontal Condensation Process,” ASME Journal of Heat Transfer, **125**, pp. 1-10.

[17] Stuetzer, O.M., 1959, “Ion Drag Pressure Generation,” Journal of Applied Physics, **30**(7), pp. 984-994.

[18] Stuetzer, O.M., 1960, “Ion Drag Pumps,” Journal of Applied Physics, **31**(1), pp. 136-146.

[19] Pickard, W.F., 1963, “Ion Drag Pumping. II. Experiment,” Journal of Applied Physics, **34**(2), pp. 251-258.

[20] Halpern, B. and Gomer, R., 1969, “ Field Emission in Liquids,” Journal of Chemical Physics, **51**(3), pp. 1031-1047.

[21] Halpern, B. and Gomer, R., 1969, “ Field Ionization in Liquids,” Journal of Chemical Physics, **51**(3), pp. 1048-1056.

[22] Crowley, J.M., Wright, G.S., and Chato, J.C., 1990, “Selecting a Working Fluid to Increase the Efficiency and Flow Rate of an EHD Pump,” IEEE Transactions on Industry Applications, **26**(1), pp. 42-49.

[23] Bryan, J.E. and Seyed-Yagoobi, J., 1991, “Experimental Study of Ion-drag Pumping Using Various Working Fluids,” IEEE Transactions on Electrical Insulation, **26**(4), pp. 647-655.

[24] Castaneda, J.A., 1992, “Fundamental and Experimental Studies of Ion-Drag Pumping,” M. S. thesis, Department of Mechanical Engineering, Texas A&M University, College Station, TX.

[25] Seyed-Yagoobi, J., Bryan, J.E., and Castaneda, J.A., 1995, “Theoretical Analysis of Ion-Drag Pumping,” IEEE Transactions on Industry Applications, **31**(3), pp. 469-476.

[26] Atten, P. and Seyed-Yagoobi, J., 2003, “Electrohydrodynamically Induced Dielectric Liquid Flow Through Pure Conduction in Point/plane Geometry,” IEEE Transactions on Dielectric and Electric Insulation, **10**(1), pp. 27-36.

[27] Jeong, S.I. and Seyed-Yagoobi, J., 2002, “Experimental Study of Electrohydrodynamic Pumping Through Conduction Phenomenon,” Journal of Electrostatics, **56**, pp. 123-133.

[28] Schmidt, W.F., 1984, “Electronic Conduction Process in Dielectric Liquids,” IEEE Transactions on Electrical Insulation, **EI-19**(5), pp. 389-418.

[29] Zhakin, A.I., 1998, “Conduction Models in Dielectric Liquids,” *Electrohydrodynamics*, edited by A. Castellanos, Springer, New York, pp. 103-120.

[30] Sato, M., Yabe, A., and Taketani, T., 1991, ”Heat Transfer Enhancement by Applying an Electro-hydrodynamical Pump Utilizing Dielectrophoretic Force,” *Proceedings of ASME/JSME Thermal Engineering*, **3**, pp. 3-8.

[31] Bryan, J.E. and Seyed-Yagoobi, J., 1997, “Heat Transport Enhancement of Monogroove Heat Pipe with Electrohydrodynamic Pumping,” AIAA Journal of Thermophysics and Heat Transfer, **11**(3), pp. 454-460.

[32] Felici, N.J., 1971, “D.C. Conduction in Liquid Dielectrics(Part I),” Direct Current, **2**(3), pp. 90-99.

[33] Felici, N.J., 1971, “D.C. Conduction in Liquid Dielectrics(Part II),” Direct Current, **2**(4) , pp. 147-165

[34] Pontiga, F. and Castellanos, A., 1992, “ The Onset of Electrothermal Convection in Nonpolar Liquids on the Basis of a Dissociation-Injection Conductivity Model,” IEEE Transactions on Industry Applications, **28**(3), pp. 520-527.

[35] Pontiga, F. and Castellanos, A., 1996, “ Electrical Conduction of Electrolyte Solutions in Nonpolar Liquids,” IEEE Transactions on Industry Applications, **33**(4), pp. 816-824.

[36] Maekawa, T., Haga, M., and Tanasawa, I., 1993, “Study on EHD Convection,” *Proceedings of the Third World Conference on Experimental Heat Transfer, Fluid Mechanics and Thermodynamics*, Honolulu, HI, Oct./Nov., **1**, pp. 164-171.

[37] Jeong, S.I., Seyed-Yagoobi, J., and Atten, P., 2003, "Theoretical/Numerical Study of Electrohydrodynamic Pumping Through Conduction Phenomenon," IEEE Transactions on Industry Applications, **39**(2), pp. 355-361.

[38] Jeong, S.I., and Seyed-Yagoobi, J., 2004, "Fluid Circulation in an Enclosure Generated by Electrohydrodynamic Conduction Phenomenon," IEEE Transactions on Dielectric and Electric Insulation, **11**(5), pp. 899-910.

[39] Jeong, S.I., Seyed-Yagoobi, J., 2003, "Innovative Electrode Designs for Electrohydrodynamic Conduction Pumping," IEEE Transactions on Industry Applications, **40**(3), pp. 900-904.

[40] Feng, Y., and Seyed-Yagoobi, J., 2004, "Understanding of Electrohydrodynamic Conduction Pumping Phenomenon," Physics of Fluids, **16**(7), pp. 2432-2441.

[41] Bryan, J.E., 1998, "Fundamental Study of Electrohydrodynamically Enhanced Convective and Nucleate Boiling Heat Transfer," Ph.D. dissertation, Department of Mechanical Engineering, Texas A&M University, College Station, TX.

[42] Seyed-Yagoobi, J., 1984, "Theoretical, Numerical, and Experimental Study of Electrohydrodynamic Pumping in Vertical Configuration," Ph.D. dissertation, Department of Mechanical Engineering, University of Illinois, Urbana-Champaign, IL.

[43] Gallagher, T.J., 1975, *Simple Dielectric Liquids – Mobility, Conduction, and Breakdown*, Oxford University Press, J.W. Arrowsmith Ltd., Bristol, Great Britain.

[44] Yang, C. and Li, D., 1998, "Analysis of Electrokinetic Effects on the Liquid Flow in Rectangular Microchannels," Colloids and Surfaces, A : Physico-chemical and Engineering Aspects, **143**, pp. 339-353.

[45] Richter, A., Plettner, A., Hofmann, K.A., and Sandmaier, H., 1991, "A Micromachined Electrohydrodynamic (EHD) Pumping," Sensors and Actuators, **A. 29**, pp. 159-168.

[46] Datta, S., 2004, "Theoretical and Numerical Study of Flow Generation Through Electrohydrodynamic Conduction Pumping," M.S. thesis, Department of Mechanical Materials, and Aerospace Engineering, Illinois Institute of Technology, Chicago, IL.

[47] Onsager, L., 1934, "Deviations from Ohm's Law in Weak Electrolytes," Journal of Chemical Physics, **2**, pp. 599-615.

[48] Langevin, P., 1903, "Recombinaison et mobilites des ions dans les gaz," Annales de Chimie et de Physique, **28**, pp. 433.

[49] Crowley, J.M., 1985, *Fundamental of Applied Electrostatics*, John Wiley & Sons, New York.

[50] Patankar, S.V., 1980, *Numerical Heat Transfer and Fluid Flow*, Hemisphere Publishing Corporation, Washington, DC.

VITA

Salem A. S. Al Dini was born on October 10, 1971 in Riyadh, Saudi Arabia. He began his undergraduate studies in mechanical engineering at King Fahad University of Petroleum and Minerals in 1988. He received his Bachelor of Science degree in mechanical engineering in January 1994. He began his master's in mechanical engineering at King Fahad University of Petroleum and Minerals in September of 1994 and completed all the requirements in August 1997. His master's research was to investigate experimentally the effect of pulsation on heat transfer characteristics in pipes. After his master course, he worked as lecturer in King Fahad University of Petroleum and Minerals for two years. He taught fluid mechanics, material science, heat transfer, and thermodynamics.

He started his Ph.D. under the guidance of Professor Jamal Seyed-Yagoobi at Texas A&M University, College Station, in August of 1999 and received his degree in December 2005. His Ph.D. research has been a theoretical and numerical study of electrohydrodynamic pumping through induction and conduction phenomenon.

He can be reached at:

ME Dept, KFUPM, Box 5069

Dhahran 31261, Saudi Arabia

Tel: 00-966-03-860-2540

Fax: 00-966-03-860-2949

Salem_aldini@yahoo.com